INAUGURAL - DISSERTATION

zur
Erlangung der Doktorwürde
der
Gesamtfakultät für Mathematik,
Ingenieur- und Naturwissenschaften der
Ruprecht-Karls-Universität
Heidelberg

vorgelegt von
M.Sc. Diana Kreitmayer
aus Ingolstadt, Deutschland

Tag der mündlichen Prüfung: 08.07.2022

Computational Fluid Dynamics Simulations of Single-Use Bioreactors for the Scale-Up of Cell Culture Processes

Gutachter: Prof. Dr. Eva Gutheil
Dr. Nora A. Urbanetz

Abstract

Monoclonal antibodies are biomolecules that are able to bind to a specific antigen. Antibodies are important drugs for the targeted treatment of various types of cancer. Due to their complex molecular structure, monoclonal antibodies are usually produced through the cultivation of genetically modified mammalian cells.

At the production scale, the cultivation is typically carried out using sparged stirred tank bioreactors and the product quality as well as the yield depend, among other factors, on the hydrodynamic conditions inside the utilized bioreactor. The optimization of cell cultivation for the production of monoclonal antibodies is of high economical importance for the pharmaceutical industry. The simulation of the flow field inside the utilized bioreactors with computational fluid dynamics enables the prediction of relevant process characteristics, which must be considered during the scale-up of cell culture processes.

The focus of the present study is on the hydrodynamic characterization and the selection of the operating conditions during scale-up of the cell culture processes of four single-use bioreactors with varying sizes ranging from the lab-scale to the production scale, the Mobius® CellReady 3 L, the Xcellerex™ XDR-10, the Xcellerex™ XDR-200, and the Xcellerex™ XDR-2000. Additionally, the hydrodynamic characteristics of a miniaturized stirred tank bioreactor, the Ambr®250, and another of the Xcellerex™ bioreactors, the Xcellerex™ XDR-500, are investigated. The simulations have been carried out with the Euler-Euler and the Euler-Lagrange approaches with the open source software OpenFOAM and the commercial software MixIT. The considered process characteristics include the mixing time, the hydrodynamic stress, the average strain rate in the impeller zone, and the volumetric oxygen mass transfer coefficient. These are representing the homogenization in the liquid phase, the mechanical stress acting on the cultivated cells and the availability of oxygen, which is essential for aerobic organisms. Only through the hydrodynamic characterization of the different bioreactors can the causal relationship of the bioreactor operating conditions like the impeller speed, the working volume, and the sparging strategy with the process performance of the cell cultivation be understood, which is required for the optimization of operating conditions for the different bioreactors.

For larger biroeactor volumes an increase in the mixing time cannot be avoided, whereas a similar maximum hydrodynamic stress, a similar average strain rate of the impeller zone, and a similar volumetric oxygen mass transfer coefficient are observed for all investigated bioreactors. To optimize mixing without risking cell damage, the maximum tolerable average strain rate of the impeller zone is selected as the scale-up criterion for the impeller speed. Experimental cell culture results provided by Yuichi Aki from Daiichi-Sankyo Japan support the suitability of this criterion through a successful scale-up of the cell cultivation from the Mobius® CellReady 3 L to the Xcellerex™ XDR-200. Other typical scale-up criteria like the volumetric power input and the impeller tip speed result in lower impeller speeds than the with presented strategy, therefore appearing less suitable to optimize the mixing time during scale-up. This emphasizes the advantages of a detailed hydrodynamic analysis over classical scale-up parameters.

Zusammenfassung

Monoklonale Anitkörper sind Biomoleküle, die in der Lage sind an ein bestimmtes Antigen zu binden. Antikörper sind wichtige Medikamente für die zielgerichtete Behandlung verschiedener Krebsarten. Aufgrund ihrer komplexen Molekülstruktur, werden monoklonale Antikörper üblicherweise durch die Kultivierung gentechnisch veränderter Säugetierzellen hergestellt.

Im Produktionsmaßstab wird die Kultivierung typischerweise mittles begaster Rührkessel-Bioreaktoren durchgeführt und die Produktqualtiät und -ausbeute hängen, neben anderen Faktoren, von den hydrodynamischen Bedingungen innerhalb des verwendeten Bioreaktors ab. Die Optimierung der Zellkultur zur Produktion monoklonaler Antikörper hat hohe wirtschaftliche Bedeutung für die pharmazeutische Industrie. Die Simulation des Strömungsfelds innerhalb der verwendeten Bioreaktoren mittels numerischer Strömungsmechanik ermöglicht die Vorhersage relevanter Prozesscharakteristika, welche bei der Maßstabsübertragung von Zellkulturporzessen berücksichtigt werden müssen.

Der Fokus der vorliegende Studie ist die hydrodynamischen Charakterisierung und die Auswahl der Betriesbedingungen im Zuge der Maßstabsvergrößerung von Zellkulturprozessen von vier Einwegbioreaktoren verschiedener Größen vom Labormaßstab bis zum Produktionsmaßstab, dem Mobius® CellReady 3 L, dem Xcellerex™ XDR-10, dem Xcellerex™ XDR-200, und dem Xcellerex™ XDR-2000. Zusätzlich, werden die hydrodynamischen Charakterisitka eines miniaturisierten Rührkesselbioreaktors, dem Ambr®250, und eines weiteren der Xcellerex™ Bioreaktoren, dem Xcellerex™ XDR-500, untersucht. Die Simulationen werden mit der Euler-Euler Methode und mit der Euler-Lagrange Methode mit der open source Software OpenFOAM und der kommerziellen Software MixIT durchgeführt. Die betrachteten Prozesscharakteristika beinhalten die Mischzeit, den hydrodynamischen Stress, die mittlere Beanspruchungsrate in der Rührerzone und den volumenbezogenen Sauerstoffübergangskoeffizienten. Diese repräsentieren die Homogenisierung in der Flüssigphase, die mechanische Beanspruchung der Zellen und die Verfügbarkeit von Sauerstoff, welcher für aerobe Organismen essentiell ist. Nur durch die hydrodynamische Charakterisierung der verschiedenen Bioreaktoren kann der kausale Zusammenhang der Betriebsbedingungen wie der Rührergeschwindigkeit, dem Arbeitsvolumen und der Begasungsstrategie mit der Porzessleistung der Zellkultur verstanden werden, was notwendig ist für die Optimierung der Betriebsbedingunen für die verschiedenen Bioreaktoren.

Mit größerem Bioreaktorvolumen kann ein Anstieg der Mischzeit nicht vermieden werden, während ein ähnlicher maximaler hydrodynamischer Stress, eine ähnliche mittlere mechanische Spannung der Rührerzone und ein ähnlicher volumnebezogener Sauerstoffübergangskoeffizient für alle untersuchten Bioreaktoren beobachtet werden. Um das Mischen zu optimieren ohne Zellschädigungen zu riskieren, wird die mittlere Beanspruchungsrate der Rührerzone als Kriterium zur Maßstabübertragung der Rührergeschwindigkeit ausgewählt. Experimentelle Zellkulturergebnisse, die von Yuichi Aki von Daiichi-Sankyo Japan zur Verfügung gestellt wurden, unterstützen die Eignung dieses Kriteriums durch eine erfolgreiche Maßstabsübertragung der Zellkultivierung vom Mobius® CellReady 3 L zum Xcellerex™ XDR-200. Andere typische Kriterien zur Maßstabsübertragung wie der volumenbezogene Leistungseintrag und die Rührerumfangsgeschwindigkeit ergeben geringere Rührergeschwindigkeiten und erscheinen weniger geeignet, die Mischzeit während der Maßstabsübertrangung zu optimieren. Dies unterstreicht die Vorteile einer detaillierten hydrodynamischen Charakterisierung gegenüber klassischer Kriterien zur Maßstabsübertragung.

Publications

Based on the research done for the present study the following peer-reviewed manuscripts have been published:

- D. Kreitmayer, S. R. Gopireddy, T. Matsuura, Y. Aki, Y. Katayama, T. Sawada, H. Kakihara, K. Nonaka, T. Profitlich, N. A. Urbanetz, and E. Gutheil. Numerical and experimental investigation of the hydrodynamics in the single- use bioreactor Mobius® CellReady 3 L. Bioeng., 9(5):206, 2022. doi: 10.3390/bioengineering9050206.

- D. Kreitmayer, S.R. Gopireddy, T. Matsuura, Y. Aki, Y. Katayama, T. Nakano, T. Eguchi, H. Kakihara, K. Nonaka, T. Profitlich, N. A. Urbanetz, and E. Gutheil. CFD-based and experimental hydrodynamic characterization of the single-use bioreactor Xcellerex™ XDR-10. Bioeng., 9(1):22, 2022. doi: 10.3390/bioengineering9010022.

- D. Kreitmayer, S. G. Gopireddy, T. Matsuura, Y. Aki, Y. Katayama, H. Kakihara, K. Nonaka, T. Profitlich, N. A. Urbanetz, and E. Gutheil. Numerical and experimental characterization of the single-use bioreactor Xcellerex™ XDR-200. Biochem. Eng. J., 177:108237, 2022. doi: 10.1016/j.bej.2021.108237.

Contents

1. Introduction

In contrast to chemically synthesized small molecule drugs, protein based biopharmaceuticals like antibodies or enzymes are larger and more complex. These biomolecules are produced by utilizing the pathways of biochemcial synthesis within living cells instead of chemical reactions. Especially for monoclonal antibodies, which require post-translational modifications, mammalian cell lines like Chinese hamster ovary (CHO), nonsecreting murine myeloma (NS0), and mouse hybridoma (Sp2/0) cells are the typical expression host [1, 2]. The cultivation of these cells is carried out using bioreactors. The term bioreactor encompasses a variety of different types of equipment, all with the function of providing a controlled environment well suited for the proliferation of the cultivated cells. The aspects of the environment within the bioreactor that need to be controlled include its hydrodynamic characteristics. Theses depend on the size, the configuration, and the operating conditions of the bioreactor. The present study uses computational fluid dynamics to quantify the hydrodynamic process characteristics of different geometrically dissimilar, single-used, stirred tan bioreactors, that are used to scale-up a mammalian cell cultivation from the lab to the production scale.

To put the present study into a broader context, the next section provides a brief overview on the types and functionality of commonly used bioreactors. The section thereafter gives an overview on the state-of-the-art of the scale-up strategies for the cultivation of mammalian cells in stirred tank bioreactors. The last section of this chapter summarizes the scope and goals of the present study.

1.1 Functions and Types of Bioreactors

Any type of bioreactor is a container for the cultivation medium, which is an aqueous solution that provides the cultivated cells with nutrients, vitamins, and electrolytes. To dampen pH excursions, buffers like the inorganic carbonate species are used and other additives like anti-foaming or shear protecting agents might also be included. Liquid agitation is needed for the cultivation medium to provide fast mixing for feed or base addition and achieve a homogeneous distribution of the suspended cells, nutrients and electrolytes. Since mammalian cells are aerobic, dissolved oxygen must be available and due to its low solubility in water [3, 4], a constant transfer of oxygen from the gas phase to the liquid phase is necessary. Moreover, the temperature and the pH of the cultivation medium must be controlled in narrow ranges and sterility is essential to avoid contamination with other microorganisms. Depending on the mode of growth of

the mammalian cells, i.e., freely suspended or adherent, the bioreactor must potentially also provide a surface for the cells to adhere to, which can either be the bioreactor wall, when using roller bottles, or suspended solid particles when using micro carriers for stirred tanks [5]. The current work is focused on freely suspended cells, since they are the more commonly used type [5]. The different types of bioreactor s can be grouped by their mode of operation into externally agitated, internally agitated and pneumatically agitated bioreactors [6, 7].

Externally agitated micro-well plates with up to several milliliters of culture volume can be used for cell cultivation at the very small scales and for slightly larger volumes up to several hundred milliliters shake flasks are available [8, 9]. Both are sterile vessels and external agitation for mixing as well as the temperature control are provided through an incubator. Although new monitoring devices are promising, typically the dissolved oxygen tension and pH are not monitored [9, 10]. Some control over the culture pH is possible trough the partial pressure of carbon dioxide in the incubator and the use of carbonate buffer systems. A larger variant of externally agitated bioreactors with volumes of up to 500 L are wave-bag bioreactors, which consist of a disposable bag placed on a rocker and which are equipped with sensors for the control of the temperature, the dissolved oxygen tension, and the pH [6, 11]. Similar to the smaller micro-well and shake flask systems, oxygen is only transfered through the liquid surface.

Internally agitated stirred tank bioreactors are the most commonly used type of bioreactors for cell cultivation at large scales [12, 1, 13]. The internal mechanical agitation is provided by one one or more impellers and oxygen can be supplied to the liquid through the liquid surface and in even larger amounts through bubbles generated by submerged sparging. Stirred tank bioreactors are typically equipped with sensors for the temperature, the pH, and the dissolved oxygen tension, which are controlled through heating or cooling, base or acid addition and adjustments to the gas flow and/or impeller speed, respectively. For process screening, miniaturized bioreactors down to several milliliters of volume are also available [14, 15, 16].

Another type of bioreactors are bubble columns and air-lift bioreactors, which are pneumatically agitated by the bubbles generated through sparging from the bottom without any mechanical agitation. Bubble column reactors are available for a wide range of process scales but are mainly used for microbial fermentation and thus not discussed further [17, 12].

The different types of bioreactors can also be categorized into multi-use and single-use bioreactors. Multi-use bioreactors are made out of glass and/or stainless steel and require cleaning and sterilization between cultivation runs. In contrast, single-use bioreactors have pre-sterilized vessels, typically rigid plastic vessels for small volumes and flexible cultivation bags placed in a solid vessel frame for larger volumes that are exchanged after each cultivation run [6]. Micro-well and wave-bag bioreactors are single-use bioreactors, while for shake flasks, bubble columns and stirred tank bioreactors both types are available [7, 8]. Currently, stirred tank single-use bioreactors are available up to a maximum volume of 4,000 L [6]. The hydrodynamic process characteristics relevant for cell culture are dependent on the configuration and size of the bioreactor and are not affected by the bioreactor being manufacture as a single-use or multi-use bioreactor [18].

The same engineering parameters that are used for multi-use bioreactors can also be applied to the characterization of single-use bioreactors [19]. Stirred tanks have been extensively studied, however, their standard configuration typically considers a baffled vessel with one or more impellers on a central shaft [20]. Baffles are static internals that suppress vortex formation. Many single-use stirred tank bioreactors have different designs [7] and in contrast to multi-use bioreactors there is little scope for customization. Instead, the cell culture relevant process characteristics are mainly adjusted through the operating conditions. The characterization of all considered bioreactors is needed to successfully transfer cell cultivations between different process scales. The next section will provide and overview of scale-up considerations for stirred tank bioreactors.

1.2 Cell Culture Scale-Up in Stirred Tank Bioreactors

Scale-up of a cell cultivation process from the initial lab-scale to the final production scale is an essential task during late stage process development after other aspects like the cell line and media composition have been decided. The goal is to increase the product amount through an increased cultivation volume without any losses in quality or yield [21]. The scale-up of cell cultivation has already been studied in the 1960's [22], and while there has been much progress in cell culture process technology with tremendously higher cell densities and product titers [5], scale-up is still investigated today [23, 24, 8, 25], since with the huge variety of available bioreactors and cultivated organisms no universal scale-up strategy, which would be applicable to any process has been identified. Typically the scale-independent operating parameters like medium composition and the set points for the temperature, the pH, and the dissolved oxygen tension are kept constant when the cell culture process is transferred to increasingly larger bioreactor scales, whereas scale-dependent operating parameters like the impeller speed and the sparging rate are set in a way that keeps one or more of the selected scale-up criteria at the specified level [1, 26, 27, 28, 29, 30].

The selection of these scale-up criteria is connected to their impact on the cultivation process. The three process aspects that are important are the oxygen supply to the liquid, which is represented by the volumetric oxygen mass transfer coefficient, the homogenization of the liquid phase considered through the mixing time, and avoiding cell damage through the mechanical stress caused by the liquid motion. These three aspects are important for any cultivated organism, however, the suitable process ranges and the typical bioreactor designs vary with the type of the cultivated organism. While bacterial cells like *Escherichia coli* and yeast cells like *Saccheromyces cerevisiae* are considered to be robust due to their cell wall, their fast growth and high cell densities result in overall high oxygen demands and the risk of concentration gradients of the nutrients and the dissolved oxygen tension is high [21, 31, 32, 25]. Consequently, harsher process conditions with a higher volumetric power input and higher sparging rates for faster mixing and higher oxygen transfer are used for these kind of cells. For filamentous microorganisms, the mechanical forces in the liquid and liquid mixing

must be more finely controlled as their morphology impacts the liquid rheology but at the same time the morphology of filamentous organisms is affected by the liquid agitation [33, 25].

In contrast to microbial cells, mammalian cells do not have a cell wall and are consequently more sensitive to mechanical forces. While this aspect may have been overemphasized in the past [34, 13], their overall lower growth rates and lower cell densities also result in lower oxygen demand [35] and much gentler agitation conditions are typical. Current concerns on the homogenization within the bioreactor are mainly focused on pH overshoots due to the addition of the base solution for pH control, whereas issues with substrate concentration gradients are unlikely because of the lower cell densities and and metabolic rates of mammalian cells [31, 36, 37] compared to microbial cells. However, with increasing cell densities knowing the upper limits of tolerable mechanical force and the corresponding impeller speed becomes more important to improve both oxygen transfer and mixing [30, 38].

Due to the differences in the cultivated organisms, scale-up studies for mammalian cells, which are the focus of the present study, investigate different bioreactor configurations and process ranges than similar work on microbial cells. Nonetheless, the considered scale-up criteria and empirical correlations are applicable to stirred tank bioreactors in general.

The selection of the scale-up criterion is critical for successful scale-up and possible criteria include but are not limited to the volumetric power input, the impeller tip speed, the mixing time, the maximum shear rate, maximum hydrodynamic stress, the volume specific sparging rate, the superficial gas velocity and the volumetric mass transfer coefficients for oxygen and carbon dioxide [20, 39, 28, 21, 40]. The success of scale-up studies is typically judged by the cell densities and viabilities as well as the product titer and quality observed across the different scales [1, 26, 27, 28, 29, 30, 23, 24, 41, 40].

The volumetric power input and the impeller tip speed are typical scale-up criteria that can be directly calculated from the impeller power number and diameter. The evaluation of other potential scale-up criteria like the mixing time, the volumetric oxygen mass transfer coefficient, the maximum hydrodynamic stress or the strain rate requires the characterization of the bioreactor through experiments or computational fluid dynamics (CFD) simulations [42, 12, 43]. This hydrodynamic characterization results are vital for a detailed understanding of local environmental aspects experienced by the cells [1] and recent scale-up studies use multi-parameter considerations supported by CFD simulations [24, 23].

If direct characterization data is not available, empirical correlations can be used to estimate the relevant process characteristics. The maximum shear stress and strain rate can be correlated to the impeller tip speed [44, 23]. The mixing time can be correlated to the volumetric power input [13, 45], which also represents the average energy dissipation in the bioreactor. However, there is significant difference between the energy dissipation in the impeller region and the liquid bulk, so that the volumetric power input is not representative of the maximum energy dissipation [34, 44, 13, 12]. The Van't Riet equation [46] is a well established empirical correlation for the prediction of the volumetric oxygen mass transfer coefficient from the volumetric power input and the

superficial gas velocity. Different empirical correlations can provide insight into the effect of the different operating parameters on the relevant process characteristics. However, when changing the bioreactor configuration or scale, especially, when geometrical similarity is not maintained, the fitted parameters used in the empirical correlation must be re-evaluated. Another difficulty in cell culture scale-up is that the oxygen requirements and the stress tolerance are cell line dependent [35, 18, 38, 47]. Due to these challenges, and despite extensive work on the subject, no universally applicable scale-up strategy could be identified so far [21, 39, 48, 23, 24].

A detailed process characterization is also an important step for including the selection of the bioreactor operating conditions into the quality by design (QbD) process development strategies. QbD is a concept that is part of the current good manufacturing practice in the pharmaceutical industry. In QbD the acceptable ranges of the critical quality attributes form the product design space. Based on the product design space, the process design space can be selected by identifying the connection between the critical quality attributes and the manufacturing process parameters [49]. While many critical process parameters for the production of antibodies through cell culture, e.g., the medium composition and the temperature [49, 2], are independent of the bioreactor operation, inhomogeneities related to insufficient liquid mixing have been reported to affect the glycosylation patterns of proteins [50, 37]. However, avoiding inhomogeneities through intensified agitation also has practical limits, since excessive hydrodynamic forces result in reduced growth and productivity of the cultivated cells [38, 47]. Consequently, the hydrodynamic characterization of bioreactors is also a necessary step to select operating conditions that reliably provide a high product quality and yield.

To gain deeper insights into scale-up related issues, the following questions must be considered: How are the cultivated cells affected by the physical process aspects? Which scale-up criterion or criteria should be used? What is the correlation between the bioreactor, the selected operating conditions and the relevant scale-up criteria? To address the last question, several studies have worked on the characterization of bioreactors across different scales [51, 132, 43, 52]. Some process characteristics like the mixing time, the maximum stress and the volumetric oxygen mass transfer coefficient are known to have a causal relationship with the cell culture process performance.

To investigate the exact effects of the physical process aspects on the cultivated cells, experimental scale-down models can be used [36, 53, 54, 55, 38, 41, 25]. For oscillations of the dissolved oxygen tension and the pH, reduced viable cell density and product quality have been reported [36, 50, 37, 56]. Similarly, hydrodynamic stress levels or maximum energy dissipation rates above a certain limit result in mechanical damage of the cells and have negative effects on the viable cell density as well as the productivity and are lethal to cells at extremely high values [38, 47, 57, 54, 55]. To maintain the dissolved oxygen tension at the set point, the maximum volumetric oxygen mass transfer coefficient must meet the oxygen requirement at the maximum cell density [32]. Otherwise, the dissolved oxygen tension and consequently the cell growth decrease. Moreover, imbalances of the volumetric mass transfer coefficients for oxygen and carbon dioxide and the subsequent carbon dioxide accumulation, which

are observed especially for large bioreactor scales, can have negative impact on cell growth [53, 40, 4, 58, 59, 41]. In addition to the variety of these possibly problematic process aspects, the tolerance of the cultivated cells to each of them is also cell line dependent [38, 47, 37]. Consequently, an established scale-up strategy has to be re-evaluated, or at least reconfirmed, not only when considering a new bioreactor but also when changing the cell line.

1.3 Research Objectives

Taking up the need for a detailed process characterization to implement improved scale-up strategies, the hydrodynamic characteristics of four industrially relevant single-use bioreactors, the Mobius® CellReady 3 L, the Xcellerex™ XDR-10, the Xcellerex™ XDR-200, and the Xcellerex™ XDR-2000 are the main focus of the present study. In addition, the Ambr® and the Xcellerex™ XDR-500 are characterized. While some of these bioreactors have already been considered in other studies [45, 60, 61, 62], the present study adds new detailed insights to the current knowledge to advance the goal of a more comprehensive process understanding.

The two-phase gas liquid flow in the Mobius® CellReady 3 L, the Xcellerex™ XDR-10, the Xcellerex™ XDR-200, and the Xcellerex™ XDR-2000 is simulated with the Euler-Euler and the one-way coupled Euler-Lagrange approach using the open source software tool OpenFOAM [63] and the commercial tool MixIT [64], respectively. The Ambr® and the Xcellerex™ XDR-500 are are characterized with one-way coupled Euler-Lagrange simulations using the open source software tool OpenFOAM [63]. For the Mobius® CellReady 3 L, two-way coupled Euler-Lagrange simulations with OpenFOAM [63] are also performed.

The effect of changes in the operating conditions as well as the impact of the configuration and the scale of the bioreactor on the flow field and different hydrodynamic characteristics are analyzed for all bioreactors investigated in the present study. The considered characteristics include the mixing time, the volumetric oxygen mass transfer coefficient, the maximum hydrodynamic stress, and the average strain rate in the impeller and the tank zone. Experimental results on the vortex formation, the mixing time, and the volumetric oxygen mass transfer coefficient have been provided by Tomomi Matsuura, Takuya Nakano, and Takuma Eguchi from Daiichi-Sankyo Japan and are used for comparison with the simulation results.

Available literature information on the requirements and tolerances of different cell lines are combined with the present evaluation of hydrodynamic characteristics to select the optimal operating ranges for each of the considered bioreactors. Moreover, the process characterization data across the different scales is also used to identify and to quantify the impact of the considered process scale on different scale-up criteria for scaling up form the CR3 to the XDR-10, the XDR-200, and the XDR-2000. In this manner, possible risks and challenges during scale-up are identified without the need for actual cell culture experiments. Furthermore, correlations between different scale-up criteria and the operating conditions are derived, enabling their targeted, knowledge-based selection. Based on this analysis, a scale-up strategy for the selection

of the impeller speed based on maintaining a constant average strain rate in the impeller zone following a similar strategy as Li et al. [23] is proposed. Cell culture results provided by Yuichi Aki from Daiichi-Sankyo Japan confirm that the proposed strategy can successfully provide reproducible cell culture results across the different bioreactor scales of the CR3, the XDR-10, and the XDR-200.

As a final process aspect of cell cultivation for large bioreactor scales the balance of oxygen and carbon dioxide is investigated and summarized, both for the diffusive transport from the bubbles to the liquid and the mass balance within the liquid. The dissolved carbon dioxide concentrations for a hypothetical batch process is evaluated for the XDR-200 and the XDR-2000.

The next chapter provides a detailed description of the governing equation their numerical solution for the considered modeling approaches.

2. Governing Equations and Numerical Solution

The present chapter is focused on the theoretical background and the numerical solution of the different modeling approaches. The first two sections summarize the state-of-the-art for the simulation of stirred tank bioreactors and the governing equation considered in the present study. The subsequent sections provide the equations used for the post-processing and the details on the simulation setup.

2.1 State-of-the-Art

The two processes determining the the flow structure in an aerated stirred tank are the mechanical agitation by the impeller(s) and the sparging of the disperse bubbles. To model the rotating motion of the impeller, the two most commonly used methods are the multiple reference frame (MRF) and the sliding mesh approaches [65, 20, 12]. For both methods, the region of the computational grid surrounding the impeller is treated differently to the tank region, which is static. In the MRF approach, the computational grid remains fixed and the velocity in the rotating reference frame region is solved relative to the angular velocity of the impeller, which is applied to this complete region [65]. In the sliding mesh approach, the rotating mesh region is moving with the angular velocity of the impeller and a specialized interface between the moving and stationary parts of the grid is required to allow for re-addressing of the interface between the moving and stationary grid regions [65]. The MRF approach are is applicable to steady state simulations and is computationally less expensive also in transient simulations [65]. However, only the sliding mesh approach can capture the periodic motion and changes in the orientation of the impeller.

Another important aspect of the flow in a bioreactor is the consideration of the different phases. During cell cultivation in a sparged, stirred tank bioreactor there are three separate phases: the continuous liquid, the disperse bubbles, and the suspended cells. The suspended cells are considered to be transported along with the liquid flow and to not affect the hydrodynamic characteristics within the bioreactor. This is justified by the small of mammalian cells, which have a diameter of 15-20 µm [18] and are of a similar size as the particles used in particle image velocimetry [60, 66, 67, 68]. If the cultivated cells considered in the simulation of the bioreactor hydrodynamics, the cells are treated as massless passive particles and the trajectories of cell traveling

through the bioreactor are analyzed to understand the exposure of the cultivates cells to the varying the hydrodynamic conditions [69, 70, 71, 72]. In most studies as well as the present one, the cultivated cells are not considered.

The sparged bubbles form the disperse gas phase. In studies that are focused on the liquid motion, the liquid mixing, or the mechanical stress in the liquid phases, the bubbles are sometimes not considered in the simulations [23, 73, 74, 75]. Moreover, studies that focus on the liquid surface and the deformation of the free surface also omit the disperse bubbles and use the volume of fluids approach to model the two segregated phases of the continuous liquid and the continuous gas phase in the head space [76, 77]. Even if only the liquid motion is simulated turbulence modeling is required to handle turbulent velocity fluctuations. While direct numerical simulations are reported for stirred tank reactors [78, 79, 80], they are limited to low Reynolds numbers and small bioreactors, due to their high requirements on the grid refinement. Both Large Eddy simulations [74, 81, 82] and the Reynolds average Navier-Stokes [75, 18, 23] approach are still commonly used.

If the disperse bubbles are considered, the Euler-Euler and the Euler-Lagrange approach are the two typically applied models [83, 35, 12]. The Euler-Lagrange approach has so far only rarely been applied to stirred tank bioreactors [84, 85, 86] and is more commonly used with bubble columns [87, 88, 89, 90, 91]. One very complex aspect when modeling the motion of bubbles is their poly-disperse size distribution, which is prone to change due to bubble break-up and coalescence. Mono-disperse simulations are computationally cheaper and have also been applied frequently [92, 45, 93, 94, 95, 96, 97, 98].

Different methods exist to consider the size distribution of the bubbles. The method of classes divides the size distribution into discrete size groups, the different method of moments approaches track the transport of the moments of the size distribution, and the one-group models transport a single average property of the size distribution [99]. For the simulations of aerated stirred tank reactors, both the method of classes [100, 101, 102, 103] and the method of moments type of models [61, 104, 105] have been applied. All types of population balance modeling require closure terms for the break-up and coalescence of the bubbles, which are still being investigated (e.g., [106, 107, 108, 109]). Moreover, experimental data on the bubble size distribution within stirred tank reactors is needed for validation but its availability is limited [110, 111, 112, 113].

When applying population balance modeling, often the same velocity is applied to all size groups of the disperse phase [105, 114]. However, the bubble size also has an impact on the forces governing the bubble motion and thus the poly-disperse size distribution also results in poly-celerity, which also affects the local size distribution [115]. In the method of classes approach, this can be considered by grouping the different size groups into several velocity groups and assigning a separate velocities for each of the velocity groups, which correspond to a subset of the size groups, which is found to improve the accuracy of the simulations [116]. One draw-back of the method of classes is that as the accuracy increases with the number of the considered size groups so does the computational cost [105]. A computationally more efficient alternative is the method of moments approaches, with an increasing number of different methods being

developed [99, 114].

While modeling of the bubble size distribution provides more detailed insights into the process and potentially allows for a more accurate simulation of the volumetric oxygen mass transfer coefficient, the model complexity and computational cost also increase [102]. Furthermore, without experimental data on the size distribution for the matching bioreactor configuration and operating condition, the validation of the modeled size distribution is difficult. Sarkar et al. [100] used the agreement of the simulated and experimental volumetric oxygen mass transfer coefficient as a criterion to optimize the size bins for their method of classes model. Bach et al. [97] fitted the bubble diameter of mono-disperse simulations based on their experimental results on the volumetric oxygen mass transfer coefficient.

Since for the bioreactors considered in the present work, no size distribution data is available in the literature and the focus of the present study is on the engineering characterization of process characteristics relevant to cell cultivation, modeling of the bubble size distribution is not included and the Reynolds average Navier-Stokes approach is used for turbulence modeling. The governing equations of the considered modeling approaches are presented in the next section.

2.2 Governing Equations

This section provides the details of the equations needed to describe the fluid motion. The conditions of the simulated flow are at low Mach number, ambient pressure, and constant temperature. Accordingly, both the liquid and the gas phases are considered to be incompressible Newtonian fluids with a constant density and dynamic viscosity [117]. The liquid density ρ_l and liquid viscosity μ_l of the culture medium [118] are 1,010.8 kg m^{-3} and 0.001126 Pa s, respectively, and a constant gas density ρ_g of 1.29 kg m^{-3} and gas viscosity μ_g for 2.1x10^{-5} Pa s for the sparged oxygen [119] are used. The disperse bubbles are considered to be spherically symmetric throughout their rise.

2.2.1 Liquid-Phase

The mass and momentum transport of a turbulent continuous liquid phase flow can be described in the Eulerian reference frame by the unsteady Reynolds-Average Navier-Stokes (URANS) equations [120, 117]

$$\frac{\partial\left(\alpha_\mathrm{l}\rho_\mathrm{l}\right)}{\partial t}+\nabla\cdot\left(\alpha_\mathrm{l}\rho_\mathrm{l}\mathbf{u}_\mathrm{l}\right)=0 \tag{2.1}$$

$$\frac{\partial\left(\alpha_\mathrm{l}\rho_\mathrm{l}\mathbf{u}_\mathrm{l}\right)}{\partial t}+\nabla\cdot\left(\alpha_\mathrm{l}\rho_\mathrm{l}\mathbf{u}_\mathrm{l}\otimes\mathbf{u}_\mathrm{l}\right)=-\nabla p+\nabla\cdot\left(\alpha_\mathrm{l}\mathbf{R}_{\mathrm{eff,l}}\right)+\alpha_\mathrm{l}\rho_\mathrm{l}\mathbf{g}+\mathbf{S}_\mathrm{l}, \tag{2.2}$$

where the volume fraction α_l allows to account for the displacement of the liquid by a second phase. Even though both the liquid and gas phase are considered to be incompressible the mass of one phase contained within a control volume can change due

to the displacement by the second phase and only if a single-phase flow is considered where α_l=1, Eq. (2.1) can be reduced to $\nabla \cdot \mathbf{u}_\mathrm{l} = 0$, where $\mathbf{u}_\mathrm{l}$ is the liquid velocity. The static pressure and the effective stress tensor, composed of the viscous and Reynolds stresses, are p and $\mathbf{R}_{\mathrm{eff,l}}$, and $\mathbf{g}$ is the gravitational acceleration. The source term for coupling with a second phase is $\mathbf{S}_\mathrm{l}$ with $\mathbf{S}_\mathrm{l} = 0$ in the case of a single-phase flow.

When using the Reynolds averaged Navier-Stokes equations, only the ensemble or time averaged velocity is tracked, while a turbulence model is used to account for the turbulent fluctuations of the velocity and to calculate the turbulence viscosity, which enters the calculation of the Reynolds stresses [120, 117]. One such turbulence model is the k-ε model, where k_l is the turbulence kinetic energy of the liquid phase and ε_l is its dissipation rate. The turbulence dynamic viscosity of the liquid is $\mu_{\mathrm{t,l}} = \rho_\mathrm{l} C_\mu \frac{k_\mathrm{l}^2}{\varepsilon_\mathrm{l}}$. The required transport equations for k and ε are

$$\frac{\partial \left(\alpha_\mathrm{l}\rho_\mathrm{l}k_\mathrm{l}\right)}{\partial t} + \nabla \left(\alpha_\mathrm{l}\rho_\mathrm{l}\mathbf{u}_\mathrm{l}k_\mathrm{l}\right) = \nabla \left(\alpha_\mathrm{l}\left[\mu_\mathrm{l} + \frac{\mu_{\mathrm{t,l}}}{\sigma_k}\right]\nabla k_\mathrm{l}\right) + \alpha_\mathrm{l}G_k - \alpha_\mathrm{l}\rho_\mathrm{l}\varepsilon_\mathrm{l} \tag{2.3}$$

$$\frac{\partial \left(\alpha_\mathrm{l}\rho_\mathrm{l}\varepsilon_\mathrm{l}\right)}{\partial t} + \nabla \left(\alpha_\mathrm{l}\rho_\mathrm{l}\mathbf{u}_\mathrm{l}\varepsilon_\mathrm{l}\right) = \nabla \left(\alpha_\mathrm{l}\left[\mu_\mathrm{l} + \frac{\mu_{\mathrm{t,l}}}{\sigma_\varepsilon}\right]\nabla \varepsilon_\mathrm{l}\right) + C_{1\varepsilon}\alpha_\mathrm{l}\frac{\varepsilon_\mathrm{l}}{k_\mathrm{l}}G_k - C_{2\varepsilon_\mathrm{l}}\alpha_\mathrm{l}\rho_\mathrm{l}\frac{\varepsilon_\mathrm{l}^2}{k_\mathrm{l}} \tag{2.4}$$

where the model coefficients $\sigma_k, \sigma_\varepsilon, C_{1\varepsilon}$ and $C_{2\varepsilon}$ are 1.0, 1.3, 1.44, and 1.92, respectively, and G_k is the turbulence production term

$$G_k = \mathbf{R}_{\mathrm{t,l}} \cdot \nabla \mathbf{u}_\mathrm{l} = \left(\mu_{\mathrm{t,l}}\left[\nabla \mathbf{u}_\mathrm{l} + \nabla \mathbf{u}_\mathrm{l}{}^\mathrm{T} - \frac{2}{3}\mathbf{I}\nabla \mathbf{u}_\mathrm{l}\right] - \frac{2}{3}\rho_\mathrm{l}\mathbf{I}k_\mathrm{l}\right)\nabla \mathbf{u}_\mathrm{l}, \tag{2.5}$$

where $\mathbf{I}$ is the identity matrix.

2.2.2 Lagrangian Treatment of the Bubbles

One method to track the motion of a disperse phase moving through a continuous fluid is the Lagrangian approach where the disperse phase, which can consist of particles, drops or bubbles, is treated as a set of individual point masses [83] that follow Newton's second law of motion. The change in the position of a bubble $\mathbf{x}_\mathrm{b}$ is

$$\frac{\mathrm{d}\mathbf{x}_\mathrm{b}}{\mathrm{d}t} = \mathbf{u}_\mathrm{b}. \tag{2.6}$$

The change in the velocity $\mathbf{u}_\mathrm{b}$ of each bubble depends on its mass m_b and the forces $\mathbf{F}_i$ acting on it

$$m_\mathrm{b}\frac{\partial \mathbf{u}_\mathrm{b}}{\partial t} = \sum_{i=1}^{n}\mathbf{F}_i. \tag{2.7}$$

The considered forces are the gravitational force $\mathbf{F}_\mathrm{G}$, the pressure gradient force $\mathbf{F}_\mathrm{P}$, the drag force $\mathbf{F}_\mathrm{D}$, the virtual mass force $\mathbf{F}_\mathrm{VM}$, and the lift force $\mathbf{F}_\mathrm{L}$ with

$$\mathbf{F}_\mathrm{G} = V_\mathrm{b}\mathbf{g}\ \left(\rho_\mathrm{g} - \rho_\mathrm{l}\right) \tag{2.8}$$

$$\mathbf{F}_{\mathrm{P}} = \rho_{\mathrm{l}} \frac{\mathrm{D}\mathbf{u}_{\mathrm{l}}}{\mathrm{D}t} \tag{2.9}$$

$$\mathbf{F}_{\mathrm{D}} = \frac{3}{4} C_{\mathrm{D}} V_{\mathrm{b}} \frac{\rho_{\mathrm{l}}}{d_{\mathrm{b}}} \left(\mathbf{u}_{\mathrm{l}} - \mathbf{u}_{\mathrm{b}}\right) \left|\mathbf{u}_{\mathrm{l}} - \mathbf{u}_{\mathrm{b}}\right| \tag{2.10}$$

$$\mathbf{F}_{\mathrm{VM}} = C_{\mathrm{VM}} V_{\mathrm{b}} \rho_{\mathrm{l}} \left(\frac{\mathrm{D}\mathbf{u}_{\mathrm{l}}}{\mathrm{D}t} - \frac{\mathrm{d}\mathbf{u}_{\mathrm{b}}}{\mathrm{d}t} \right) \tag{2.11}$$

$$\mathbf{F}_{\mathrm{L}} = C_{\mathrm{L}} V_{\mathrm{b}} \rho_{\mathrm{l}} \left(\mathbf{u}_{\mathrm{l}} - \mathbf{u}_{\mathrm{b}}\right) \times \left(\nabla \times \mathbf{u}_{\mathrm{l}}\right). \tag{2.12}$$

The bubble volume and diameter are V_{b} and d_{b} and C_{D}, C_{VM}, and C_{L} are the respective coefficients for the drag, virtual mass, and lift forces. The drag coefficient of a spherical bubble is a function of its Reynolds number $\mathrm{Re}_{\mathrm{b}} = \frac{d_{\mathrm{b}} |\mathbf{u}_{\mathrm{l}} - \mathbf{u}_{\mathrm{b}}| \rho_{\mathrm{l}}}{\mu_{\mathrm{l}}}$ at low Reynolds numbers and approaches a constant value at high Reynolds numbers [121, 122]

$$C_{\mathrm{D}} = \begin{cases} \frac{24}{\mathrm{Re}_{\mathrm{b}}} \left(1 + c_{\mathrm{D},1} \mathrm{Re}_{\mathrm{b}}^{c_{\mathrm{D},1}}\right) & \text{if } \mathrm{Re}_{\mathrm{b}} \leq 1000 \\ c_{\mathrm{D},1} & \text{if } \mathrm{Re}_{\mathrm{b}} > 1000 \end{cases} \tag{2.13}$$

Slightly different values in the coefficients $c_{\mathrm{D},1}$,$c_{\mathrm{D},2}$, and $c_{\mathrm{D},3}$ can be found across different studies. Schiller and Naumann [121] report values of 0.15, 0.687, and 0.44, whereas Amsden et al.[122] report $\frac{1}{6}$, $\frac{2}{3}$ and 0.424. The virtual mass coefficient is set to the value of 0.5 for spherical particles [35, 123, 124]. The lift coefficient C_{L} is calculated according to the lift model by Tomiyama et al. [125] and depends on the bubble Eötvös number $\mathrm{Eo} = \Delta\rho |\mathbf{g}| d_{\mathrm{b}}^2 / \sigma$, where σ is the surface tension.

$$C_{\mathrm{L}} = \begin{cases} \min\left(0.28 \tanh\left[0.121\ \mathrm{Re}_{\mathrm{b}}\right], f\right) & \text{if } \mathrm{Eo} \leq 4 \\ f & \text{if } 4 < \mathrm{Eo} \leq 10 \\ -0.27 & \text{if } \mathrm{Eo} > 10 \end{cases} \tag{2.14}$$

where $f = 0.00105\ \mathrm{Eo}^3 - 0.0159\ \mathrm{Eo}^2 - 0.0204\ \mathrm{Eo} + 0.474$ [125].

Since drag, virtual mass, and lift are reported to be the most important for bubbles moving in a aerated stirred tank, other forces like the Basset force, the Marangoni effect and the Magnus force are neglected [124].

For the momentum exchange of the disperse and the continuous phase there exist two possible approaches: one-way coupling, where only the momentum transfer from the liquid to the bubbles is included, and two-way coupling, where in addition to momentum transfer from the liquid to the bubbles the momentum transfer from the bubbles to the liquid is also included. In the former case, the Lagrangian tracking of the disperse phase can be performed as an independent second simulation step, which utilizes single-phase liquid flow results as an input. For the latter, the liquid flow results enter the calculation of the forces acting on the bubbles but, additionally, the momentum transfer of the bubbles to the liquid is considered in the momentum transport of the continuous liquid Eq. (2.2). Accordingly, the motion of both phases has to be calculated in combination with alternating solution of the liquid flow and bubble motion. The bubbles are mapped to the Eulerian grid based on their position

$\mathbf{x}_\mathrm{b}$ and the momentum transfer is accounted for via the source term

$$\mathbf{S}_\mathrm{l} = -\frac{\alpha_\mathrm{g}}{V_\mathrm{b}} \left(\mathbf{F}_\mathrm{D} + \mathbf{F}_\mathrm{VM} + \mathbf{F}_\mathrm{L} \right), \tag{2.15}$$

where $\alpha_\mathrm{g} = \sum_{k=1}^{n_\mathrm{b}} V_{\mathrm{b},k} / V_\mathrm{CV}$ is the volume fraction of the disperse phase inside a computational grid cell of volume V_CV, with n_b the total number of bubbles within the control volume and $V_{\mathrm{b},k}$ the volume of the $k-th$ bubble. The corresponding volume fraction of the liquid phase is $\alpha_\mathrm{l} = 1 - \alpha_\mathrm{g}$.

2.2.3 Eulerian Treatment of the Bubbles

An alternative approach to the Lagrangian treatment of the disperse bubbles is the Eulerian approach. In this case, an additional set of equations of the same form as Eqs. (2.1) and (2.2) needs to be solved for the gas phase with α_g, ρ_g, $\mathbf{u}_\mathrm{g}$, $\mathbf{R}_\mathrm{eff,g}$, and $\mathbf{S}_\mathrm{g}$ as the respective volume fraction, density, velocity, effective stress tensor, and interface momentum transfer term:

$$\frac{\partial \left(\alpha_\mathrm{g} \rho_\mathrm{g} \right)}{\partial t} + \nabla \cdot \left(\alpha_\mathrm{g} \rho_\mathrm{g} \mathbf{u}_\mathrm{g} \right) = 0 \tag{2.16}$$

$$\frac{\partial \left(\alpha_\mathrm{g} \rho_\mathrm{g} \mathbf{u}_\mathrm{g} \right)}{\partial t} + \nabla \cdot \left(\alpha_\mathrm{g} \rho_\mathrm{g} \mathbf{u}_\mathrm{g} \otimes \mathbf{u}_\mathrm{g} \right) = -\nabla p + \nabla \cdot \left(\alpha_\mathrm{g} \mathbf{R}_\mathrm{eff,g} \right) + \alpha_\mathrm{g} \rho_\mathrm{g} \mathbf{g} + \mathbf{S}_\mathrm{g}, \tag{2.17}$$

The static pressure p is typically considered to be shared for both phases [126]. The presence of one or the other phase for this inter-penetrating continuous phases and the identification of disperse or continuous conditions is then defined by the volume fraction. In contrast to the Lagrangian approach, this method does not account for the exact location of individual bubbles and instead tracks the presence of the phases within the control volumes of the Eulerian grid. With this approach phase inversion, i.e., the shift from disperse to continuous conditions for different regions of the bioreactor is possible and the continuous gas-phase in the head space can be included in the simulations. To close the second set of equations the turbulence of the second phase has to be modeled as well. Behzadi et al. [127] proposed a variant of the $k-\varepsilon$ model for the mixture of two phases, which reduces to that of the single phase if only one phase is present

$$\frac{\partial \left(\rho_\mathrm{m} k_\mathrm{m} \right)}{\partial t} + \nabla \cdot \left(\rho_\mathrm{m} \mathbf{u}_\mathrm{m} k_\mathrm{m} \right) = \nabla \cdot \left(\frac{\mu_{\mathrm{t,m}}}{\sigma_k} \nabla k_\mathrm{m} \right) + G_{k,\mathrm{m}} - \rho_\mathrm{m} \varepsilon_\mathrm{m} \tag{2.18}$$

$$\frac{\partial \left(\rho_\mathrm{m} \varepsilon_\mathrm{m} \right)}{\partial t} + \nabla \cdot \left(\rho_\mathrm{m} \mathbf{u}_\mathrm{m} \varepsilon_\mathrm{m} \right) = \nabla \cdot \left(\frac{\mu_{\mathrm{t,m}}}{\sigma_\varepsilon} \nabla \varepsilon_\mathrm{m} \right) + \frac{\varepsilon_\mathrm{m}}{k_\mathrm{m}} \left(C_1 G_{k,\mathrm{m}} - C_2 \rho_\mathrm{m} \varepsilon_\mathrm{m} \right). \tag{2.19}$$

The turbulence kinetic energy and turbulence energy dissipation rate are obtained as

$$\{k_\mathrm{m} \text{ or } \varepsilon_\mathrm{m}\} = \left(\alpha_\mathrm{c} \frac{\rho_\mathrm{c}}{\rho_\mathrm{m}} + \alpha_\mathrm{d} \frac{\rho_\mathrm{d}}{\rho_\mathrm{m}} C_\mathrm{t}^2 \right) \{k_\mathrm{c} \text{ or } \varepsilon_\mathrm{c}\}, \tag{2.20}$$

where the indices d and c indicate the continuous and the disperse phase and the mixture density is $\rho_\mathrm{m} = \alpha_\mathrm{l}\rho_\mathrm{l} + \alpha_\mathrm{g}\rho_\mathrm{g}$. The turbulence response coefficient C_t [127] is

$$C_\mathrm{t} = 1 + (C_{\mathrm{t},0} - 1)\exp\left(-180\ \alpha_\mathrm{d} - 4.71\ 10^3\alpha_\mathrm{d}^2 + 4.26\ 10^4\alpha_\mathrm{d}^3\right). \tag{2.21}$$

where $C_{\mathrm{t},0}$ is the turbulence response coefficient for a volume fraction of the disperse phase close to zero

$$C_{\mathrm{t},0} = \frac{3+\beta}{1+\beta+2\frac{\rho_\mathrm{d}}{\rho_\mathrm{c}}} \quad \text{with} \quad \beta = \frac{6\alpha_\mathrm{d}C_\mathrm{D}|\mathbf{u}_\mathrm{rel}|\rho_\mathrm{c}}{4d_\mathrm{d}}\frac{1}{\sqrt{2/3}}\frac{k_\mathrm{c}}{\varepsilon_\mathrm{c}}. \tag{2.22}$$

The mixture velocity is

$$\mathbf{u}_\mathrm{m} = \frac{\alpha_\mathrm{c}\rho_\mathrm{c}\mathbf{u}_\mathrm{c} + \alpha_\mathrm{d}\rho_\mathrm{d}\mathbf{u}_\mathrm{d}C_\mathrm{t}^2}{\alpha_\mathrm{c}\rho_\mathrm{c} + \alpha_\mathrm{d}\rho_\mathrm{d}C_\mathrm{t}^2} \tag{2.23}$$

and the turbulence viscosity of the mixture is

$$\mu_{\mathrm{t,m}} = \frac{\left(\alpha_\mathrm{c}\mu_{\mathrm{t,c}} + \alpha_\mathrm{d}\mu_{\mathrm{t,d}}C_\mathrm{t}^2\right)\rho_\mathrm{m}}{\alpha_\mathrm{c}\rho_\mathrm{c} + \alpha_\mathrm{d}\rho_\mathrm{d}C_\mathrm{t}^2}. \tag{2.24}$$

The turbulence kinetic energy production of the mixture is

$$G_{k,\mathrm{m}} = \alpha_\mathrm{c}G_{k,\mathrm{c}} + \alpha_\mathrm{d}G_{k,\mathrm{d}}, \tag{2.25}$$

where $G_{k,\mathrm{c}}$ and $G_{k,\mathrm{d}}$ are turbulence kinetic energy production terms of the individual phases. The turbulence kinetic energy, the turbulence energy dissipation rate, and the turbulent dynamic viscosity of disperse phase can be obtained as

$$k_\mathrm{d} = C_\mathrm{t}^2 k_\mathrm{c},\ \varepsilon_\mathrm{d} = C_\mathrm{t}^2\varepsilon_\mathrm{c} \quad \text{and} \quad \mu_{\mathrm{t,d}} = C_\mathrm{t}^2\left(\frac{\nu_\mathrm{c}\rho_\mathrm{d}}{\nu_\mathrm{d}\rho_\mathrm{c}}\right)\mu_{\mathrm{t,c}}. \tag{2.26}$$

The additional turbulence energy generation by the disperse phase [127] resulted in excessive turbulence generation in the region of the liquid surface and is neglected to improve model stability and is omitted in Eqs. (2.18) and (2.19).

The calculation of the momentum exchange terms of the two-phase $\mathbf{S}_\mathrm{g}$ and $\mathbf{S}_\mathrm{l}$ requires a modifier function f_φ with $\varphi \in [\mathrm{l}, \mathrm{g}]$ to distinguish, which phase is the disperse one

$$f_\phi = \begin{cases} 1 & \text{if } 0 \le \alpha_\varphi < 0.3 \\ (0.7 - \alpha_\varphi)/0.4 & \text{if } 0.3 \le \alpha_\varphi \le 0.7 \\ 0 & \text{if } 0.7 < \alpha_\varphi \le 1. \end{cases} \tag{2.27}$$

The transfer terms then are

$$\begin{aligned} \mathbf{S}_\mathrm{g} = -\mathbf{S}_\mathrm{l} &= \frac{3}{4}\alpha_\mathrm{g}\alpha_\mathrm{l}\left(\frac{f_\mathrm{g}C_{\mathrm{D,g}}\rho_\mathrm{l}}{d_\mathrm{g}} + \frac{f_\mathrm{l}C_{\mathrm{D,l}}\rho_\mathrm{g}}{d_\mathrm{l}}\right)|\mathbf{u}_\mathrm{l} - \mathbf{u}_\mathrm{g}|\,(\mathbf{u}_\mathrm{l} - \mathbf{u}_\mathrm{g}) \\ &+ \alpha_\mathrm{g}\alpha_\mathrm{l}\left(f_\mathrm{g}C_{\mathrm{VM,g}}\rho_\mathrm{l} + f_\mathrm{l}C_{\mathrm{VM,l}}\rho_\mathrm{g}\right)\left(\frac{\mathrm{D}\mathbf{u}_\mathrm{l}}{\mathrm{D}t} - \frac{\mathrm{D}\mathbf{u}_\mathrm{g}}{\mathrm{D}t}\right), \end{aligned} \tag{2.28}$$

where the drag coefficient C_D is obtained from the Schiller-Naumann model [121] (see Eq. (2.13)) and the virtual mass coefficient C_VM is set to 0.5 [35, 123, 124]. The drag force is reported to have the strongest impact on the motion of bubbles within a stirred tank and the virtual mass force is also not negligible near the impeller, while the lift force is much smaller than both the drag and the virtual mass forces [124]. Other forces are neglected.

2.3 Determination of Process Characteristics

This subsection provides the details on all additional calculation steps required to extract all considered hydrodynamic characteristics from the flow simulations.

2.3.1 Vortex Depth

For unbaffled bioreactors, liquid surface deformation can be observed at high impeller speeds [77]. The surface vortex is marked by a lower liquid level in the center of the bioreactor and a higher liquid level at the wall of the reactor. In the case of a single continuous phase, i.e., for single-phase or Euler-Lagrange simulations, the liquid surface is represented by the flat top boundary of he computational grid and the surface vortex formation cannot be captured directly. Instead, the pressure gradient across this boundary Δp can be correlated to the vortex depth Δh [128, 64] by

$$\Delta h = \frac{\Delta p}{\mathbf{g}\rho_\mathrm{l}}. \tag{2.29}$$

If the continuous gas-phase in the head space is also considered in the simulations as is the case for the volume of fluids or the Euler-Euler approach the free surface can be directly evaluated from the iso-surface of the gas and liquid volume fraction $\alpha_\mathrm{g} = 1 - \alpha_\mathrm{l} = 0.5$. The height difference across the iso-surface is the vortex depth Δh. In addition to the vortex depth, the liquid height change at the vessel wall compared to that of the same liquid volume without agitation and a flat free surface can also be evaluated.

2.3.2 Volumetric Power Input

The volumetric power input P/V is a classical engineering parameter for stirred tank reactors and represents the power transferred to the liquid by the impeller motion normalized by the liquid volume [20]. The power input can be calculated from the torque M acting on the impeller obtained from the simulations

$$P = M 2\pi n, \tag{2.30}$$

where n is the impeller speed in revolutions per second.

2.3.3 Mixing Time

The mixing process is evaluated through the simulation of the transport of a passive tracer with properties identical to the liquid phase and a concentration c_T

$$\frac{\partial\left(\alpha_\mathrm{l} c_\mathrm{T}\right)}{\partial t} + \nabla\cdot\left(\alpha_\mathrm{l}\mathbf{u}_\mathrm{l} c_\mathrm{T}\right) - \nabla\cdot\left(\alpha_\mathrm{l} D_\mathrm{eff}\nabla c_\mathrm{T}\right) = 0, \tag{2.31}$$

where $\mathbf{u}_\mathrm{l}$, α_l, and ν_t are taken from the liquid simulation results at steady conditions. The effective diffusivity $D_\mathrm{eff} = D + \nu_\mathrm{t}/\mathrm{Sc}_\mathrm{t}$ is calculated from the molecular diffusivity D and the turbulent Schmidt number $Sc_\mathrm{t} = 0.7$ [129, 18, 61].

A spherical region below the liquid surface is initialized with c_T=1, while the remaining liquid is assigned c_T=0. The change in c_T over time is monitored at multiple positions distributed over the liquid volume. The mixing time is taken as the time at which the concentration change relative to the local concentration is less than 3% s^{-1} at all monitor positions.

2.3.4 Volumetric Oxygen Mass Transfer Coefficient

The volumetric oxygen mass transfer coefficient $k_\mathrm{L}a$ is the product of the liquid transfer coefficient k_L and the volume specific interface area a [32]. For bubbles rising in a turbulent liquid, the liquid transfer coefficient can be evaluated with the eddy cell model of Lamont and Scott [130]

$$k_\mathrm{L} = 0.4\sqrt{D_{\mathrm{O}_2}}\left(\frac{\varepsilon_\mathrm{l}\rho_\mathrm{l}}{\mu_\mathrm{l}}\right)^{0.25}, \tag{2.32}$$

where $D_{\mathrm{O}_2} = 3\mathrm{x}10^{-9}$ m^2 s^{-1} is the diffusion coefficient of oxygen in water at 37 ℃ [131]. The specific interface area a is the total area of the interface divided by the liquid volume. In the case of disperse bubbles, a is the sum of the surface area of all bubbles A divided by the liquid volume V_l

$$a = \frac{A}{V_\mathrm{l}} = \frac{n_\mathrm{b} d_\mathrm{b}^2\pi}{\alpha_\mathrm{l} V_\mathrm{tot}} = \frac{6\alpha_\mathrm{g}}{\left(1-\alpha_\mathrm{g}\right) d_\mathrm{b}} \tag{2.33}$$

Typically the average gas volume fraction, i.e., the gas hold-up $\alpha_{\mathrm{g,avg}}$ is larger than zero but much smaller then average liquid volume fraction $\alpha_\mathrm{l} = 1-\alpha_\mathrm{g} \approx 1$, so that the interface area is typically [132, 24, 61, 32, 97, 45, 18, 102, 133] calculated as

$$a = \frac{6\alpha_\mathrm{g}}{d_\mathrm{b}}. \tag{2.34}$$

In the one-way coupled Euler-Lagrange simulations, the Lagrangian results are not mapped to the Eulerian grid so that the local gas volume fraction is not available. Only its average value, the gas hold-up $\alpha_{\mathrm{g,avg}}$ can be determined from the average bubble

residence time $t_{\mathrm{r,avg}}$ as

$$\alpha_{\mathrm{g,avg}} = t_{\mathrm{r,avg}} \frac{Q}{V_{\mathrm{L}}}. \tag{2.35}$$

Accordingly the $k_{\mathrm{L}}a$ is calculated by substituting ε_{l} and α_{g} in Eqs. (2.32) and (2.34) with the respective average values. The same is done for the two-way coupled Euler-Lagrange simulations. In the Euler-Euler simulations the local values of each control volume are used for the calculation of local $k_{\mathrm{L}}a$ and the overall value for the complete bioreactor is obtained by the averaging over the liquid volume.

2.3.5 Risk of cell damage

In contrast to microbial cells, mammalian cells are not protected by a cell wall and instead only have a cell membrane consisting of a phospholipid bilayer. The cell membrane can be damaged by the hydrodynamic force of the surrounding liquid. Moreover, even below force levels that would result in rupture of the cell membrane, negative impact on cell growth and productivity can be observed [134, 38, 57]. Different parameters exist for the quantification of these forces and their definitions are briefly summarized here.

Shear stress

The shear stress τ_{tn} in a laminar flow along a solid wall, the wall shear stress can be obtained from the velocity gradient in the direction normal to the wall which is termed the shear rate γ_{tn}

$$\tau_{\mathrm{tn}} = \mu_{\mathrm{l}} \gamma_{\mathrm{tn}}, \tag{2.36}$$

where μ_{l} is the dynamic viscosity of the liquid. However, the flow inside a bioreactor is a three-dimensional turbulent flow for which the normal direction cannot be easily defined. Wollny [135] proposed a definition of the shear rate as the component of the strain tensor normal to the flow direction $\widetilde{\gamma_{tn}}$. To obtain this, Wollny [135] proposed a rotation of the local velocity gradient tensor so that the $\widetilde{x}$-component of the transformed tensor is always parallel to the flow direction:

$$\begin{pmatrix} \frac{\partial \tilde{u}_x}{\partial \tilde{x}} & \frac{\partial \tilde{u}_x}{\partial \tilde{y}} & \frac{\partial \tilde{u}_x}{\partial \tilde{z}} \\ \frac{\partial \tilde{u}_y}{\partial \tilde{x}} & \frac{\partial \tilde{u}_y}{\partial \tilde{y}} & \frac{\partial \tilde{u}_y}{\partial \tilde{z}} \\ \frac{\partial \tilde{u}_z}{\partial \tilde{x}} & \frac{\partial \tilde{u}_z}{\partial \tilde{y}} & \frac{\partial \tilde{u}_z}{\partial \tilde{z}} \end{pmatrix} = \mathbf{C} \cdot \begin{pmatrix} \frac{\partial u_x}{\partial x} & \frac{\partial u_x}{\partial y} & \frac{\partial u_x}{\partial z} \\ \frac{\partial u_y}{\partial x} & \frac{\partial u_y}{\partial y} & \frac{\partial u_y}{\partial z} \\ \frac{\partial u_z}{\partial x} & \frac{\partial u_z}{\partial y} & \frac{\partial u_z}{\partial z} \end{pmatrix} \cdot \mathbf{C}^T, \tag{2.37}$$

where the transformation matrix $\mathbf{C}$ is

$$\mathbf{C} = \begin{pmatrix} \vec{u}_{C1} \\ \vec{u}_{C2} \\ \vec{u}_{C3} \end{pmatrix} \tag{2.38}$$

with

$$\vec{u}_{C1} = \begin{pmatrix} \frac{u_x}{|u|} & \frac{u_y}{|u|} & \frac{u_z}{|u|} \end{pmatrix}, \tag{2.39}$$

$$\vec{u}_{C2} = \begin{pmatrix} \frac{u_y - u_z}{u_O} & \frac{u_z - u_x}{u_O} & \frac{u_x - u_y}{u_O} \end{pmatrix} \tag{2.40}$$

$$u_O = \sqrt{(u_y - u_z)^2 + (u_z - u_x)^2 + (u_x - u_y)^2} \tag{2.41}$$

and

$$\vec{u}_{C3} = \vec{u}_{C1} \times \vec{u}_{C2}. \tag{2.42}$$

The corresponding shear rate then is

$$\widetilde{\gamma_{\mathrm{tn}}} = \sqrt{\left(\frac{\partial \widetilde{u_{\mathrm{x}}}}{\partial \widetilde{y}} + \frac{\partial \widetilde{u_{\mathrm{y}}}}{\partial \widetilde{x}}\right)^2 + \left(\frac{\partial \widetilde{u_{\mathrm{x}}}}{\partial \widetilde{z}} + \frac{\partial \widetilde{u_{\mathrm{z}}}}{\partial \widetilde{x}}\right)^2}, \tag{2.43}$$

and the shear stress is

$$\widetilde{\tau}_{\mathrm{tn}} = \mu_{\mathrm{l}} \widetilde{\gamma_{\mathrm{tn}}}. \tag{2.44}$$

Strain rate

The strain rate $\overline{\gamma}$ is another criterion for the mechanical forces that is also derived from the velocity gradient [23, 24] and

$$\overline{\gamma} = \left(2\left[\left(\frac{\partial u_{\mathrm{x}}}{\partial x}\right)^2 + \left(\frac{\partial u_{\mathrm{y}}}{\partial y}\right)^2 + \left(\frac{\partial u_{\mathrm{z}}}{\partial z}\right)^2\right] + \left(\frac{\partial u_{\mathrm{x}}}{\partial y} + \frac{\partial u_{\mathrm{y}}}{\partial x}\right)^2 + \left(\frac{\partial u_{\mathrm{x}}}{\partial z} + \frac{\partial u_{\mathrm{z}}}{\partial x}\right)^2 + \left(\frac{\partial u_{\mathrm{y}}}{\partial z} + \frac{\partial u_{\mathrm{z}}}{\partial y}\right)^2\right)^{0.5}. \tag{2.45}$$

The strain rate represents the magnitude of the strain tensor

$$\mathbf{T} = \left(\nabla \mathbf{u} + \nabla \mathbf{u}^T\right). \tag{2.46}$$

In the case of turbulent flow, turbulence modeling is typically used and with the RANS approach the Reynolds-Average velocities are calculated, while the turbulent velocity fluctuations are modeled. The Kolmogorov length scale and the hydrodynamic stress are calculated from the turbulence energy dissipation rate.

Kolmogorov Length Scale

The Kolmogorov length scale l_{K} is the size of the smallest turbulent eddies. In turbulent flow, energy is transferred from larger eddies to smaller eddies until the viscous dissipation by the smallest eddies with a size equal to the Kolmogorov scale [136]. It can be calculated from the turbulence energy dissipation rate as

$$l_{\mathrm{K}} = \left(\frac{\nu_{\mathrm{l}}^3}{\varepsilon_{\mathrm{l}}}\right)^{0.25}. \tag{2.47}$$

With respect to cell damage, the suspended cells are expected to be damaged by turbulent eddies of the same size. Since there is a cascade of increasingly smaller eddies, turbulent eddies of similar size are only absent when the Kolmogorov length scale is larger than the cell size [13, 137]. In that case cells will only be convected by the turbulent eddies but not damaged by them.

Hydrodynamic stress

In turbulent flow the hydrodynamic stress τ_l caused by the velocity fluctuations can be calculated from the turbulence energy dissipation rate [74] as

$$\tau_l = \sqrt{\rho_l \mu_l \varepsilon_l}. \tag{2.48}$$

Cells are damaged if the maximum values of the hydrodynamic stress exceeds the cell line specific tolerance [134, 38].

2.4 One-way coupled Euler-Lagrange simulations

The one-way coupled Euler-Lagrange simulations for the CR3, XDR-10, XDR-200, and XDR-2000 have been performed with the commercial software tool MixIT [64], which provides a user interface for the creation of the reactor geometry, the physical properties, the operating conditions, and controlling the simulations. The geometry module already provides various typical impeller types but also allows for the addition of customized impellers as .stl files as was done in the present study. The simulation module of MixIT is based on the OpenFOAM code structure and the grid generation is integrated into the software using the *snappyHexMesh* utility. MixIT only considers the continuous liquid and creates a separate grid for each working volume. All simulation steps are specified via the user interface and executed by MixIT's *smartFoam* solver and can be run in parallel.

The simulations are split into the separate steps, which are the solution of the liquid flow, the Lagrangian tracking of bubbles, and the tracer transport calculations for analyzing the mixing process. The liquid flow calculations are executed as single-phase steady state simulations using the SIMPLE algorithm and are run for 1,000 iterations with first order schemes for the generation of an initial flow estimate. From this result the simulation is continued with second order schemes until 20,000 iterations are reached and the final residuals are below $1x10^{-6}$. In rare cases, when 20,000 iteration are not sufficient for the volume average liquid velocity magnitude, volume average turbulence energy dissipation rate, and impeller torque, which are recorded for each iteration, to approach constant value the simulations are run longer until those criteria are met. The impeller motion is modeled with the MRF approach for which in the region surrounding the impeller, the velocity is solved relative to the angular velocity of the impeller, i.e., with a rotating reference frame, while the remaining part of the domain is solved with a static reference frame. For all solid walls, a fixed velocity boundary condition, wall functions for all turbulence fields and zero gradient condition

for pressure are applied. To the top boundary, which represents the liquid surface, a slip boundary condition is applied.

The Lagrangian treatment of the bubbles is one-way coupled and uses the steady result of the liquid flow calculation as an input for calculating the bubble trajectories and residence time. The force applied to the bubbles are the gravitational force $\mathbf{F}_{\mathrm{G}}$, the pressure gradient force $\mathbf{F}_{\mathrm{P}}$, and the drag force $\mathbf{F}_{\mathrm{D}}$. The drag coefficient is calculated according to Eq. (2.13) using the coefficients proposed by Amsden et al. [122]. All bubbles are generated at random positions across the sparger surface and tracked until they are removed from the simulation, once they reach the top boundary.

The tracer transport calculation also requires the steady liquid flow results as an input and the user has to specify the tracer addition spot around which a spherical volume with $c_{\mathrm{T}} = 1$ is defined as well as the monitor positions for which the tracer concentration is reported for each simulation time step of 0.001 s. The volumetric power input, average liquid velocity, average turbulence kinetic energy, and average turbulence energy dissipation rate are automatically reported. Further post-processing is carried out in paraView [138].

For the Ambr250 and the XDR-500, the same work flow as described above using MixIT [64] has been implemented in OpenFOAM [63] using the *simpleFoam*, *icoUncoupledKinematicParcelFoam*, and a customized version of the *scalarTransportFoam* solvers, respectively.

2.5 Two-way coupled Euler-Lagrange and Euler-Euler simulations

Except for the one-way coupled Euler-Lagrange simulations, all simulations are carried out with the open-source software tool OpenFOAM version 7 [63]. OpenFOAM provides multiple functionalities including tools for mesh generation and modifications, different solvers for different types of flow, and post-processing utilities called *functionObject*. The OpenFOAM installation also includes the open-source data visualization and analysis tool paraView 5.6 [138]. The following subsections describe all steps from the grid generation to the processing of the final results.

2.5.1 Grid Generation

There are two main tools for grid generation in OpenFOAM, *blockMesh* and *snappyHexMesh*. The former allows for the direct definition of geometric shapes with straight or circular edges and direct specification of the number of volume elements in each spatial direction. Accordingly, *blockMesh* can provide well structured, purely hexahedral grids for simple geometries. For more complex geometries *snappyHexMesh* allows to create grids that have hexahedral structure as a basis but are adjusted to conform to complex surface shapes, which results in a small fraction of polyhedral cells at the surfaces. The surface information can be supplied in .stl format and all files representing interior surfaces of the bioreactor are generated in Gmsh [139]. The grid

fineness for the grid independence studies is adjusted by changing the fineness of the hexahedral background mesh specified in *blockMesh*.

2.5.2 Initialization of Liquid Flow

For initializing the liquid flow of the two-phase simulations and for the testing of different grid refinements single-phase steady state of the liquid flow are run with the *simpleFoam* solver which uses the SIMPLE algorithm. The impeller motion is modeled with the MRF approach in the same manner as described in Sect. 2.4. The simulations are run for 20,000 iterations until steadiness is reached with second order schemes, except for the convection the turbulence kinetic energy and the turbulence kinetic energy dissipation rate for which first order upwind schemes are used. All residuals are below $1x10^{-6}$. The boundary conditions are the same for the MixIT simulations described in Sect. 2.4. The liquid velocity, turbulence kinetic energy, and the turbulence kinetic energy dissipation rate are copied to the initial time step of simulations with the *mapFields* utility to start with the simulations with fully developed liquid flow surrounding the impeller. In the Euler-Lagrange simulations, the liquid volume is defined by the volume of the computational domain and in the Euler-Euler the *setFields* utility is used to specify the volume fractions of the gas and liquid phase in the head space and the working volume.

For the Euler-Euler simulations of the XDR-200 and the XDR-2000, volume of fluid simulations are performed as an intermediate step to also initialize the liquid surface. The volume of fluid simulations are run with the *interFoam* solver for 1 s and the time step is set to $5x10^{-5}$ s for which the Courant number remains below 0.5. All residuals are below $1x10^{-6}$. The liquid flow is initialized from the single-phase results and the continuous liquid and the continuous gas of the working volume and the head space are defined by setting the volume fraction with the *setFields* utility. For these simulations sparging is not considered. For the volume of fluid simulation, the impeller motion is also modeled with the multiple reference frame approach, and the transient equations are solved with the PIMPLE algorithm, a combination of the PISO and SIMPLE algorithm. In the volume of fluid simulations, the impeller motion is also modeled with the MRF approach and all boundaries are treated as solid walls.

2.5.3 Two-way Coupled Euler-Lagrange Simulations

The two-way coupled Euler-Lagrange simulations are run with the *DPMFoam* solver. As the continuous gas phase in the head space in not considered in the Euler-Lagrange simulations the computational grid of the complete reactor is reduced to the respective liquid height with the *subsetMesh* function, which only retains computational cells within a predefined region. For the initial time step the liquid flow is taken from single-phase simulations and bubbles are absent. The impeller motion is modeled with the sliding mesh approach [65], where the rotating region of the computational grid, which is the same as the rotating reference frame region of the other approaches, is moved with the angular velocity of the impeller motion around its rotational axis. The spacial coordinates of the control volumes within the rotating mesh region are

updated for each time step and to connect the rotating region to the stationary grid the faces of all control volumes forming the interface between the static and the rotating region region are duplicated and collected in two "Arbitrary Mesh Interface" (AMI) boundaries. These two boundaries are coupled to allow for reconnecting the adjacent control volumes of the static and rotating region according to their current position. Sparging is considered by the injection of bubbles at random positions across the sparger surface. The rate at which the bubbles are added is the sparging rate divided by the volume of an individual bubble. All forces described in Eqs. (2.8)-(2.12) are considered in the simulations. The added bubbles are tracked until they reach the top boundary, where they are removed and their residence time is recorded in a separate output file.

The top boundary, which represents the liquid surface is treated with a slip boundary condition across which no flow is possible. To compensate for the displacement of liquid by the bubbles an artificial pressure dependent in and outflow boundary is defined as a ring along the vertical reactor wall close to the liquid surface. All physical walls and the sparger surface are treated with a wall boundary condition as described already in Sect. 2.4. The transient equations are solved with the PIMPLE algorithm and the time step is dynamically adjusted to maintain a Courant number below 0.2 and the resulting time steps are in the range of 5x10^{-5} s and 1x10^{-6} s and the residuals are below 1x10^{-5}. The simulations are run until steady conditions are reached.

2.5.4 Euler-Euler Simulations

The Euler-Euler simulations are performed with the *reactingTwoPhaseEulerFoam* solver. For the CR3 and the XDR-10, the liquid flow is initialized from the single phase simulation results, for the XDR-200 and XDR-2000 the simulations are initialized from the volume of fluid simulations described in Sect. 2.5.2. The impeller motion is modeled with MRF approach. The working volume is defined with *setFields* by setting initial liquid and gas volume fractions of $\alpha_\mathrm{l} = 1$ and $\alpha_\mathrm{g} = 1 - \alpha_\mathrm{l} = 0$ for all control volumes below the liquid surface and $\alpha_\mathrm{l} = 0$ and $\alpha_\mathrm{g} = 1 - \alpha_\mathrm{l} = 1$ above the liquid surface. At the initial time bubbles are absent from the liquid and the sparging rate is set through the sparger's inflow velocity, which is the sparging rate divided by the sparger area. The impeller motion is modeled with the MRF approach. All physical walls are treated with wall boundary conditions and the top boundary is a pressure based in outflow boundary to allow exchange between the head space and the ambient air. The transient equations are solved with the PIMPLE algorithm and the time step is dynamically adjusted to maintain a Courant number below 0.2 and the resulting time steps are in the range of 5x10^{-5} s and 1x10^{-6} s and the residuals are below 1x10^{-5}. The simulations are run until steady conditions are reached.

2.5.5 Tracer Simulations and Post-Processing

For analyzing the mixing process, simulations similar to those described for the post-processing of the one-way coupled Euler-Lagrange simulations described in Sect. 2.4 are run. To this purposes the OpenFOAM solver *scalarTransportFoam* is customized

by adding the liquid volume fraction and the turbulent diffusion term to the transport equation. The region of the initial tracer volume for which $c_{\mathrm{T}} = 1$ is defined with the *setFields* utility and the *sampling functionObject* is used to report the tracer concentration at the considered monitor positions.

For post-processing of the torque and the shear and strain rate, the *forces* and *gradient functionObject*s are used to obtain the torque acting on the impeller and the gradient of the liquid velocity, respectively. The *codedFunctionObject* utility has been used to implement the rotation of the velocity gradient tensor to calculate the shear stress Eq. (2.43) proposed by Wollny [135]. Visualization and all further post-processing steps according to the equations in Sect. 2.3 are executed in paraView 5.6 [138] using the available calculator, histogram, and integrateVariables functions.

3. Carbon Dioxide Mass Transfer

The aerobic metabolism of the cultivated cells requires a constant supply of oxygen and results in a continuous production of carbon dioxide [4]. To supply oxygen and remove the carbon dioxide through diffusive transport, sparging is required during cell cultivation. The diffusive transport of oxygen and carbon dioxide is considered from the point of view of the individual bubbles and is described in the next subsection. Then the equations for describing the carbon dioxide balance in the culture medium are described in the following subsection.

3.1 Diffusion between the Bubbles and the Liquid

The diffusion of oxygen and carbon dioxide from a bubble to the liquid phase and vice versa depends on the driving concentration gradient, the transfer coefficient, and the transfer area. The diffusive transport can be described through [4]

$$\frac{dn_i}{dt} = k_\mathrm{L} A \left(p_i \mathrm{He}_i - c_{i,\mathrm{l}} \right), \tag{3.1}$$

where n_i is the amount of species i in the gas bubble at time t. In the present study, the liquid transfer coefficient k_L is calculated according to Eq. (2.32). The transfer area $A = \pi d_\mathrm{b}^2$ is the surface area of a spherical bubble with the diameter d_b, which is considered to be constant. The concentration of the dissolved species i at equilibrium is determined from the partial pressure of species i in the gas phase p_i and the Henry constant He_i [3] and $c_{i,\mathrm{l}}$ is the actual dissolved concentration in the liquid phase, where i is either oxygen or carbon dioxide. If $c_{i,\mathrm{l}} < p_i \mathrm{He}_i$, which is the case for oxygen, then the mass transfer is from the bubble to the liquid. Analogous, if $c_{i,\mathrm{l}} > p_i \mathrm{He}_i$, which is the case for carbon dioxide, then the mass transfer is from the liquid to the bubble. The partial pressure p_i is the mole fraction

$$y_i = \frac{n_i}{n_{\mathrm{O}_2} + n_{\mathrm{CO}_2} + n_{\mathrm{N}_2}} \tag{3.2}$$

multiplied with the total pressure.

The initial value of $n_{\mathrm{O}_2,0}$ is determined through the ideal gas law and the bubble composition of either pure oxygen or air with mole fractions for oxygen and nitrogen of 0.21 and 0.79. respectively. The initial value of $n_{\mathrm{CO}_2,0}$ is always zero. The total pressure is set to the constant value of atmospheric pressure of 101,325 Pa. The effect of

the hydrostatic pressure, which varies with the working volume and the position of the bubble, is neglected. In the present study, the surface area of the bubbles is considered to be constant. Furthermore, the bubble residence time, which is in the order of seconds, is considered to be much shorter than the time scale of concentration changes of carbon dioxide or oxygen in the liquid. Thus, $c_{i,\mathrm{l}}$ is also considered to be constant for the evaluation of single bubbles. Different values of $c_{i,\mathrm{l}}$ have been considered to investigate the effect of changes in the liquid concentration on the diffusive transport between the bubble and the liquid.

3.2 Carbon Dioxide Concentration in the Liquid

The concentration of the dissolved inorganic carbon species in the liquid is a result of the mass transfer between the dispersed bubbles and the consumption of oxygen and generation of carbon dioxide by the cultivated cells. The dissolved oxygen concentration changes according to

$$\frac{dc_{\mathrm{O_2}}}{dt} = OTR - c_{\mathrm{x}} q_{\mathrm{O_2}}, \tag{3.3}$$

where $c_{\mathrm{O_2}}$ is the dissolved oxygen concentration in the liquid, OTR is the oxygen transfer rate, c_{x} is the viable cell density, and $q_{\mathrm{O_2}}$ is the cell specific oxygen uptake rate. As summarized by Sieblist et al. [4], the oxygen transfer rate can be determined from the total amount of oxygen transferred by a bubble during its total residence time, the volumetric sparging rate $Q_{\mathrm{v}} = Q/V$, and the volume of the bubble. For a spherical bubble the oxygen transfer rate is

$$OTR = \left(n_{\mathrm{O_2},t_0} - n_{\mathrm{O_2},t_{\mathrm{final}}}\right) \frac{6 Q_{\mathrm{v}}}{\pi d_{\mathrm{b}}^3}, \tag{3.4}$$

where $n_{\mathrm{O_2},t_0}$ and $n_{\mathrm{O_2},t_{\mathrm{final}}}$ are the moles of oxygen inside a single bubble at the initial time and at the time at which the bubble reaches the liquid surface. Similar equations can be used to describe the dissolved carbon dioxide concentration $\mathrm{dCO_2}$. However, $\mathrm{dCO_2}$ is in equilibrium with the carbonic acid ($\mathrm{H_2CO_3}$), bicarbonate ($\mathrm{HCO_3^-}$), and carbonate ($\mathrm{CO_3^{2-}}$) [140]. The equilibrium of theses species forms the carbonate buffer system. The only species in equilibrium with carbon dioxide in the gas phase is $\mathrm{dCO_2}$. The $\mathrm{dCO_2}$ concentration can be approximately treated as a combined pool with $\mathrm{H_2CO_3}$, since the equilibrium of $\mathrm{dCO_2}$ and $\mathrm{H_2CO_3}$ is independent of the pH and their ratio at 25°C is 99.76:0.24 [141]. If the pH is controlled at a constant set point, the fraction of the combined pool $\mathrm{CO_2^*}$ of the total inorganic carbonate species $\phi_{\mathrm{CO_2^*}}$ is constant. For a pH of 7, Contreras [140] reports a fraction $\phi_{\mathrm{CO_2^*}}$ of 0.1663. The change of the concentration of the combined pool $c_{\mathrm{CO_2^*}}$ is

$$\frac{dc_{\mathrm{CO_2^*}}}{dt} = \phi_{\mathrm{CO_2^*}} \left(c_{\mathrm{x}} q_{\mathrm{CO_2}} - CTR\right), \tag{3.5}$$

where the carbon dioxide stripping rate CTR can be evaluated from the single bubble mass transfer as

$$CTR = \left(n_{\mathrm{CO_2},t_{\mathrm{final}}} - n_{\mathrm{CO_2},t_0}\right) \frac{6Q_{\mathrm{v}}}{\pi d_{\mathrm{b}}^3}, \tag{3.6}$$

where n_{CO_2,t_0} and $n_{CO_2,t_{\mathrm{final}}}$ are the moles of carbon dioxide inside a single bubble at the initial time and at the time at which the bubble reaches the liquid surface.

During cell cultivation, the dissolved oxygen concentration is typically kept constant by controlling the sparging rate [142], so that $\frac{dc_{\mathrm{O_2}}}{dt} = 0$ and Eq. (3.3) can be reordered to

$$Q_{\mathrm{v}} = \frac{c_{\mathrm{x}} q_{\mathrm{O_2}} \pi d_{\mathrm{b}}^3}{6\left(n_{\mathrm{O_2},t_0} - n_{\mathrm{O_2},t_{\mathrm{final}}}\right)}. \tag{3.7}$$

By entering Eqs. (3.6) and (3.7) into Eq. (3.5) $\frac{dc_{\mathrm{CO_2^*}}}{dt}$ can be calculated as

$$\frac{dc_{\mathrm{CO_2^*}}}{dt} = f_{\mathrm{CO_2^*}} c_{\mathrm{x}} \left(q_{\mathrm{CO_2}} - \frac{n_{\mathrm{CO_2},t_{\mathrm{final}}} - n_{\mathrm{CO_2},t_0}}{n_{\mathrm{O_2},t_0} - n_{\mathrm{O_2},t_{\mathrm{final}}}} q_{\mathrm{O_2}} \right). \tag{3.8}$$

The amount of CO_2 taken up by a bubble increases with the concentration of CO_2^*, which reaches a steady value for $\frac{dc_{\mathrm{CO_2^*}}}{dt} = 0$. This corresponds to

$$\frac{n_{\mathrm{CO_2},t_{\mathrm{final}}} - n_{\mathrm{CO_2},t_0}}{n_{\mathrm{O_2},t_0} - n_{\mathrm{O_2},t_{\mathrm{final}}}} = \frac{q_{\mathrm{CO_2}}}{q_{\mathrm{O_2}}}. \tag{3.9}$$

The ratio of the cell specific uptake and production rates is the respiratory quotient of the cultivated cell line

$$RQ = \frac{q_{\mathrm{CO_2}}}{q_{\mathrm{O_2}}}. \tag{3.10}$$

Goudar et al. [143] report respiratory quotients for CHO cells cultivated at different conditions close to unity.

The differential equations are solved in MATLAB [144] using the *ode*15*s* solver.

4. Characterization of the Individual Bioreactors

The basis for the scale-up analysis presented in the next chapter is the hydrodynamic characterization of each of the considered bioreactors. The cell culture relevant process aspects of mixing, liquid stress, and oxygen transfer depend on the liquid agitation by the impeller and the sparging of the disperse bubbles but are not directly known. The causal relation between the operating conditions and the cell culture relevant process characteristics is the flow that develops within each of the considered bioreactors. To understand the effect of changes in the operating conditions, including the working volume, the impeller speed, the sparging rate, and where applicable the sparger type, a set of different operating conditions is considered for each bioreactor.

The sections on each of the bioreactors start with a description of the bioreactor, the considered operating conditions and the numerical gird used in the simulations. The results on the liquid flow structure and the bubble dispersion are presented first. In a next step, the effect of the operating conditions on the different process characteristics are analyzed. Except for the Ambr® 250, which is presented last, the sections on the individual bioreactors are ordered by the bioreactor volume, starting with the Mobius® CellReady 3 L (CR3), and then continuing with the XDR-10, the XDR-200, the XDR-500, and the XDR-2000. The larger bioreactors are all part of the Xcellerex™ single-use bioreactor product line [145],which offers different maximum working volumes of 10 L, 50 L, 200 L, 500 L, 1000 L, and 2000 L. The CR3, the XDR-10, the XDR-200, the XDR-500, and the XDR-2000 all have a single impeller and at least one microporous sparger. The CR3 is the only bioreactor that is investigated with both one-way and two-way coupled Euler-Lagrange (EL) simulations, whereas for all other bioreactors only the one-way coupled EL approach is used. In addition, Euler-Euler (EE) simulations are performed for the CR3, the XDR-10, the XDR-200, and the XDR-2000. Since the CR3 is presented first, the considered process characteristics are reported and explained in more detail than for the other bioreactors. Each sections also points out differences and similarities to the bioreactors presented in the sections above.

The experimental results on the volumetric oxygen mass transfer coefficient of the CR3, the XDR-10, and the XDR-200 have been provided by Tomomi Matsuura, Takuya Nakano, and Takuma Eguchi from Daiichi-Sankyo Co., Ltd.. Additionally, Tomomi Matsuura provided the experimental data on the vortex formation in the XDR-10 and the mixing time of the CR3, the XDR-10, and the XDR-200. The experimental results

are reported in [146, 128, 118].

4.1 The Mobius® CellReady 3 L

The Mobius® CellReady 3 L (CR3) is a lab-scale bioreactor that can be used for the initial testing of different cell lines, in the seed train, and as the starting point for cell culture scale-up. The results of the two-way EL simulations on the liquid flow structure, the bubble dispersion, the gas hold-up, the volumetric oxygen mass transfer coefficient, the mixing time, the hydrodynamic stress, and the strain rate are reported in [146]. The characterization of the CR3 starts with description of the configuration of the bioreactor, the considered operating conditions, the selection of the numerical grid and its boundaries, continues with the numerical results on the flow structure and process characteristics, and closes with a summary of the same from the perspective of selection of the operating conditions for cell cultivation.

4.1.1 Bioreactor Configuration

The CR3 has a rigid, transparent, single-use plastic vessel with a diameter d_V of 13.7 cm and a total height of , which is equipped with a marine blade impeller, see Fig. 4.1, with three blades and a diameter d_{imp} of 7.6 cm. The impeller is mounted on a central rod that is mechanically rotated in the up-pumping clockwise direction. A microporous sparger and an open pipe spargerare integrate into the CR3, both entering the rounded bottom of the vessel from the side. Up to three probes can be entered through the lid of the vessel and a hollow truncated cone is inbuilt for inserting a temperature sensor. The present work considers two cylindrical sensors, one for pH and one for the dissolved oxygen tension, entering from the top in addition to the inbuilt truncated cone.

4.1.2 Operating Conditions

The considered operating conditions cover changes in the impeller speed, the working volume, the sparging rate, and the sparger type. For the modeling approaches that include the effect of bubbles on the liquid motion, i.e., the two-way coupled EL and the EE simulations, the effect of all four operating parameters on the liquid flow is captured. The selected operating conditions for these modeling approaches summarized in Tab. 4.1, represent changes in a single parameter relative to the condition #4, for which the

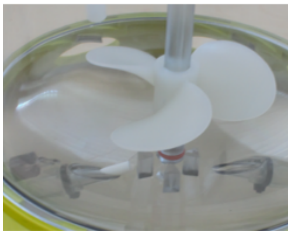

Figure 4.1: Impeller of the Mobius® CellReady 3 L

Table 4.1: Operating conditions for the EE and the two-way coupled EL simulations of the CR3.

Condition #	Impeller speed n [rpm]	Working volume V [L]	Sparging rate Q [mL min^{-1}]	Sparger type
1	50	1.0	50	microporous
2	100	1.7	50	microporous
3	250/150	1.7	50	microporous
4	100	1.0	50	microporous
5	100	2.4	50	microporous
6	100	1.7	10	microporous
7	100	1.7	100	microporous
8	100	1.7	50	open pipe

impeller speed, the working volume, and the sparging rate are at the intermediate level and the microporous sparger is used. If the set of conditions in Tab. 4.1 was extended to cover a full design of experiments, condition #4 would correspond to the center point. For the impeller speed, low intermediate and high values of 50 rpm, 100 rpm, and 250 rpm are considered. For the two-way coupled Euler-Lagrange simulations 150 rpm instead of 250 rpm are used as the maximum level, which is further discussed in the section 4.1.4. For the working volume, the supplier specified minimum and maximum volume of 1.0 L and 2.4 L, and the intermediate value of 1.7 L are tested. For the sparging rate, the levels are 10 mL min^{-1}, 50 L min^{-1}, and 100 mL min^{-1}. The second sparger option is the open pipe sparger. The opening of the open pipe sparger is a hole in the curved part of the vessel bottom, which has an elliptical outline with a major axis length of 2.3 mm and a minor axis length of 1.0 mm. In the

Table 4.2: Operating conditions for the one-way coupled EL simulations of the CR3.

Condition #	Impeller speed n [rpm]	Working volume V [L]
1	50	1.0
2	100	1.0
3	250	1.0
4	50	1.7
5	100	1.7
6	250	1.7
7	50	2.4
8	100	2.4
9	250	2.4

one-way coupled EL simulations, the gas hold-up and volumetric oxygen mass transfer coefficient are evaluated for all conditions in Tab. 4.1 with 250 rpm for condition #3. However, since the effect of the bubbles on the liquid motion is neglected, the liquid flow for conditions #6, #7, and #8 is identical to condition #4. The sparger type is reflected in the simulations by its position and the diameter selected to represent the generated bubbles and the sparging rate is only included in the calculation of the gas hold-up and the volumetric oxygen mass transfer coefficient. Since different sparging rates do not require separate simulations, an extended set of simulation conditions is used to characterize the liquid flow. This set of conditions is summarized in Tab. 4.2 and consists of all possible combinations of the three levels of working volume and the three levels of impeller speed.

4.1.3 Grid Independence Study

For the one-way coupled EL simulations with MixIT and for the EE simulations, separate grid studies are performed. The tested grids for the one-way coupled EL simulations are shown in Fig. 4.2a and those for the EE simulations are shown in

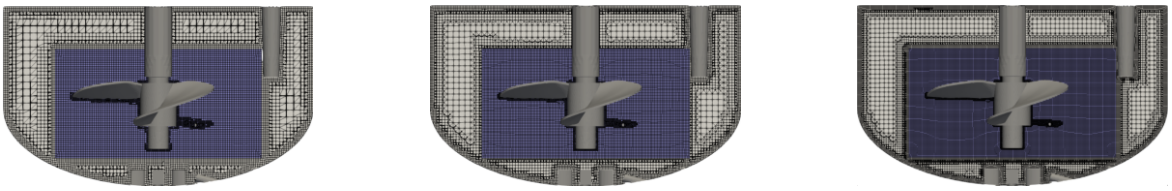

(a) Grids for the one-way coupled EL simulation for 1.0 L working volume. Left to right: 1.4×10^6, 2.2×10^6, and 4.4×10^6 grid cells.

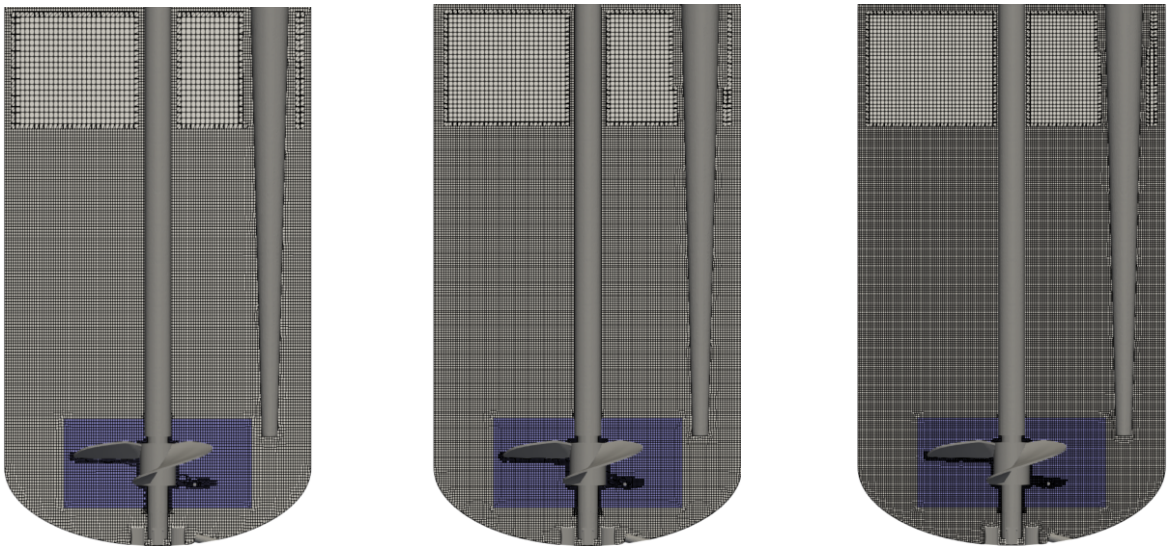

(b) Grids for the EE simulations for the complete reactor including the head space. Left to right: 2.0×10^6, 2.8×10^6, and 4.9×10^6 grid cells.

Figure 4.2: Computational grids for the CR3 considered in the grid study. The rotating reference frame region is highlighted in blue.

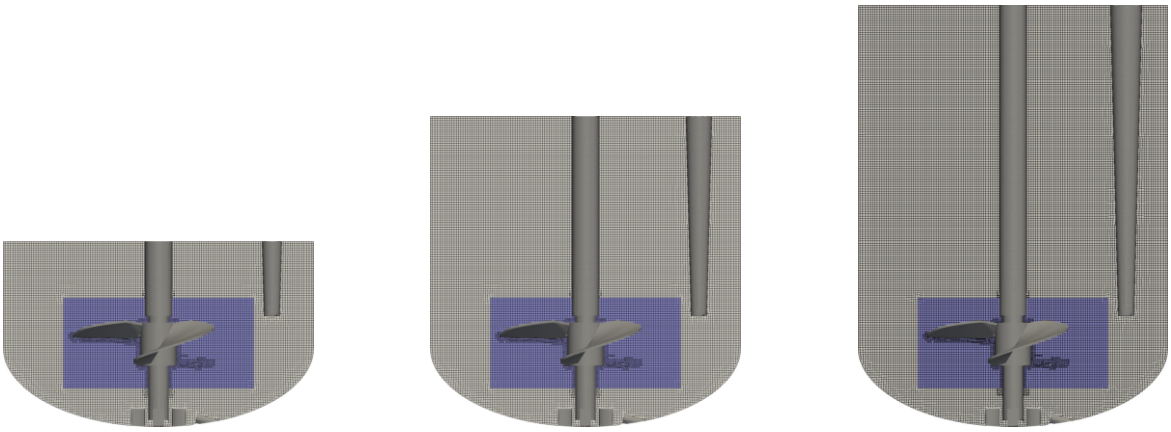

Figure 4.3: Computational grids for the CR3 for the two-way Euler-Lagrange simulations for the different working volumes. The rotating mesh region is highlighted in blue. Left to right: 1.1x10^6, 1.9x10^6, and 2.6x10^6 grid cells for 1.0 L, 1.7 L and 2.4 L of working volume, respectively.

Fig. 4.2b. The meshing strategy implemented in MixIT [64] applies high refinement for the rotating reference frame region, which results in a grid spacing of a quarter of that of the largest grid cells in each spatial direction, which results in a volume of 1/64 of the largest cells. The same refinement is used for all solid walls, except for the impeller where the refinement is increased by another level resulting in a spacing of one eighth of the largest grid distance. The grid generated in OpenFOAM [63] uses a different strategy with a coarse grid for the gas filled head space and one level of refinement at the solid walls and another level of refinement directly at the impeller.

Grid independence is evaluated based on the average velocity magnitude, turbulence kinetic energy, turbulence kinetic energy dissipation rate, and turbulence viscosity and considered to be reached when less than 5 % deviation compared to the finest investigated grid are found. These criteria are met for the intermediate grids shown in the center of Fig. 4.2 with 2.2x10^6 and 2.8x10^6 for the one-way coupled EL approach for 1.0 L working volume and for the grid of the complete bioreactor used in EE simulations, respectively.

The grids for the two-way coupled Euler-Lagrange (two-way coupled EL) simulations are derived from the grid selected for the EE simulations by cutting the grid to the height corresponding to the selected liquid volume, see Fig. 4.3.

To illustrate where which boundary conditions are used in the simulations, the different boundaries are marked in different colors in the perspective projection of the bioreactor for which the front of the vessel wall is missing in Fig. 4.4. Both spargers are located at the bottom of the vessel and highlighted in green in Fig. 4.4. In the one-way and two-way coupled EL simulations, the top boundary represents the liquid surface and is treated with a slip boundary condition and is shown as the dark blue area in Figs. 4.4a and 4.4b. In the EE simulations, the liquid surface is inside the computational domain and must be evaluated from the gas and liquid volume fraction. However, a circular region of the top boundary, which represents the connection to

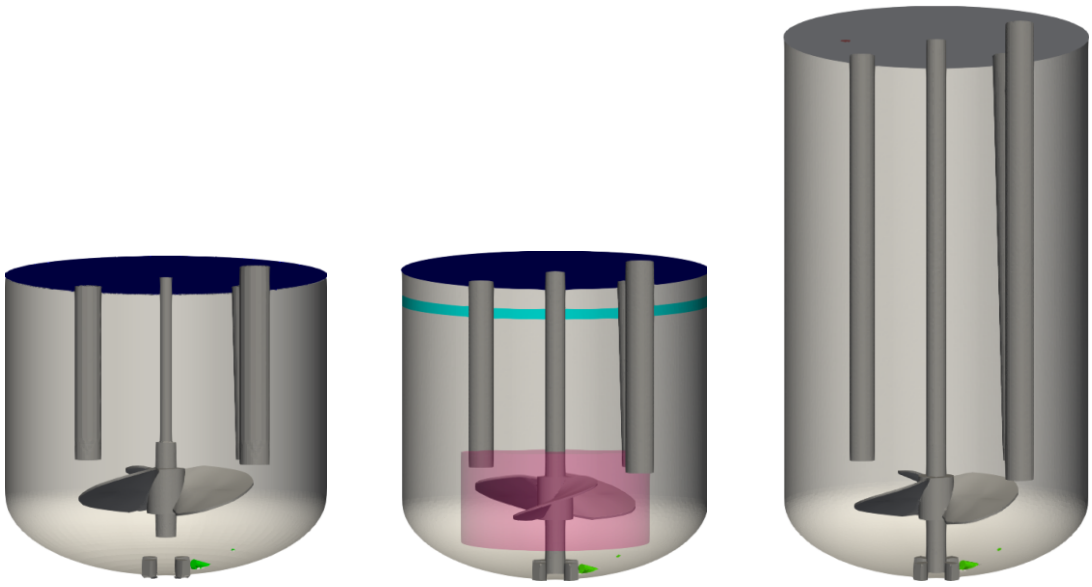

(a) One-way coupled EL (b) Two-way coupled EL (c) EE

Figure 4.4: Boundary structure of the numerical grid of the CR3 for the different modeling approaches.

the gas outlet pipe, is treated with an atmospheric boundary condition, which allows exchange of gas in the head space with the ambient air. This boundary is indicated by the small red area in the top left of Fig. 4.4c. In the two-way coupled EL simulations, the volumetric coupling is included and requires in- and out-flow of liquid to compensate for the volume gained and lost by the addition and removal of bubbles at the sparger, and the top boundary, respectively. For this purpose, a segment of boundary faces along the circumference of the vertical reactor wall with a height of 0.5 cm is selected as a separate, artificial boundary that allows for in- and outflow of liquid, which is similar to the strategy applied by Masterov et al. [88] for a bubble column. The back part of this boundary is indicated in teal in Fig 4.4a. The location of the interface between the rotating and static mesh regions of the sliding mesh approach of the two-way EL simulations is indicated by the transparent pink cylinder in Fig. 4.4b. All other boundaries colored gray in Fig. 4.4 correspond to solid walls and are treated with a no slip condition.

4.1.4 Process Characterization

To provide insight into the general flow structure, a description of the liquid flow and the bubble dispersion are provided first. Then the effect of the operating conditions on the cell culture relevant process characteristics of liquid mixing, liquid stress, and oxygen transfer is discussed. For each of these aspects, results for the one-way coupled EL, two-way coupled EL and EE approaches are presented side by side and differences in their capabilities pointed out.

Liquid Flow and Bubble Dispersion

The mechanical agitation by the impeller defines the liquid motion and determines the mixing and the mechanical stress in the liquid phase, while the sparging and the bubble dispersion determine the gas hold-up and oxygen transfer. Cell culture relevant process characteristics are not directly evident from the flow pattern, but it can provide better understanding why and how the process characteristics are affected by the operating conditions. The liquid flow field and bubble dispersion within the CR3 for condition #4 with $V = 1.7$ L, $n = 100$ rpm, and $Q = 50$ mL min^{-1} with the microporous sparger are shown in Fig. 4.5 for all three modeling approaches. The impeller is rotating in the up-pumping, clockwise direction, which results in a dominant rotational motion of the liquid. The secondary flow structure shows two circulation zones, where the flow ejected from the impeller is redirected in upwards and downwards direction at the vessel wall and then drawn back in to the impeller from below and above the impeller, which is observed with all three modeling approaches. This general structure agrees well to the simulation results by Kaiser et al. [45, 147] and the particle image velocimetry of Odeleye et al. [60, 148]. The impeller speed determines the liquid velocity, while the working volume defines the height of the upper recirculation zone. For the considered sparging rates the bubbles only have small localized impact on the liquid flow, which is

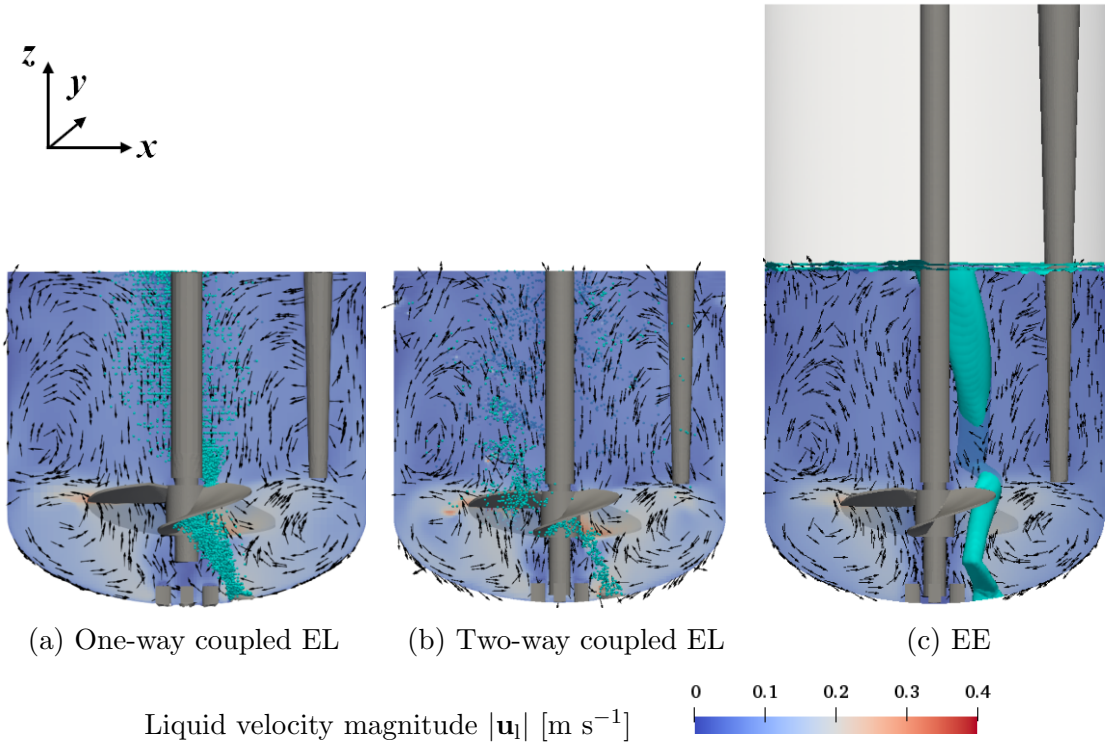

(a) One-way coupled EL (b) Two-way coupled EL (c) EE

Figure 4.5: Liquid flow and bubble dispersion for $V = 1.7$ L, $n = 100$ rpm, $Q = 50$ mL min^{-1} for the microporous sparger for all three considered modeling approaches in the x-z-plane through the center of the CR3. Arrows indicate the direction of the x-z-velocity.

underlined by the high similarity between the one-way coupled EL simulations, which neglect the impact of the bubbles on the liquid flow, with the two-way coupled EL and EE results.

In addition to the liquid flow structure, Fig. 4.5 also shows the bubble dispersion for the base case. The bubble positions of the one-way and two-way coupled EL simulations are indicated by individual spheres in Fig. 4.5. For the EE approach, the 1 % gas volume fraction iso-surface indicates the region where the majority of bubbles are rising. For all three simulation approaches, similar bubble dispersion is observed: the bubbles rise from the microporous sparger to the impeller and then further along the backside of the impeller blade. After they detach from the upper edge of the impeller, they rise close to the center of the vessel, while also following the clockwise motion of the liquid due to drag. The horizontal dispersion of the bubbles increases while they are rising from the impeller to the liquid surface. One obvious difference between the different simulation approaches is the effect of the modeling of the impeller motion on the position at which the bubbles detach from the impeller blades. For the multiple reference frame approach , which is used for the one-way coupled EL and EE simulations, the grid around the impeller is fixed and the rotation is captured by calculating the velocity in the rotating reference frame relative to the angular velocity of the impeller. As consequence the bubbles do not move with the impeller's rotational motion and the bubble plume above the impeller is shifted in the anti-clockwise direction, when compared to the two-way coupled EL simulations, where the sliding mesh approach moves the computational grid in the rotating region according to the impeller motion. The sliding mesh allows for a more detailed understanding of the interaction of individual bubbles with the moving impeller and the bubbles detach on the side opposite to the microporous sparger. This difference in the bubble detachment does not have a significant impact on the related process characteristics of the gas hold-up and the volumetric oxygen mass transfer coefficient, which is discussed below.

For the different modeling approaches, there are also some differences in the consideration of the sparging rate. For the one-way coupled EL simulations, the bubble motion is not affecting the liquid flow and is calculated in a separate second simulation step. Thus, the bubbles do not affect the liquid flow and the number of tracked bubbles only needs to be sufficiently high to give a good estimate of the average residence time. For the evaluation of the average residence time 2000 bubbles are tracked for each considered combination of impeller speed, working volume, and bubble diameter. The actual sparging rate then only enters in the calculation of the gas hold-up and volumetric oxygen mass transfer coefficient.

For the two-way coupled EL simulations, the volume of bubbles with 1 mm diameter considered for the microporous sparger is about $5\text{x}10^{-10}$ m^3 and is only slightly below the average volume of the computational grid cells of $1\text{x}10^{-9}$ m^3. Even smaller volumes of down to $1.5\text{x}10^{-11}$ m^3 are found for refined and truncated cells directly at the impeller. Due to the small size difference between the bubbles and the control volumes, the requirement that the disperse bubbles are significantly smaller than the Eulerian grid is not fulfilled [149] and numerical instability is observed. To alleviate this issue "parcels sizes" smaller than 1 are considered to reduce the local source terms for the

volumetric and momentum coupling by multiplying with the parcel size (Henry Weller, personal communication, 16th April 2019). At the same time, the number of injected parcels, which is the number of bubbles divided by the parcels size, is larger than the number of actual bubbles, so that the sum of the coupling terms of all parcels in the computational domain is the same as expected for the actual number of bubbles (Henry Weller, personal communication, 16th April 2019). This can be interpreted as a statistical approach that considers a certain probability of a bubble being present at the parcel location and affecting the liquid flow. While this treatment improves numerical stability, the increase in the number of parcels present in the domain also increases the computational cost of the Lagrangian approach, which is in contrast to the classical parcel concept where multiple particles, bubbles, or droplets of the same size are grouped in a parcel to reduce the computational cost by reducing the number of tracked entities. Moreover, for the two-way coupled EL simulations bubbles are found to be trapped in the center of the lower recirculation zone at the maximum impeller speed of 250 rpm, when using the combination of drag, virtual mass, lift, gravity and pressure gradient forces described in Sect. 2.2.2. A maximum impeller speed of 150 rpm is considered instead at which the bubbles are not trapped. Another option to handle this issue might be the addition of a turbulent dispersion term that randomly modifies the bubbles velocity according to the intensity of the liquid turbulence. The randomness of the modifications is required because the anisotropic and unsteady nature of the turbulent velocity fluctuations is not captured correctly with turbulence models base on the Reynolds-Average Navier Stokes Equations like the $k - \varepsilon$ model used in the present study.

For the EE approach, the gas volume fraction is tracked instead of the individual bubbles. The EE method does not resolve the interfacial structure, i.e., an intermediate volume fraction can mean that disperse bubble or droplets are present within a control volume or that a segregated interface of gas and liquid is present within that control volume. In the present study, the disperse or continuous conditions are selected based on the volume fraction less than 0.3 and higher than 0.7, respectively, and for volume fractions in between there is interpolation of disperse and continuous behavior as specified by the modifier function defined in Eq. (2.27). One benefit of this method is that the volume of the gas phase cannot be larger than the control volume, which makes it less sensitive to the ratio of the volume of the disperse bubbles and the control volumes of the Eulerian grid. Another benefit is the ability to consider two continuous phases, so that the continuous gas phase in the head space can also be included and the same grid can be used for all filling volumes. A draw back is that the liquid surface cannot be resolved, resulting in some instability and fluctuations.

Liquid Velocity, Turbulence, Volumetric Power Input, and Mixing Time

With increasing impeller speed, the liquid velocity and turbulence increase, which allows for faster mixing and better homogenization. The velocity and turbulence kinematic viscosity of the liquid phase are vital inputs for the tracer simulations that are used to determine the mixing time. The power draw of the impeller normalized by the working volume yields the volumetric power input that is a classical scale-up criteria

that can be correlated to the mixing time [20, 13, 18]. Accordingly, the present section is dedicated to theses different flow characteristics related to the liquid mixing.

Fig. 4.6a shows the average liquid velocity magnitude $|\mathbf{u}_l|$ of the one-way coupled EL simulations across the different impeller speeds and the different working volumes are indicated by the different colors. In the computationally cheaper one-way coupled EL simulations,i.e., simulations times of one to two days instead of several weeks, all possible combinations of the three considered levels of working volume and impeller speed have been considered as given in Tab. 4.2. For the two-way coupled EL and EE simulations, conditions #1 to #5 in Tab. 4.1 cover the effect of the working volume at the intermediate impeller speed of 100 rpm and the effect of impeller speed at the intermediate working volume of 1.7 L and are shown in Fig. 4.6b. Due to the issues with the simulations of the bubble dispersion in the two-way coupled EL simulations explained above the maximum impeller speed for this simulation approach is 150 rpm instead of 250 rpm. For all three modeling approaches, the average liquid velocity increases with the impeller speed. The effect of the working volume is smaller than that of the impeller speed and is shown for the intermediate impeller speed of 100 rpm in Fig. 4.6c, where all three modeling approaches are compared. At a constant impeller speed, the average liquid velocity is lower for a larger working volume, since with the

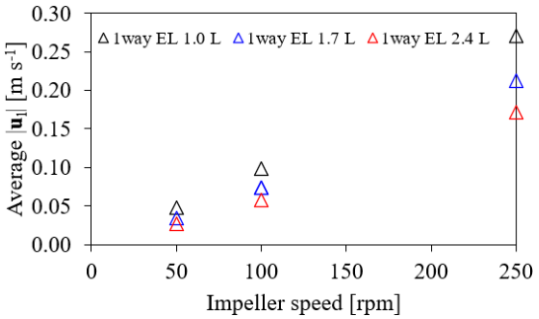

(a) One-way coupled EL

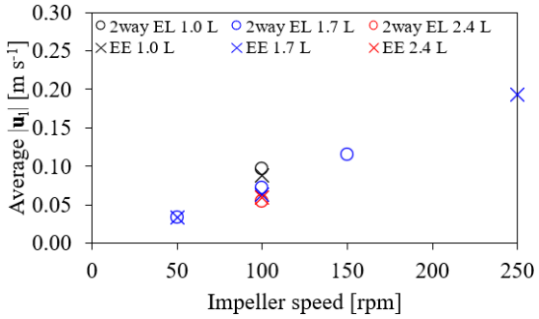

(b) Two-way coupled EL and EE

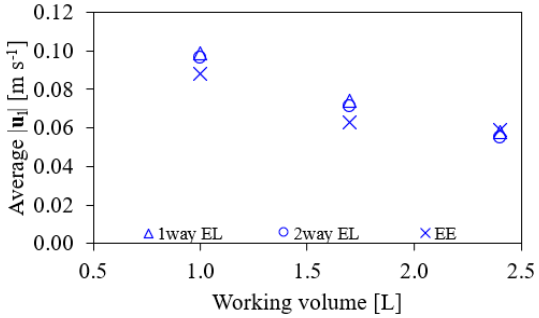

(c) One-way and two-way coupled EL, and EE at 100 rpm

Figure 4.6: Average liquid velocity for different impeller speeds for (a) the one-way coupled EL simulations, (b) the two-way coupled EL and EE simulations, and (c) for different working volumes at 100 rpm for all three modeling approaches, with $Q = 50$ mL min^{-1} for the microporous sparger.

same power transferred by the impeller motion a larger volume is agitated and the size of the upper recirculation zone with lower velocity increases. This is also indicated by the differently colored markers in Figs. 4.6a and 4.6b. The two-way coupled EL and EE simulations show slightly lower average velocities at the lowest and intermediate working volume. Overall, the differences between the different modeling approaches are minor, which is in agreement to the strong similarity of the liquid flow pattern in Fig. 4.5 and the small impact of the sparging on the overall flow structure.

With increasing liquid velocity the turbulence also increases, which also corresponds to a higher impeller Reynolds number [20]

$$\mathrm{Re}_{\mathrm{imp}} = \frac{n d_{\mathrm{imp}}^2}{\nu_{\mathrm{l}}} \tag{4.1}$$

at higher impeller speeds n. For $\mathrm{Re}_{\mathrm{imp}}$ larger than about 10^4, the flow conditions are considered to be fully turbulent for stirred tanks [13, 20, 42]. When using the $k-\varepsilon$ model, the kinetic energy contained in the turbulent eddies is represented by the turbulence kinetic energy k. Figure 4.7a shows the average turbulence kinetic energy of the liquid phase for the one-way coupled EL simulations and Fig 4.7b for

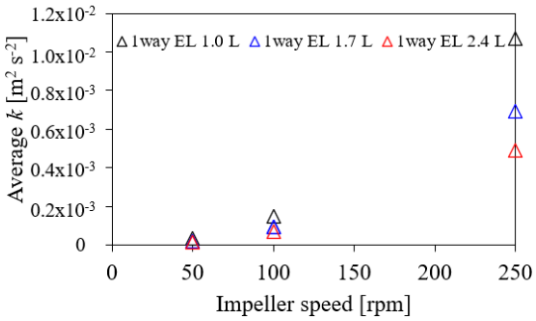

(a) One-way coupled EL

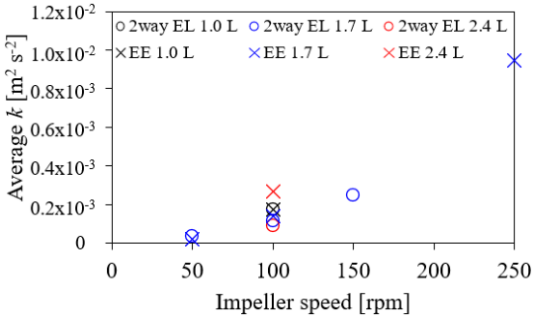

(b) Two-way coupled EL and EE

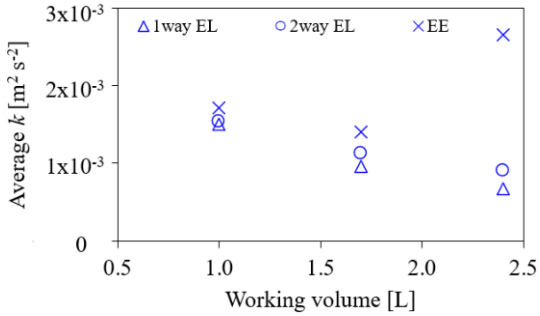

(c) One-way and two-way coupled EL, and EE at 100 rpm

Figure 4.7: Average turbulence kinetic energy for different impeller speeds for (a) the one-way coupled EL simulations, (b) the two-way coupled EL and EE simulations, and (c) for different working volumes at 100 rpm for all three modeling approaches, with $Q = 50$ mL min^{-1} for the microporous sparger.

the two-way coupled EL and EE simulations. Similar to the average velocity, the average turbulence kinetic energy increases with a higher impeller speed, which also corresponds to an increased $\mathrm{Re}_{\mathrm{imp}}$ number. Figure 4.7c shows the average turbulence kinetic energy for the different working volumes at an impeller speed of 100 rpm. For the one-way coupled EL simulations, a decrease of the turbulence kinetic energy for a larger working volume is observed similar to the decrease of the average velocity described above. The reduction of the average is turbulent kinetic energy for increasing working volumes is due to the lower turbulence in the upper part of the liquid above the impeller region. The heterogeneity of turbulence inside stirred tank reactors with high turbulence around the impellers and lower turbulence in the remaining liquid is observed in the present simulations, which is also in good agreement with the particle image velocimetry results on the single-phase liquid flow inside the CR3 of Odeleye et al. [60]. For the two-way coupled EL simulations, the same qualitative trend is observed but in contrast to the velocity, which is lower than for the one-way coupled EL simulations, the turbulence kinetic energy is higher. This increased turbulence is related to the turbulence caused by the interaction of the dispersed bubbles with the liquid phase. For the EE simulations, this higher turbulence is even more pronounced and at the maximum working volume the average turbulence kinetic energy is increased instead of decreased.

The turbulence enters the calculation of the Reynolds average velocity through the turbulence kinematic viscosity $\nu_{\mathrm{t,l}}$, which represents the additional dissipation of energy by turbulent eddies, and enters Eq. (2.2) through the effective stress tensor $\mathbf{R}_{\mathrm{eff,l}}$. Moreover, the simulation of the mixing process is affected by $\nu_{\mathrm{t,l}}$ through the effective diffusivity of the tracer as described in Sect. 2.3.3. For the one-way coupled EL simulations, ν_{t} increases with the impeller speed with slightly lower average values at a higher working volume, as shown in Fig. 4.8a. These observations are again similar to those made for the average velocity and turbulence kinetic energy. For the two-way coupled EL and EE simulations, ν_{t} also increases with the impeller speed, see Fig. 4.8b. However, similar to the turbulence kinetic energy there is some deviation between the different modeling approaches regarding the effect of changes in the working volume shown in Fig. 4.8c. For the EE approach, the values for the average ν_{t} at 100 rpm are almost the same for the different working volumes and very similar to the average ν_{t} of the one-way coupled EL result for a working volume 1.0 L. This indicates that the average ν_{t} in the upper recirculation zone at the intermediate and maximum working volume for the EE simulations is higher than for the one-way coupled EL simulations but comparable at the minimum volume. Similar to the turbulence kinetic energy this deviation between the one-way coupled EL and EE simulations is related to the turbulence induced by the rising bubbles. For the two-way coupled EL approach, a slightly lower turbulence kinematic viscosity is observed at 100 rpm, because ν_{t} in the lower recirculation zone is smaller. The reasons for this are unknown. Like for the EE simulations, the turbulence generated by the bubbles affects the average ν_{t}. The values are very similar values for the smallest and intermediate working volume. For the largest working volume of 2.4 L an increase in ν_{t} is observed, see Fig. 4.8b.

The kinetic energy dissipated by viscous and turbulent effects matches the volumetric

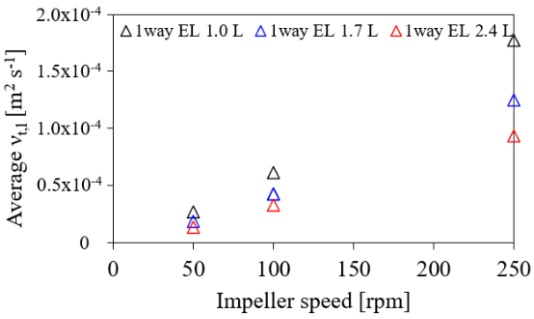

(a) One-way coupled EL

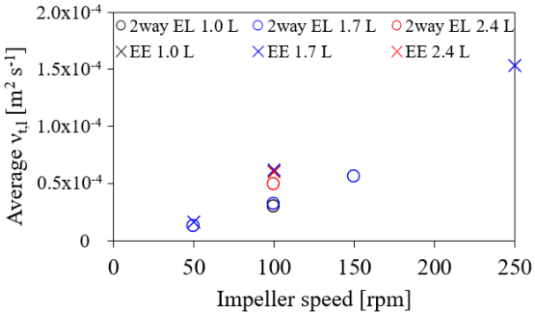

(b) Two-way coupled EL and EE

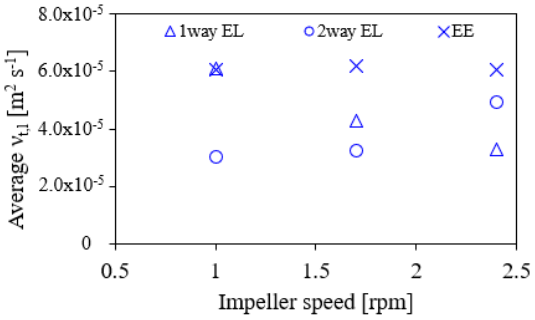

(c) One-way coupled EL, two-way coupled EL, and EE at 100 rpm

Figure 4.8: Average turbulence kinematic viscosityfor different impeller speeds for (a) the one-way coupled EL simulations, (b) the two-way coupled EL and EE simulations, and (c) for different working volumes at 100 rpm for all three modeling approaches, with $Q = 50$ mL min^{-1} for the microporous sparger.

power input, for which a cubic relationship with the impeller speed is described in literature [20]. The expected increase of the volumetric power input with the impeller speed for each of the considered volumes with the one-way coupled EL simulations as well as the EE and two-way coupled EL simulations shown in Figs. 4.9a and 4.9b, respectively. Figure 4.9c shows the effect of the working on the volumetric power input for the different modeling approaches. The expected decrease for larger volumes is observed but the impact of the volume on the volumetric power input is quite small compared to that of the impeller speed. For further evaluation of the volumetric power input the Power or Newton number

$$\mathrm{N_P} = P/\left(\rho_\mathrm{l} n^3 d_\mathrm{imp}^5\right) \tag{4.2}$$

is considered. Fully turbulent flow in a stirred tank is characterized by a constant $\mathrm{N_P}$. The average values of the simulated power numbers across all the investigated operating conditions are 0.68, 0.53, and 0.57 for the one-way coupled EL, the two-way coupled EL, and the EE approach, respectively. The observed minimum and maximum values are 0.55 and 0.75 for the one-way coupled EL simulations, 0.22 and 0.67 for the two-way coupled EL simulations, and 0.43 and 0.67 for the EE simulations. Even

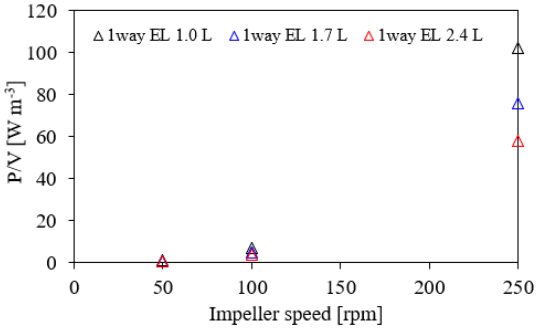

(a) One-way coupled EL

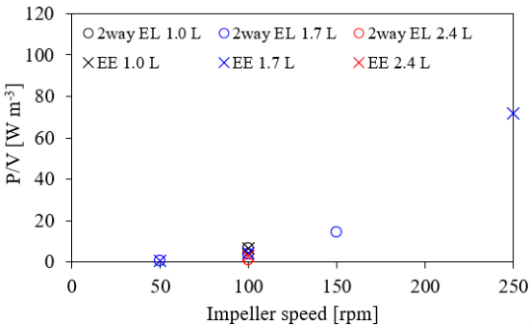

(b) Two-way coupled EL and EE

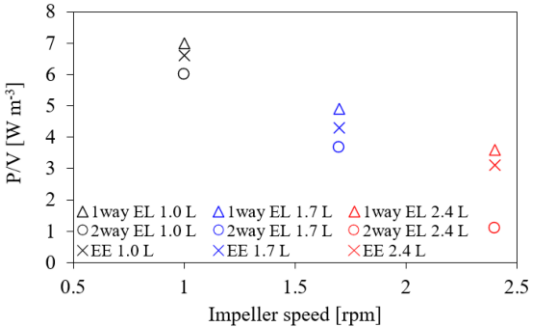

(c) One-way coupled EL, two-way coupled EL, and EE at 100 rpm

Figure 4.9: Volumetric power input (P/V) for different impeller speeds for (a) the one-way coupled EL simulations, (b) the two-way coupled EL and EE simulations, and (c) for different working volumes at 100 rpm for all three modeling approaches, with $Q = 50$ mL min^{-1} for the microporous sparger.

though $\mathrm{Re}_{\mathrm{imp}}$ for the lowest impeller speed of 50 rpm is only about 4300, there are only small differences in the power numbers across all operating conditions, which is typical for transient and turbulent conditions [20]. The power numbers obtained in the present study are very similar for the three considered modeling approaches but about twice as high as the value of 0.3 reported by Kaiser et al. [45, 147]. This difference might be related to different number of sensors, which act as baffles even though the bioreactor is unbaffled, since Kaiser et al. [45, 147] considered two sensors, whereas the present study considers three. The power numbers of the present study are in the expected low range that is typically observed for propeller type impellers [20].

Figure 4.10a shows the effect of the impeller speed on the mixing time for the one-way coupled EL simulations. Figure 4.10b compares the two-way coupled EL and EE simulation results to the experimental values for sparged conditions reported in [146]. For higher impeller speeds, the mixing time decreases because the liquid velocity and turbulence kinematic viscosity increase (see Figs. 4.6 and 4.8), which is also reflected in a higher power input (see Figs. 4.9a and 4.9b). This holds true for all simulation approaches, and the experiments. Empirical correlations [150, 45, 20] describe the correlation of the mixing time with volumetric power input as $t_{\mathrm{m}} \propto (P/V)^{-1/3}$ and consequently the expected correlation to the impeller speed is $t_{\mathrm{m}} \propto n^{-1}$. This hyperbolic

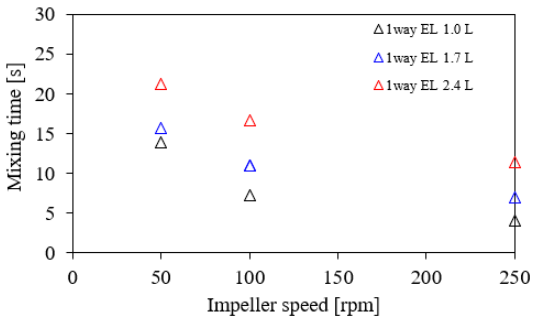

(a) One-way coupled EL

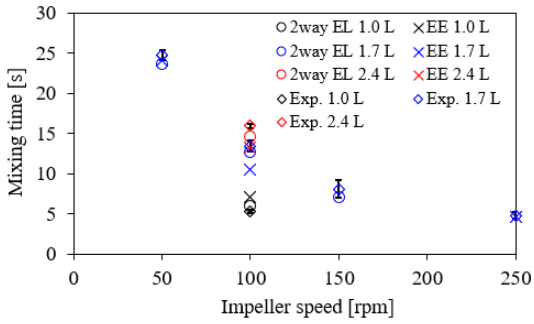

(b) Two-way coupled EL and EE

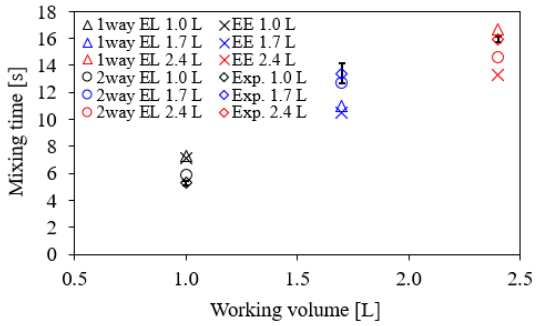

(c) One-way coupled EL, two-way coupled EL, and EE at 100 rpm

Figure 4.10: Mixing time for for different impeller speeds for (a) the one-way coupled EL simulations, (b) the two-way coupled EL and EE simulations, and (c) for different working volumes at 100 rpm for all three modeling approaches, with $Q = 50$ mL min^{-1} for the microporous sparger.

correlation corresponds to a rapid increase of the mixing time when reducing the impeller speed in the range of very low impeller speeds and a minor decrease of mixing time when increasing the impeller speed in the range of very high impeller speeds, which is in agreement to the present results.

In addition to the impeller speed, the mixing time also depends on the working volume, which is the volume that needs to be mixed. Moreover, the volumetric power input is reduced at a larger working volume. Figure 4.10c shows a clear reduction of the mixing times for lower working volumes within each of the individual data sets, i.e., for the three different simulation approaches as well as the experimental results. For the EE and two-way coupled EL approach as well as the experiments, the different working volumes are only tested for a fixed impeller speed of 100 rpm, but the one-way coupled EL simulations confirm this effect also for the other working volumes, see Fig 4.10a. Due to the variation of the mixing times obtained with different methods for a volume 1.7 L and 2.4 L at 100 rpm, there is overlap of the ranges of mixing times observed for maximum and intermediate working volume. The slightly larger variation between mixing times obtained with the different methods for working volume 2.4 L with a longer mixing time than for 1.0 L and 1.7 L is likely caused by

the slower transport of the tracer. Consequently, more time is needed to achieve a homogeneous distribution of the tracer and slight differences in the liquid flow, which is used as the input for the tracer simulations, to result in larger absolute differences in the mixing time. No clear trend of systematic over- or under-prediction of the mixing time associated with a specific modeling approach is observed. Moreover, the mixing criterion in experiments, i.e., the visually observed de-colorization, is observer dependent [151] and cannot easily be converted to a numerical criterion for the mixing time as no quantitative measurement data is available. This also contributes to the deviation between simulations and experiment.

As already mentioned, the liquid flow pattern is barely affected by the sparging and so far the discussion was focused on the effects of the working volume and the impeller speed. The impact of the sparging rate on the volumetric power input, the mixing time, and the average velocity magnitude is shown in Figs. 4.11a, 4.11b, and 4.11a, respectively. The impeller speed and the working volume are fixed at 100 rpm and 1.7 L, respectively. For a sparging rate of 50 mL min^{-1}, both the open pipe sparger and the microporous sparger results are shown, where the open pipe sparger results are indicated by bold symbols. The one-way coupled EL results are added on the y-axis as a reference for unsparged conditions because the effect of the bubbles on the liquid

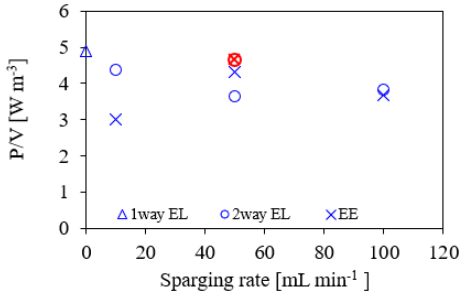

(a) Volumetric power input

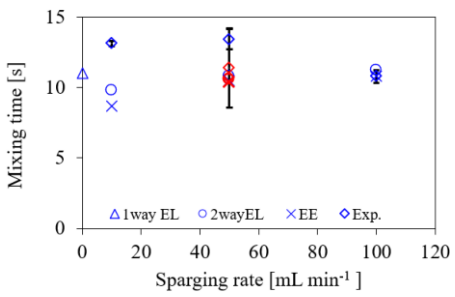

(b) Mixing time

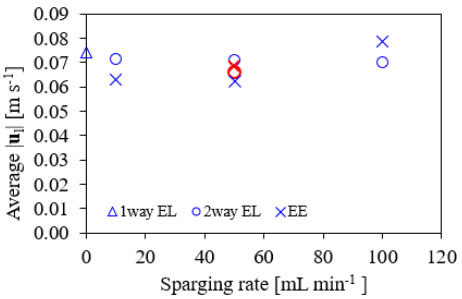

(c) Average liquid velocity

Figure 4.11: Volumetric power input P/V, mixing time, and average liquid velocity at $V = 1.7$ L and $n = 100$ rpm for sparging rates of 10 mL min^{-1}, 50 mL min^{-1}, and 250 mL min^{-1}. The results for the open pipe sparger at $Q = 50$ mL min^{-1} are indicated with bold markers, all other markers are for the microporous sparger. The experimental results are reported in [146].

flow is not taken into account as described in Sect. 2.4. In Fig. 4.11b experimental results are indicated by diamonds and the error bars represent the standard deviation of measurements taken in triplicate. The experimental results are reported in [146]. Overall, there is only small variation between the results for the different sparging rates and sparger types for both the two-way coupled EL and the EE simulations, which is comparable to the differences observed between the different modeling approaches. For the mixing time shown in Fig. 4.11b the markers for the two sparger types at 50 mL min^{-1} strongly overlap for both the two-way coupled EL and EE simulations. The effect of sparging on the mixing time is negligible compared to that of the impeller speed and the working volume due to the significantly smaller effect of the bubbles on the liquid motion than the agitation by the impeller. This is partly due to the low volume specific sparging rates of less than 0.06 vvm, which are too small to form gas cavities at the impeller, which would disrupt the liquid agitation. While the liquid motion and mixing are one process aspect that is strongly affected by the impeller speed, the exposure of cells to stress is another important aspect that is depending strongly on the impeller speed and is discussed next.

Risk of cell Damage

The mechanical stress acting on the suspended cells can be a critical issue, due to their negative effects on the productivity, growth, and viability of cells. This is especially true for mammalian cells, which only have a cell membrane consisting of a phospholipide bilayer that is much more sensitive to mechanical stress than the cell wall of microbial cells. Different criteria to quantify the mechanical force the cells are exposed to are reported in literature [135, 23, 74, 47, 13]. These criteria include the strain rate, the shear stress, the Kolmogorov length scale and the hydrodynamic stress, which are presented in this section.

The evaluation of mechanical stress in turbulent flow conditions is complicated by fact that the unsteady turbulent velocity fluctuations can only fully be captured with direct numerical simulations. However, their high requirements on the resolution of time and size scales makes direct numerical solutions still computationally too expensive for the simulation of complex and large equipment used in many industrial applications, despite the recent increase in computing power [120]. Thus, in most practical applications, either all turbulent fluctuations or the small scale turbulent fluctuations remain unresolved, when using Reynolds averaged Navier-Stokes equations or large eddy simulations, respectively [120, 136]. The transport and dissipation of energy through the unresolved turbulent eddies is approximated with the selected turbulence model and the strain rate or shear stress can only be calculated for the Reynolds-averaged or resolved velocities.

Li et al. [23] and Wollny [135] report simulations of the liquid flow in stirred tank reactors with the $k-\varepsilon$ turbulence model using the Reynolds average velocity to evaluate the strain rate and shear stress, respectively. Both criteria are derived from the velocity gradient, which is highest at the edges of the impeller blades. To give an idea of the spatial distribution of high and low stress regions evaluated from the velocity gradient, the shear stress obtained for an impeller speed of 250 rpm and a working volume of

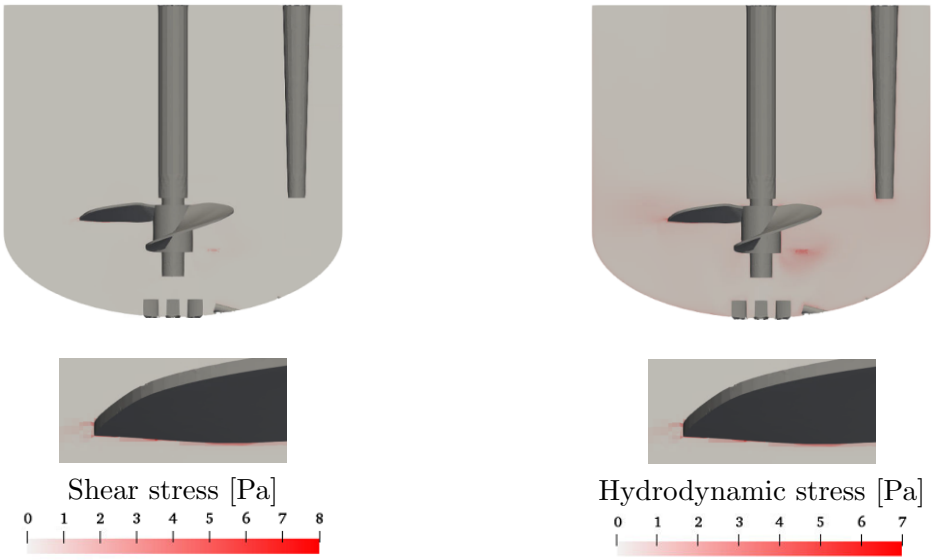

(a) Shear stress following Eq. (2.43) (b) Hydrodynamic stress following Eq. (2.48)

Figure 4.12: Shear stress and hydrodynamic stress for the maximum impeller speed of 250 rpm at a working volume of 1.7 L for the one-way coupled EL approach in the x-z plane through the center of the CR3 for the complete reactor and for a zoomed view of the region around the left impeller blade.

1.7 L obtained with the one-way coupled EL approach is shown in Fig. 4.12a.

The regions of highest velocity are also associated with the highest turbulence. The risk of cell damage through turbulent eddies can be evaluated by calculating the Kolmogorov length scale or the hydrodynamic stress from the turbulence energy dissipation rate as defined by Eqs. (2.47) and (2.48), respectively. The hydrodynamic stress obtained for 250 rpm at a working volume of 1.7 L obtained with the one-way coupled EL approach is shown in Fig. 4.12b. The spatial distribution of high and low stress regions evaluated from the velocity gradient, i.e., the shear stress in Fig. 4.12a, and those evaluated from the turbulence energy dissipation rate, i.e., the hydrodynamic stress in Fig. 4.12b, have a similar spatial distribution, where the maximum values of both are located at the edges of the impeller blades. The shear stress and the hydrodynamic stress also are of a similar magnitude but the shear stress does not show the same regions of elevated stress levels in the flow from the impeller towards the vessel wall observed for the hydrodynamic stress.

The different criteria for the quantification of the exposure of cell to mechanical stress all share a similar spatial distribution with a large volume of low stress in the liquid bulk and a small volume of high stress in the region of the highest velocity and turbulence surrounding the impeller. To judge the effect of each of these criteria on cell cultivation, thresholds for the tolerance of the cell line of interest must be known. This data is partially available in the literature [134, 23, 38] and otherwise must be obtained by comparing the stress characterization and cell cultivation results for identical process conditions. Another aspect to consider is that the exposure time and frequency of the

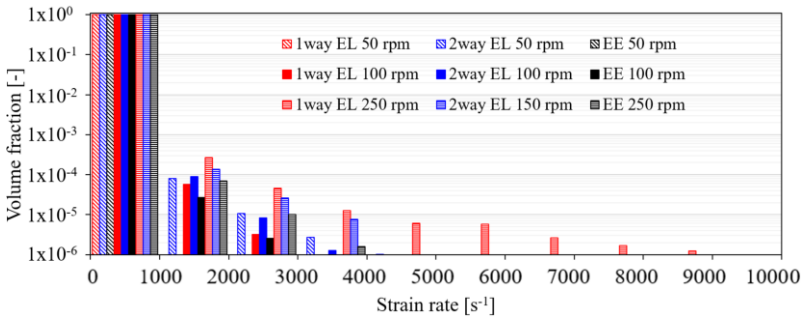

(a) Strain rate

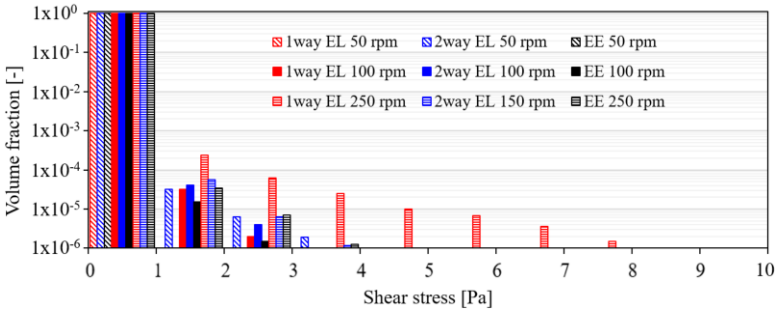

(b) Shear stress

Figure 4.13: Liquid volume fraction distributions of the strain rate and the shear stress for the impeller speeds of 50 rpm, 100 rpm, and 150 rpm or 250 rpm with $V = 1.7$ L and $Q = 50$ mL min^{-1} for the microporous sparger.

cultivated cells, which are convected by the liquid, depends on the volume fraction associated with a certain stress level. Negative effects on growth and productivity can be observed long before lethal stress levels are reached [57, 134] and cells have a certain capability to recover from and adapt to the exposure to elevated but sub-lethal stress levels. Consequently, the effect of the violation of a certain sub-lethal stress criterion on the cell growth at the scale of the complete bioreactor might also depend on the volume (fraction) associated with this violation. Volume fraction distributions [132] or time profiles of the mechanical stress experienced by cells traveling through the bioreactor [152] may also help to get a better understanding than the average or the local maximum stress values.

The volume fraction distributions of the strain rate and the shear stress are shown in Fig. 4.13. Due to the reasons given in the previous section on the liquid flow pattern, a lower maximum impeller speed of 150 rpm instead of 250 rpm is used for the two-way coupled EL simulations. The shear stress is obtained from the product of the tangential strain components, which are a subset of the total strain rate, and the liquid's dynamic viscosity $\mu_l = 0.001126$ Pa s. This results in a very similar distribution of both stress criteria with the strain rate being approximately 1,000 times larger than the shear stress, even though the selected bin sizes do not match exactly. As the shear stress is only considering a subset of the strain tensor, the shear stress is slightly lower than the product of the strain rate and μ_l. While the shear stress and the strain rate are separate

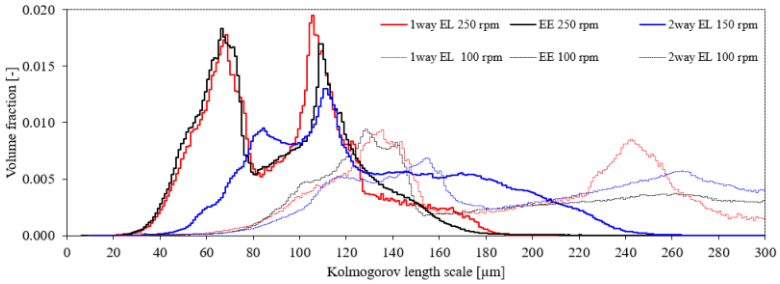

Figure 4.14: Liquid volume fraction distributions of the Kolmogorov length scale from 0 µm to 300 µm for the impeller speeds of 100 rpm, and 150 rpm or 250 rpm with $V = 1.7$ L and $Q = 50$ mL min^{-1} for the microporous sparger.

criteria for the evaluation of the mechanical stress in the liquid, the fact that they are both derived from the velocity gradient and show very similar distributions suggests that they would not provide significantly different results on the risk of cell damage. Both volume fraction distributions further emphasize that only a very small region of the bioreactor is exposed to high stress levels. For the one-way coupled EL and EE simulations indicated in Fig. 4.13 by red and black, respectively, the maximum levels of the strain rate and the shear stress increase with the impeller speed as indicated by the differently patterned bars. The two-way coupled EL simulations do not show the same clear effect of the impeller speed and are discussed separately below.

Figure 4.14 shows the liquid volume fractions of the full range of the simulated local Kolmogorov length scales for the maximum impeller speeds of 150 rpm for the two-way coupled EL approach and 250 rpm for the one-way coupled EL and the EE approaches. With decreasing impeller speed the distribution becomes broader and shifts to larger values and part of the distributions for the intermediate impeller speed of 100 rpm are also shown in Fig. 4.14.

Figure 4.15a shows the liquid volume fractions for the smallest observed values of the Kolmogorov length scale for the different impeller speeds and modeling approaches. For the lowest impeller speed of 50 rpm, only in the two-way coupled EL simulations Kolmogorov length scales in the considered range of up to 25 µm are observed. The smallest minimum values the are observed for the highest impeller speed for the one-way coupled EL and EE simulations. Similar to the maximum values of the strain rate and the hydrodynamic stress, the two-way coupled EL show similar minimum Kolmogorov length scales for all impeller speeds and are discussed separately below.

Figure 4.15b shows the liquid volume fractions of the hydrodynamic stress, which is also derived from the turbulence energy dissipation rate. Since the Kolmogorov length scale and the hydrodynamic stress are both calculated from the turbulence energy dissipation rate, the Kolmogorov length scale is correlated to the inverse of the square root of the hydrodynamic stress as

$$l_{\mathrm{K}} = \sqrt{\frac{\mu_{\mathrm{l}}\nu_{\mathrm{l}}}{\tau_{\mathrm{l}}}}. \tag{4.3}$$

In contrast to the Kolmogorov length scale, the maximum not the minimum values of

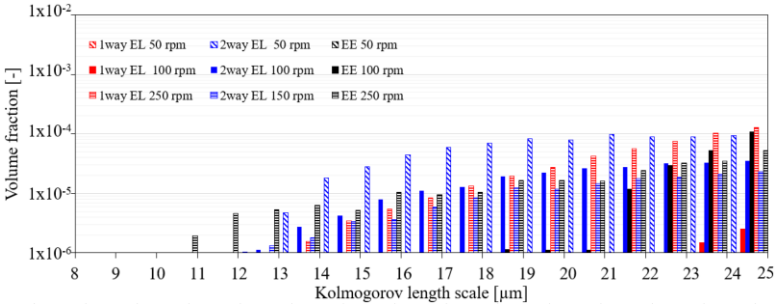

(a) Kolmogorov length scale up to 25 µm

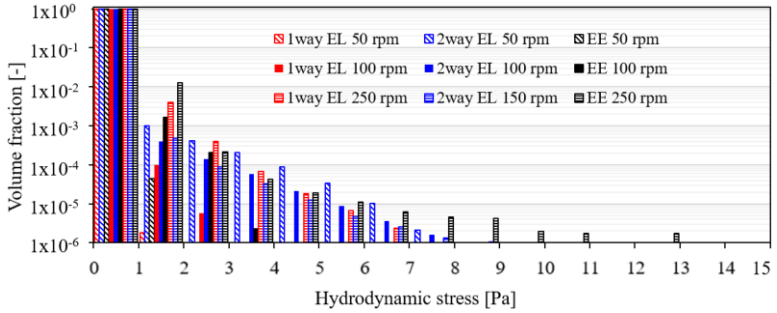

(b) Hydrodynamic stress

Figure 4.15: Volume fraction distributions for the Kolmogorov length scale from 8 µm to 25 µm and the hydrodynamic stress for the impeller speeds of 50 rpm, 100 rpm, and 150 rpm or 250 rpm with $V = 1.7$ L and $Q = 50$ mL min^{-1} for the microporous sparger.

τ_l correspond to the highest turbulence and stress levels. Like for the strain rate and the shear stress, the maximum hydrodynamic stress increases with increasing impeller speeds for the one-way coupled EL and EE simulations but nor for the two-way coupled EL simulations. However, while the one-way coupled EL simulations show a higher maximum strain rates and shear stress, the EE simulations show a higher hydrodynamic stress. This is caused by the differences in the liquid velocity and turbulence found for these two approaches and is also reflected in the average values discussed in the previous sections, see Figs. 4.6c, 4.7cand 4.8c. Accordingly, the stress criteria evaluated from the velocity gradient, i.e., the strain rate and shear stress, are higher and the hydrodynamic stress evaluated from the turbulence energy dissipation rate, i.e., the hydrodynamic stress, is lower in the one-way coupled EL simulations.

As mentioned above the results of the two-way coupled EL simulations differ from the other two modeling approaches, since the maximum values of the strain rate, the shear stress, and the hydrodynamic stress as well as the minimum values of the Kolmogorov length scale do not show the same clear dependence on the impeller speed. While the maximum impeller speed of 150 rpm is lower than for the one-way coupled EL and EE simulation, the maximum stress levels are similar to those observed for 250 rpm with the one-way coupled EL and EE approach.However, the overall

distribution of the Kolmogorov length scale at 150 rpm in Fig. 4.14 fits quite well with the one-way coupled EL simulations in so far as that the peaks of the distribution for the two-way coupled EL simulations are between those of the higher and lower impeller speeds of 250 rpm and 100 rpm observed with the one-way coupled EL simulations. A comparison of the shear stress observed in the two-way coupled EL simulations for the different impeller speeds in Fig. 4.16 indicates that the maximum values of the shear stress are associated with the velocity fluctuations around the rising bubbles and are of a similar magnitude as or higher than those caused by the impeller motion at the maximum impeller speed. The experiments by Villiger et al. [153] on the size of shear sensitive aggregates for sparged and un-sparged indicate that sparging can significantly contribute to the hydrodynamic stress especially at $\mathrm{Re}_{\mathrm{imp}}$ below 10,000, which supports the observations made for the two-way EL simulations made in the present study. However, due to the large size of the bubbles compared to that of the control volumes of the numerical grid and the selection of a parcel size smaller than 1 to avoid difficulties with the coupling terms as discussed above, further experiments on the magnitude of the hydrodynamic stress generated by the bubbles would be needed for validating the present results.

To further evaluate the risk of cell damage, thresholds for the respective stress criteria are required. Neunstoecklin et al. [134] report hydrodynamic stress thresholds of 25.2 ± 2.4 Pa and 32.4 ± 4.4 Pa for mouse hybridoma Sp2/0 and Chinese hamster ovary cells, respectively. Both the simulated hydrodynamic stress and the shear stress are significantly lower than 25 Pa, indicating no risk of cell damage across the considered range of impeller speeds. The Kolmogorov length scale is another criterion to assess the risk of cell damage based on the turbulence energy dissipation rate. The general hypothesis is that cells are damaged by turbulent eddies of similar

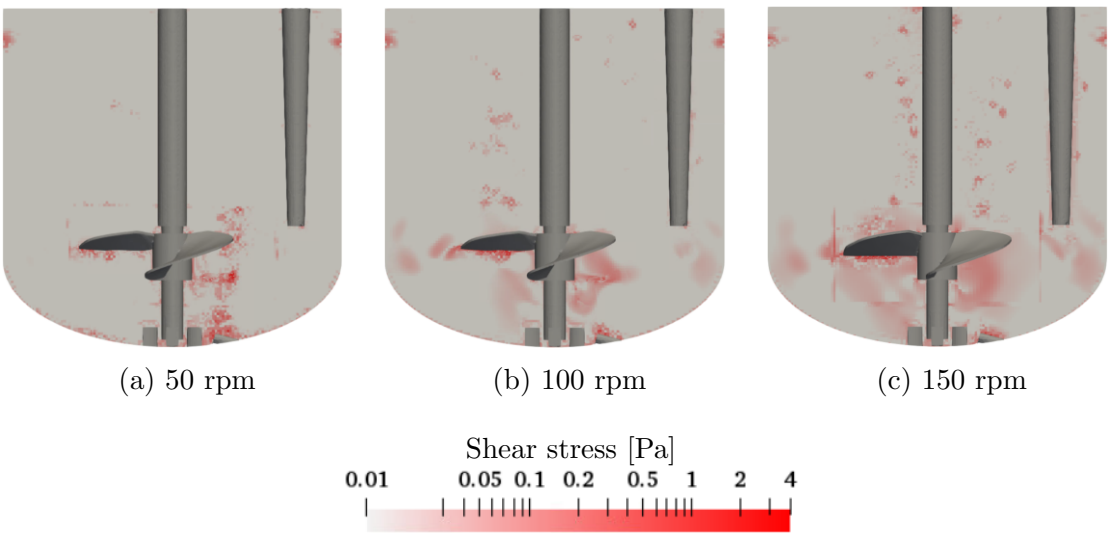

(a) 50 rpm (b) 100 rpm (c) 150 rpm

Figure 4.16: Shear stress for the impeller speeds of 50 rpm, 100 rpm, and 150 rpm with $V = 1.7$ L and $Q = 50$ mL min^{-1} for the microporous sparger for the two-way coupled EL approach in the x-z-plane through the center of the CR3.

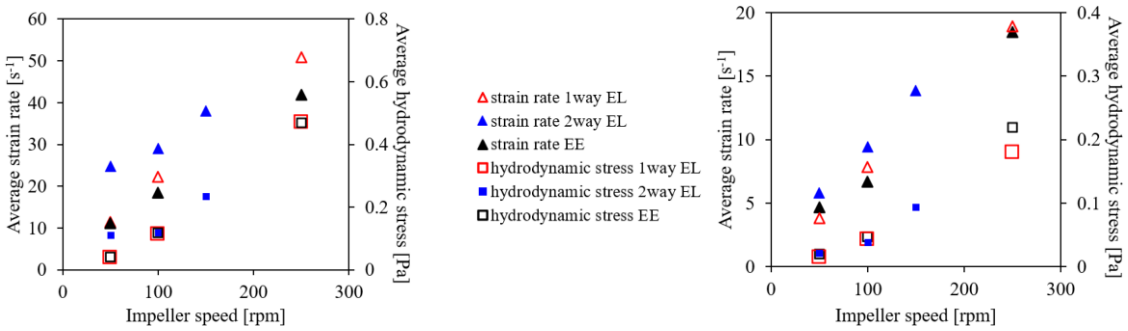

(a) Impeller zone (b) Tank zone

Figure 4.17: Average strain rate and average hydrodynamic stress for the impeller (left) and tank zone (right) of the CR3 at $V = 1.7$ L and $Q = 50$ mL min^{-1} for the microporous sparger.

size [13, 45, 137]. Minimum Kolmogorov length scales in a range similar to the size of suspended mammalian cells, i.e., below 20 µm are found for the maximum impeller speeds of the one-way coupled EL and EE simulations and at all impeller speeds for the two-way coupled EL simulations for a small volume fraction of less than 0.05 %. While the associated volume is very small, this finding still contradicts the threshold of Neunstoecklin et al. [134] derived for the hydrodynamic stress, which indicates that the turbulence energy dissipation rate is sufficiently low to avoid cell damage. This different interpretations of the turbulence energy dissipation rate show the need for further investigations on the sensitivity of the cultivated cell lines to damage by turbulent eddies. In the light of the available experimental evidence, the present study focuses on the hydrodynamic stress as the stress criterion obtained from the simulated turbulence energy dissipation rate, while the Kolmogorov is not reported for the other bioreactors.

For the stress criteria obtained from the velocity gradient, the strain rate and the shear stress, no thresholds for the maximum tolerable value are available. Li et al. [23] report ranges for the average the strain rate of the impeller and the tank zones as criteria for the selection of the impeller speed during scale-up. Li et al. [23] considered bioreactors with different size and impeller configurations for the scale-up of a cultivation of *Spodoptera frugiperda* Sf9 cells. To test the applicability of the approach described by Li et al. [23] to the present study, the strain rate is selected for further evaluation and the shear stress is not reported for the other bioreactors.

In reference to the method of Li et al. [23], the average strain rate for impeller and tank zones obtained with the three different modeling approaches are shown in Figs. 4.17a and 4.17b, respectively. The impeller region is selected as a cylinder centered on the impeller with a height of 0.33 d_{imp}, which corresponds to the height reported by Li et al. [23] for pitched-blade and marine blade impellers. Instead of a diameter of 1.3 d_{imp}, a diameter of 1.2 d_{imp}, which corresponds to the diameter reported by Li et al. [23] for 'Elphant Ear' impellers, is selected to exclude the sensors from the impeller zone. The same dimension of the impeller zone as for the CR3 are also used for all larger bioreactors. In addition to the strain, the same analysis is also performed for the hydrodynamic stress and included in Figs. 4.17a and 4.17b. The simulation

results suggest a linear correlation with the impeller speed for both the impeller as well as the tank zone for all simulation approaches. The linear correlation of the average strain rate and the impeller speed agrees well with the findings of Li et al. [23]. The two to three times higher average values of the average strain rate and hydrodynamic stress in the impeller zone compared to the tank zone, emphasize the large difference in the liquid stress observed in the proximity of the impeller compared to that far from it. The fact that the linear correlation is also found for the two-way coupled EL simulations also emphasizes that the maximum values observed in Figs. 4.13a, 4.13b, and 4.15b, as well as the minimum values in Fig. 4.15a are associated with the small volume fraction surrounding the bubbles and have little impact on the average values of the bulk liquid flow.

Gas Hold-Up and Volumetric Oxygen Mass Transfer Coefficient

The previous sections presented the two aspects of homogenization and cell damage by the liquid motion. Since faster mixing is associated with a higher mechanical stress in the liquid phase, the optimization of these two process aspects leads to contradicting goals of high and low impeller speeds but is barely affected by the sparging. However, the third process aspect covered in this section, the oxygen transfer is highly dependent on the sparging strategy.

The cumulative surface area of all bubbles dispersed in the liquid defines the available transfer area, which depends on the number and the size of the bubbles present in the liquid. The number of bubbles added for a given time interval increases with the sparging rate and for a given sparging rate a smaller bubble size results in a higher number of bubbles, which provide a larger specific interface area for a given gas hold-up. Figures 4.18a and b show the average bubble residence times for one-way coupled EL simulations with a monodisperse bubble size for different diameters and

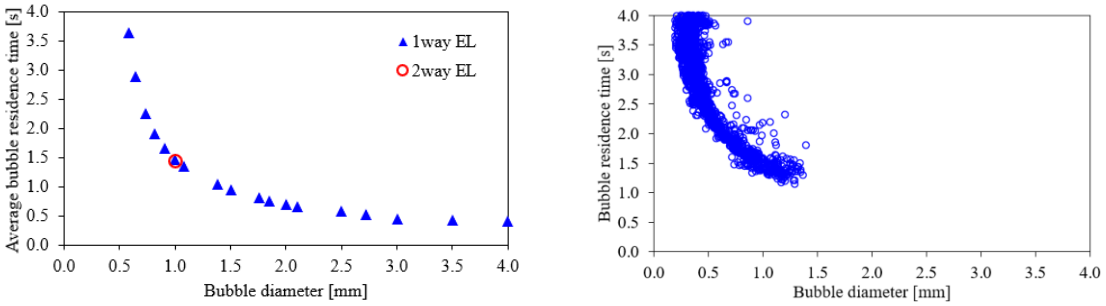

(a) One-way and two-way coupled EL (b) Two-way coupled EL

Figure 4.18: Average bubble residence times of one-way coupled EL simulations for different monodisperse bubble diameters as well as for 1.0 mm bubble diameter for the two-way coupled EL simulation and residence times for individual bubbles of a two-way coupled EL simulation with a polydisperse bubble size distribution with diameters from 0.3 mm to 1.35 mm for the base case (V = 1.7 L, n = 100 rpm, Q = 50 mL min^{-1}, microporous sparger).

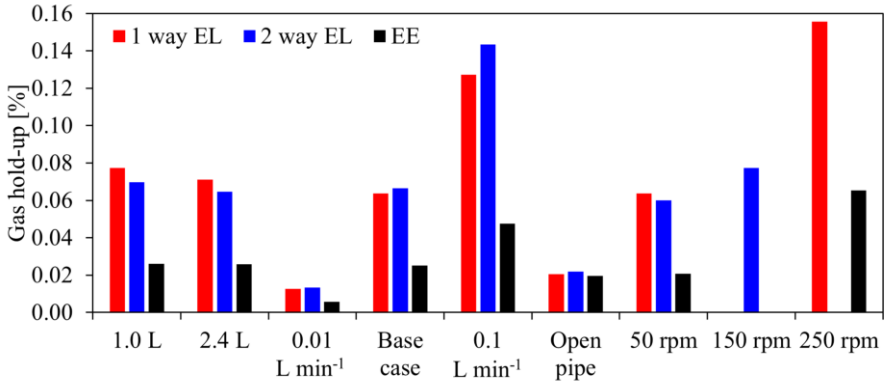

Figure 4.19: Gas hold-up for the CR3 for different operating conditions with the labels indicating the value of the operating parameter deviating from the base case (V = 1.7 L, n = 100 rpm, Q = 50 mL min^{-1}, microporous sparger).

the residence time observed for individual bubbles in a two-way coupled EL simulation with a polydisperse bubble size distribution, respectively. The same impeller speed and working volume of 100 rpm and 1.7 L is selected in both cases. The residence time of smaller bubbles increases due to their lower buoyancy, which results in a higher number of bubbles present in the liquid at steady conditions. The cumulative volume of all bubbles normalized by the total volume of the gas-liquid dispersion is the gas hold-up shown in Fig. 4.19. It is related to the specific interface area according to Eq. (2.34). A higher sparging rate, which corresponds to an addition of more bubbles per time, and a higher impeller speed, which results in a longer bubble residence time due to better bubble dispersion and a longer rise path, both increase the gas hold-up.

The present simulations treat the bubbles as disperse elements that enter the computational domain at the sparger and the grid is to coarse to refine the interface of individual bubbles. Consequently, the growth and detachment of individual bubbles at the different sparger orifices cannot be included in the simulations. Instead, the effect of the sparger type on the bubble size is reflected in the simulations by setting different bubble diameters, where 1 mm and 4 mm are selected for the microporous and the openpipe sparger, respectively. The shorter bubble residence time for the larger bubble diameter of 4 mm is also reflected in a lower gas hold-up for the open pipe sparger. Changes in the working volume barely affect the gas hold-up. This indicates that after passing the impeller, the bubbles have an approximately constant rise velocity, since the increase in the liquid height caused by the larger working volume results in a proportionally longer bubble residence time and higher number of disperse bubbles at steady conditions. The one-way and two-way coupled EL simulations give quite similar results across all test conditions, while for the EE simulations a lower gas hold-up is found across all operating conditions. The simulated volumetric oxygen mass coefficient $k_{\mathrm{L}}a$ is the product of the liquid transfer coefficient k_{L}, see Eq. (2.32), and the specific interface area a, see Eq. (2.34). Since the interface area is proportional to the gas hold-up, the $k_{\mathrm{L}}a$ shows similar dependence on the operating conditions as the gas hold-up, i.e., the $k_{\mathrm{L}}a$ increases with the sparging rate and the impeller speed shown in

Fig. 4.20b and Fig. 4.20a, respectively. The experimental values used for comparison are reported in [146]. For the increase in the sparging rate, the experimental results confirm the increase in the k_La for higher sparging rates observed in the simulations. For a higher impeller speed, the experimental k_La values also increase but due to the high standard deviation this is not significant based on a two-tailed t-test. The severe impact of the sparger type on the bubble size and consequently the k_La for sparging rate of 50 mL min^{-1} with the open pipe sparger results indicated in bold symbols in Fig. 4.20a is in close agreement between the simulations and the experiments. One difference between the gas hold-up and the k_La is the dependence on the working volume: while the gas hold-up is barely affected, the k_La increases slightly for a smaller working, as shown in Fig. 4.20c. This is related to the higher volumetric power input at increased impeller speed, which corresponds to a higher turbulence energy dissipation that enters into the calculation of the k_L according to Eq. (2.32). In contrast to the simulations, the experimental values for the k_La slightly increase for a larger working volume, which, however, is not significant based on a two-tailed t-test. The simulations as well as the experiments indicate that the effect of the working volume on the k_La is small.

While the agreement on the qualitative effect of the operating conditions between the simulations and the experiments is quite good, the quantitative agreement of the

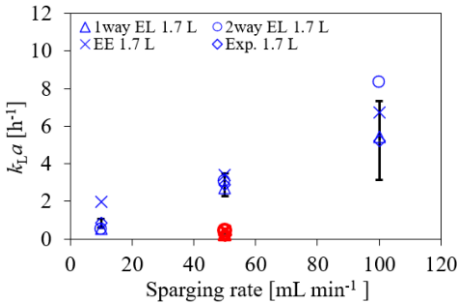

(a) Effect of the sparging rate

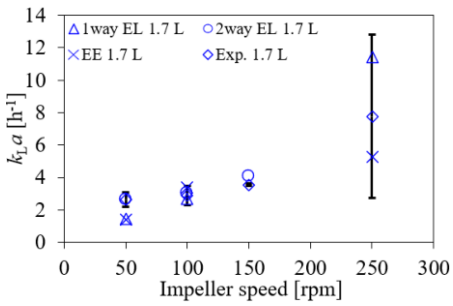

(b) Effect of the impeller speed

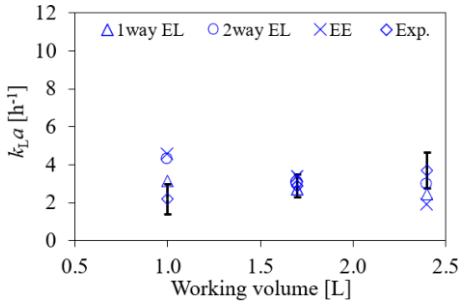

(c) Effect of the working volume

Figure 4.20: Impact of changes of a single operating parameter on the k_La for the CR3 with the other operating parameters at the intermediate value of 1.7 L for the working volume, 100 rpm for the impeller speed, and 50 mL min^{-1} for the sparging rate. The experimental and two-way coupled EL results are reported in [146].

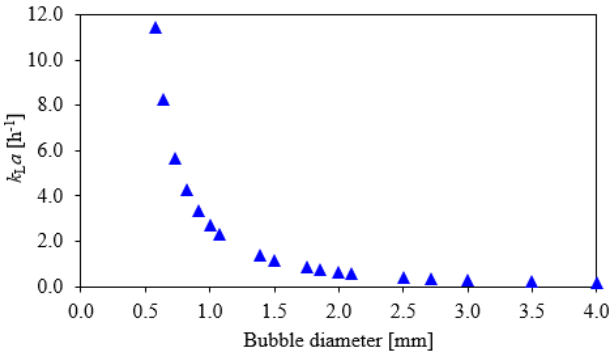

Figure 4.21: Effect of the bubble diameter on the $k_{\mathrm{L}}a$ for the one-way coupled EL simulations of the CR3 for the base case with $V = 1.7$ L, $n = 100$ rpm, $Q = 50$ mL min^{-1} for the microporous sparger.

individual conditions varies quite strongly. This might partly be related to the high standard deviation in the experiments but also to the fact that only a single bubble diameter is considered in the simulations. Accordingly, variations of the bubble size distribution due to changes in the operating conditions are neglected. Even small deviations of the bubble diameter can have a strong impact on the k_{L}, due to changes in the bubble residence time. This is shown in Fig. 4.21 for the one-way coupled EL simulations results for the base case condition. As mentioned above, for the one-way coupled EL approach, the simulated liquid flow does not consider the impact of the bubbles. Accordingly, the observed changes in the $k_{\mathrm{L}}a$ shown in Fig. 4.21 for different bubble sizes are only caused by the changes in the bubble residence time, which changes the gas hold-up and the specific interface area a.

For this complete section the one-way coupled EL, the two-way coupled EL, and the EE simulations have been presented side-by-side. All three approaches show similar agreement to the experimental values for the volumetric oxygen mass transfer coefficient, indicating no obvious differences in the accuracy of the EE and the two-way coupled EL simulations. The phase inversion in the EE simulations allows for the inclusion of the head space, which allows the gas added through sparging to leave the bioreactor through the head space and consequently the additional artificial boundary described for the two-way coupled EL simulations in Sect. 4.1.3 is not required. Moreover, the inclusion of the head space allows to capture the surface vortex formation. For these reasons the EE approach is selected as the modeling for the simulation of all larger bioreactor scales. Due to their low computational cost the one-way coupled EL simulations are also performed to provide data for all combinations of the considered working volume and impeller speeds.

4.1.5 Selection of Operating Conditions for Cell Cultivation

This section summarizes the results of section 4.1.4 from the point of view of selecting operating conditions according to cell culture requirements. The operating parameters that must be selected or controlled are the impeller speed, the working volume, the

sparger type, and sparging rate. A higher working volume increases the mixing time, while it does not affect the risk of cell damage or the k_La. Assuming that the same final product concentration c_{pro} can be achieved for all working volumes, the maximum product mass m_{pro}

$$m_{pro} = c_{pro}V \tag{4.4}$$

is obtained for the maximum working volume V. Accordingly, it is the preferred operating condition, despite its negative effect on the mixing time. Typically the cultivation of mammalian cells is operated in fed-batch mode, where the maximum working volume is reached at the final day of the cultivation.

A higher impeller speed has a positive impact on both the mixing time and the volumetric oxygen mass transfer coefficient. However, the benefit a higher impeller speed has on the mixing time reduces with increasing impeller speed. Thus, an impeller speed of 100 rpm is clearly more favorable than the lowest impeller speed of 50 rpm, but a further increase to 150 rpm or 250 rpm may not be necessary for a small lab-scale reactor like the CR3 with overall short mixing times. Moreover, very high impeller speeds result in a significantly higher volumetric power input and risk of cell damage. However, for the investigated impeller speeds of up to 250 rpm critical levels are not reached for the CR3.

Regarding the sparging strategy, the open pipe sparger results in very low k_La values and appears unsuitable to provide sufficient oxygen even for the cultivation of mammalian cells, which have quite low oxygen requirements compared to microbial cells. The microporous sparger generates much smaller bubbles and is better suited to meet the oxygen requirements. During cell cultivation, the required oxygen transfer increases with the number of cells suspended in the liquid, which in turn increase due to cell growth. Cell growth in this context refers to the increase of the number of cells by cell division. To maintain a constant dissolved oxygen level, which is typically set at 50 % air saturation, the bioreactor control unit can dynamically adjust the oxygen flow rate during the cultivation. For the investigated impeller speed of 100 rpm and a sparging rate of 100 mL min^{-1}, a k_La between 5 h^{-1} and 9 h^{-1} is observed for the different modeling approaches. The typical k_La range for the cultivation of mammalian cells is reported as 1 h^{-1} to 20 h^{-1} [13, 35, 18]. Consequently, the k_La obtained with the present operating conditions might be already sufficient for some cell lines, while for other cell line slightly higher sparging rates might be required to further increase the k_La.

In summary, for the CR3, the mixing times are relatively short especially for an impeller speed of 100 rpm or higher due to the small volume. No risk of cell damage up to the highest investigated impeller speed of 250 rpm is indicated and only the microporous sparger can match the oxygen requirements typically observed for cell cultivation.

4.2 The Xcellerex^{TM} XDR-10

The Xcellerex^{TM} XDR-10 with a maximum working volume of 10 L is the smallest of the Xcellerex^{TM} bioreactors [145]. Thus, the XDR-10 is often the first step in cell culture scale-up to 2000 L, which is the largest scale available for the Xcellerex^{TM} bioreactors. All of them are equipped with pitched-blade, bottom mounted impellers and microporous spargers. Only the two smallest XDR bioreactors, the XDR-10 and XDR-50 have centered impellers, whereas all of the larger Xcellerex^{TM} bioreactors have off-centered impellers. The unbaffled vessel in combination with the centered impeller of the XDR-10 results in surface vortex formation at high impeller speeds, which is evaluated in addition to the other process characteristics. For the XDR-10, one-way coupled EL and EE simulations have been performed.

4.2.1 Bioreactor Configuration

The Xcellerex^{TM} XDR-10 consists of a rigid, multi-use vessel frame supporting in which single-use, flexible cultivation bag is placed. The pitched-blade impeller with three blades, see Fig. 4.22, is fixed onto a rigid plastic plate at the bottom of the single-use bag. All sparger openings are integrated into this plate and located directly below the impeller blades. The XDR-10 has a flat bottom and a vessel diameter d_V of 20.3 cm. The impeller diameter d_{imp} is 13.6 cm. The impeller is driven by magnetic coupling and rotated in the anti-clockwise direction. Only the two microporous spargers with 2 µm and 20 µm pore size are considered in the simulations, while the two drilled hole spargers with five drilled holes of 0.5 mm and 1.0 mm diameter, respectively, are not used.

4.2.2 Operating Conditions

The considered operating conditions are selected in the same manner as described for the CR3 in section 4.1.2 and cover changes in the impeller speed, the working volume, the sparging rate, and the sparger type. The selected operating conditions for the simulations are summarized in Tab. 4.3. For the impeller speed, low, intermediate, and high values of 40 rpm, 100 rpm, and 360 rpm are considered. For the working volume, the supplier specified minimum and maximum volume of 4.5 L and 10.0 L, and the intermediate value of 7.0 L are tested. For the sparging rate, the levels are

Figure 4.22: Impeller of the Xcellerex^{TM} XDR-10

Table 4.3: Operating conditions for the EE simulations of the XDR-10.

Condition #	Impeller speed n [rpm]	Working volume V [L]	Sparging rate Q [mL min^{-1}]	Sparger type
1	40	7.0	250	2 µm
2	100	7.0	250	2 µm
3	360	7.0	250	2 µm
4	100	4.5	250	2 µm
5	100	10.0	250	2 µm
6	100	7.0	20	2 µm
7	100	7.0	500	2 µm
8	100	7.0	250	20 µm

20 mL min^{-1}, 250 mL min^{-1}, and 500 mL min^{-1}. The sparger options are the two microporous spargers with 2 µm and 20 µm pore size of which the 2 µm sparger is selected as the standard setting. Condition #4 with the intermediate impeller speed, working volume and sparging rate of 100 rpm, 7.0 L, and 250 mL min^{-1} and the 2 µm sparger is the base case relative to which changes in a single operating parameter are evaluated.

In the one-way coupled EL simulations, the gas hold-up and volumetric oxygen mass transfer coefficient are evaluated for all conditions in Tab. 4.3 and an extended set of simulation conditions is used to characterize the liquid flow as summarized in Tab. 4.4. Similar to the CR3, the extended set of conditions consists of all possible combinations of the three levels of working volume and the three levels of impeller speed.

Table 4.4: Operating conditions for the one-way coupled EL simulations of the XDR-10.

Condition #	Impeller speed n [rpm]	Working volume V [L]
1	40	4.5
2	100	4.5
3	360	4.5
4	40	7.0
5	100	7.0
6	360	7.0
7	40	10.0
8	100	10.0
9	360	10.0

4.2.3 Grid Independence Study

Similar to the CR3, different grids with resolutions are created for the one-way coupled EL and EE simulations with the respective software tools MixIT [64] and OpenFOAM [63]. The grid structure is analogous to the one described for the CR3 with a hexhedral grid as the basis and refinement and polyhedral cells at the boundaries. For the one-way coupled EL simulations a finer grid is used for the rotating reference frame region, which is the same as for the CR3. Figures 4.23a and 4.23b show the investigated grids. The intermediate grids with 3.0x10^6 and 1.9x10^6 grid cells for the one-way coupled EL and EE simulations, respectively, are selected based on less than 5 % deviation from the respective finest investigated grid for the average velocity magnitude, turbulence kinetic energy, turbulence energy dissipation rate, and turbulence viscosity.

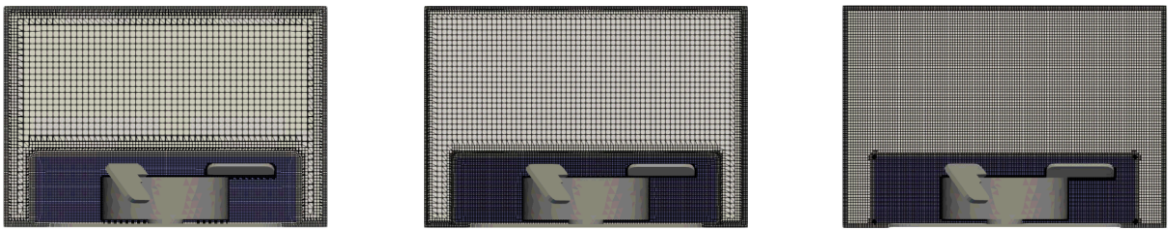

(a) Grid for the one-way coupled EL simulations for 4.5 L working volume. Left to right: 2.0x10^6, 3.0x10^6, and 5.7x10^6 grid cells.

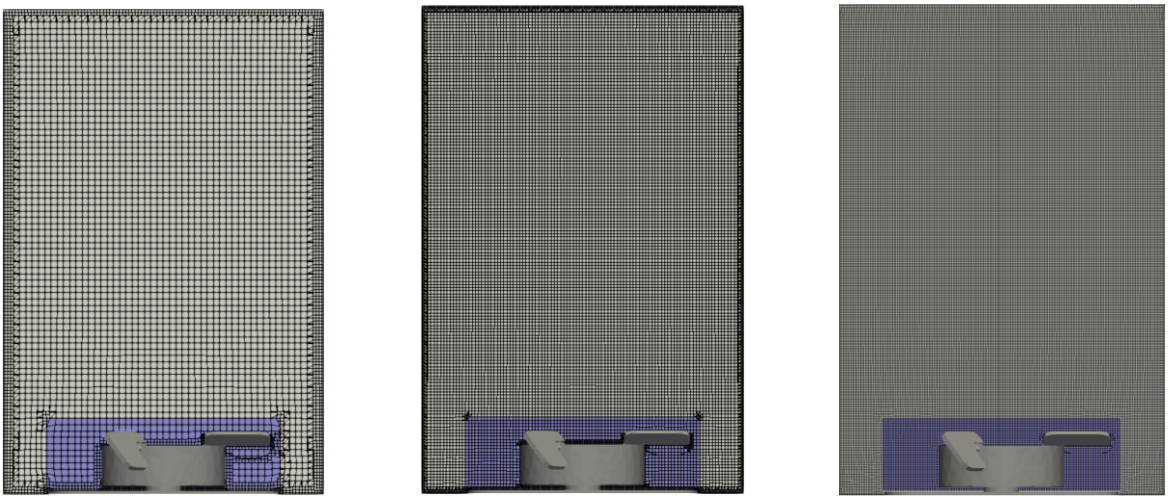

(b) Grid for the EE for the complete reactor including the head space. Left to right: 0.3x10^6, 1.9x10^6, and 10.0x10^6 grid cells.

Figure 4.23: Computational grids for the XDR-10 considered in the grid study. The rotating reference frame region is highlighted in blue.

4.2.4 Process Characterization

First the liquid flow structure and the bubble dispersion are described. Surface vortex formation is found to occur at the highest investigated impeller speed and is presented as part of the results on the liquid flow structure. In the next part, the effect of the operating conditions on the process characteristics is evaluated and finally the selection of operating conditions suitable for cell cultivation is discussed.

Liquid Flow Field, Surface Vortex Formation, and Bubble Dispersion

The liquid flow and bubble dispersion within the XDR-10 are shown in Fig. 4.24. Both the liquid and the bubble motion are dominated by the rotation of the impeller in the up-pumping, anti-clockwise direction. This strong rotational motion also is emphasized by the dominant tangential velocity component that for the x-z-plane coincides with the y-component of the cartesian velocity components shown in Fig. 4.25. At the impeller blades, the liquid is not only pushed in the anti-clockwise direction but also outwards to the vessel wall. There the flow is directed up- and downwards, forming two recirculation zones. One recirculation zone is located above the impeller and one with a smaller size and higher velocity below the impeller, similar to the CR3. However, due to the smaller distance of the impeller to the vessel bottom, the flat bottom shape and the width of the cylindrical base of the impeller, the lower recirculation zone is

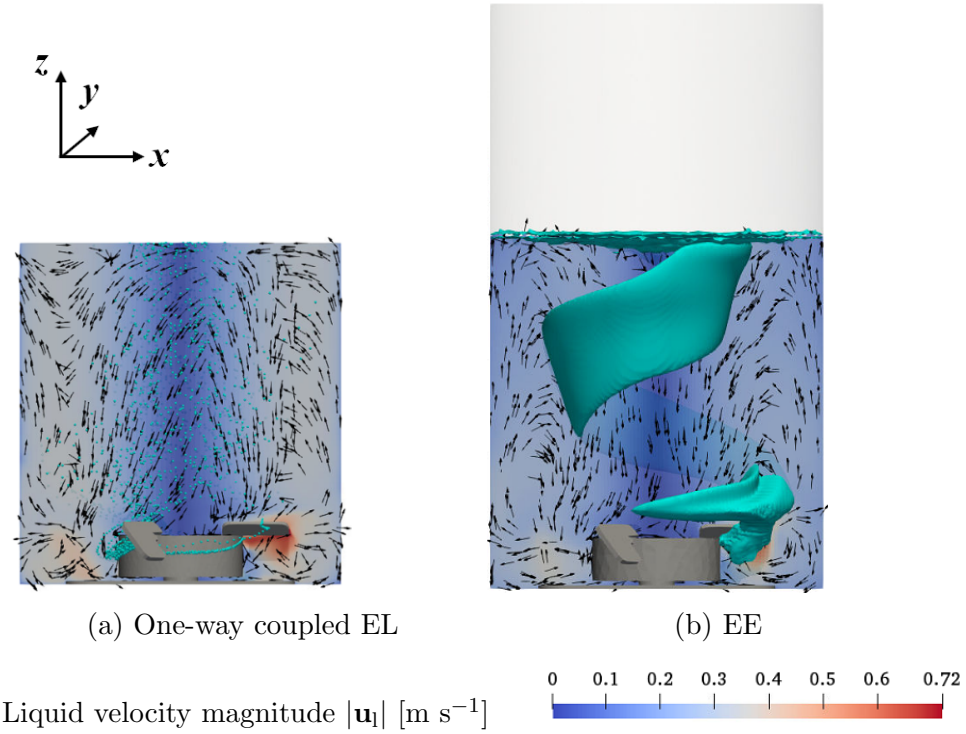

(a) One-way coupled EL (b) EE

Figure 4.24: Liquid flow and bubble dispersion for the base case ($V = 7.0$ L, $n = 100$ rpm, $Q = 250$ mL min^{-1}, 2 µm sparger) in the x-z-plane through the center of the XDR-10. Arrows indicate the direction of the x-z-velocity.

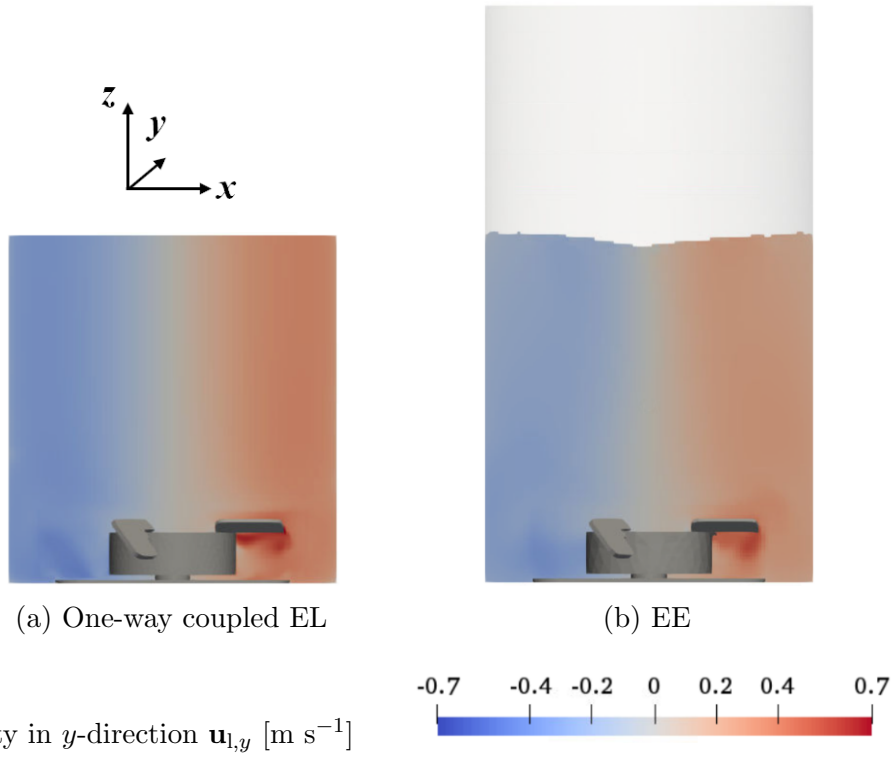

(a) One-way coupled EL (b) EE

Figure 4.25: Tangential liquid velocity for the base case (V = 7.0 L, n = 100 rpm, Q = 250 mL min^{-1}, 2 µm sparger) in the x-z-plane through the center of the XDR-10.

much smaller than the one observed in the CR3. The described flow pattern is found for both the one-way coupled EL and EE simulations.

Bubble positions of the one-way coupled EL simulations and the 1 % gas volume fraction iso-surface show the regions where the bubbles are rising in Fig 4.24. The bubbles rise from the microporous sparger disk integrated into the bottom of the reactor towards the impeller blade above it, where they move upwards behind the impeller blade. Above the impeller they rise in a spiraling motion that indicates the strong effect of the combination of buoyancy and drag forces. A similar pattern is also found for the 20 µm sparger for which a slightly larger bubble diameter is selected. In contrast to the spargers of the CR3, i.e., the open pipe sparger and the microporous sparger, the difference between the two different microporous spargers of the XDR-10 is minor, since the difference in the orifice size and the number of orifices is much smaller for microporous spargers with different pore sizes than between a microporous and an openpipe sparger.

While for the CR3 the sensors deeply enter into the liquid from the top and act as cylindrical baffles, for all Xcellerex^{TM} bioreactors the sensors enter only for about 1 cm in the lower part of the vessel. Since the sensors do not enter deeply into the liquid, their effect on the liquid flow is considered to be minor and the sensors are not considered in the simulations. Since the XDR-10 is unbaffled, surface vortex formation is observed for the highest investigated impeller speed of 360 rpm, as shown in Fig. 4.27.

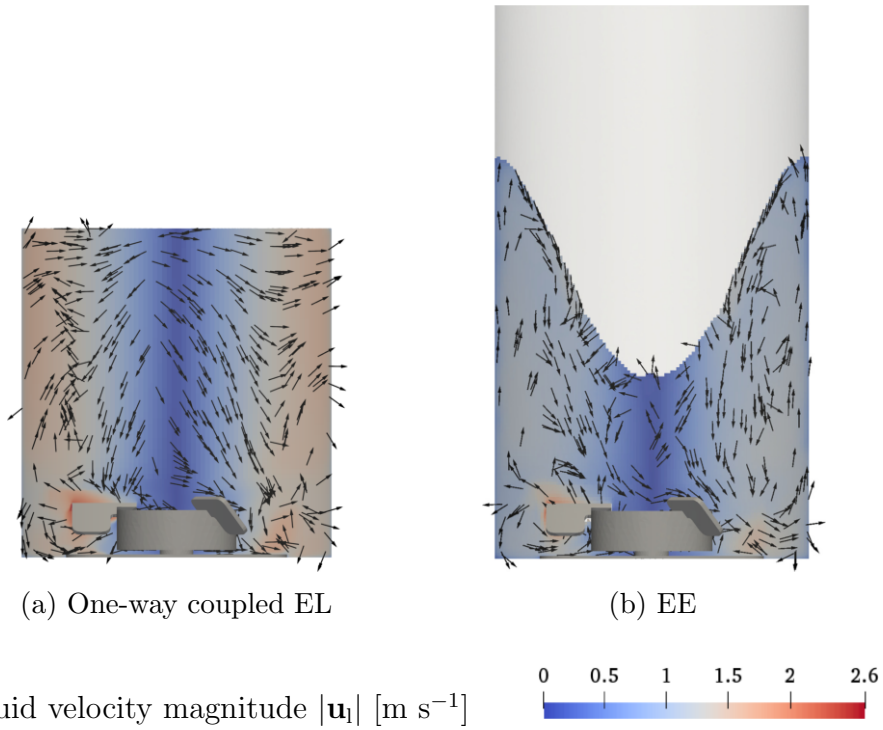

(a) One-way coupled EL (b) EE

Figure 4.26: Liquid flow pattern for the maximum impeller speed condition (7 L, 360 rpm, 0.25 L min^{-1}, 2 µm) in the x-z plane through the center of the vessel. Arrows indicate the liquid velocity in x-z direction [128].

For the EE simulations, this can be directly evaluated from the $\alpha_l = 1 - \alpha_g = 0.5$ volume fraction iso-surface. For the one-way coupled EL simulation, the surface vortex formation can be inferred from the pressure gradient across the top boundary through Eq. (2.29).

For both simulation approaches, the observed presence and absence of the surface vortex formation at 360 rpm and 100 rpm, respectively, agrees well with the experimental observations reported in [128]. The surface vortex results in the deformation of the shape of the upper recirculation zone, which can only be captured in the EE simulation. Even if there is a surface vortex, the overall structure of one recirculation zone above and one below the impeller is still maintained. In the one-way coupled EL simulations, the shape of the liquid volume is fixed to that of the computational grid and the liquid surface corresponds to the top boundary, which remains flat for all simulation conditions. The forced flat boundary impacts the simulated flow structure above the impeller through a low velocity region in the center of the vessel, which is absent in the EE simulations, and a higher velocity towards the vessel wall compared to the EE simulation, which is shown in Fig. 4.26.

Across the different operating conditions, the general liquid flow structure of the two recirculation zones is maintained for both modeling approaches with a higher working volume increasing the size of the upper recirculation zone and higher impeller

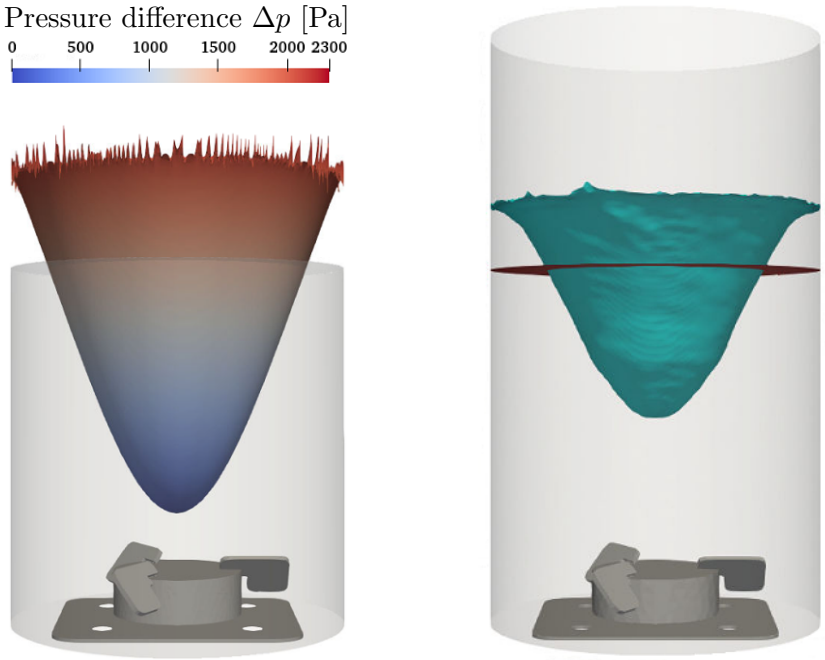

(a) One-way coupled EL (b) EE

Figure 4.27: Vortex formation for the XDR-10 at the maximum impeller speed of 360 rpm (V = 7.0 L, Q = 250 mL min^{-1}, 2 µm sparger)

(a) One-way coupled EL (b) EE

Figure 4.28: Bubble positions and 1 % gas volume fraction iso-surface for the XDR-10 at the minimum impeller speed of 40 rpm (V = 7.0 L, Q = 250 mL min^{-1}, 2 µm sparger)

speeds resulting in a higher the liquid velocity in both zones. At the lowest considered impeller speed of 40 rpm, the liquid velocity is lowest and the drag force is too weak to create a spiraling bubbles rise path. Instead, the bubbles rise path is almost straight with only a slight inclination in the anti-clockwise direction and the bubbles are not dispersed across the complete cross-section of the XDR-10 shown in Fig. 4.28.

Liquid Velocity, Turbulence, Volumetric Power Input, and Mixing Time

Similar to the CR3, the average liquid velocity and the liquid turbulence of the XDR-10 increase with the impeller speed as is expected for stirred tank reactors [20]. Figures 4.29a and 4.29c show the average liquid velocity and average turbulence kinetic energy, respectively, across the different impeller speeds for the one-way coupled EL and EE simulations. The simulation conditions are selected as described in section 4.2.2 and similar to the CR3 for the EE approach changes in the working volume are only considered at the intermediate impeller speed of 100 rpm and changes in the impeller speed are only considered at the intermediate working volume of 7.0 L. Figure 4.29b shows the average liquid velocity for different working volumes at the intermediate impeller speed of 100 rpm. Analogous for the CR3, there is a reduction of the average velocity for larger working volumes because the upper recirculation zone with lower velocity than in the region close to the impeller is larger then for smaller volume. This

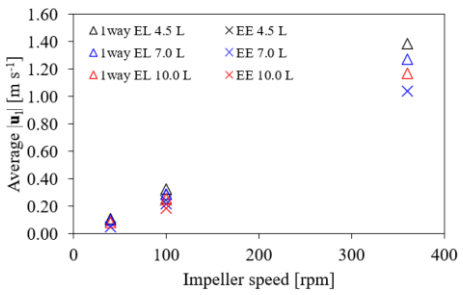

(a) Average $|\mathbf{u}_\mathrm{l}|$

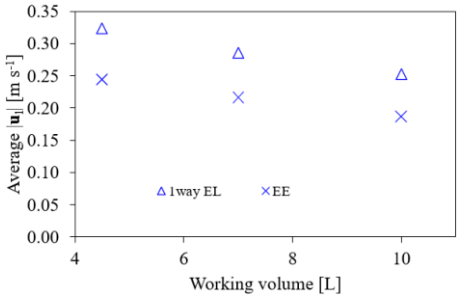

(b) Average $|\mathbf{u}_\mathrm{l}|$ at 100 rpm

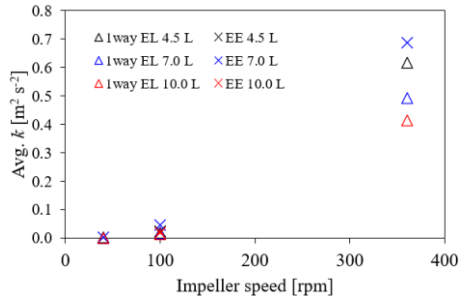

(c) Average k

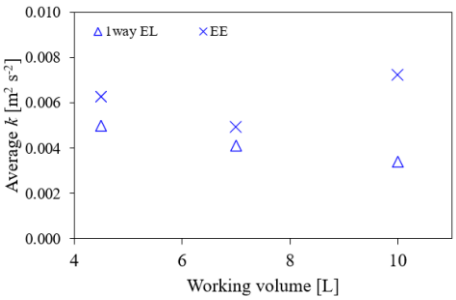

(d) Average k at 100 rpm

Figure 4.29: Average liquid velocity and average turbulence kinetic energy for impeller speeds of 40 rpm, 100 rpm, and 360 rpm and working volumes of 4.5 L, 7.0 L, and 10.0 L for the one-way coupled EL and the EE simulations for the 2 µm sparger with $Q = 250$ mL min^{-1}.

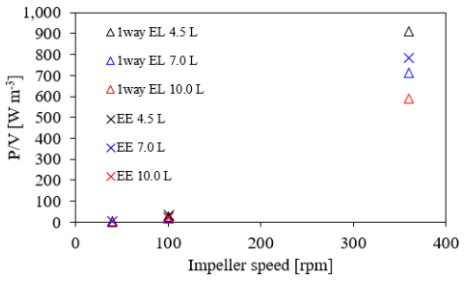

(a) Volumetric power input

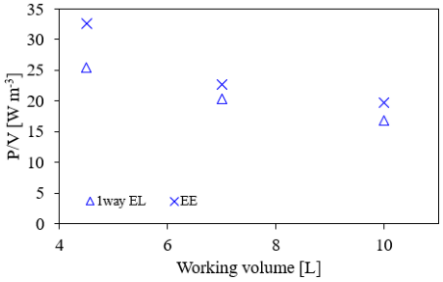

(b) Volumetric power input at 100 rpm

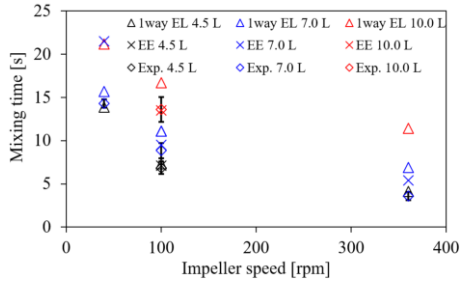

(c) Mixing time

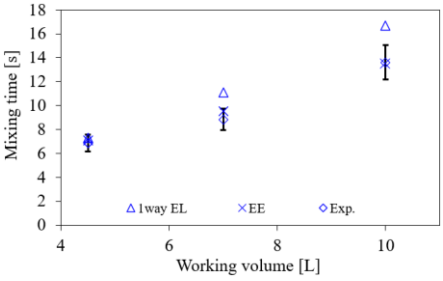

(d) Mixing time at 100 rpm

Figure 4.30: Volumetric power input P/V and mixing time for impeller speeds of 40 rpm, 100 rpm, and 360 rpm and working volumes of 4.5 L, 7.0 L, and 10.0 L for the one-way coupled EL and the EE simulations for the 2 µm sparger with $Q = 250$ mL min^{-1}. The dotted lines in Fig. 4.30a represent the fitted correlations based on the one-way coupled EL results and are colored according to the respective volumes. The experimental results for the mixing time are reported in [128].

is also associated with a lower volumetric power input. Also similar to the CR3, the EE simulations show slightly lower velocities than the one-way coupled EL simulations. At the maximum impeller speed, this effect is much more pronounced than for the lower impeller speeds and the CR3, which is likely caused by the differences in the flow structure between the one-way coupled EL and EE simulations caused by the surface vortex formation discussed above. Figure 4.29d shows the average turbulence kinetic energy for different working volumes at the intermediate impeller speed of 100 rpm. Similar to the CR3, for the EE simulations the turbulence induced by the bubbles results in a higher average turbulence kinetic energy than that of the one-way coupled EL simulations. Moreover, for the EE approach from the intermediate to the maximum working volume of 1.7 L and 2.4 L, respectively, the average turbulence kinetic energy increases. This is caused by the turbulence generated by the bubbles in the upper recirculation zone and is in contrast to the decrease of the average turbulence kinetic energy from the minimum to the intermediate volume of 1.0 L and 1.7 L, respectively.

Fig. 4.30a shows the volumetric power input for the different operating conditions for both the one-way coupled EL and the EE simulations. The volumetric power input at the maximum impeller speed of 360 rpm for the maximum working volume (red triangle in Fig. 4.30a) is about 600 W m^{-3}, which is much higher than the typical

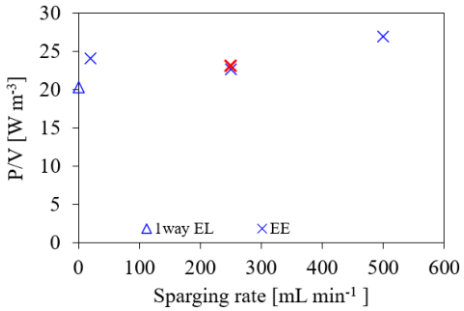

(a) Volumetric power input

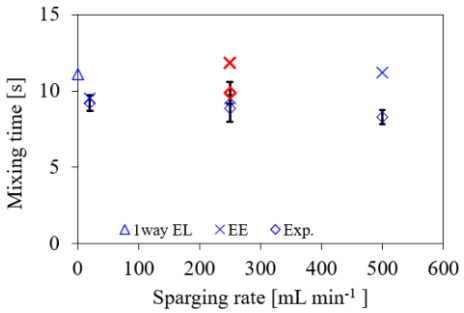

(b) Mixing time

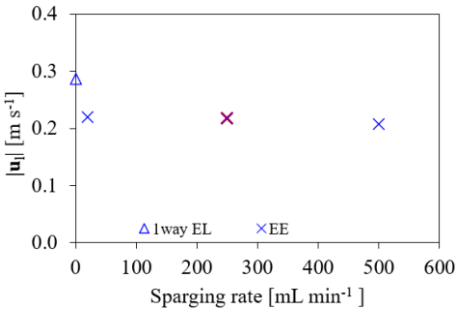

(c) Average liquid velocity

Figure 4.31: Volumetric power input P/V, mixing time, and average liquid velocity for the different sparging rates and sparger types at 100 rpm, and 7.0 L. The results for 20 µm sparger at $Q = 250$ mL min^{-1} are indicated with red markers, blue markers are for the 2 µm sparger. The experimental results for the mixing time are reported in [128].

range for mammalian cell culture of 10 W m^{-3} to 100 W m^{-3} [12]. Figure 4.30a shows the effect of the working volume on the volumetric power input, and the expected decrease of the volumetric power input for larger working volumes is observed. The average power numbers obtained from the one-way coupled EL and the EE simulations are 0.65 and 0.81, respectively, with minimum and maximum values of 0.4 and 0.93 for the one-way coupled EL simulations and 0.54 and 1.27 for the EE simulations. The power numbers of the one-way coupled EL and EE simulations are similar but only about half of the supplier specified power number of 1.5 [154].

As expected, the mixing time decreases with higher impeller speed for both modeling approaches, see Fig. 4.30c, which also agrees to the experimental results reported in [128]. The increase in the impeller speed from the minimum level of 40 rpm to the intermediate level of 100 rpm has a similar impact on the mixing time as that from the intermediate level to the maximum level of 360 rpm. This shows a reduced improvement of the mixing time for high impeller speeds as for the CR3. Figure 4.30d shows the increase of the mixing time for larger working volumes at the intermediate impeller speed of 100 rpm. For most operating conditions, the simulation results agree well with the experimental values and between the one-way coupled EL and EE simulations. Similar

to the CR3, the deviations between the one-way coupled EL and EE simulations are largest for the conditions with the slowest mixing, i.e., the lowest impeller speed and the largest working volume.

Figures 4.31a-c show the volumetric power input, the mixing time, and the average velocity at 100 rpm and 7.0 L for the different sparging rates and sparger types. As the effect of bubbles on the liquid flow is neglected in the one-way coupled EL simulations, they represent the results without sparging in Fig. 4.31. Similar to the CR3, there is only minor variation for the different sparging rates. There is almost no difference for the 2 µm and 20 µm spargers and the red and blue cross marks at 250 mL min^{-1} strongly overlap. Overall, the impact of sparging on the liquid velocity and the mixing time is minor compared to that of the impeller speed and the working volume.

Risk of Cell Damage

The the liquid volume fraction distributions of the strain rate and the hydrodynamic stress are shown in Figs. 4.32a and 4.32b. The expected increase of hydrodynamic stress with the impeller speed [44, 23], which is also found for the CR3, is observed. Again the one-way coupled EL simulations predict higher strain and lower hydrodynamic stress than the EE simulations, due to the higher liquid velocity and lower turbulence found with the one-way coupled EL approach. In agreement with the volumetric power

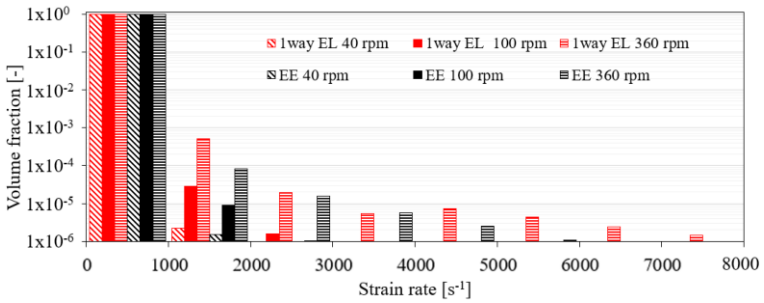

(a) Strain rate

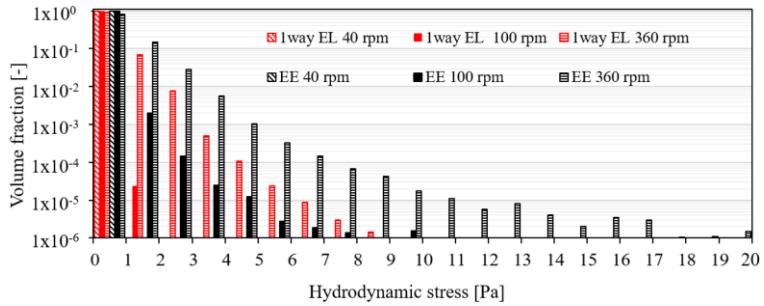

(b) Hydrodynamic stress

Figure 4.32: Volume fraction distributions of the strain rate and the hydrodynamic stress for the impeller speeds of 40 rpm, 100 rpm, and 360 rpm with $V = 7.0$ L, $Q = 250$ mL min^{-1} for the 2 µm sparger.

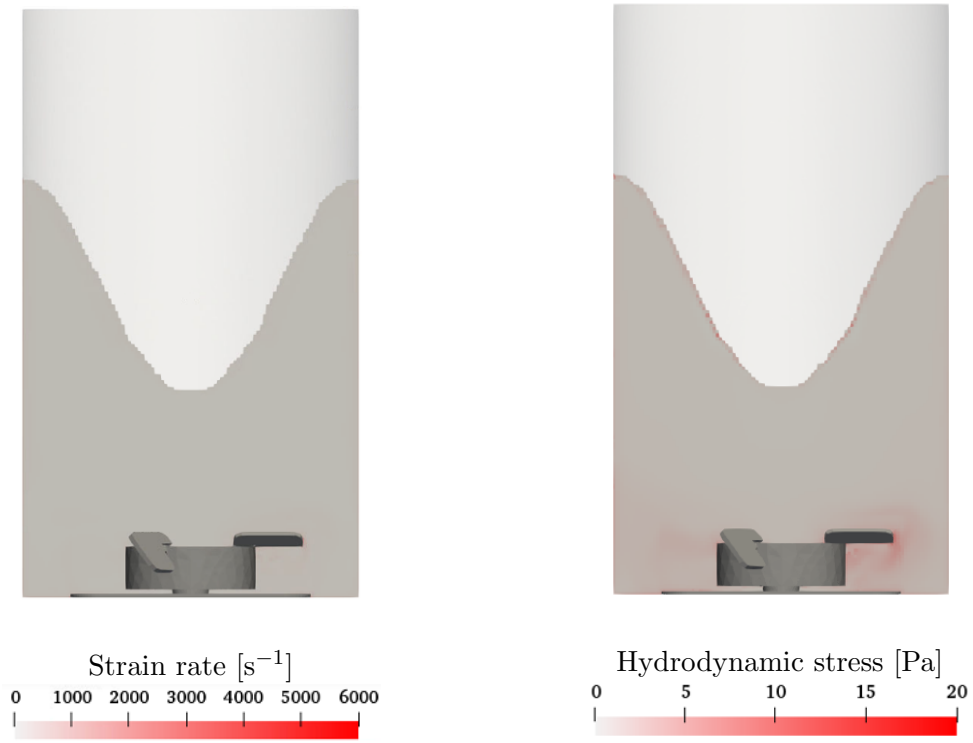

(a) Strain rate following Eq. (2.45) (b) Hydrodynamic stress following Eq. (2.48)

Figure 4.33: Shear stress and hydrodynamic stress in the x-z plane through the center of the XDR-10 for the EE approach for $V = 7.0$ L, $n = 360$ rpm, $Q = 250$ mL min^{-1} with the 2 µm sparger.

input at the maximum impeller speed of 360 rpm being higher than for the CR3 at the maximum impeller speed of 250 rpm, the maximum hydrodynamic stress is also higher but still below the critical thresholds of 25.2 ± 2.4 Pa and 32.4 ± 4.4 Pa above which negative impact on the growth rate of Sp2/0 and CHO cells, respectively, is reported[134].

The spatial distribution of the strain rate and the hydrodynamic stress are shown in Figs. 4.33a and 4.33b. Similar to the CR3, the highest strain rate and hydrodynamic stress levels are located at the edges of the impeller blades and intermediate stress levels are found in the high velocity zone surrounding the impeller. Both the spatial distribution and the the volume fraction distributions indicate the heterogeneous conditions of high strain rate and hydrodynamic stress in the impeller region and low values in the tank region. This is typical for stirred tank bioreactors and similar observations have been made for the CR3 in the present study and by Kaiser [147] are reported for other bioreactors in literature [23, 74]. One difference between the strain rate and the hydrodynamic stress is the region of the liquid surface, where high turbulence and hydrodynamic stress are found for control volumes with intermediate volume fractions of $\alpha_\mathrm{l} = 1 - \alpha_\mathrm{g}$ between 0.3 and 0.7. This range of volume fractions corresponds to the transition from the disperse to continuous treatment and vice versa

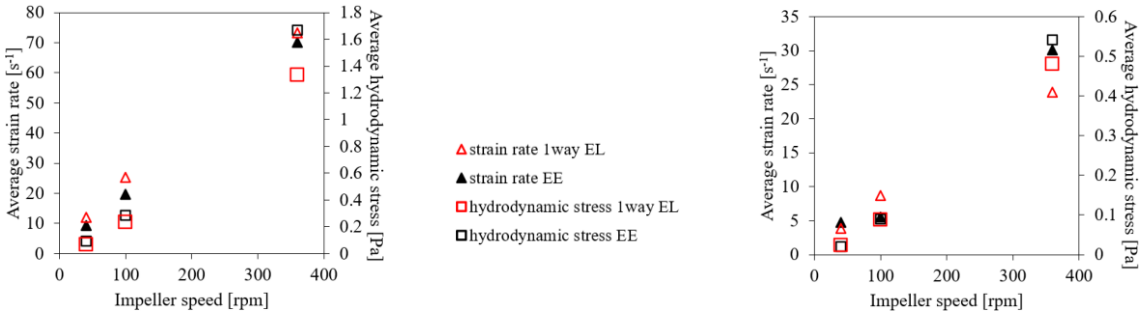

(a) Impeller zone (b) Tank zone

Figure 4.34: Average strain rate and average hydrodynamic stress for the impeller (left) and tank zone (right) of the XDR-10 at $V = 7.0$ L and $Q = 250$ mL min^{-1} for the 2 µm sparger.

for the gas and liquid phases in the EE simulations for which interpolation of the coupling terms for fully continuous and fully disperse conditions is performed. This interpolation does not correctly capture the segregated interface of the liquid surface, which is a limitation of the EE approach that cannot differentiate between disperse and segregated interface types. In the EE simulations in increased turbulence directly at the liquid surface is observed. However, the volume of the grid cells associated with the liquid surface region is minor compared to the total liquid volume and the impact of this region on the process characteristics is considered to be negligible.

The average strain rate and the average hydrodynamic stress of the impeller zone and of the tank zone are shown in Figs. 4.34a and 4.34b, respectively. The height and diameter of the impeller zone are 0.33 d_{imp} and 1.2 d_{imp}, which is the same as for the CR3. The observed range of the average strain rate and hydrodynamic stress is quite similar to those observed for the CR3. For the higher maximum impeller speed of 360 rpm for the XDR-10 compared to 250 rpm for the CR3, higher average strain rates and hydrodynamic stress values than for the CR3 are found in both, the impeller and the tank, zones. The average values of the strain rate and the hydrodynamic stress of the impeller zone are about twice as high as those of the tank zone, also reflecting the difference between the mechanical stress close to the impeller and in the liquid bulk.

Gas Hold-Up and Volumetric Oxygen Mass Transfer Coefficient

As presented in Sect. 2.3.4, the volumetric oxygen transfer coefficient $k_{\mathrm{L}}a$ depends on the specific transfer area a and the liquid transfer coefficient k_{L}. The specific transfer area is the total surface area of all bubbles present in the liquid normalized by the total volume. At a constant sparging rate, a smaller bubble diameter leads to a higher number of bubbles added per time step and longer bubble residence times, increasing the available transfer area and the $k_{\mathrm{L}}a$, see Fig. 4.35. The residence time of smaller bubbles is longer since a decrease in diameter results in a stronger reduction of the gravitational force $\mathrm{F_G} \propto d_{\mathrm{b}}^3$, which accelerates the bubbles towards the liquid surface, than that of the drag force $\mathrm{F_D} \propto d_{\mathrm{b}}^2$, which acts opposite to the relative motion of the

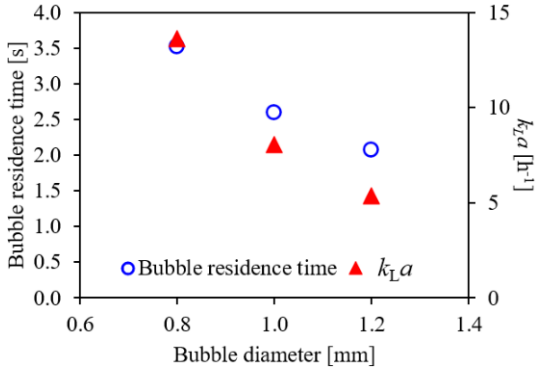

Figure 4.35: Effect of the bubble diameter on the bubble residence time and the k_La for the one-way coupled EL simulations of the XDR-10 for $V = 7.0$ L, $n = 100$ rpm, $Q = 250$ mL min^{-1}, 2 µm sparger.

bubbles with respect to the surrounding liquid. For the 20 µm sparger the pore size is within the range of 15 µm to 30 µm of the microporous sparger of the CR3 and the same bubble diameter of 1.0 mm is selected, while a slightly smaller bubble diameters of 0.8 mm is used for the 2 µm sparger.

The cumulative volume of all bubbles divided by the total volume is the gas hold-up, which is presented in Fig. 4.36. The gas hold-up increases with the number of bubbles added, i.e., the sparging rate, and is slightly reduced by the larger bubble diameter selected for the 20 µm sparger. Stronger liquid agitation at a higher impeller speed also results in an increased gas hold-up due to a longer average residence time of the bubbles. The sparging rate, the sparger type, and impeller speed show the same qualitative effects on the gas hold-up as for the CR3. The gas hold-up for the XDR-10 is higher than for the CR3 for each of the test conditions. This is caused by the higher volume per volume sparging rate, e.g. 0.036 vvm instead of 0.029 vvm for the CR3 at the intermediate volume and sparging rate, and the better dispersion of the bubbles above the impeller, indicated by the spiraling rise path for the XDR-10 (see Fig. 4.24) instead of the relatively straight rise path of the CR3 (see Fig. 4.5).

Since both the CR3 and the XDR-10 have a constant circular cross-section in the upper part of the vessel, a larger working volume results in an increased liquid height, which in turn increases the vertical extent of the upper recirculation zone. The height of the upper recirculation zone also affects the liquid velocity in this region. In contrast to the CR3, for the XDR-10 this has a clear impact on the gas hold-up. For a smaller working volume, the upper recirculation zone is smaller and has a higher velocity resulting in a better bubble dispersion and a higher gas hold-up. The vortex formation for the maximum impeller speed of 360 rpm also affects the gas hold-up. For the one-way coupled EL simulations, where the effect of the vortex on the liquid flow field is not captured, the gas hold-up is lower than for the EE simulations at the maximum impeller speed of 360 rpm, while the opposite effect is observed for the lower impeller speeds of 40 rpm and 100 rpm (base case), shown in Fig. 4.36. For the EE simulations, bubble diameters of 0.8 mm and 1.0 mm are both tested for the maximum impeller speed of 360 rpm ($V = 7.0$ L, $Q = 250$ mL min^{-1}, 2 µm sparger) and the

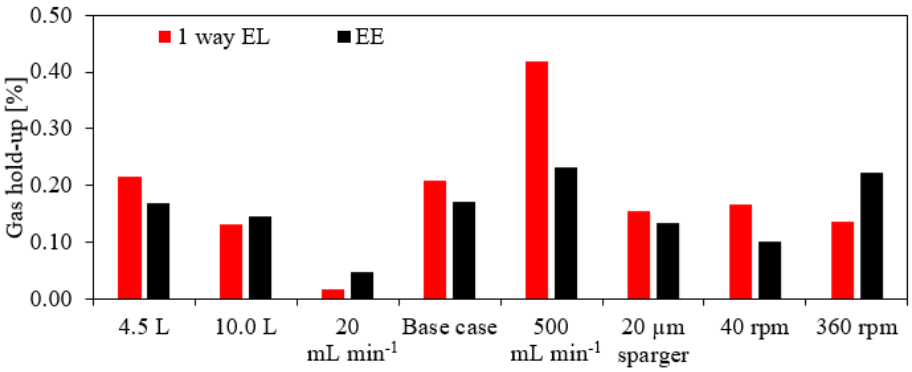

Figure 4.36: Gas hold-up for the XDR-10 for different operating conditions with the labels indicating the value of the operating parameter deviating from the base case (V = 7.0 L, n = 100 rpm, Q = 250 mL min^{-1}, 2 µm sparger).

results for the 1.0 mm diameter are in better agreement with the experimental results for the $k_{\mathrm{L}}a$. Through the increase of the bubble diameter from 0.8 mm to 1.0 mm, the gas hold-up is reduced from 0.27 % to 0.22 % and the $k_{\mathrm{L}}a$ is reduced from 42.9 h^{-1} to 28.5 h^{-1} in the EE simulations. In Fig. 4.36 for the impeller speed of 360 rpm, the gas hold-up for 1.0 mm bubble diameter is reported. Bach et al. [97] adjusted the bubble size to improve the agreement between the simulated and the experimental values of $k_{\mathrm{L}}a$ and used the obtained bubble diameters to derive a correlation between the operating conditions and the bubble size. Following this line of thinking, the improved agreement of the simulated and experimental $k_{\mathrm{L}}a$ values for a larger bubble diameter suggests that the average bubble diameter is increased for this operating condition, indicating increased coalescence due to the higher gas hold-up.

The effects of the sparging rate, the impeller speed, and the working volume on the $k_{\mathrm{L}}a$ are shown in Figs. 4.37a, 4.37b, and 4.37c, respectively. In Fig. 4.37b at the maximum impeller speed of 360 rpm, the results for a bubble diameter of 1.0 mm are shown for the EE simulation, whereas 0.8 mm are used for the remaining conditions with the 2 µm sparger, similar to Fig. 4.36. In Figs. 4.37a-c, the experimental values are represented by the open diamonds with the vertical error bars indicating the standard deviation of the triplicate measurements. Similar to the gas hold-up, a higher sparging rate and impeller speed both increase the $k_{\mathrm{L}}a$. In contrast to the one-way coupled EL simulations for which the bubble residence time is independent of the sparging rate, the $k_{\mathrm{L}}a$ values obtained from the EE simulations and the experiments do not increase linearly with the sparging rate. This points to a reduced bubble residence time at higher sparging rates due to the stronger impact of the bubbles on the liquid motion, which is also supported by the fact that the gas hold-up of the EE simulations at the maximum sparging rate of 500 mL min^{-1} is 0.19 % lower than for the one-way coupled EL simulations, while at the lower sparging rates the deviation is less than 0.04 %, shown in Fig. 4.36. This effect poses a limit on how much the $k_{\mathrm{L}}a$ can be increased through higher sparging rates. The 20 µm sparger results are indicated by

bold symbols in Fig. 4.37a. The larger bubble diameter of 1.0 mm instead of 0.8 mm selected for the 20 µm sparger results in a slightly lower k_La, which is found for both simulation approaches as well as the experiments. The differences in the k_La for the two different microporous spargers are much smaller than those observed between the microporous and the open pipe sparger of the CR3. With both, the 2 µm and the 20 µm, microporous spargers of the XDR-10, k_La values sufficiently high for the cultivation of mammalian cells are achieved.

For the increase of the k_La with the impeller speed, the experiments show a reduced increase for the maximum impeller speed of 360 rpm (Fig. 4.37b), indicating reduced benefits of increasing the impeller speed not only for the mixing time but also for the k_La. The reduction of the k_La for larger working volumes shown in Fig. 4.37c is qualitatively similar but more pronounced than observed for the CR3. The reason for this is that for the XDR-10 the volume does not only affect the liquid transfer coefficient k_L through the volumetric power input but also through the specific interface area a due to the reduced gas hold-up. The increase in k_La for lower working volumes is even more pronounced in the experiments than in the simulations suggesting a reduction of the bubble size for smaller volumes that is not considered in the simulations. The comparison of the simulations and the experimental results emphasizes the need for accurate bubbles size data. While there are studies available that investigate the bubbles size in stirred

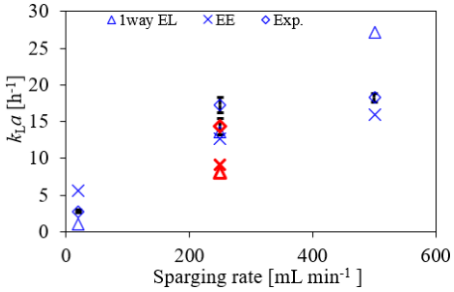

(a) Effect of the sparging rate

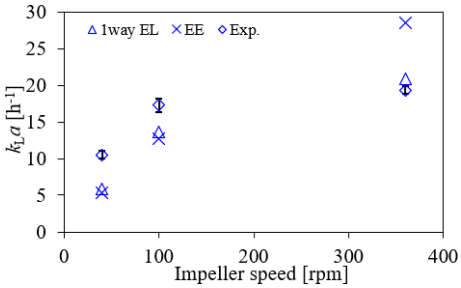

(b) Effect of the impeller speed

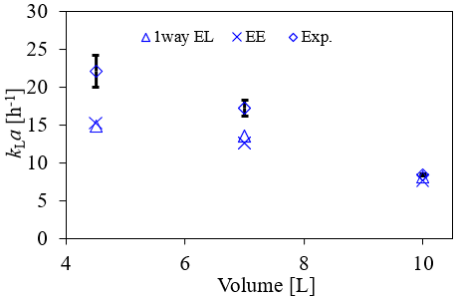

(c) Effect of the working volume

Figure 4.37: Impact of changes of a single operating parameter on the volumetric oxygen mass transfer coefficient k_La for the XDR-10 with the other operating parameters at the intermediate value of 7.0 L for the working volume, 100 rpm for the impeller speed, and 250 mL min^{-1} for the sparging rate The values are reported in [128]

tank bioreactors [155, 156, 110, 102, 157, 158, 159, 160, 161, 162], these studies are not able to cover the huge variety of possible bioreactor configurations. Moreover, the bubble size is not only affected by the bioreactor and the operating conditions but also and strongly dependent on the solutes in the liquid phase [155, 110, 45, 163], which also affects the $k_{\mathrm{L}}a$ during cell cultivation since cell culture media contain a variety of solutes [142].

4.2.5 Selection of Operating Conditions for Cell Cultivation

Similar to the CR3, the XDR-10 is a lab-scale bioreactor that provides short mixing times, which are below 25 s across the investigated operating conditions. The hydrodynamic stress is below the critical values for all operating conditions. However, surface vortex formation is observed at the maximum impeller speed of 360 rpm. Since the entrainment and disengagement of bubbles at the surface vortex is considered a possible cause of cell damage, this should either be avoided by suing low impelelr pseeds or bioreactors equipped with baffles [34] or counteracted by protective agents like Pluronic [164]. The observed values of the volumetric oxygen mass transfer coefficient of the XDR-10 are higher than those of the CR3 and cover the typical range for cultivation of mammalian cells of 1 h^{-1} to 20 h^{-1} [18, 35]. Sufficient oxygen transfer can be achieved with both considered microporous sparger types but slightly higher values are found for the smaller pore size of 2 µm instead of 20 µm. Similar to the CR3, the intermediate impeller speed of 100 rpm appears advantageous over the lowest impeller speed of 40 rpm due to faster mixing and better bubble dispersion but further increases may not be necessary as both mixing and oxygen transfer are already suitable for cell culture.

4.3 The Xcellerex™ XDR-200

The Xcellerex™ XDR-200 represents one of the intermediate bioreactor scales of the Xcellerex product line and is the smallest bioreactor for which the impeller is positioned 15° off-center [145]. As a pilot scale reactor the XDR-200 is suited for the manufacturing of small amounts of product or as an intermediate scale of the inoculum train.

4.3.1 Bioreactor Configuration

Similar to the XDR-10, the Xcellerex™ XDR-200 has a rigid, multi-use vessel frame in which a single-use cultivation bag is placed. The pitched-blade impeller with three blades is fixed onto a rigid plastic plate at the bottom of the single-use bag, see Fig. 4.38, at a position 15° off-center to the central vessel axis. The XDR-200 has a curved bottom and a vessel diameter d_V of 56 cm. The impeller has three blades pitched at an angle of 40° and a diameter d_{imp} is 22 cm. While the XDR-200 is can be purchased with same sparger options as the XDR-10, i.e., 2 µm and 20 µm microporous spargers as well as drilled hole spargers, the present study considers the 2 µm microporous sparger with three microporous disks connected to the same inlet tube. Similar to the XDR-10, the sparger openings are integrated into the plastic plate on which the impeller is fixed and located directly below the impeller blades. Two of the gray sparger disks are well visible in Fig. 4.38, while the third is hidden by the impeller blade. Analogous to the XDR-10, the impeller is driven by magnetic coupling and rotated in the anti-clockwise direction. Similar to the XDR-10, the sparger openings are integrated into the plastic plate on which the impeller is fixed and located directly below the impeller blades, see Fig. 4.38. Furthermore, a variant of the single-use bag with a T-shaped drilled hole sparger, which can be used with a separate sparging line for carbon dioxide stripping, is also available. The sensors enter the bioreactor for about 1 cm in the lower part of the vessel on the side opposite to the impeller and are not considered in the bioreactor configuration.

4.3.2 Operating Conditions

The considered operating conditions are selected in a similar manner as described for the CR3 and the XDR-10 in sections 4.1.2 and 4.2.2 and cover changes in the

Figure 4.38: Impellers of the Xcellerex™ XDR-200

Table 4.5: Operating conditions for the EE of the XDR-200.

Condition #	Impeller speed n [rpm]	Working volume V [L]	Sparging rate Q [L min^{-1}]	Sparger type
1	30	120	5.0	2 µm
2	120	120	5.0	2 µm
3	200	120	5.0	2 µm
4	120	40	5.0	2 µm
5	120	200	5.0	2 µm
6	120	120	0.5	2 µm
7	120	120	10.0	2 µm

impeller speed, the working volume, and the sparging rate. The selected operating conditions for the EE simulations are summarized in Tab. 4.5. For the impeller speed, low, intermediate, and high values of 30 rpm, 120 rpm, and 200 rpm are considered. For the working volume, the supplier specified minimum and maximum volume of 40 L and 200 L, and the intermediate value of 120 L are tested. For the sparging rate, the levels are 0.5 L min^{-1}, 5.0 L min^{-1}, and 10.0 L min^{-1}.

In the one-way coupled EL simulations, the gas hold-up and volumetric oxygen mass transfer coefficient are evaluated for all conditions in Tab. 4.5 and an extended set of simulation conditions is used to characterize the liquid flow as summarized in Tab. 4.6. Similar to the CR3 and the XDR-10, this set of conditions consists of all possible combinations of the three levels of working volume and the three levels of impeller speed.

Table 4.6: Operating conditions for the one-way coupled EL simulations of the XDR-200.

Condition #	Impeller speed n [rpm]	Working volume V [L]
1	30	40
2	120	40
3	200	40
4	30	120
5	120	120
6	200	120
7	30	200
8	120	200
9	200	200

4.3.3 Grid Independence Study

Analogous to the bioreactors described above, separate grid independence studies have been performed for the one-way coupled EL and the EE simulations. While the supplier information states that the rotational axis of the impeller is 15° off center, the exact shape of the bottom curvature and radial distance of the impeller were not accessible for reconstructing the vessel shape. For the one-way coupled EL and the EE simulations two slightly different configurations are considered. For the one-way coupled EL simulations, a dish-shaped vessel bottom is considered, while for the EE simulations performed later on an elliptical bottom shape is used. For both configurations, the impeller position is selected in such a way that the flat plastic plate on which the impeller is located and which is also inclined at 15° relative to the vertical vessel axis is matching the curvature of the bottom as closely as possible. For grid for the EE simulations, this results in an impeller position 4 cm closer to the center of the vessel. Moreover, a different rotation of the impeller is considered and the T-sparger is only

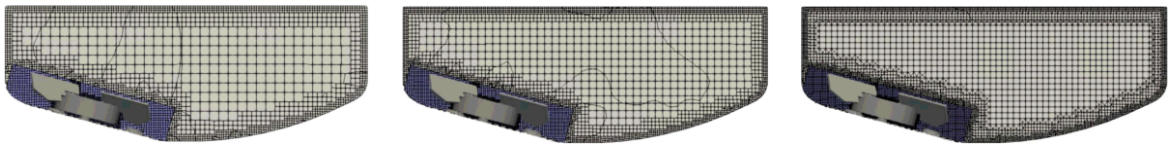

(a) Grids for the one-way coupled EL simulations for 40 L working volume. Left to right: $0.3x10^6$, $0.6x10^6$, and $1.0x10^6$ grid cells.

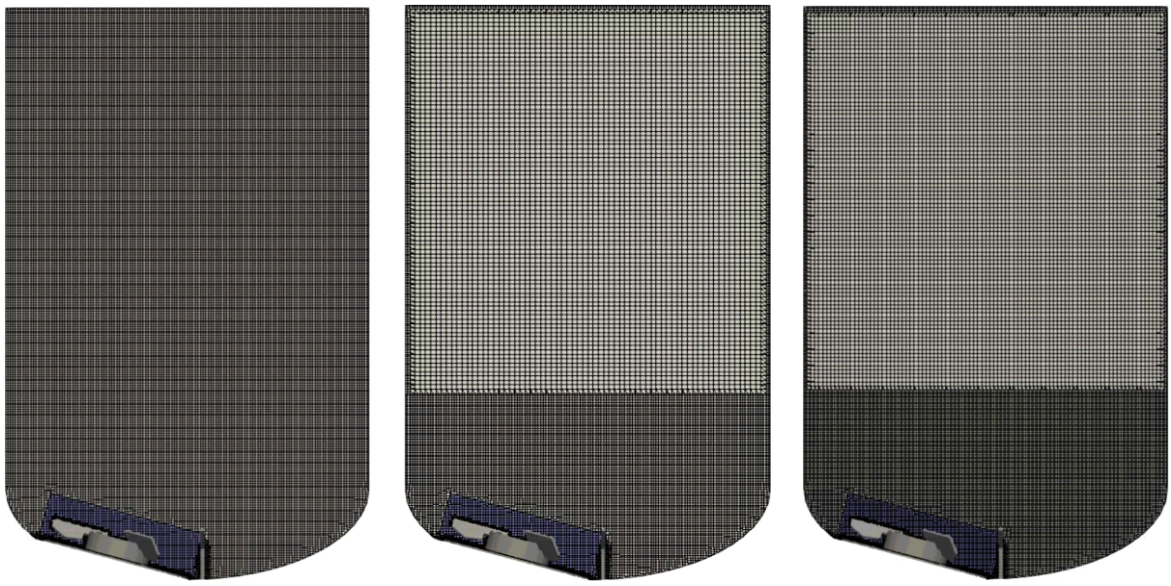

(b) Grids for the EE simulations for the complete bioreactor. Left to right: $4.0x10^6$, $1.8x10^6$, and $3.3x10^6$ grid cells.

Figure 4.39: Computational grids for the XDR-200 considered in the grid study. The rotating reference frame region is highlighted in blue.

included in the EE simulations. The effect of this differences on the liquid flow is discussed with the characterization results and is found to be minor for most operating conditions.

The investigated grids for the one-way coupled EL simulations follows the same meshing strategy as those for the CR3 and XDR-10 with high refinement in the region surrounding the impeller, see Fig. 4.39a. The intermediate grid with $0.6\text{x}10^6$ cells for 40 L volume is selected based on less than 1 % deviation of the average liquid velocity magnitude to that of the finest grid with $1.0\text{x}10^6$. The bioreactor configuration does not include the T-sparger, the addition of which resulted in less than 0.5 % deviation in the average liquid velocity magnitude. The final grid sizes for the one-way coupled Euler-Lagrange simulations for the volumes of 40 L, 120 L, and 200 L are $0.6\text{x}10^6$, $0.9\text{x}10^6$, and $1.3\text{x}10^6$ grid cells, respectively.

For the EE simulations different grid structures have been tested. An initial grid with a homogeneous grid spacing throughout the whole reactor resulted in $4.0\text{x}10^6$ cells. To reduce the number of cells, a coarser grid is used for the upper part of the bioreactor, while the same grid spacing is kept in the lower part up to a working volume of about 60 L, see Fig. 4.39b left and center. For these two grids, the average liquid velocity magnitude differs less than 1 %. When reducing the grid spacing by 25 %, the number of grid cells is almost doubled from $1.8\text{x}10^6$ to $3.3\text{x}10^6$ cells, see Fig. 4.39b right hand side, and the average velocity changes by 5 %. The $1.8\text{x}10^6$ cells grid is selected for further simulations.

4.3.4 Process Characterization

One major difference of the XDR-200 to the CR3 and the XDR-10, is the off-centered impeller, which causes an asymmetric flow structure and suppresses surface vortex formation, similar to the observations for eccentric impellers by Yamamoto et al. [77]. The flow structure is described in detail before the process characteristics are summarized.

Liquid Flow Field and Bubble Dispersion

Figs. 4.40a and 4.40b show the liquid velocity for the base case (V = 120 L, n = 120 rpm, $Q = 5.0$ L min^{-1}) for the one-way coupled EL and EE simulations, respectively. The differences in the shape of the vessel bottom slightly affect the liquid height for the same working volumes because the dished bottom shape holds more liquid than the elliptical one. The impeller is rotating in the up-pumping anti-clockwise direction and pushes the liquid outwards from the impeller region towards the vessel wall. The overall flow structure is very similar for both configurations of the vessel bottom. The liquid is pushed outwards and spirals upwards along the vessel wall. The center of the rotational motion of the liquid flow is also the center of the down-flow region and its horizontal position varies along the liquid height. In the lower part of the bioreactor, the down-flow region is oriented towards the center of the impeller. For increasing impeller speeds, the structure of the flow remains similar to that shown in Figs. 4.40a and 4.40b, while the velocity magnitude increases. At the minimum working volume of 40 L, shown in Figs. 4.40c and 4.40d, the recirculation in the lower part of the vessel

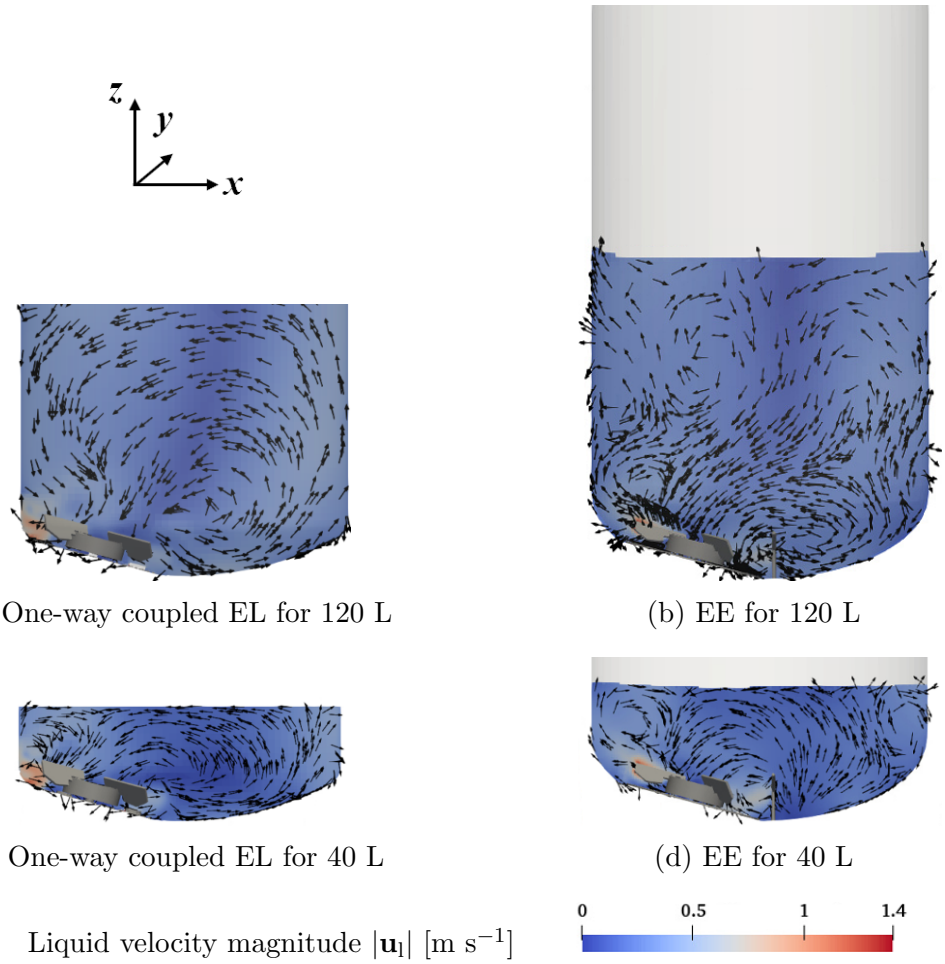

(a) One-way coupled EL for 120 L

(b) EE for 120 L

(c) One-way coupled EL for 40 L

(d) EE for 40 L

Figure 4.40: Liquid flow for $V = 120$ L (top) and $V = 40$ L (bottom) at $n = 20$ rpm, $Q = 5.0$ L min^{-1} in the x-z-plane through the center of the XDR-200. Arrows indicate the direction of the x-z-velocity.

remains similar, however, due to the small liquid height the down flow region is not as well developed as for the larger volumes.

To better show the three dimensional structure of the liquid flow and the effect of the working volume on the liquid flow, representative streamlines for the liquid velocity for the considered working volumes of 40 L, 120 L, and 200 L are shown in Fig. 4.41. The green streamlines indicate the up-flow of the liquid along the vessel wall, the blue streamlines the down-flow in the center and the red streamlines visualize the flow in the bottom part of the vessel. The off-centered position of the impeller and its close proximity to the bottom of the vessel do not allow for the development of a clearly structured recirculation zone below the impeller, which is in contrast to the CR3 and XDR-10. Instead, there is an almost horizontal recirculation zone where the liquid flow from the impeller is pushed out along the bottom to the vessel wall opposite the impeller and then drawn back in behind the impeller blades. For the lowest working volume of 40 L (Fig. 4.41a), the liquid height is too small for a clear separation of the down-flow region in the upper region of the bioreactor and the recirculation in the

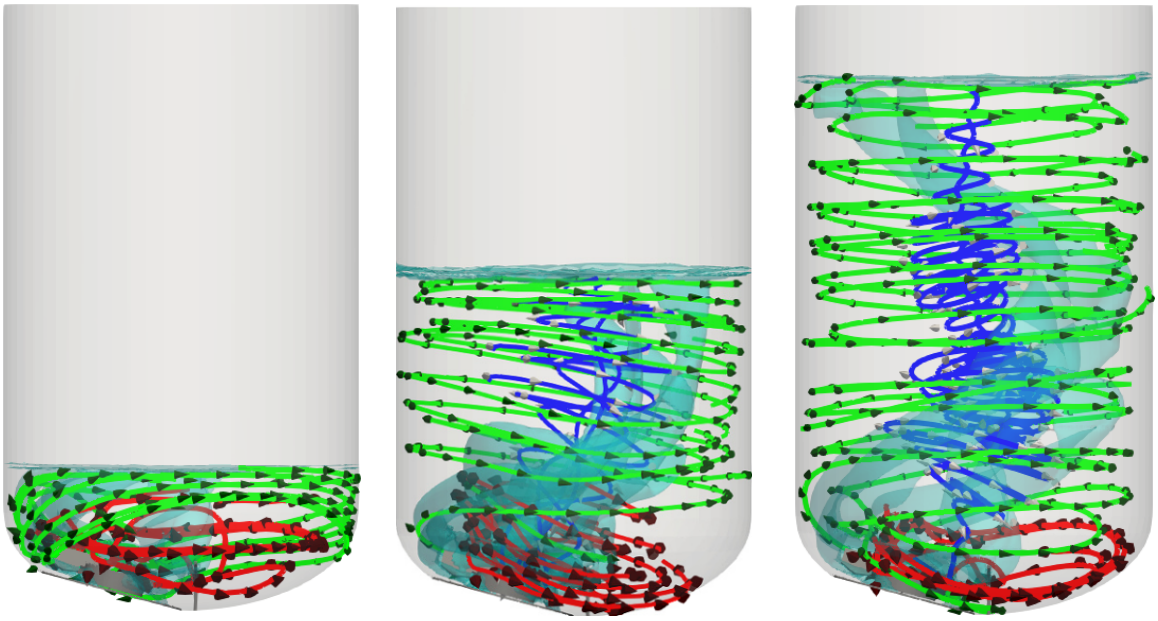

(a) EE for 40 L (b) EE for 120 L (c) EE for 200 L

Figure 4.41: Liquid velocity streamlines and 1 % gas volume fraction iso-surface for the EE simulations at working volumes of 40 L, 120 L, and 200 L for $n = 120$ rpm and $Q = 5.0$ L min^{-1}.

bottom part of the bioreactor and consequently the blue streamlines are not shown.

Similar to the XDR-10, the bubbles rising from the sparger openings directly below the impeller are captured behind its blades and above the impeller they move along with the anti-clockwise motion of the liquid. The bubble motion is also influenced by the effect of the liquid height on the liquid flow as indicated by the transparent 1 % gas volume fraction iso-surfaces in Fig. 4.41. For the minimum working volume of 40 L, the liquid height is too small to allow for the spiraling rise paths that are observed for 120 L and 200 L. Consequently, while at 40 L the bubbles are following the liquid motion, they are not as well dispersed across the bioreactor cross-section as for the larger volumes.

The effect of the impeller speed on the dispersion of the bubbles is shown in Fig. 4.42 for both modeling approaches. At the lowest considered impeller speed of 30 rpm, see Figs. 4.42a and 4.42d, the liquid velocity and the drag force are too small to cause a spiraling bubble rise path, which is similar to the observations for the XDR-10 at 40 rpm (see Sect. 4.2.4). For increasing impeller speeds, the bubbles are carried by the liquid motion towards the center of the vessel and the wall opposite the impeller increasing the horizontal dispersion of the bubbles. Since the three sparger openings of the 2 µm sparger are evenly distributed around the cylindrical base of the impeller, the bubbles interact with all three impeller blades simultaneously. This is in contrast to the CR3 and XDR-10 with a single sparger opening where the bubbles are mainly interacting with the impeller blade currently above the sparger. The three sparger openings of the XDR-200 allow for a better dispersion of the bubbles in the lower part

(a) One-way coupled EL for 30 rpm

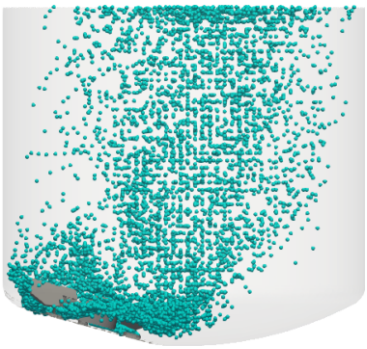

(b) One-way coupled EL for 120 rpm

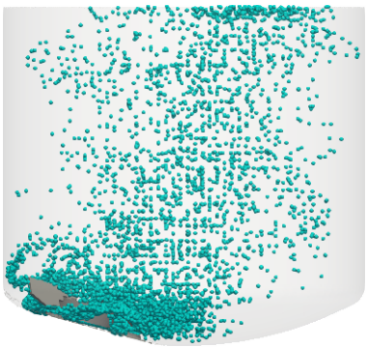

(c) One-way coupled EL for 200 rpm

(d) EE for 30 rpm

(e) EE for 120 rpm

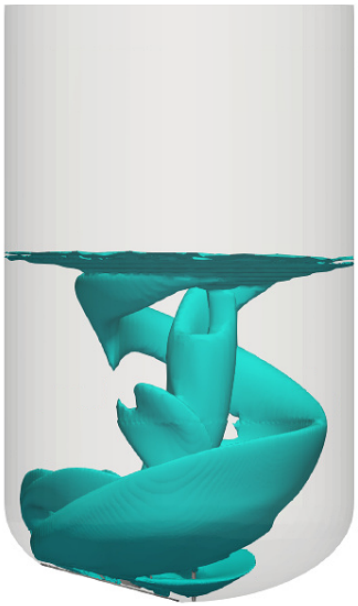

(f) EE for 200 rpm

Figure 4.42: Bubble positions and 1 % gas volume fraction for the one-way coupled EL (top) and the EE simulations (bottom), respectively, at impeller speeds of 30 rpm, 120 rpm, and 200 rpm for $V = 120$ L and $Q = 5.0$ L min^{-1}. The bubbles are shown three times larger than their actual size to improve visibility.

of the vessel than that observed for the CR3 and the XDR-10.

Liquid Velocity, Turbulence, Volumetric Power Input, and Mixing Time

The average liquid velocity magnitude across the considered impeller speeds is shown in Fig. 4.43a. Similar to the CR3 and the XDR-10, the average velocity increases with the impeller speed. Fig. 4.43b shows the average velocity for the considered working volumes at the intermediate impeller speed of 120 rpm. In contrast to the CR3 and the XDR-10, the highest average liquid velocity for the one-way coupled EL simulations is

observed for the intermediate working volume. This is likely caused by the differences in the flow structures for the working volumes of 40 L and 120 L, shown in Figs. 4.40c and 4.40a, since at of 40 L lower velocities are found in the bottom center zone of the liquid. In contrast to the one-way coupled EL results, the average velocity observed in the EE simulations slightly decreases for the larger working volumes, similar to the results for the CR3 and XDR-10. This difference between the one-way coupled EL and the EE simulations is likely related to the difference in the shape of the vessel bottom mentioned above.

For both simulation approaches, the increase of the average turbulence kinetic energy for higher impeller speeds is shown in Fig. 4.43c. The decrease of the average turbulence kinetic energy for larger working volumes at the intermediate impeller speed of 120 rpm is shown in Fig. 4.43d. This is similar to the observations for the one-way coupled EL simulations of the CR3 and the XDR-10 across all working volumes and also for the EE simulations except for the maximum working volume. Similar to CR3 and the XDR-200 the region around the impeller with the highest velocity is also associated with the highest turbulence, which is typical for stirred tank reactors [20]. Thus, the decrease of the average turbulence kinetic energy for larger working volumes is caused by the increase volume above the impeller region where both liquid velocity and the turbulent kinetic energy are lower.

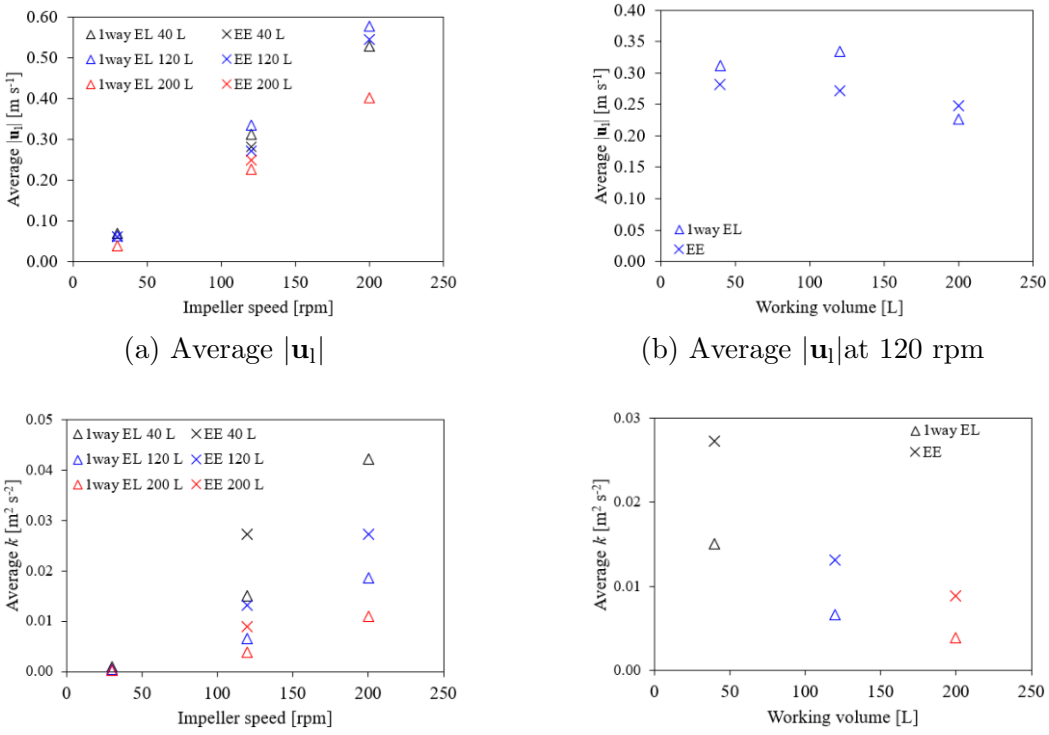

(a) Average $|\mathbf{u}_l|$

(b) Average $|\mathbf{u}_l|$at 120 rpm

(c) Average k

(d) Average k at 120 rpm

Figure 4.43: Average liquid velocity and average turbulence kinetic energy for impeller speeds of 30 rpm, 120 rpm, and 200 rpm and working volumes of 40 L, 120 L, and 200 L for the one-way coupled EL and EE simulations for $Q = 5.0$ L min^{-1}.

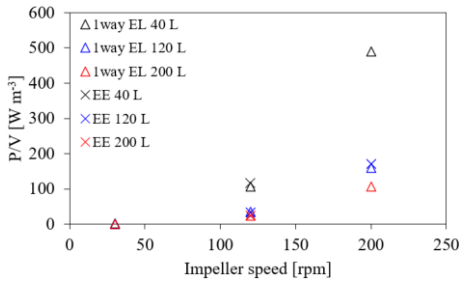

(a) Volumetric power input

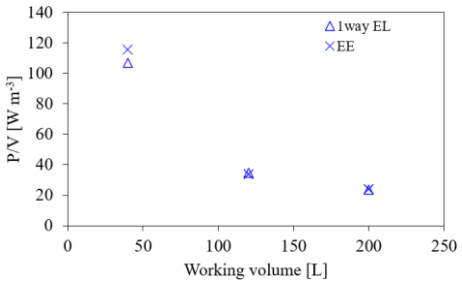

(b) Volumetric power input at 120 rpm

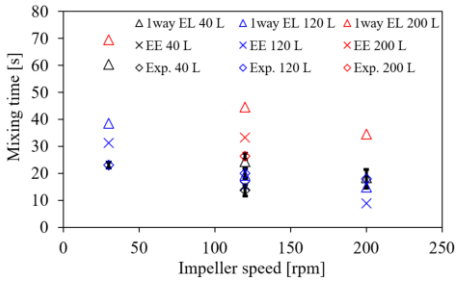

(c) Mixing time

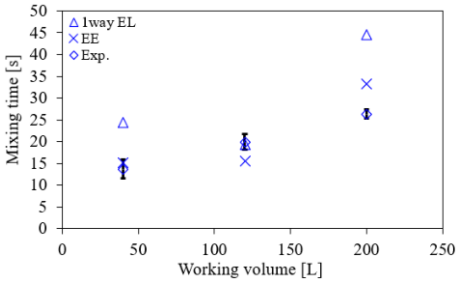

(d) Mixing time at 120 rpm

Figure 4.44: Volumetric power input and mixing time for impeller speeds of 30 rpm, 120 rpm, and 200 rpm and working volumes of 40 L, 120 L, and 200 L for the one-way coupled EL and EE simulations for $Q = 5.0$ L min^{-1}. The results of the EE simulations and the experiments for the mixing time are reported in [118].

Figure 4.44a shows that the volumetric power input also increases with the impeller speed. Figure 4.44a shows the expected decrease of the volumetric power input for larger working volumes at the intermediate impeller speed of 120 rpm. The minimum and maximum values of the power number across all operating conditions are 1.09 and 1.25 for the one-way coupled EL simulations and 1.04 and 1.27 for the EE simulations, showing good agreement between the two simulation approaches. Moreover, the average values of 1.15 for both simulation approaches are identical to the supplier specification [154].

The higher volumetric power input and average liquid velocity for an increased impeller speed also result in a reduced mixing time at a higher impeller speed, shown in Fig. 4.44c. The expected increase of the mixing time for larger working volumes can be seen in Fig. 4.44d. In contrast to the bioreactors presented above, for the smallest working volume of 40 L, the one-way coupled EL simulations predict mixing times in between those for the intermediate and the maximum working volume of 120 L and 200 L, respectively, as is evident form the differently colored triangles in Figs. 4.44c and 4.44d. This is in agreement with the slightly reduced average liquid velocity magnitude mentioned for the working volume of 40 L. For the EE simulations, the effect of the working volume is only evaluated at the intermediate impeller speed of 120 rpm. For 120 rpm, there is a slight increase of 0.3 s of the mixing time from the minimum to the intermediate working volume, which is better visible in Fig. 4.44d, since in Fig. 4.44c

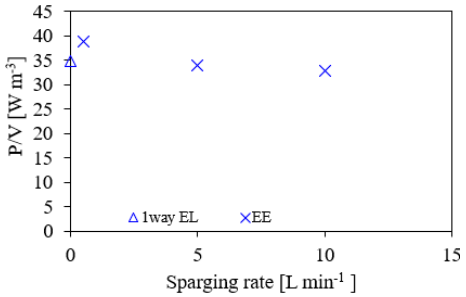

(a) Volumetric power input

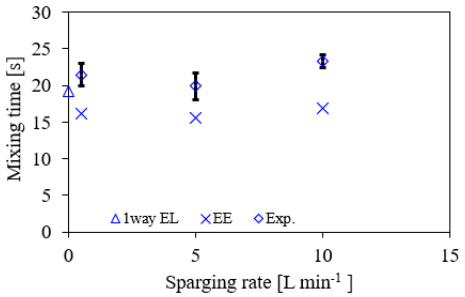

(b) Mixing time

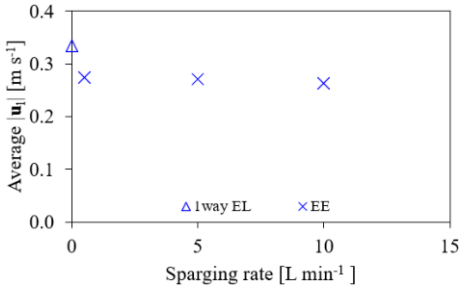

(c) Average liquid velocity

Figure 4.45: Volumetric power input P/V, mixing time, and average liquid velocity for the different sparging rates and sparger types atat $V = 120$ L, $n = 120$ rpm for sparging rates of 0.5 L min^{-1}, 5.0 L min^{-1}, and 10.0 L min^{-1}. The experimental results for the mixing time are reported in in [118].

the black and blue cross marks overlap with the error bar for experimental value for 40 L (black diamond). The very similar mixing times for 40 L and 120 L in the EE simulations also match with the small differences in the average velocities for these conditions shown in Fig. 4.43b. In the experiments, the mixing time for 120 L is longer than for the lowest working volume. According to this evaluation, the mixing times for the EE simulations are in better agreement to the experiments than those of the one-way coupled EL simulations.

The effect of sparging on the volumetric power input, the mixing time, and the average velocity magnitude is evaluated in Fig. 4.45. The one-way coupled EL results are represent unsparged conditions, since the effect of bubbles on the liquid motion is not considered. Similar to the CR3 and XDR-10, the effect of the sparging rate on the average velocity, the volumetric power input, and the mixing time shown in Fig. 4.45 is minor and negligible compared to that of the working volume and the impeller speed shown in Figs. 4.43a, 4.43b, and 4.44. At the maximum sparging rate, there is a small decrease in the volumetric power input and the average velocity, and a slight increase in the mixing time, indicating that the bubbles interfere with the power transfer from the impeller to the liquid and reduce the liquid mixing.

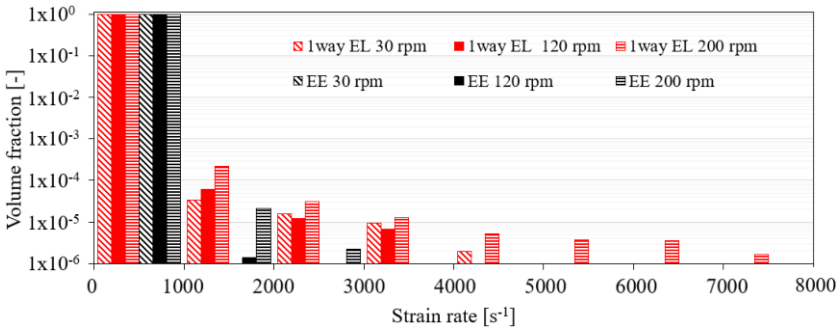

(a) Strain rate

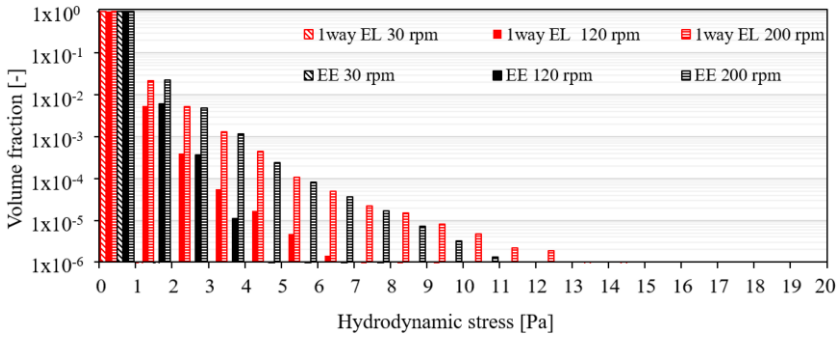

(b) Hydrodynamic stress

Figure 4.46: Volume fraction distributions of the strain rate and the hydrodynamic stress for the impeller speeds of 30 rpm, 120 rpm, and 200 rpm for $V = 120$ L, and $Q = 5.0$ L min^{-1}.

Risk of Cell Damage

While higher impeller speeds improve the mixing, they also increase the mechanical stress in the liquid that would be acting on the cells during cell cultivation. The distributions of the volume fractions for the strain rate and the hydrodynamic stress at a working volume of 120 L for the impeller speeds of 30 rpm, 120 rpm, and 200 rpm, and in the case of the EE simulations at a sparging rate of 5.0 L min^{-1}, are shown in Figs. 4.46a and 4.46b. Similar to the CR3 and the XDR-10, the maximum stress increases with the impeller speed, which is found with both modeling approaches. For the EE simulations at 30 rpm, the maximum strain rate is below 1000 and only the first fraction is present in Fig. 4.46a. The observed ranges of the strain rate and the hydrodynamic stress are comparable to those observed with the CR3 and the XDR-10 and the hydrodynamic stress is well below the critical limits of 25.2 Pa and 32.5 Pa for Sp2/0 mouse hybridoma and CHO cells [47], respectively.

In contrast to the CR3 and XDR-10, the EE simulations do not predict higher hydrodynamic stress compared to the one-way coupled EL simulations. This is likely related to the slight differences in the position of the impeller described in Sect. 4.3.3, with a smaller distance to the vessel wall in the one-way coupled EL simulations resulting in a region of higher hydrodynamic stress between the impeller and the

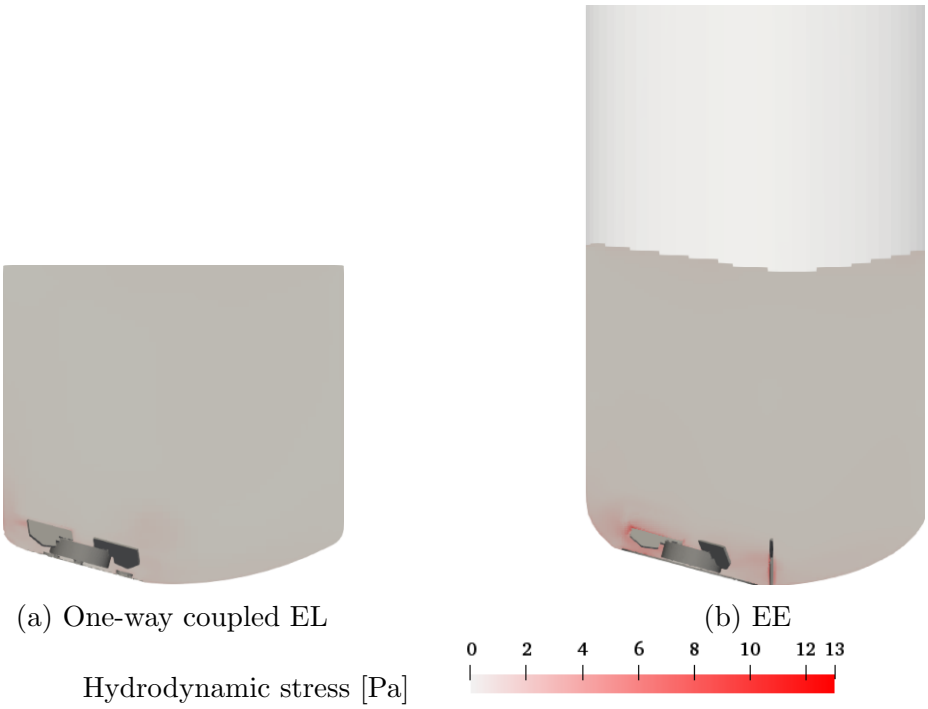

(a) One-way coupled EL (b) EE

Figure 4.47: Hydrodynamic stress on the x-z plane through the center of the XDR-200 for the one-way coupled EL and EE approaches for $V = 120$ L, $n = 200$ rpm, $Q = 5.0$ mL min^{-1}.

closest vessel wall, see Fig. 4.47a. The T-sparger that is not included in the bioreactor configuration of the one-way coupled EL simulations results in a region of intermediate hydrodynamic stress in the EE simulations, see Fig. 4.47b. These observations show that slight difference in the bioreactor configuration in the proximity of the impeller do affect the hydrodynamic stress. The low hydrodynamic stress in the upper part of the liquid is in good agreement between both modeling approaches.

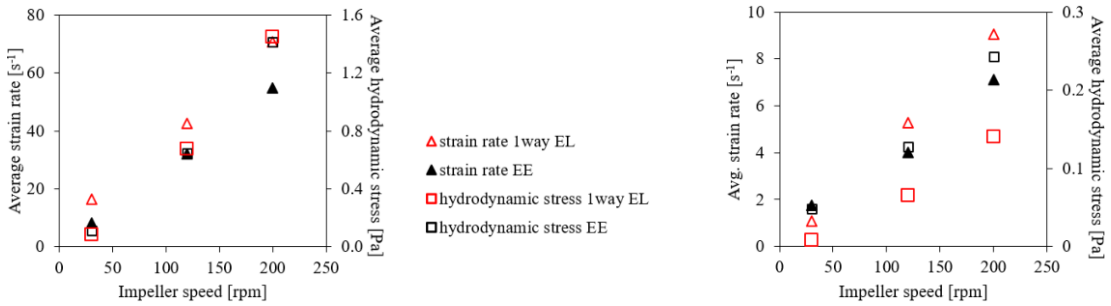

(a) Impeller zone (b) Tank zone

Figure 4.48: Average strain rate (triangles) and average hydrodynamic stress (squares) for the impeller (left) and tank zone (right) of the XDR-200 at $V = 120$ L and $Q = 5.0$ L min^{-1} with one-way coupled EL and EE results in red and black, respectively.

The average hydrodynamic stress and strain rate of the tank zone and the impeller zone at a working volume of 120 L and a sparging rate of 5.0 L min^{-1} at the different impeller speeds are shown Figs. 4.48a and 4.48b. Similar to the CR3 and the XDR-10, the average strain rate and hydrodynamic stress in both zones increase with the impeller speed. In agreement with the corresponding distribution of the volume fractions in Fig. 4.46a, the average strain rate for both, the impeller and the tank zone, is slightly higher for the one-way coupled EL simulations. The average hydrodynamic stress in the impeller zone is in close agreement between the one-way coupled EL and EE approaches, whereas in the tank region higher average hydrodynamic stress is found with the EE approach. This is similar to the XDR-10 and is caused by the interaction of the liquid phase with the bubbles, which generates additional turbulence. While the average values for the impeller zone are comparable to those of the CR3 and the XDR-10, those for the tank zone are smaller than for the CR3 and XDR-10, indicating that for the larger volume of the XDR-200 the single impeller cannot agitate the liquid in the tank zone as well as for the smaller bioreactors.

Gas Hold-Up and Volumetric Oxygen Mass Transfer Coefficient

For the bubble diameter, 1.3 mm are selected after an initial comparison of the simulated volumetric oxygen mass transfer coefficient for different bubble diameters to the experimental values provided by Tomomi Matsuura. The volume of all bubbles present in the liquid at steady conditions divided by the total volume is the gas hold-up, which is shown in Fig. 4.49. After the bubbles have passed the impeller region, they rise within the upper recirculation zone. The almost identical gas hold-up values for the different working volumes indicate that the average bubbles rise velocity in this zone is independent of the working volume as both the bubble residence time and the working volume increase linearly with the liquid height. A higher sparging rate results in a higher gas hold-up as more bubbles are generated in a given time interval. For the one-way coupled EL simulations, the gas hold-up increases linearly with the sparging rate, since the effect of sparging rate on the liquid flow and consequently the bubble

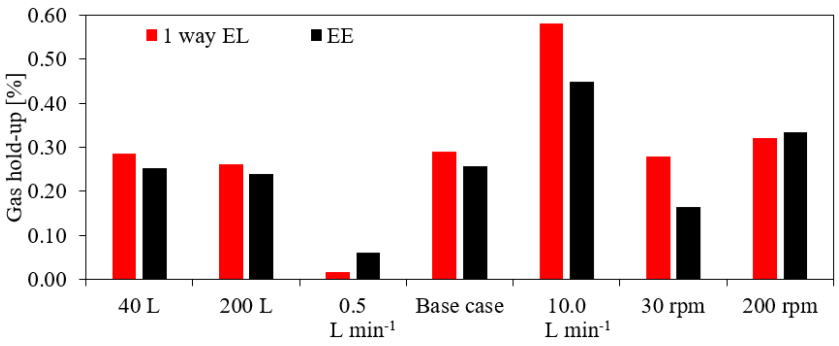

Figure 4.49: Gas-hold-up for the XDR-200 with the labels indicating how the operating conditions deviate from the base case (V = 120 L, n = 120 rpm, Q = 5.0 L min^{-1}).

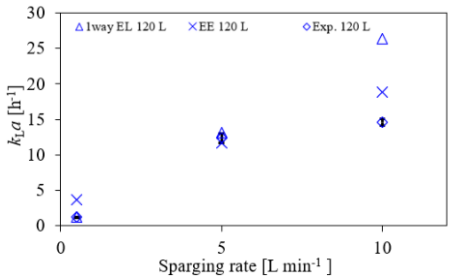

(a) Effect of the sparging rate

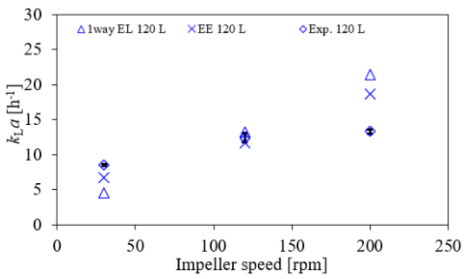

(b) Effect of the impeller speed

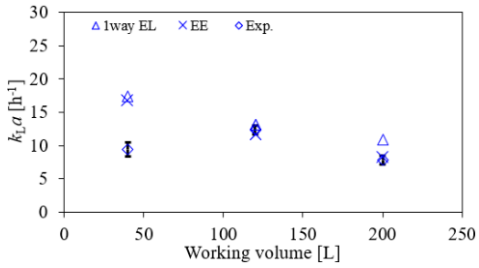

(c) Effect of the working volume

Figure 4.50: Impact of changes of a single operating parameter on the volumetric oxygen mass transfer coefficient k_La for the XDR-200 with the other operating parameters at the intermediate value of 120 L for the working volume, 120 rpm for the impeller speed, and 5.0 L min^{-1} for the sparging rate. The experimental and EE results are reported in [118].

residence time is not captured. For the EE simulations, the slower increase of the gas hold-up for the higher sparging rates indicates a reduction of the bubble residence time with increasing sparging rates. A stronger horizontal dispersion of the bubbles with longer bubble rise paths at a higher impeller speed also increases the gas hold-up. However, for the EE simulations this effect is found to be much more pronounced than for the one-way coupled EL simulations, where the differences are quite small, even though the effects on the bubble rise paths shown in Fig. 4.42 are quite similar.

Similar to the gas hold-up, the k_La increases with a higher sparging rate and a higher impeller speed, see Figs. 4.50a and 4.50b. Moreover, the one-way coupled EL simulations always assume a linear increase of the k_La with the sparging rate. This is in contrast to the EE simulations and the experiments, see Fig. 4.50a, where the increase for the maximum sparging rate is smaller than for the one-way coupled EL simulations. This is even more pronounced in the experiments, indicating that in addition to the effect of the sparging rate on the bubble residence time, the bubble size is also affected by the changes of the operating conditions. Since a longer residence time results in a higher gas hold-up, the probability of coalescence increases and leads to the formation of larger bubbles that are less efficient for oxygen transfer. To achieve the same k_La as in the experiments, a larger bubble diameter would be needed in the simulations. Similarly, for the maximum impeller speed, both the one-way coupled EL and EE simulations predict a higher k_La than that observed in the experiments.

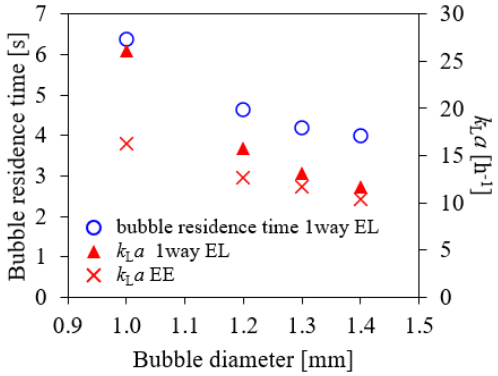

Figure 4.51: Effect of the bubble diameter on the bubble residence time for the one-way coupled EL simulations and the k_La for both, the one-way coupled EL simulations and EE simulations of the XDR-200 for $V = 120$ L, $n = 120$ rpm, $Q = 5.0$ L min^{-1}.

At a higher impeller speed, the bubbles are strongly entrained behind the impeller blades and which increases the probability of coalescence in this region. Consequently, a slightly larger bubble diameter would improve the agreement between simulations and experiments. Changes to the bubble size distribution and the average bubble size do not have to be large to explain the observed deviation. The bubble residence time and k_La for different bubble diameters are shown in Fig. 4.51 and the increase from 1.0 mm to 1.4 mm reduces the k_La by 55 % and 36 % for the one-way coupled EL and EE simulations, respectively.

The effect of the working volume on the k_La is shown in Fig. 4.50c. Similar to the CR3 and XDR-10, the k_La is reduced for a higher working volume despite negligible differences for the gas hold-up, due to the lower k_L. This is observed for the one-way coupled EL and EE simulations both. Moreover, the larger absolute difference in volume appears to also increase the impact of the volume on the k_La compared to the smaller CR3 and XDR-10. In the experiments, the k_La for the minimum working volume of 40 L is between that of the intermediate and the maximum working volume, which is likely caused by experimental error due to the large head space volume discussed in [118].

4.3.5 Selection of Operating Conditions for Cell Cultivation

The main effect of the increased working volume for the pilot-scale bioreactor XDR-200 compared to the smaller lab-scale bioreactors CR3 and XDR-10 are the longer mixing times. The mixing times of about 20 s for the intermediate working volume of 120 L and the intermediate impeller speed of 120 rpm are about twice as high as those for the CR3 and XDR-10 for 1.7 L at 100 rpm and for 7.0 L at 100 rpm, respectively.

With regard to the mechanical stress in the liquid phase, both the strain rate and the hydrodynamic stress are in a comparable range to that of the CR3 and XDR-10 and the maximum hydrodynamic stress is below the critical values of 25.2 ± 2.4 Pa and 32.4 ± 4.4 Pa for Sp2/0 and CHO cells, respectively, [134]. Considering both the mixing time and the hydrodynamic stress, the impeller speed should be at least

at the intermediate level or higher to provide good mixing, while even at the highest considered impeller speed of 200 rpm the hydrodynamic stress is too low to have a negative impact on cell growth.

Furthermore, only at the intermediate and maximum impeller speeds of 120 rpm and 200 rpm, the bubbles are well dispersed across the bioreactor cross-section, suggesting a more homogeneous transfer of oxygen in different regions of the bioreactor. The observed $k_{\mathrm{L}}a$ values are within the range typically required for cell cultivation of 1 h^{-1} to 20 h^{-1} [18, 35]. At the intermediate sparging rate of 5.0 L min and the intermediate impeller speed of 120 rpm, the simulated $k_{\mathrm{L}}a$ of 13.2 h^{-1} to 11.7 h^{-1} for the one-way coupled EL and the EE approach, respectively, is already sufficient to support the peak cell density of many cell lines. For achieving even higher values, increasing only the sparging rate or the impeller speed, while maintaining the other operating parameters at a constant level is found to give diminishing improvements, see Figs. 4.50a and 4.50b. Instead, both should be adjusted in tandem, since a higher number of bubbles only can achieve its maximum effect, when it is well dispersed and a good bubble dispersion only provides its full benefits, when the number of bubbles is sufficiently high.

4.4 The Xcellerex™ XDR-500

While the hydrodynamic characterization of the CR3, the XDR-10, the XDR-200, and the XDR-2000 and the operating conditions for scale-up with these reactors are the main focus of the present study, one-way coupled Euler-Lagrange simulations have also been carried out for the Xcellerex™ XDR-500 with a maximum working volume of 500 L. The XDR-500 is part of the Xcellerex™ product line and the next larger scale after the XDR-200 [145]. The XDR-500 is a pilot scale bioreactor that can be used to generate more cells to inoculate larger bioreactors or for generating small product amounts.

In contrast to the CR3, the XDR-10, the XDR-200, and the XDR-2000, the one-way coupled simulations are carried out with OpenFOAM [63] instead of MixIT [64]. Kristof Pandi, Bachelor student in mechanical engineering at the Technical University of Munich, has run the simulations of the XDR-500 during his time as working student at Daiichi-Sankyo Europe.

4.4.1 Bioreactor Configuration

Similar to the XDR-200, the XDR-500 consists of a rigid vessel frame and a flexible inner bag equipped with a pitched-blade impeller with three blades and a diameter of 26.7 cm, which is shown in Fig. 4.52. The XDR-200 and the XDR-500 have the highest geometric similarity of all bioreactors investigated in the present study, and both are equipped with an off-centered, bottom-mounted impellers with three blades angled at 40° relative to the cylindrical base. However, the exact shape of the impeller blades differs. Same as for the XDR-200, the impeller of the XDR-500 is positioned 15° off-center. Analogous to the XDR-10 and the XDR-200, the impeller is driven by magnetic coupling and rotated in the up-pumping, anti-clockwise direction. The vessel diameter is 0.76 m and the liquid height for the maximum working volume of 500 L is 1.17 m. Similar to the XDR-200, the sparger of the XDR-500 consists of multiple microporous sparger disks connected to the same inlet[145]. For the XDR-500 four microporous sparger disks with a pore size of 2 µm that are integrated into the solid plate on which the impeller is fixed. Three of the gray sparger disks are well visible in Fig. 4.52, while the fourth is hidden behind the impeller blade. Additionally,

Figure 4.52: Impeller of the XDR-500

Table 4.7: Operating conditions for the XDR-500.

Condition #	Impeller speed n [rpm]	Working volume V [L]
1	140	100
2	30	300
3	140	300
4	500	300
5	30	500
6	140	500
7	250	500

a T-shaped sparging wand for carbon dioxide stripping with drilled holes of 2 mm diameter is located close to the center of the vessel on the side opposite to the impeller. Analogous to the XDR-10 and XDR-200 the sensors only enter for about 1 cm from the side of the vessel in the lower part of the biroeactor and are neglected in the bioreactor configuration considered in simulations.

4.4.2 Operating Conditions

For the working volumes of 300 L and 500 L, three different levels of impeller speed, i.e., 30 rpm, 140 rpm, and 250 rpm, are investigated, while for the minimum working volume of 100 L only the intermediate impeller speed of 140 rpm is considered. The resulting seven different test conditions are summarized in Tab. 4.7. Condition #3 with the intermediate working of 300 L and the intermediate impeller speed of 140 rpm is considered as the base case. For each test condition, the bubble residence time is determined and the volumetric oxygen mass transfer coefficient is calculated for a sparging rate of 5 L min^{-1}.

4.4.3 Grid Independence Study

Similar to the EE simulations of the XDR-200, a hexahedral grid in the center of the domain is used with a finer grid spacing in the lower part of the vessel, up to a volume of about 90 L. Moreover, polyhedral cells are present at walls and at the transition between different grid spacings. An elliptical shape is used for meshing the rounded bottom of the bioreactor.

Grids with different resolutions, shown in Fig. 4.53, have been tested. The grid with $4.0x10^6$ cells is selected for all further simulations based on less than 2.5 % deviation of the average liquid velocity magnitude, turbulence kinetic energy, and turbulence kinetic energy dissipation rate to the finest investigated grid with $4.9x10^6$ cells. For the lower working volumes of 100 L and 300 L the corresponding grids consist of $2.4x10^6$ cells and $3.2x10^6$ cells, respectively.

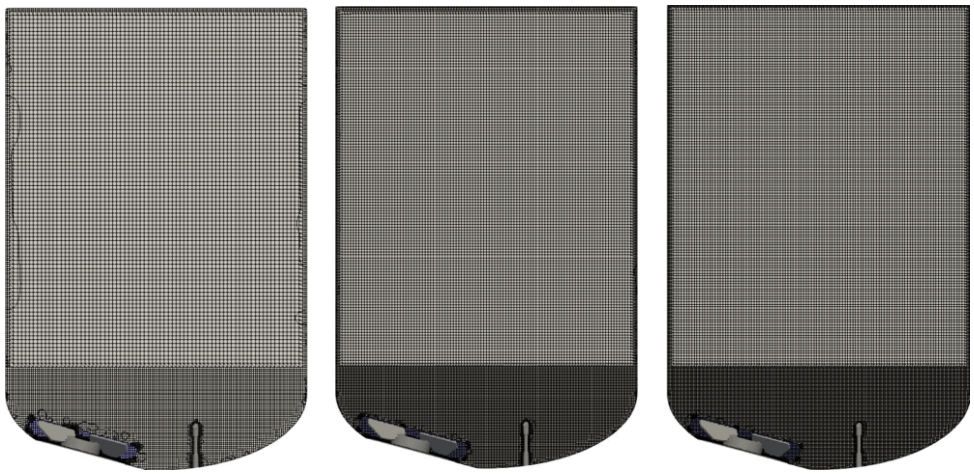

Figure 4.53: Computational grids for the XDR-500 considered in the grid study. Left to right: 2.2x10^6, 4.0x10^6, and 4.9x10^6 grid cells. The rotating reference frame regions are highlighted in blue.

4.4.4 Process Characterization

Since the bioreactor configuration of the XDR-500 is very similar to that of the XDR-200, the flow structure and bubble dispersion are also quite similar and are described first. Then the effect of the operating conditions on the different process characteristics is presented.

Liquid Flow Field and Bubble Dispersion

The pitched-blade impeller of the XDR-500 is rotating in the up-pumping anti-clockwise direction. The resulting liquid flow structure on the vertical cut plane through the vessel center at the intermediate impeller speed of 140 rpm for the considered working volumes of 100 L, 300 L, and 500 L is shown in Fig. 4.54. Similar to the XDR-200, the off-centered position of the impeller results in an asymmetric flow field. The bioreactor configuration of the XDR-500 is very similar to that of the XDR-200, which also has a pitched-blade impeller with three blades that is positioned at the bottom of the reactor. As has already been described for the XDR-200 in section 4.3.4, there is a large recirculation zone in the region above the impeller with up-flow along the vessel wall and down-flow close to the center of the vessel. The horizontal position of the center of the down flow region changes its position with the liquid height. Along the bottom of the vessel there also is recirculation, with flow from the impeller to the vessel wall opposite the impeller and back flow towards the impeller. At the minimum working volume of 100 L shown in Fig. 4.54a a similar flow structure is observed, however, due to the small liquid height no separate recirculation zone in the upper part of the vessel is formed. This is again similar to the flow structure found for the XDR-200 at its minimum working volume 40 L.

Similar to the XDR-200, the microporous sparger disks of the XDR-500 are integrated into the plate on which the impeller is fixed and located directly beneath the

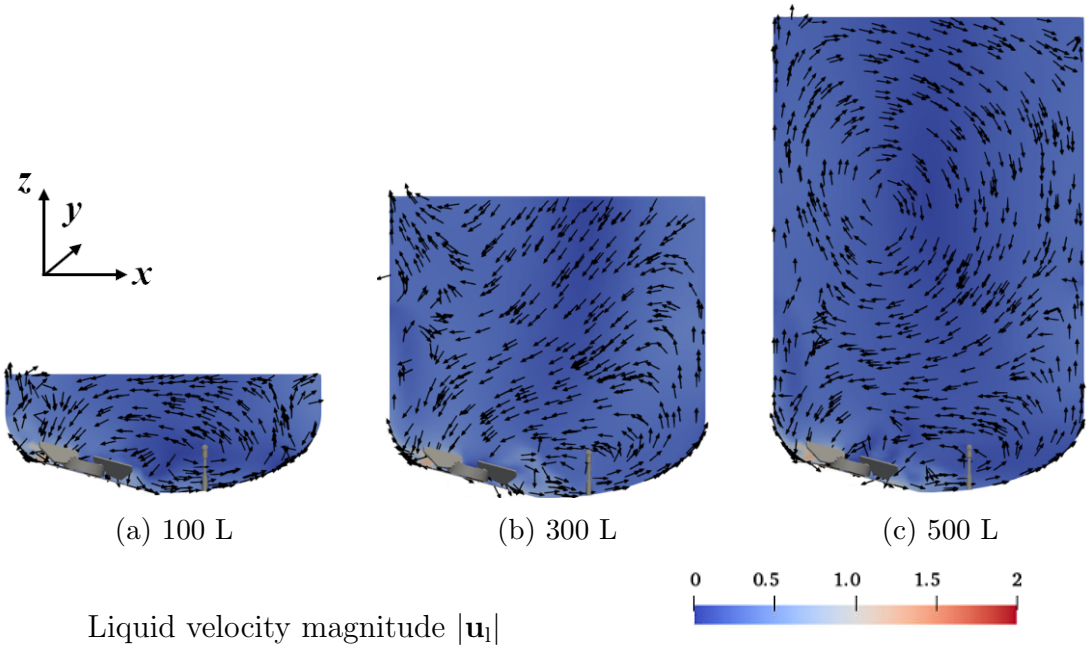

(a) 100 L (b) 300 L (c) 500 L

Figure 4.54: Liquid flow for the XDR-500 for the considered working volumes of 100 L, 300 L, and 500 L at the intermediate impeller speed of 140 rpm in the x-z plane through the center of the vessel. Arrows indicate the direction of the x-z velocity.

impeller blades and have with a pore size of 2 µm. Without any experimental evidence on the $k_L a$ the same bubble diameter as for the XDR-200 of 1.3 mm is selected. Bubble positions for the intermediate working volume at impeller speeds of 30 rpm, 140 rpm, and 250 rpm are shown in Fig. 4.55. Similar to the XDR-200 and the XDR-2000, at the lowest impeller speed the liquid velocity is too low to achieve horizontal dispersion of the bubbles, resulting in a relatively small region in which the bubbles are rising directly above the impeller, which is shown in Fig. 4.55a. With increasing impeller speed, see Figs. 4.55b and 4.55c, the bubbles are dispersed over a wider region, rising

(a) 30 rpm (b) 140 rpm (c) 250 rpm

Figure 4.55: Bubble dispersion inside the XDR-500 for different impeller speeds at a working volume of 300 L and for a bubble diameter of 1.3 mm.

around the down-flow region of the upper recirculation zone and close to the vessel wall at impeller speeds of 140 rpm and 250 rpm, respectively.

Liquid Velocity, Turbulence, Volumetric Power Input, and Mixing Time

The average liquid velocity for the considered impeller speeds of 30 rpm, 140 rpm, and 250 rpm is shown in Fig. 4.56a. The average liquid velocity increases for higher impeller speeds and decreases for larger working volumes. At the intermediate impeller speed of 140 rpm, the average liquid velocity for the minimum working volume of 100 L is very similar to that of the intermediate working volume of 300 L. This observation is similar to the small difference in the liquid velocity for the minimum and intermediate working volume of the XDR-200 of 40 L and 120 L, respectively. The small difference in the average liquid velocity despite the three times higher working volume is related to the changed liquid flow structure for the lowest working volume. For higher impeller speeds, which correspond to higher impeller Reynolds numbers, a higher the turbulence kinetic energy is observed as shown in Fig. 4.56b. For a higher working volume, the region of low velocity and turbulence in the upper part of the liquid becomes larger and the average turbulence kinetic energy decreases.

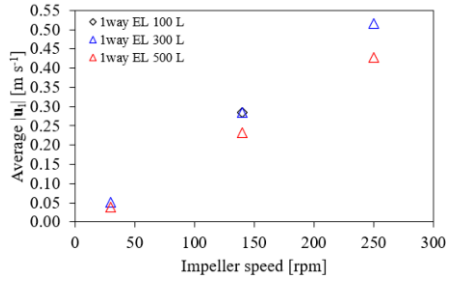

(a) Average liquid velocity

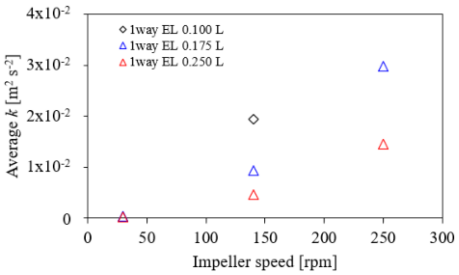

(b) Average turbulence kinetic energy

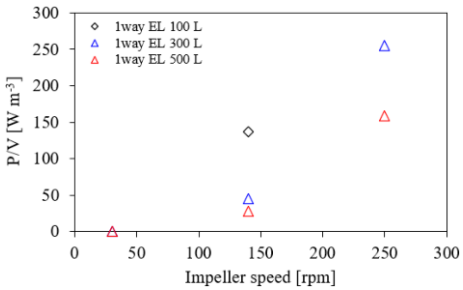

(c) Volumetric power input

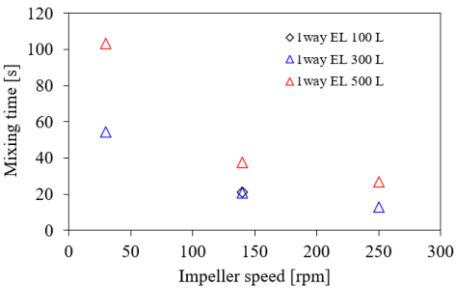

(d) Mixing time

Figure 4.56: Average liquid velocity, average turbulence kinetic energy, volumetric power input P/V, and mixing time for the considered impeller speeds of 30 rpm, 140 rpm, and 250 rpm and working volumes of 100 L, 300 L, and 500 L. The dotted lines in Fig. 4.56c represent fitted correlations based on the one-way coupled EL results and are colored according to the respective volumes.

As is typical for stirred tank bioreactors, the volumetric power input also increases with the impeller speed and decreases with the working volume as shown in Fig. 4.56c. The average impeller power number of the simulations for the different operating conditions is 0.86 with a minimum value of 0.84 and a maximum value of 0.88. The simulated power numbers are slightly lower than for the XDR-200 and the supplier specification, which both are 1.15 [154]. For stronger liquid agitation and a reduced working volume the mixing time decreases. Similar to the average liquid velocities, the mixing times for 100 L and 300 L working volume at 140 rpm are almost identical, which is again related to the difference in the flow structure mentioned above. At the minimum impeller speed of 30 rpm, the simulated volumetric power input is similar to that of the XDR-200 at 30 rpm for both the respective intermediate working volumes. However, the mixing times observed for the XDR-500 are higher than those for the XDR-200, due to the larger working volumes of 300 L and 500 L instead of 120 L and 200 L, respectively. The intermediate and maximum impeller speeds of the XDR-500 of 140 rpm and 250 rpm are slightly higher than that of the XDR-200 of 120 rpm and 200 rpm and result in a slightly higher volumetric power input and result in similar mixing times for the respective intermediate and maximum working volumes.

Risk of Cell Damage

The volume fraction distribution of the strain rate and the hydrodynamic stress for a working volume of 300 L and impeller speeds of 30 rpm, 140 rpm, and 250 rpm are shown in Figs. 4.57a and 4.57b. Similar to the bioreactors discussed above, the maximum strain rate and the maximum hydrodynamic stress increase with the impeller speed. The maximum values observed for the maximum impeller speed of 250 rpm are higher than those observed for the XDR-200 at the maximum impeller speed of 200 rpm. The maximum values of the hydrodynamic stress are still below the critical limits reported by Neunstoecklin et al. [134].

The distribution of the hydrodynamic stress in the x-z plane through the center of the XDR-500 is shown in Fig. 4.58. Analogous to the XDR-200, the highest hydrodynamic stress is located in the region of maximum velocity and turbulence directly around the impeller blades. Intermediate levels of hydrodynamic stress are found in the region around the impeller, at the T-sparger, and the vessel walls close to the impeller. In the remaining liquid, the hydrodynamic stress is low.

The average strain rate and hydrodynamic stress of the impeller zone and tank zone for the intermediate working volume of 300 L are shown in Fig. 4.59. The impeller zone is selected as a cylinder with a diameter of 1.2 d_{imp} and a height of 0.33 d_{imp} centered on the impeller, which are the same dimensions as for the CR3, XDR-10, XDR-200, and XDR-2000. The selection of the dimension of the impeller zone is discussed in more detail in section 4.1.4. Analogous to all other bioreactors presented above, the average strain rate and hydrodynamic stress increase with the impeller speed, both in the impeller zone and the tank zone. The average values for the strain rate and the hydrodynamic stress for both zones are very close to those observed for the XDR-200, which is the most similar of the considered bioreactors both in size and shape.

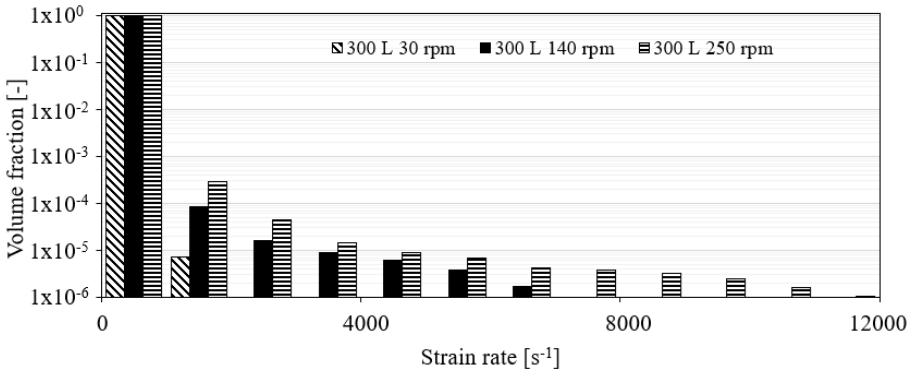

(a) Strain rate

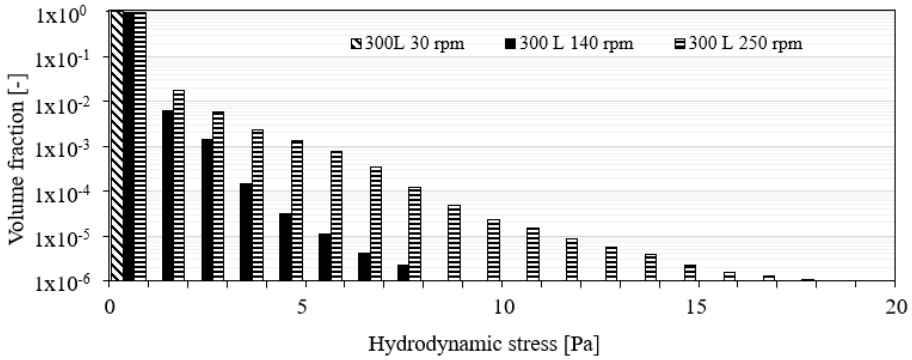

(b) Hydrodynamic stress

Figure 4.57: Volume fraction distributions of the strain rate and the hydrodynamic stress for the intermediate working volume of 300 L and the impeller speeds of 30 rpm, 140 rpm, and 250 rpm.

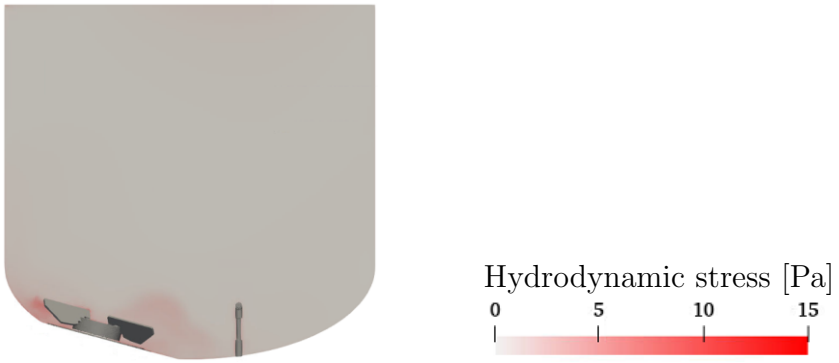

Figure 4.58: Hydrodynamic stress in the x-z plane through the center of the XDR-500 for the intermediate working volume of 300 L and the highest considered impeller speed of 250 rpm.

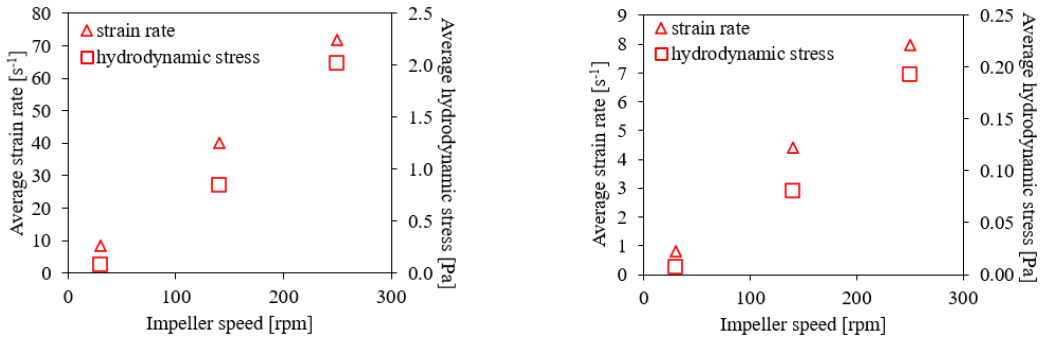

(a) Impeller zone (b) Tank zone

Figure 4.59: Average strain rate (triangles) and average hydrodynamic stress (squares) for the impeller (left) and tank zone (right) of the XDR-500 for the intermediate working volume of 300 L and the impeller speeds of 30 rpm, 140 rpm, and 250 rpm.

Gas Hold-Up and Volumetric Oxygen Mass Transfer Coefficient

The simulated average bubble residence time $t_{r,avg}$ and the k_La for a bubble diameter of 1.3 mm and a sparging rate of 5 L min^{-1} are shown in Fig. 4.60. Despite the better bubble dispersion for higher impeller speeds mentioned above, values of $t_{r,avg}$ of 4.9 s and 4.8 s for 30 rpm and 140 rpm, respectively, are almost identical, see Fig. 4.60a.

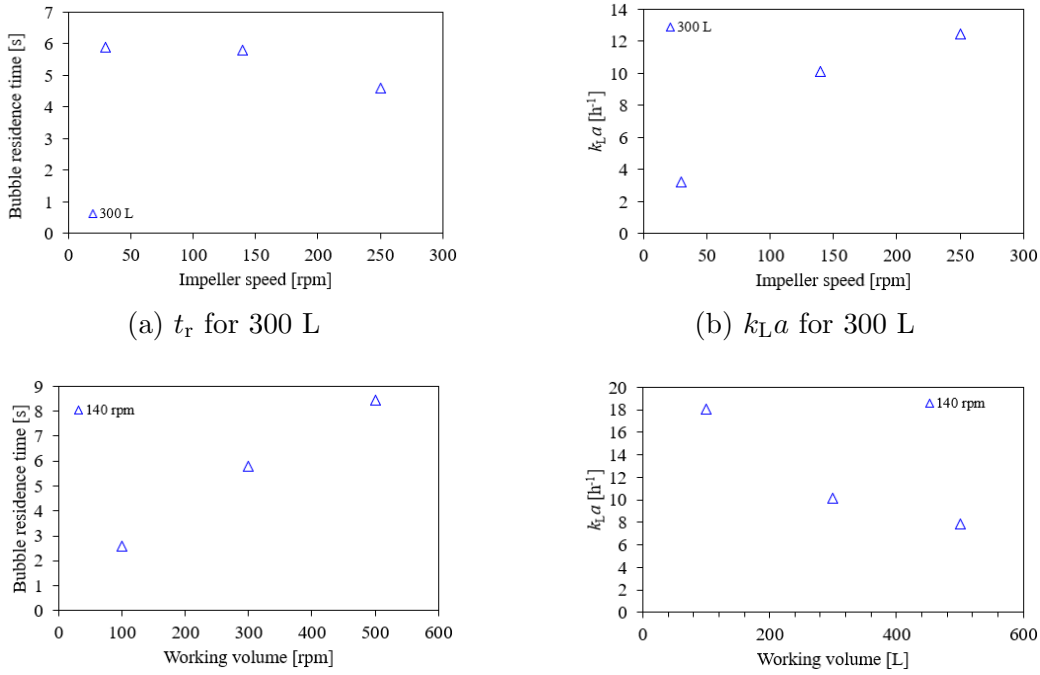

(a) t_r for 300 L (b) k_La for 300 L

(c) t_r for 140 rpm (d) k_La for 140 rpm

Figure 4.60: Bubble residence time and k_La for different impeller speeds at the intermediate working volume of 300 L (top) and for different working volumes at the intermediate impeller speed of 140 rpm (bottom). The bubble diameter is 1.3 mm.

For the maximum impeller speed of 250 rpm, $t_{r,avg}$ slightly decreases to 4.6 s . The reduction $t_{r,avg}$ at the maximum impeller speed is associated with the bubbles rising in the liquid up-flow region close to the vessel wall and is in contrast to the observations made for the CR3 and the XDR-10, where the gas hold-up increased for higher impeller speeds. Despite the reduction of the residence time the k_La increases for higher impeller speed due to the higher k_L as show in Fig 4.60b.

In Figs. 4.60c and 4.60d $t_{r,avg}$ and k_La for the different working volumes at the intermediate impeller speed of 140 rpm are shown. The increased liquid height for larger working volumes leads to a higher $t_{r,avg}$, however, due to the lower volumetric power input and k_L, the k_La decreases for a larger working volume. The sparging rate of 5 L min^{-1} is the same as the intermediate sparging rate of the XDR-200. The k_La for the XDR-200 for the intermediate working volume of 120 L and the intermediate impeller speed of 120 rpm with the 2 µm sparger is 13.2 h^{-1} for the one-way coupled EL simulations and 11.7 h^{-1} for the EE simulations. These values are only 30.7 % and 15.8 % larger than the value of of 10.1 h^{-1} for the XDR-500 at the intermediate working volume and impeller speed of 300 L and 140 rpm with the 2 µm sparger, even though the superficial gas velocity and volumetric sparging rate of the XDR-200 are about 1.8 and 2.5 times higher than those of the XDR-500.

4.4.5 Selection of Operating Conditions for Cell Cultivation

Based on the maximum hydrodynamic stress no risk of the cell damage is expected up to the highest impeller speed of 250 rpm. Since the mixing time is reduced and the k_La increases for a higher impeller speed, 250 rpm provide better conditions for cell culture than the lower impeller speeds of 30 rpm and 140 rpm. The range of observed k_La values is similar to that of the XDR-200 and covers the typically required range for cell cultivation well.

4.5 The Xcellerex^{TM} XDR-2000

The largest of the Xcellerex^{TM} single-use bioreactors is the Xcellerex^{TM} XDR-2000, which is a production scale-bioreactor and the largest bioreactor considered in the present study. Cell cultivation in the XDR-2000 is the final production step when using the Xcellerex^{TM} bioreactors. If even larger culture volumes are required, different bioreactor systems offering larger working volumes must be used. Especially at the very large scales above 2000 L, multi-use stainless steel bioreactors are still the norm.

4.5.1 Bioreactor Configuration

Similar to the XDR-10, the XDR-200, and the XDR-500, the Xcellerex^{TM} XDR-2000 consists of a rigid, multi-use vessel frame in which a single-use cultivation bag is placed. In contrast to the smaller Xcellerex^{TM} bioreactors, the pitched-blade impeller has four blades angled at 40° relative to the cylindrical base, see Fig. 4.61. Similar to the XDR-200 and the XDR-500, the impeller is fixed onto a rigid plastic plate at the bottom of the single-use bag at a position 15° off-center to the central vessel axis. However, the distance between the impeller blades and vessel bottom is increased through an additional intermediate part that connects the cylindrical base mounted on the bottom plate and the upper cylindrical part on which the impeller blades are fixed shown in Fig. 4.61. The XDR-2000 has a curved bottom and a vessel diameter d_V of 1.22 m. The impeller diameter d_{imp} is 42 cm. Analogous to the XDR-10, the XDR-200, and the XDR-500 the impeller is driven by magnetic coupling and rotated in the anti-clockwise direction. Similar to the XDR-200 and the XDR-500, the XDR-2000 can be purchased with different sparger options [145]. In the present study, the 20 µm sparger consisting of eight microporous disks integrated into the plastic plate below the impeller and all connected to a shared inlet tube is considered. Similar to the XDR-10, the XDR-200, and the XDR-500, the sparger openings are integrated into the plastic plate on which the impeller is fixed. Six of the gray sintered disks are visible in Fig. 4.61, while two are hidden behind the cylindrical base of the impeller. Furthermore, a variant of the single-use bag with a T-shaped drilled hole sparger like for the XDR-200 and the XDR-500 is also available.

Figure 4.61: Impellers of the Xcellerex^{TM} XDR-2000

Table 4.8: Operating conditions for the EE simulations of the XDR-2000.

Condition #	Impeller speed n [rpm]	Working volume V [L]	Sparging rate Q [L min^{-1}]	Sparger type
1	25	1200	13.5	20 µm
2	65	1200	13.5	20 µm
3	105	1200	13.5	20 µm
4	65	400	13.5	20 µm
5	65	2000	13.5	20 µm
6	65	1200	2.0	20 µm
7	65	1200	25.0	20 µm

4.5.2 Operating Conditions

The considered operating conditions are selected in a similar manner as described for the CR3, the XDR-10, and the XDR-200 in sections 4.1.2, 4.2.2, and 4.3.2 and cover changes in the impeller speed, the working volume, and the sparging rate. The selected operating conditions for the EE simulations are summarized in Tab. 4.8. The selected impeller speeds are 25 rpm, 65 rpm, and 105 rpm. The supplier specified minimum and maximum working volume of 400 L and 2000 L, and the intermediate value of 1200 L are considered. The low, intermediate and high sparging rates are 2.0 L min^{-1}, 13.5 L min^{-1}, and 25.0 L min^{-1}. Condition #4 with the intermediate impeller speed, working volume, and sparging rate of 65 rpm, 1200 L and 13.5 L min^{-1} is the base case.

In the one-way coupled EL simulations, the gas hold-up and volumetric oxygen mass transfer coefficient are evaluated for all conditions in Tab. 4.3 and an extended

Table 4.9: Operating conditions for the one-way coupled EL simulations of the XDR-2000.

Condition #	Impeller speed n [rpm]	Working volume V [L]
1	25	40
2	65	40
3	105	40
4	25	120
5	65	120
6	105	120
7	25	200
8	65	200
9	105	200

set of simulation conditions summarized in Tab. 4.4 is used to characterize the liquid flow. This set of conditions consists of all possible combinations of the three levels of working volume and the three levels of impeller speed. The selection of operating conditions for the one-way coupled EL simulations is again analogous to that of the CR3, the XDR-10, and the XDR-200.

4.5.3 Grid Independence Study

Similar to the XDR-200, the exact configuration of the vessel bottom is not known and a dished shaped bottom is considered for the one-way coupled EL simulations, while a elliptical bottom is considered for the EE simulations. Also in this case the position of the impeller differs by 4 cm in the radial direction. The initial grid study does not consider the T-sparger, which can be used for CO_2-stripping. When it is later added to the bioreactor configuration for the EE simulations, the change in the average velocity was less than 0.1 %.

For the one-way coupled EL simulations, the same grid structure as for the CR3, the XDR-10 and the XDR-200 is used, with higher refinement for the rotating reference

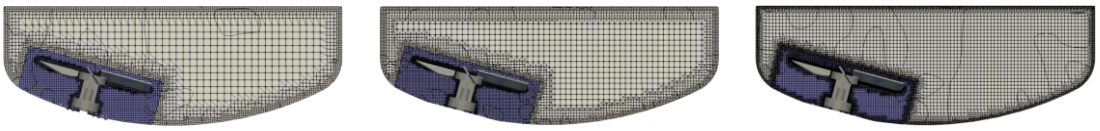

(a) One-way coupled EL, 400 L working volume. Left to right: 0.6x10^6, 1.0x10^6, and 2.3x10^6 grid cells.

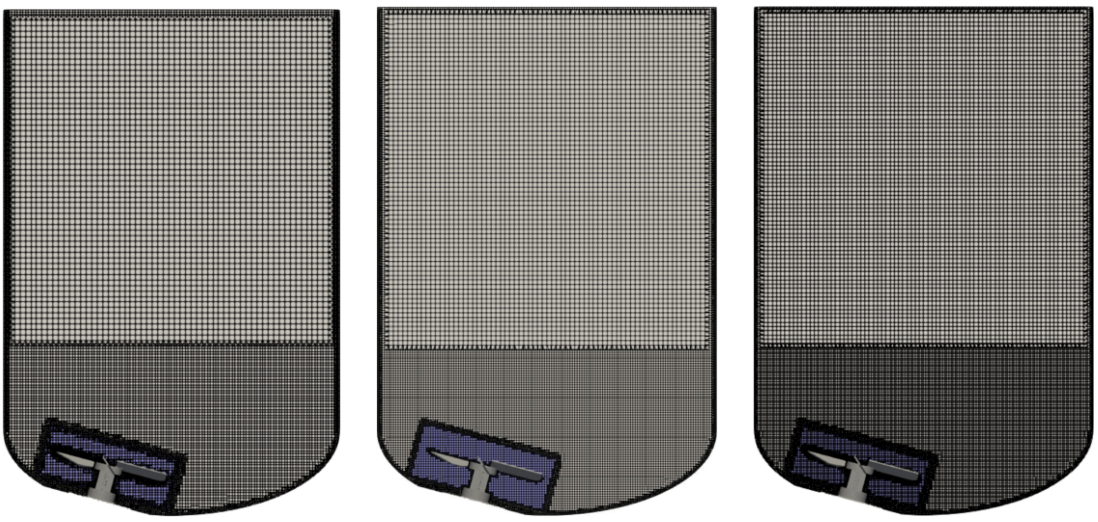

(b) EE, complete bioreactor. Left to right: 1.5x10^6, 2.3x10^6, and 3.0x10^6 grid cells.

Figure 4.62: Computational grids for the one-way coupled EL and EE simulations of the XDR-2000 considered in the grid study. The rotating reference frame region is highlighted in blue.

frame region is used. The grids for the one-way coupled EL simulations for the working volume of 400 L are shown in Fig. 4.62a. The intermediate grid with 1.0x10^6 cells is selected based on less than 1 % deviation of the average liquid velocity magnitude to that of the finest considered grid with 2.3x10^6 cells. The corresponding grid sizes for 1200 L and 2000 L volume are 1.6x10^6 and 2.1x10^6 grid cells, respectively.

For the EE simulations, a similar grid structure as for the XDR-200 is used, which has a higher refinement in the lower part of the vessel corresponding to a working volume of almost 600 L, see Fig. 4.62. The boundary of the rotating reference frame region is considered with additional refinement compared to the surrounding grdi in the lower part of the XDR-2000. The grid with 2.3x10^6 cells is selected based on less than 0.5 % deviation of the average liquid velocity magnitude to the finest considered grid with 3.0x10^6 cells.

4.5.4 Process Characterization

The flow structure and the bubble dispersion, which are the basis of all further process characteristics, are presented first. Then the effect of the operating conditions on the cell culture relevant process characteristics is analyzed. Finally, the range of investigated operating conditions is discussed from the perspective of selecting optimal conditions for cell cultivation.

Liquid Flow Field and Bubble Dispersion

Figures 4.63a and 4.63b show the liquid velocity for the base case (V = 1200 L, n = 65 rpm, Q = 13.5 L min^{-1}) for the one-way coupled EL and the EE approach, respectively. The impeller is rotating in the up-pumping anti-clockwise direction and the flow is dominated by this rotational motion, similar to the bioreactors presented above. The flow structure is similar to that of the XDR-200 and the XDR-500 with a large recirculation zone in the upper part of the vessel, where the liquid moves up along the vessel wall and flows down close to the center of the vessel. In agreement with the observations made for the XDR-200 and the XDR-500, the center of the down-flow region is also the center of the rotating motion of the liquid and its horizontal position changes with the liquid height. One major difference of the XDR-200 and the XDR-500 compared to the XDR-2000 is the increased distance between the impeller blades and the bottom of the vessel. This allows for more recirculation directly below the impeller blades but its effect is limited to the bottom part of the bioreactor. A higher impeller speed results in a higher liquid velocity and a higher working volume increases the vertical extent of the upper recirculation zone, similar to the bioreactors presented above. However, at the minimum working volume, see Figs. 4.63c and 4.63d, the liquid height is too small for the upper recirculation zone to develop. Instead, the liquid is pushed upwards and outwards from the impeller region and the back flow towards the impeller interferes with the flow coming from the impeller. This results in a low velocity zone in the bottom part of the vessel on the side opposite to the impeller. For the one-way coupled EL approach, this further changes the simulated flow profile from the radial pumping profile observed at 1200 L in Fig. 4.63a to an axial pumping profile

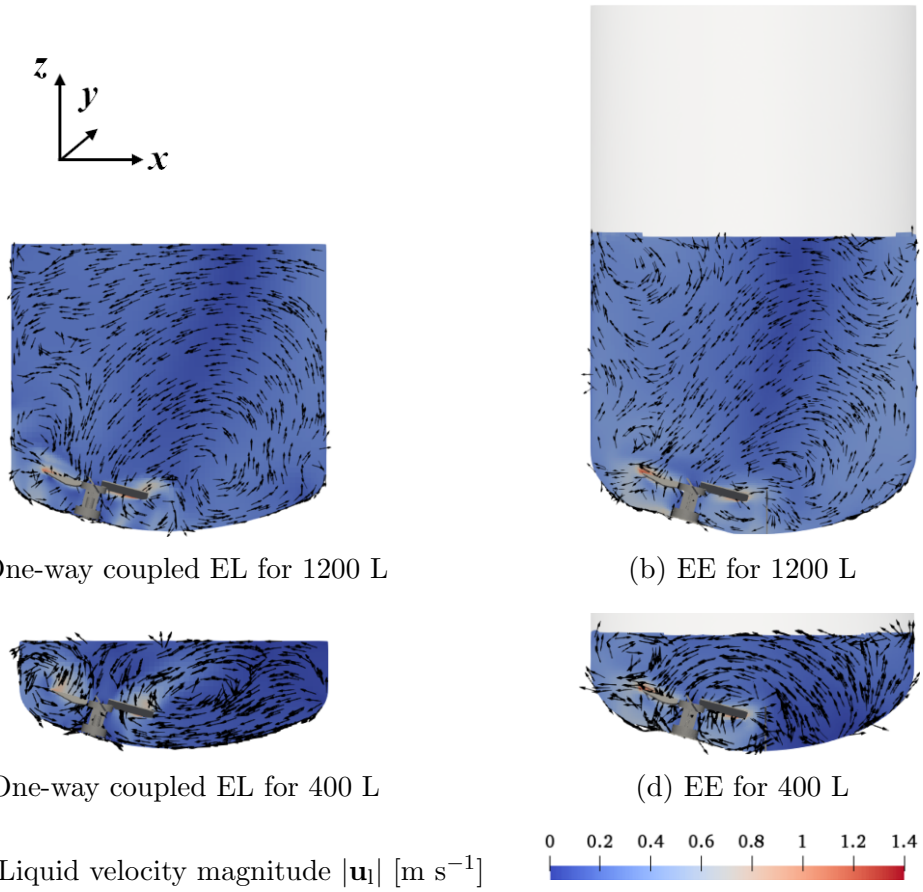

(a) One-way coupled EL for 1200 L

(b) EE for 1200 L

(c) One-way coupled EL for 400 L

(d) EE for 400 L

Figure 4.63: Liquid flow for the intermediate impeller speed of 65 rpm for 1200 L (top) and 400 L (bottom) working volume at a sparging rate of13.5 L min^{-1} in the x-z-plane through the center of the XDR-2000. Arrows indicate the direction of the x-z-velocity.

in Fig. 4.63a, where the flow is pushed up-ward by the impeller and drawn back in from the bottom of the vessel. In the EE simulations, the radial profile observed at 1200 L is also maintained at 400 L. This is caused by the differences in the considered shape of the vessel bottom, where the slightly larger liquid height for the elliptical bottom allows to accommodate liquid back-flow from the vessel wall opposite the impeller both from the top and the bottom in two radial recirculation zones.

The rotating motion of the liquid flow also impacts the bubble dispersion. In Fig. 4.64, the region in which the bubbles are rising is indicates by bubble positions and the 1 % gas volume fraction iso-surface for the one-way coupled EL and EE simulations, respectively, for different impeller speeds at a working volume of 1200 L and a sparging rate of 13.5 L min^{-1}. In Figs. 4.64a-c the diameter of the spheres indicating the bubble positions is ten times larger then the actual bubble diameter to improve their visibility. Similar to the spargers of the XDR-200 and the XDR-500, the eight opening connected to the shared inlet are evenly distributed around the cylindrical base of the impeller and the rising bubbles interact with all four impeller blades simultaneously. At the lowest impeller speed of 25 rpm, shown in Figs. 4.64a and 4.64d, the liquid velocity is

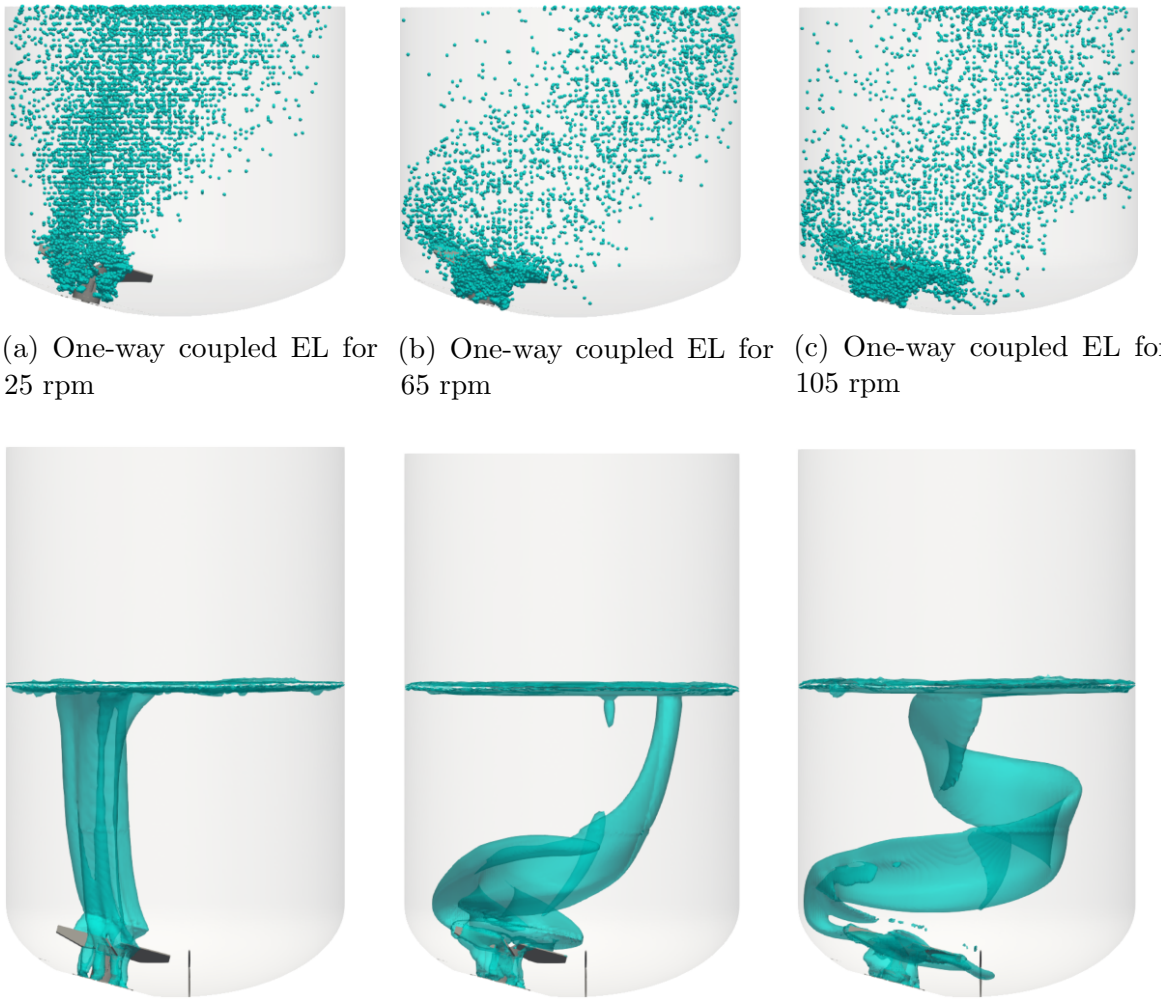

(a) One-way coupled EL for 25 rpm

(b) One-way coupled EL for 65 rpm

(c) One-way coupled EL for 105 rpm

(d) EE for 25 rpm

(e) EE for 65 rpm

(f) EE for 105 rpm

Figure 4.64: Bubble positions and 1 % gas volume fraction for the one-way coupled EL (top) and the EE simulations (bottom), respectively, for impeller speeds of 25 rpm, 65 rpm, and 105 rpm for $V = 1200$ L and $Q = 13.5$ L min^{-1}. The bubbles are shown three times larger than their actual size to improve visibility.

too small to disperse the bubbles horizontally and they rise around the inner parts of the impeller blades. Above the impeller, the bubbles move in a relatively straight line towards the liquid surface. The inclination of this rise path slightly differs between the one-way coupled EL and EE simulations but the overall structure is very similar. At the intermediate impeller speed of 65 rpm, Figs. 4.64b and 4.64e, the bubble dispersion is stronger and the bubbles are pushed from the inner part to the outer edges of the impeller blades. Their rise path above the impeller is strongly inclined in the anti-clockwise direction. At the maximum impeller speed of 105 rpm, Figs. 4.64c and 4.64f, the bubble are dispersed even better and show a spiraling rise path similar to those observed for the XDR-10, the XDR-200, and the XDR-500.

Liquid Velocity, Turbulence, Volumetric Power Input, and Mixing

The increase in the average liquid velocity for higher impeller speeds can be seen in Fig. 4.65a. The effect of the working volume on the average velocity at the intermediate impeller speed of 65 rpm is shown in Fig. 4.65b. In contrast to the CR3 and the XDR-10, the average liquid velocity for the minimum working volume is smaller than for the intermediate working volume. In the case of the one-way coupled EL simulations, the average velocity for the minimum working volume is even smaller than that for the maximum working volume. This lower average velocity is caused by the different flow structures and the low velocity region at the vessel bottom on the side opposite to the impeller, which is discussed above and only observed for a working volume of 400 L (also see Fig. 4.63). In contrast to the average velocity, the average turbulence kinetic energy not only increases with a higher impeller speed, see Fig. 4.65c, but also for a lower working volume, see Fig. 4.65d. Analogous to the other bioreactors presented above, the liquid flow in the in the upper part of the liquid is less turbulent than that around the impeller and a larger working volume results in a lower average turbulence kinetic energy. The average turbulence kinetic energy is higher for the EE simulations, which is similar to but more pronounced than for the CR3, the XDR-10, and the XDR-200. For the XDR-2000, this is most likely not only related to the turbulence caused by the interaction with the dispersed bubbles but also with the overall higher velocity at the bottom of the vessel due to the difference between the considered dish shaped and elliptical bottom shape.

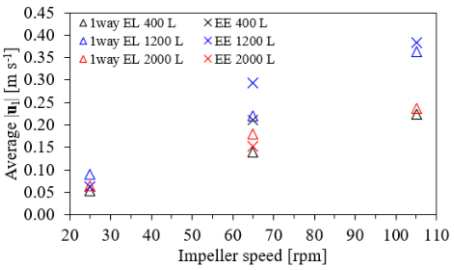

(a) Average $|\mathbf{u}_l|$

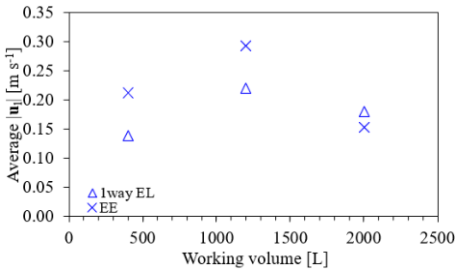

(b) Average $|\mathbf{u}_l|$ at 65 rpm

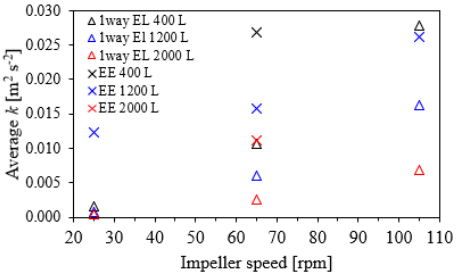

(c) Average k

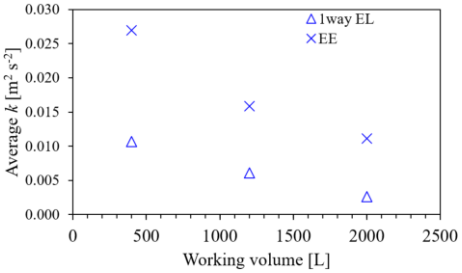

(d) Average k at 65 rpm

Figure 4.65: Average liquid velocity and average turbulence kinetic energy for impeller speeds of 25 rpm, 65 rpm, and 105 rpm and working volumes of 400 L, 1200 L, and 2000 L for sparging with $Q = 13.5$ L min^{-1}.

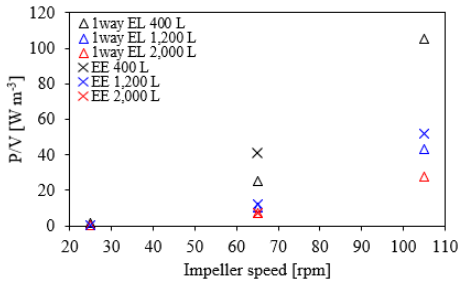

(a) Volumetric power input

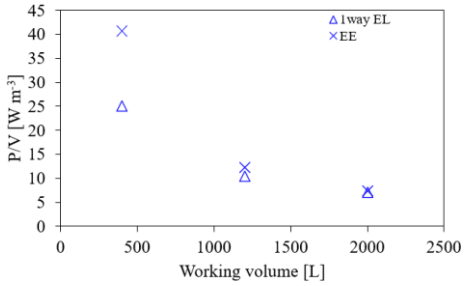

(b) Volumetric power input at 65 rpm

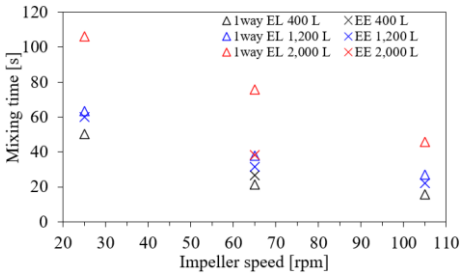

(c) Mixing time

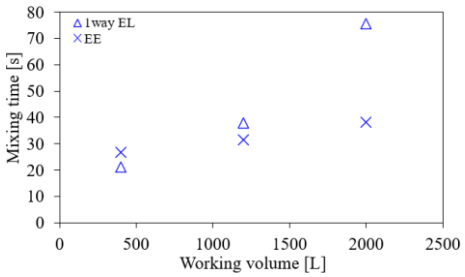

(d) Mixing time

Figure 4.66: Volumetric power input P/V and mixing time for impeller speeds of 25 rpm, 65 rpm, and 105 rpm and working volumes of 400 L, 1200 L, and 2000 L, for sparging with $Q = 13.5$ L min^{-1}.

The volumetric power input for different impeller speeds are shown in Fig. 4.66a. Figure 4.66b shows the the volumetric power input for increasing working volumes at the intermediate impeller speed of 65 rpm. The expected reduction of the volumetric power input for increasing working volumes and the increase of the volumetric power input for higher impeller speeds is observed. For the one-way coupled EL simulations, a lower volumetric power input is observed, which is especially pronounced at the minimum working volume of 40 L. The lower volumetric power input of the one-way coupled EL simulations is reflected in a lower power number of 0.74 compared to 0.88 for the EE simulations. The minimum and maximum values across all operating conditions are 0.59 and 0.85 for the one-way coupled EL simulations and 0.74 and 0.96 for the EE simulations. The simulated power numbers are slightly higher but very close to the supplier specification with a value of 0.72 [154].

Figures 4.66c and 4.66d show the mixing time across the different impeller speeds and for the different working volumes at the intermediate impeller speed of 65 rpm, respectively. Similar to the slightly higher volumetric power input, also slightly shorter mixing times are observed for the EE simulations, except for the minimum working volume of 400 L, see Fig. 4.66d. The mixing time for the lowest impeller speed of 25 rpm at the intermediate working volume is about 60 s, which is much higher than for the smaller bioreactors. While a higher impeller speed decreases the mixing time, it remains above 20 s for the intermediate working volume even at the highest considered impeller speed of 105 rpm. This emphasizes that for the larger working volume of the

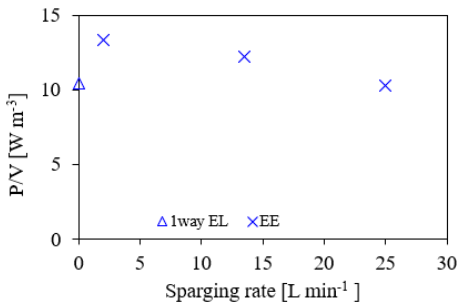

(a) Volumetric power input

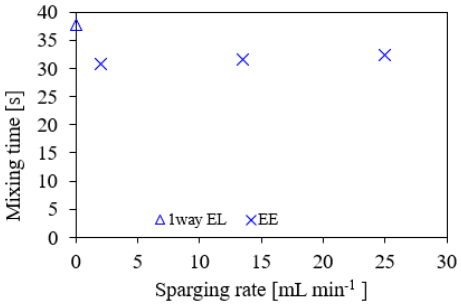

(b) Mixing time

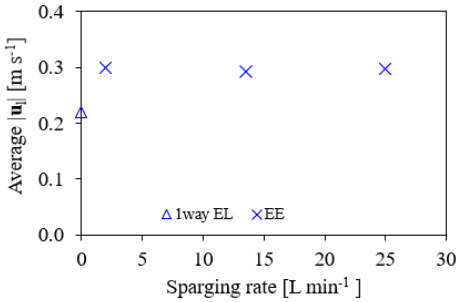

(c) Average liquid velocity

Figure 4.67: Volumetric power input P/V, mixing time, and average liquid velocity for the different sparging rates and sparger types at $V = 1200$ L, $n = 65$ rpm for sparging rates of 2.0 L min^{-1}, 13.5 L min^{-1}, and 25.0 L min^{-1}.

XDR-2000, the time needed to achieve homogeneous conditions is much longer than for the smaller CR3, XDR-10, and XDR-200.

Figure 4.67 shows the effect of the sparging rate on the volumetric power input, the mixing time, and the average liquid velocity for a working volume of 1200 L and an impeller speed of 65 rpm. The one-way coupled EL results are added as the condition without sparging, since the effect of bubbles on the liquid is neglected. Similar to the XDR-200, the volumetric power input is slightly reduced and the mixing time is slightly increased at a higher sparging rate. This indicates that volumetric power input of the impeller is reduced due to the sparging and the turbulence generated by the interaction of the bubbles is insufficient to compensate for this. However, the effect is minor and negligible compared to the effects of the working volume and the impeller speed shown in Figs. 4.66a, and 4.66c.

Risk of Cell Damage

Due to the long mixing times caused by the large working volume of the XDR-2000, knowing upper limits of the impeller speed can be increased without the risk of cell damage due to mechanical forces is even more important for the XDR-2000 than for the smaller bioreactors presented above with shorter mixing time because of their smaller working volume. Figures 4.68a and 4.68b show the distributions of the volume

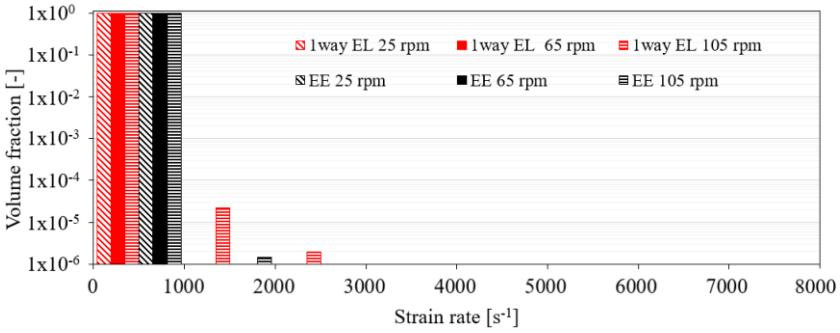

(a) Strain rate

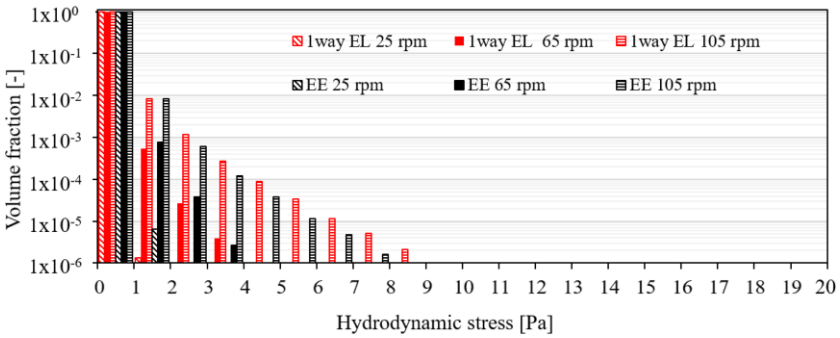

(b) Hydrodynamic stress

Figure 4.68: Volume fraction distributions of the strain rate and the hydrodynamic stress for the impeller speeds of 25 rpm, 65 rpm, and 105 rpm with $V = 1200$ L and $Q = 13.5$ L min^{-1}.

fractions of the strain rate and the hydrodynamic stress. Both the maximum strain rate and the maximum hydrodynamic stress at the maximum impeller speed are lower than at the respective maximum impeller speeds of the smaller bioreactors presented above. The hydrodynamic stress is below the critical values given by Neunstoecklin et al. [134] across all impeller speeds, indicating that the maximum impeller speed of 105 rpm does not indicate any risk of cell damage.

The volume fractions distributions of the strain rate and the hydrodynamic stress in Fig. 4.68 indicate the same heterogeneous distribution of the mechanical stress that is also observed for the smaller bioreactors presented above. For the majority of the liquid volume the strain rate and the hydrodynamic stress are low, and for a small volume strain rate and hydrodynamic stress are high, which is analogous to the for all the smaller bioreactor scales presented above and the results for other bioreactors reported in the literature [132, 23]. The maximum hydrodynamic stress found for the one-way coupled EL simulations his higher than that for the EE simulations, despite the higher average turbulence kinetic energy found with the EE simulations discussed above. This is similar to the results for the XDR-200 but in contrast to the results for the CR3 and the XDR-10.

Figs. 4.69a and 4.69b show the spatial distribution of hydrodynamic stress at the maximum impeller speed of 105 rpm on the central cut plane of the XDR-2000 for a

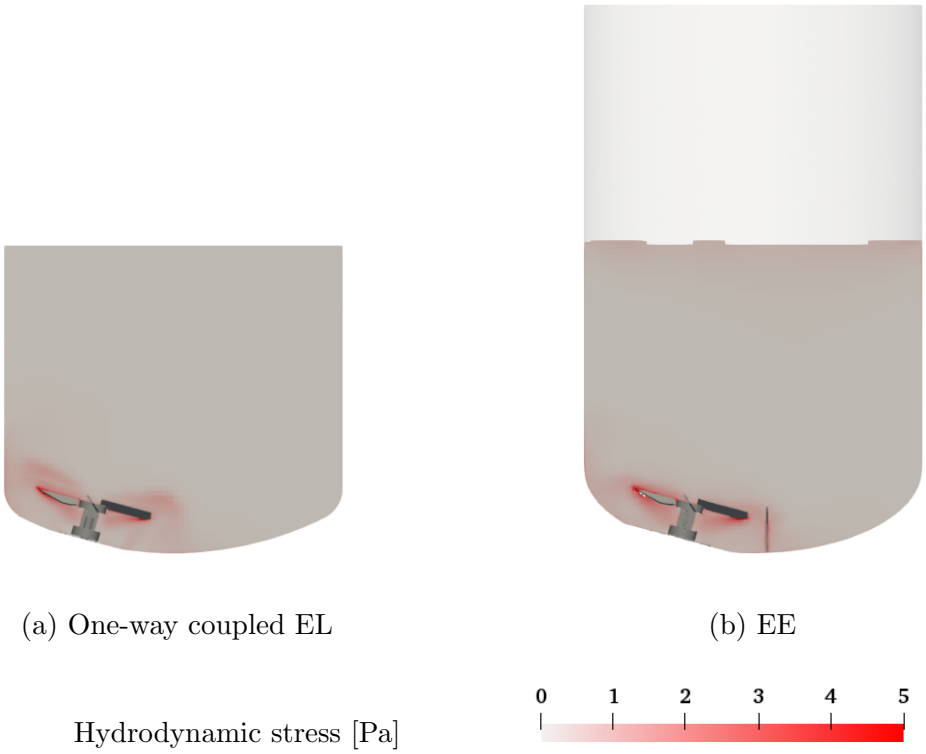

(a) One-way coupled EL (b) EE

Figure 4.69: Hydrodynamic stress on the $x - z$ plane through the center of the XDR-2000 for the one-way coupled EL and the EE approaches for $V = 1200$ L, $n = 105$ rpm, and $Q = 13.5$ L min^{-1}.

working volume of 1200 L at a sparging rate of 13.5 L min^{-1} for the one-way coupled EL and EE simulations, respectively. The maximum hydrodynamic stress is located in the proximity of the impeller, which is similar to the bioreactors presented above.

The average strain rate and the average hydrodynamic stress of the impeller and the tank zone are shown in Figs. 4.70a and 4.70b, respectively. Similar to the smaller bioreactors, the average strain rate and the average hydrodynamic stress in the impeller

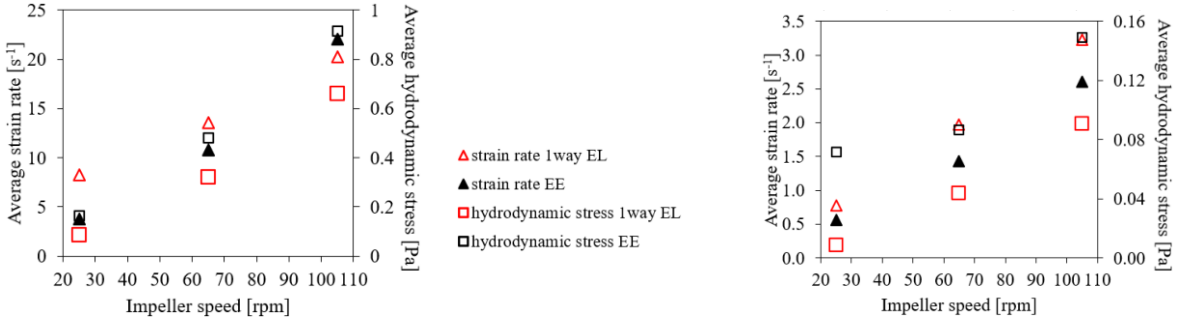

(a) Impeller zone (b) Tank zone

Figure 4.70: Average strain rate and average hydrodynamic stress for the impeller (left) and tank zone (right) of the XDR-2000 at $V = 1200$ L and $Q = 13.5$ L min^{-1}.

and the tank zones increase with the impeller speed. At similar impeller speeds, the average strain in the impeller zone is again in a range that is comparable to the smaller bioreactors and the average values of the tank zone are slightly lower than for all smaller bioreactors including the XDR-200. The lower strain rate is in agreement with the higher mixing times for the XDR-2000, which indicates that for the XDR-2000 with the largest working volume of all bioreactors the liquid bulk is less well agitated and mixed by the single bottom-mounted impeller. The average hydrodynamic stress for the EE simulations is higher than for the one-way coupled EL simulations in the impeller zone as well as in the tank zone, despite the higher maximum hydrodynamic stress for the one-way coupled EL simulations. This higher averages hydrodynamic stress is in agreement with the higher average turbulence kinetic energy and is caused by the turbulence generated by the interaction of the bubbles with the liquid.

Gas Hold-Up and Volumetric Oxygen Mass Transfer Coefficient

The third important hydrodynamic process characteristic aspect for cell cultivation is the oxygen transfer by the disperse bubbles. The gas hold-up is the volume of bubbles present in the liquid normalized by the total volume and is shown in Fig. 4.71. A bubble diameter of 1.3 mm is selected, which is the same as for the XDR-200, since it is the most similar to the XDR-2000 and experimental data for the XR-2000 is not available. As expected, the gas hold-up increases with the sparging rate. Similar to the XDR-200, the increase for the EE simulations is much smaller than that for the one-way coupled EL simulations, indicating a reduction of the residence time for higher sparging rates. In contrast to the XDR-200, the gas hold-up is found to be reduced for a larger working volume. This corresponds to a higher average bubble rise velocity at a lower volumetric power input, i.e., on average bubbles rise slightly faster if the upper recirculation zone is larger and has a lower average velocity, which is similar to the observations made for the XDR-10.

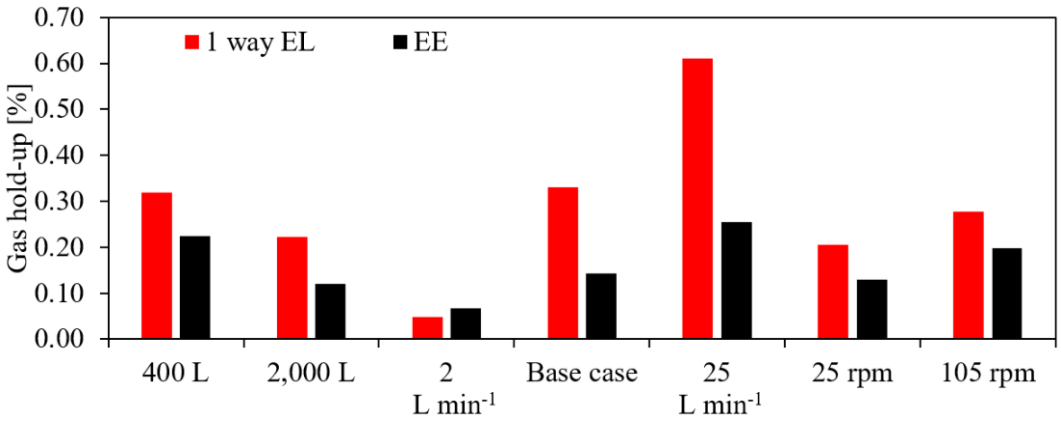

Figure 4.71: Gas hold-up for the XDR-2000 with the labels indicating how the operating conditions deviate from the base case (V = 1200 L, n = 65 rpm, Q = 13.5 L min^{-1}).

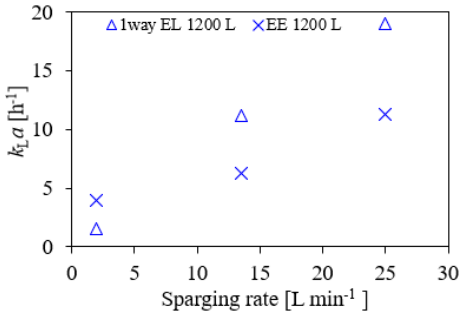

(a) Effect of the sparging rate

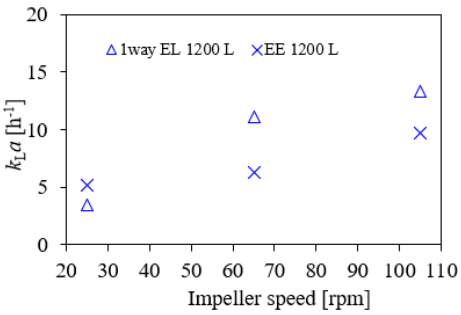

(b) Effect of the impeller speed

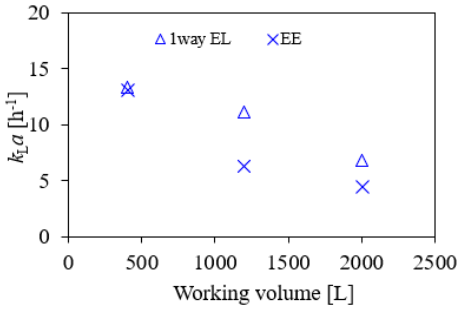

(c) Effect of the working volume

Figure 4.72: Impact of changes of a single operating parameter on the volumetric oxygen mass transfer coefficient k_La for the XDR-2000 with the other operating parameters at the intermediate value of 1200 L for the working volume, 65 rpm for the impeller speed, and 13.5 L min^{-1} for the sparging rate.

For the gas hold-up found in the EE simulations, the expected increase for higher impeller speeds is observed, which has already been presented above for the CR3, the XDR-10, and the XDR-200. In contrast to this, the average bubble residence and consequently obtained from the one-way coupled EL simulations, is slightly higher at the intermediate impeller speed of 65 rpm than at the maximum impeller speed of 105 rpm. Similar results have been presented above for the intermediate and maximum impeller speed of the XDR-500. For both the XDR-500 and the XDR-2000 this is related to the stronger horizontal dispersion of the bubbles at the maximum impeller speed, see Figs. 4.64c and 4.64b for the XDR-2000, due to which bubbles rise faster in the liquid up-flow region closer to the vessel wall. That the same effect is not observed with the EE simulations must be related to the impact of bubbles on the liquid motion. For the the intermediate impeller speed of 65 rpm are less dispersed horizontally and thus the bubbles are rising in a smaller region compared to the maximum impeller speed at 105 rpm, see Figs. 4.64e and 4.64f. The smaller rise region might result in a stronger wake acceleration similar to what has been described for bubble columns [165], where the acceleration of the liquid by the bubbles results in a higher rise velocity of the bubbles swarm compared to the rise velocity of a single bubble. This interpretation also matches with the observed increasingly stronger effect of a lower gas hold-up of the EE simulation compared to that of the one-way coupled EL simulations at the intermediate and maximum sparging rates, see Fig. 4.71.

The effects of the sparging rate, the impeller speed, and the working volume on the k_La are shown in Fig. 4.72a-c, respectively. Similar to the gas hold-up and the results for the other bioreactors presented above, the k_La increases with a higher sparging rate, a higher impeller speed, and a lower working volume, which is found for both the one-way coupled EL and EE simulations. The lower gas hold-up for the maximum impeller speed of 105 rpm compared to the intermediate impeller speed of 65 rpm observed for the one-way coupled EL simulations is compensated by the higher liquid transfer coefficient k_L at 105 rpm and consequently the k_La still increases.

4.5.5 Selection of Operating Conditions for Cell Cultivation

For the XDR-2000, the mixing times are quite high compared to the other bioreactors, since the XDR-2000 has the largest working volume out of all. To improve the mixing as much as possible, the impeller speed should be increased as much as possible, while still avoiding cell damage due to mechanical forces. Since even at 105 rpm the hydrodynamic stress is far below the critical values, the horizontal dispersion of the bubbles is better, and the k_La is higher, the highest considered impeller speed of 105 rpm appears to be the most favorable. The simulated k_La values are in the typical range for cell culture of 1 h^{-1} to 20 h^{-1} [18, 35] and adjusting the sparging rate through the dynamic process control, while operating at the maximum impeller speed is expected cover the oxygen requirements of most mammalian cell lines. Overall, the optimal operating window of the XDR-2000 is smaller than for the CR3, the XDR-10, the XDR-200, and the XDR-500 and focused around the maximum impeller speed of 105 rpm considered impeller speed. With the the operating range of impeller speed of 25 rpm to 115 rpm used in the supplier characterization [166], the capability to increase the impeller speed much further, i.e., beyond 115 rpm appears to be limited.

4.6 The Ambr® 250

The Ambr® 250 is a parallelized miniature stirred tank bioreactor system with a maximum working volume of 250 mL for the individual vessels. The Ambr® 250 that can be used for process screening [38, 15] and as a scale-down model [167, 168, 169, 53]. Analogous to the XDR-500, the hydrodynamic characterization of the Ambr® 250 through one-way coupled EL simulations is carried out with OpenFOAM [63] instead of MixIT [64]. Christopher Maske performed the simulations of Ambr® 250 for his Master thesis [170] at the Technical University of Munich, which was conducted in collaboration with Daiichi-Sankyo Europe. The simulations of the Ambr® 250 have been performed and supervised at Daiichi-Sankyo as an addition to the collaboration that enabled the present study.

4.6.1 Bioreactor Configuration

The single-use, rigid plastic vessel of the Ambr® 250 is available in different configurations with or without baffles and with either two Rushton turbine impellers or with two pitched-blade impellers [171]. The present study considers the configuration with four flat baffles at the walls extending over the full height of the bioreactor and with two pitched-blade impellers, which are shown in Fig. 4.81a. Each impeller has three blades and a diameter of 2.6 mm. The vessel has a circular cross section with a diameter of about 6 cm, that slightly increases with the vessel height. The maximum working volume is 250 mL for which the liquid height is 8.8 cm. A pH sensor and a sparging tube enter the reactor from the top.

Figure 4.73: Impellers of the Ambr® 250

Table 4.10: Operating conditions for the Ambr® 250.

Condition #	Impeller speed n [rpm]	Working volume V [mL]
1	150	100
2	400	100
3	650	100
4	150	175
5	400	175
6	650	175
7	150	250
8	400	250
9	650	250

4.6.2 Operating Conditions

The investigated operating conditions consist of all possible combinations of the three considered levels of working volume of 100 mL, 175 mL, and 250 mL and the three considered levels of impeller speed of 150 rpm, 400 rpm, and 650 rpm. The resulting nine different test conditions are listed in Tab. 4.10. Due to the small impeller diameter, the tip speed at the maximum impeller speed of 650 rpm is only 0.88 m s^{-1} and the Re_{imp} is 6574. At the minimum working volume of 100 mL, only the lower impeller enters the liquid, while the upper impeller is located in the head space. The residence time of the bubbles is evaluated for each combination of the working volume and impeller speed. Since the Ambr® 250 is only considered with one-way coupled Euler-Lagrange simulations, different sparging rates do not require separate simulations and a sparging rate of 5 mL min^{-1} is considered in the calculation of the volumetric oxygen mass transfer coefficient.

4.6.3 Grid Independence Study

Similar to the bioreactors presented above, a hexahedral grid in the bulk with truncation of the grid cells at the boundaries and increased refinement at the baffles, the impeller shaft, and the impeller blades is created. Grids with different resolutions have been tested and vertical and horizontal cuts of the grids are shown in Fig. 4.74. The sparging tube and the pH sensor entering the Ambr® 250 from the top are shown in front of the vertical cut plane to the left and the right of the impellers, respectively.

The grid with 4.6x10^6 cells is selected for further simulations based on less then 4 % deviation of the average velocity magnitude, turbulence kinetic energy, and turbulence kinetic energy dissipation rate to the finest investigated grid with 8.6x10^6 grid cells. For the lower working volumes of 100 mL and 175 mL the corresponding grid consist of 2.4x10^6 cells and 3.5x10^6 cells, respectively.

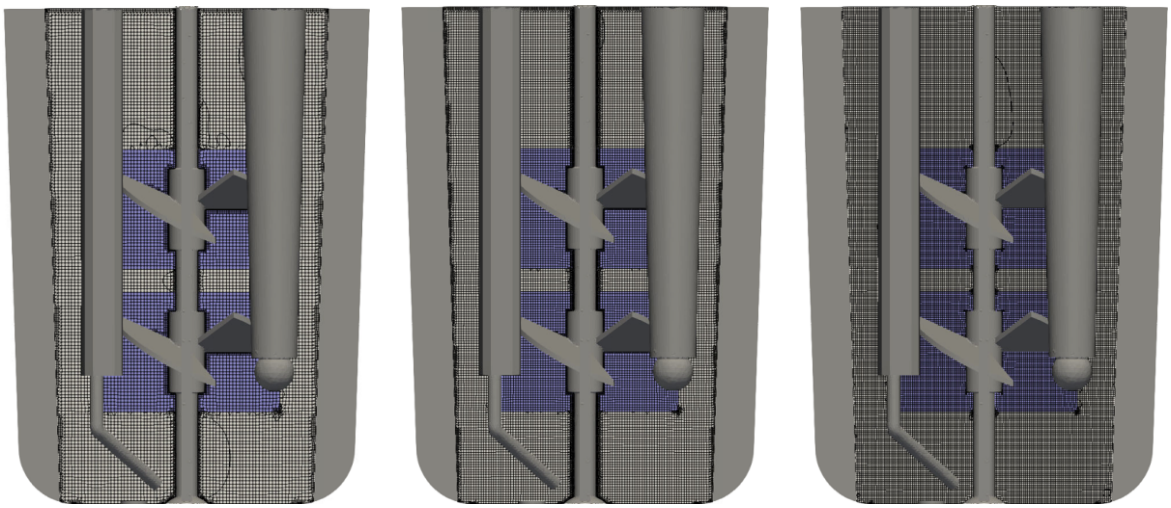

(a) Vertical cut through the grid. Left to right: 2.3x10^6, 4.6x10^6, and 8.6x10^6 grid cells.

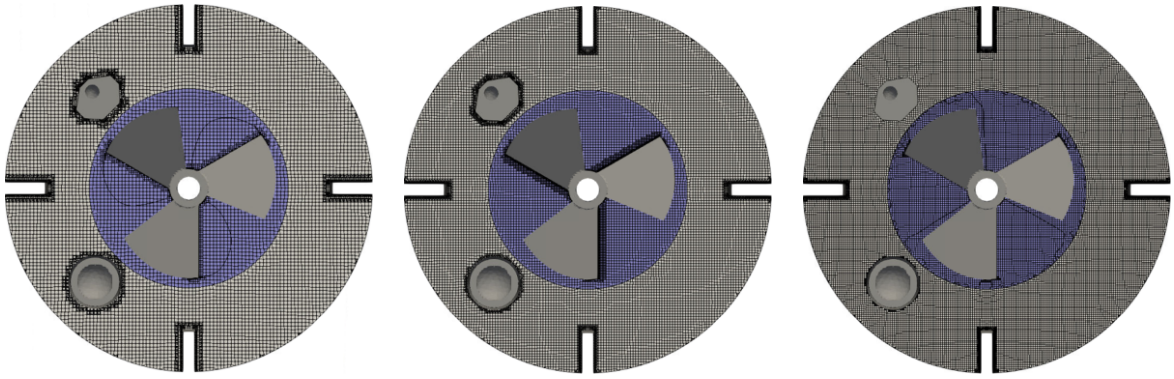

(b) Horizontal cut through the center of the lower impeller. Left to right: 2.3x10^6, 4.6x10^6, and 8.6x10^6 grid cells.

Figure 4.74: Computational grids for the Ambr® 250 considered in the grid study. The rotating reference frame regions are highlighted in blue.

4.6.4 Process Characterization

The flow structure and the bubble dispersion are presented first, followed by the description of the effect of the operating conditions on the cell culture relevant process characteristics.

Liquid Flow Field and Bubble Dispersion

The pitched-blade impellers of the Ambr® 250 are rotating in the up-pumping anti-clockwise direction. The liquid flow pattern for the considered working volumes of 100 mL, 175 mL, and 250 mL at the intermediate impeller speed of 400 rpm are shown in Fig. 4.75. The flow structure in the vertical cut plane shown in Fig. 4.75a is influenced by the working volume. At the minimum working volume of 100 mL only the lower of the two impellers is entering into the liquid and an axial flow pattern with up-flow in

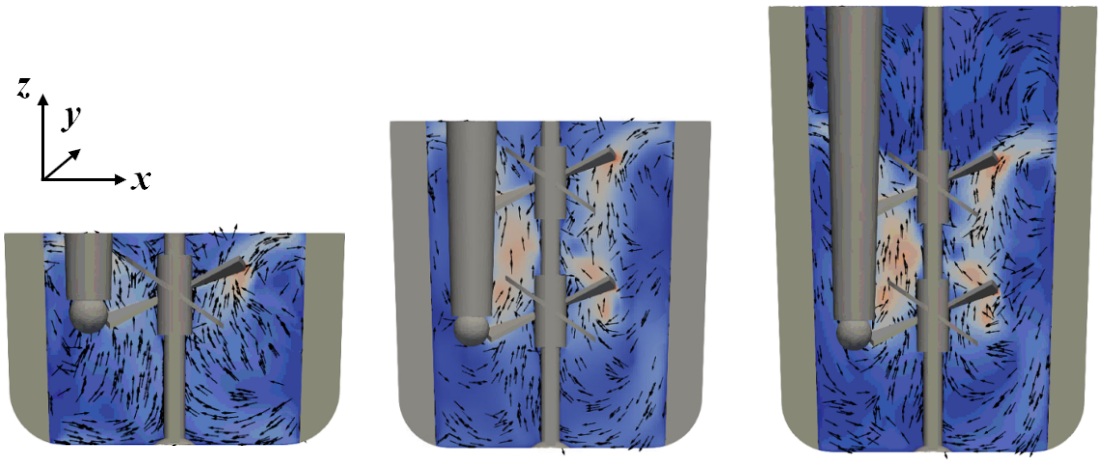

(a) Liquid velocity on the x-z plane through the center of the vessel. Arrows indicate the direction of the x-z velocity.

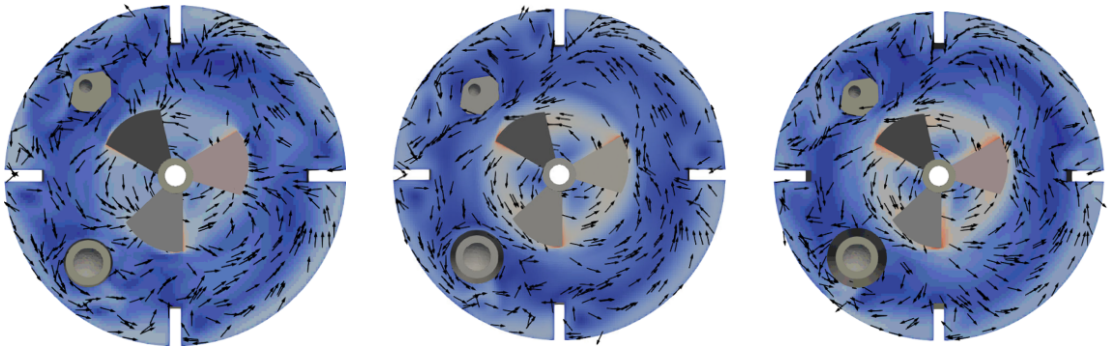

(b) Liquid velocity in the x-y plane trough the center of the lower impeller. Arrows indicate the direction of the x-y velocity.

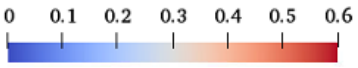

Figure 4.75: Liquid flow field for the Ambr® 250 for the working volumes of 100 mL, 175 mL, and 250 mL (left to right) at an impeller speed of 400 rpm on (a) a vertical cut plane and (b) a horizontal cut plane.

the center of the vessel and down-flow along the vessel wall is observed. This axial flow pattern is different to the radial one described by Li et al. [172] for the variant of the Ambr® 250 equipped with Rushton turbine impellers, which is in agreement with the expectations for the respective impeller types [20]. For 175 mL volume, there is also up-flow in the center and down-flow along the vessel wall, however, between the two impellers, there is also flow from the vessel wall towards the impellers disturbing the axial flow pattern. The same observation is made for the maximum working volume of 250 mL. The distance between the upper impeller for the intermediate and maximum working volume of 175 mL and 250 rpm, and for the minimum working volume of 100 mL the lower impeller, which is the only one entering the liquid, and the liquid

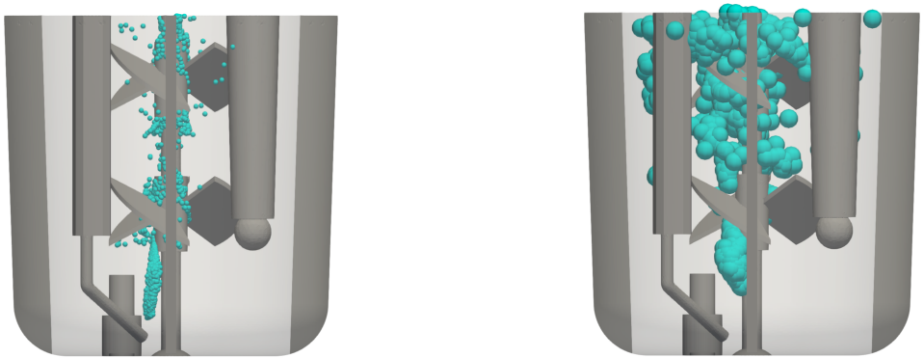

(a) Bubble diameter 1.00 mm

(b) Bubble diameter 3.59 mm

Figure 4.76: Bubble dispersion inside the Ambr® 250 for different bubble diameters at a working volume of 175 mL and an impeller speed of 400 rpm.

surface also has an effect on the liquid flow pattern. At 100 mL and 175 mL the distance between the liquid surface and the lower and upper impeller, respectively, is relatively small. Thus, the recirculation zone from above the impeller towards the center of the vessel is constrained to a small region directly above the impeller. For 250 mL, a larger recirculation zone than for the lower working volumes is formed by the up-flow from the impeller eject stream towards and along the vessel wall and down-flow from the liquid surface towards the center of the vessel.

The flow structure in the horizontal cut plane in Fig. 4.75b shows the expected dominant anti-clockwise motion of the liquid following the impellers' rotational motion. Behind the baffles small recirculation zones are formed. The flow pattern in the horizontal direction is quite similar for the different working volumes.

Gas is sparged into the Ambr® 250 from the single opening of the sparging pipe below the lower impeller. An initial bubble diameter of 3.59 mm is expected, based on the correlation of Jamialahmadi et al. [173]

$$\frac{d_\mathrm{b}}{d_\mathrm{o}} = \left[\frac{5}{\mathrm{Bo}_\mathrm{O}^{1.08}} + \frac{9.261\mathrm{Fr}^{0.36}}{\mathrm{Ga}^{0.39}} + 2.147\mathrm{Fr}^{0.51}\right]^{1/3} \tag{4.5}$$

where $\mathrm{Bo}_\mathrm{o} = \rho_\mathrm{l}\mathbf{g}d_\mathrm{o}^2\sigma^{-1}$ is the Bond number in terms of the sparger orifice, $\mathrm{Fr} = u_\mathrm{s}^2 d_\mathrm{o}^{-1}\mathbf{g}^{-1}$ the Froude number of the sparger orifice, and $\mathrm{Ga} = \rho_\mathrm{l}^2 d_\mathrm{o}^3 \mathbf{g}\mu_\mathrm{l}^{-2}$ the Galileo number of the sparger orifice, where u_s, σ, and μ_l are superficial velocity at the sparger, the surface tension and the dynamic viscosity of the liquid. However, the bubbles are rising directly past the impeller blades, where the turbulence is high and bubble break up is likely. The correlation by Calderbank et al. [174]

$$d_\mathrm{b} = 4.15\left[\frac{\sigma^{0.6}}{\left(\frac{P}{V}\right)^{0.4}\rho_\mathrm{l}^{0.2}}\right]\alpha_\mathrm{g}^{0.5} + 0.0009 \tag{4.6}$$

can be used to calculate the average bubble diameter based on the balance of break-up

and coalescence of the bubbles in the liquid and approaches a value of about 1 mm for low gas volume fractions and a high volumetric power input. Bubble positions for both diameters are shown in Fig. 4.76. The bubbles rise from the sparger towards the center of the lower impeller and further along the stirrer rod in the center of the vessel. There is some slight horizontal dispersion of the bubbles around the impellers but with little liquid motion in radial direction the majority of the bubbles remains close to the center of the vessel. This pattern is very similar for both of the considered bubble diameters.

Liquid Velocity, Turbulence, Volumetric Power Input, and Mixing Time

The average liquid velocity of the Ambr® 250 for the different impeller speeds is shown in Fig. 4.77a and increases with the impeller speed. From 175 mL to 250 mL the average liquid velocity decreases for the larger volume as expected. For the working volumes of 100 mL (black triangles) and 175 mL (blue triangles), the liquid velocity is very similar because additional liquid agitation is provided by the second impeller, which is only submerged at 175 mL. The turbulence kinetic energy also increases with the impeller speed and decreases for higher working volumes as shown in Fig. 4.77b. This is in agreement to the observations made for the other bioreactors and in contrast

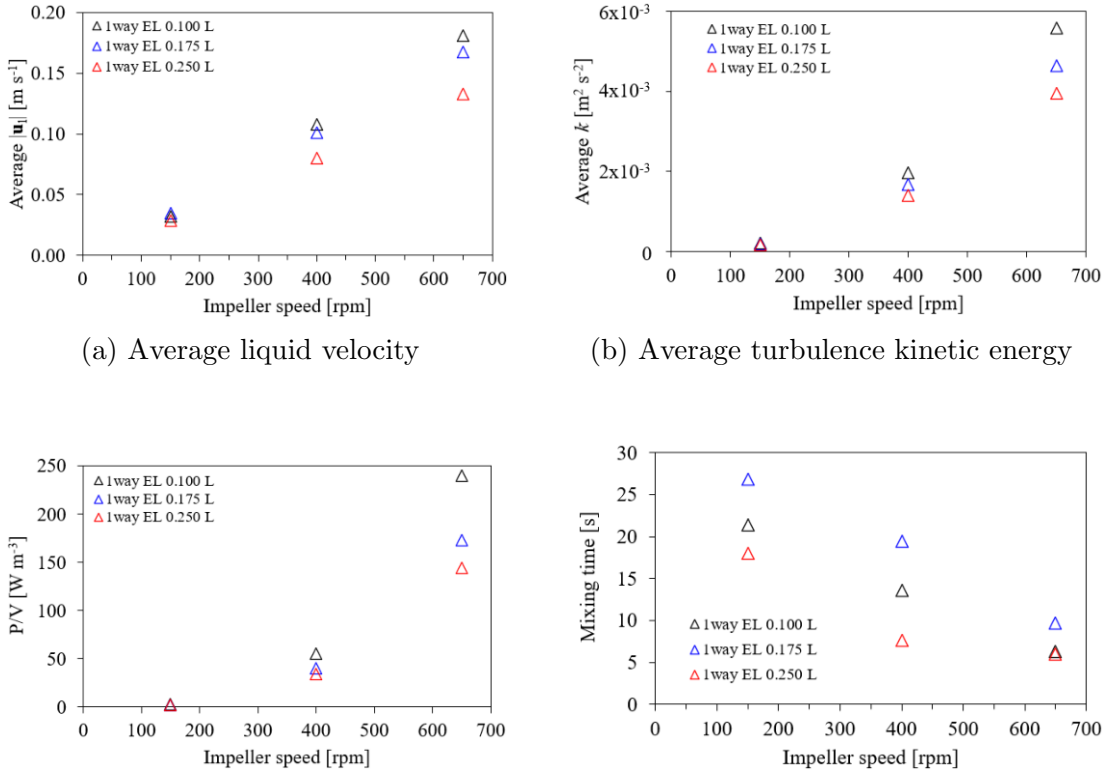

(a) Average liquid velocity

(b) Average turbulence kinetic energy

(c) Volumetric power input

(d) Mixing time

Figure 4.77: Average liquid velocity, average turbulence kinetic energy, volumetric power input P/V, and mixing time for the considered impeller speeds of 150 rpm, 400 rpm, and 650 rpm and working volumes of 100 mL, 175 mL, and 250 mL.

to the average velocity, the difference between the results for 100 mL and 175 mL is comparable to that between 175 mL and 250 mL.

Similar to the average velocity and the average turbulence kinetic energy, stronger agitation also leads to an increase in the volumetric power input, while a larger volume results in a decrease of the volumetric power input, which is shown in Fig. 4.77c. For a working volume of 100 mL, where only the lower impeller is submerged in the liquid, the average of the simulated power numbers for the different impeller speeds is 1.53 with a minimum value of 1.45 and maximum value 1.57. For the combination of both impellers for working volumes of 175 mL and 250 mL, the average power number across the considered operating conditions is 2.13 with a minimum value of 1.73 and maximum value 2.39, which is higher than for the single impeller but less than twice that of the single impeller. This is in agreement with observations reviewed by You et al. [175], who report that the power number of multiple impeller systems is less than the sum of power numbers of the individual impellers, if the impeller spacing is less than 1.5 d_{imp} as is the case for Ambr® 250 . The simulated power numbers are higher than the supplier specified value of 1.34 reported by Xu et al. [169]. Similar to the bioreactors presented above, the mixing time increases for lower impeller speeds. In contrast to the bioreactors presented above, the longest mixing time is found for the intermediate working volume of 175 mL, while for the largest volume of 250 mL it is shorter than for both 175 mL and 100 mL. This can only be explained by the differences in the liquid flow field, however, the exact reasons are difficult to identify. Most likely, the additional recirculation zone above the upper impeller at 250 mL working volume discussed previously improves the distribution of the tracer across the reactor cross-section and speeds up the mixing process.

Risk of Cell Damage

The volume fraction distribution of the strain rate and the hydrodynamic stress are shown in Fig. 4.78. The maximum strain rate is much higher than for the other considered bioreactor scales, even though the tip speed of 0.88 m s^{-1} for the highest considered impeller speed of 650 rpm is lower than for the larger bioreactors. The maximum hydrodynamic stress is similar or lower than that of the other presented bioreactor scales and does not indicate a risk of cell damage. The simulated maximum values of 4 Pa at 400 rpm and 8 Pa at 650 rpm of the present study for the configuration with two pitched-blade impellers are slightly lower than the experimental values of 5.4 Pa at 400 rpm and 13.8 Pa at 613 rpm for the configuration with two Rushton turbine impellers reported by Šrom et al. [38]. This indicates that the pitched-blade impellers provide slightly lower hydrodynamic stress.

As for all other bioreactors, the average strain rate and hydrodynamic stress increase with the impeller speed both for the impeller zone(s) and the tank zone. Similar to the maximum strain rate, the average strain rate of the Ambr® 250 is much higher than for all larger bioreactors, both in the impeller zone and in the tank zone, whereas the average hydrodynamic stress is comparable. This suggests that the impeller average strain rate proposed by Li et al. [23] as part of the criteria for cell culture scale-up, might not be applicable to the very small scale of the Ambr® 250. Based on the the

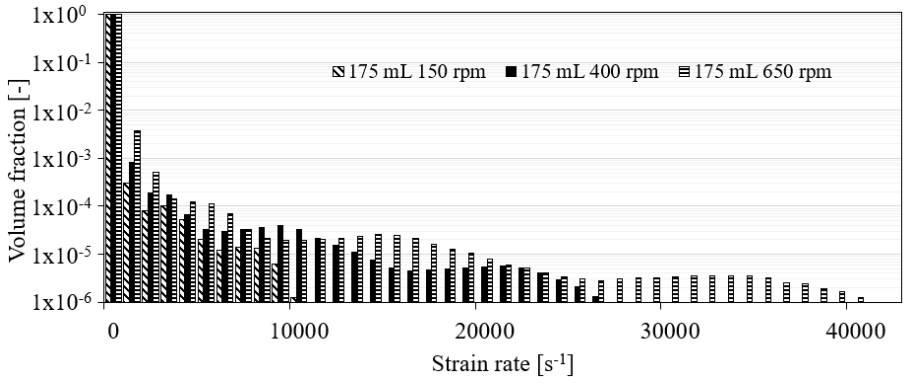

(a) Strain rate

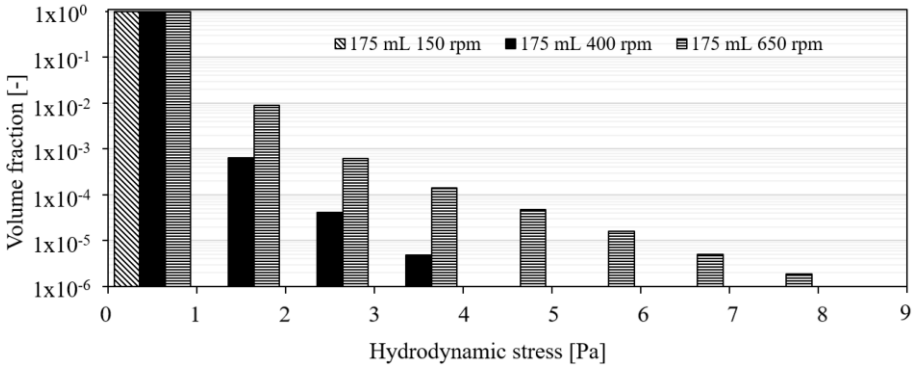

(b) Hydrodynamic stress

Figure 4.78: Volume fraction distributions of the strain rate and the hydrodynamic stress for the intermediate working volume of 175 mL and the impeller speeds of 150 rpm, 400 rpm, and 650 rpm.

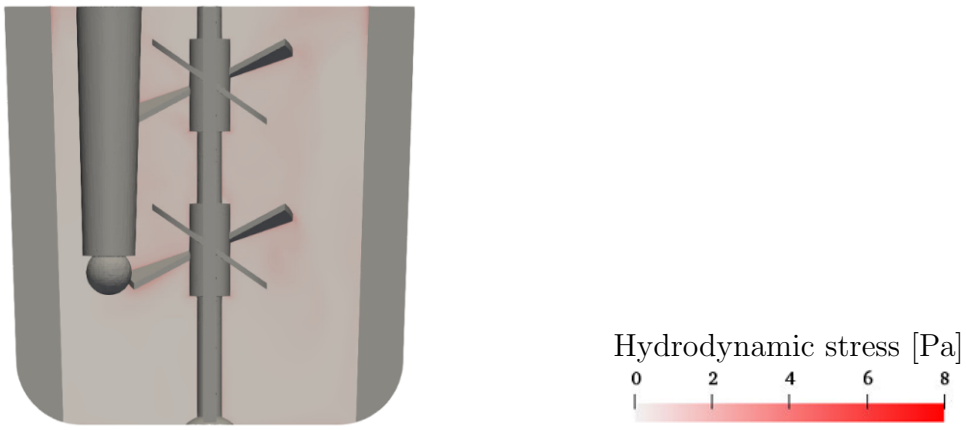

Figure 4.79: Hydrodynamic stress in the x-z plane through the center of the Ambr® 250 for the intermediate working volume of 175 mL and the highest impeller speed of 650 rpm.

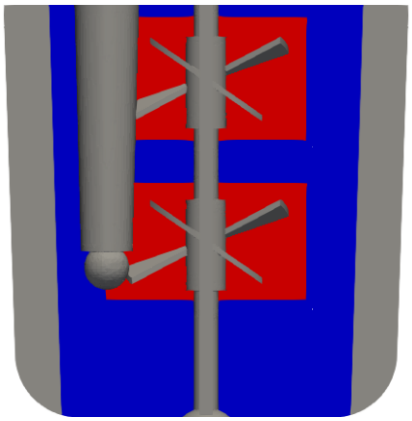

Figure 4.80: Impeller (red) and tank (blue) zones in the x-z plane through the center of the Ambr® 250 for the intermediate working volume of 175 mL.

maximum hydrodynamic stress limits by reported by Neunstoecklin et al. [47] no cell damage is expected. Figure 4.79 shows the hydrodynamic stress on a vertical cut plane through the center of the Ambr® 250. Similar to the other bioreactors presented above, the hydrodynamic stress is highest at the edges of the impeller blade. Intermediate values of hydrodynamic stress are observed in the high velocity region around and between the impellers and around the baffles, while low values are observed in the remaining liquid.

The average strain rate and hydrodynamic stress for the impeller and the tank zone are shown in Figs. 4.81a and 4.81b. The impeller zone in this case corresponds to the average of the two zones each centered on the respective impeller with a diameter of 1.2 d_{imp}, which is the same as for all other bioreactors. Due to the larger height of the impeller, the height of the impeller zone is increased from 0.33 d_{imp} to 0.75 d_{imp}, which corresponds to the height used by Li et al. [23] for 'Elephant Ear' impellers. The zones

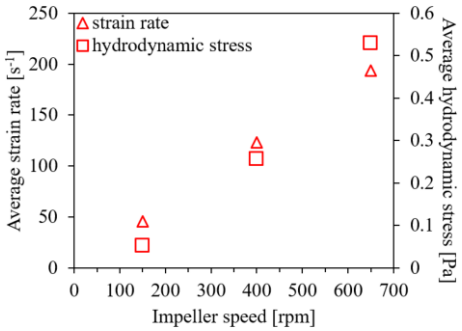

(a) Impeller zone

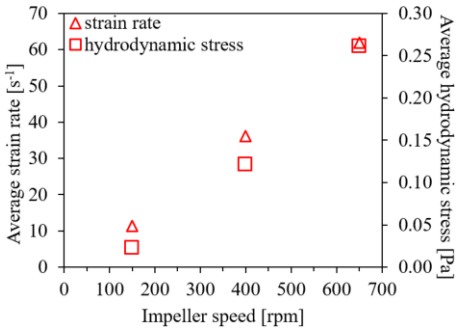

(b) Tank zone

Figure 4.81: Average strain rate (triangles) and average hydrodynamic stress (squares) for the impeller (left) and tank zone (right) of the Ambr® 250 for the intermediate working volume of 175 mL and the speeds of 150 rpm, 400 rpm, and 650 rpm.

are indicated on a vertical cut thought the center of the vessel in Fig. 4.80 with the impeller and tank zones shown in red and blue, respectively.

Bubble Residence Time and Volumetric Oxygen Mass Transfer Coefficient

The effect of the impeller speed on the average bubble residence time $t_{r,avg}$ and the volumetric oxygen mass transfer coefficient k_La is shown for the intermediate working volume of 175 mL in Figs. 4.82a and 4.82b. Overall, the impact of the impeller speed on $t_{r,avg}$ is minor, which is caused by the small liquid height and the lack of horizontal dispersion of the bubbles. For both considered bubble diameters, $t_{r,avg}$ is slightly reduced for the increase in impeller speed from 150 rpm to 400 rpm but $t_{r,avg}$ for 650 rpm is longer than for 400 rpm. In contrast to $t_{r,avg}$, the k_La increase with the impeller speed due to the higher k_L at a higher impeller speed. The increase in k_La is more pronounced for the smaller bubble diameter of 1.00 mm but also observed for 3.59 mm.

The effect of the working volume on $t_{r,avg}$ and k_La is shown for the intermediate impeller speed of 400 rpm in Figs. 4.82c and 4.82d. Due to the increased liquid height, the $t_{r,avg}$ increases for a larger working volume for both of the considered bubble diameters, whereas the volumetric oxygen mass transfer coefficient shows only slight variation for the different working volumes. Xu et al. [169] report a k_La of 1.5 h^{-1}

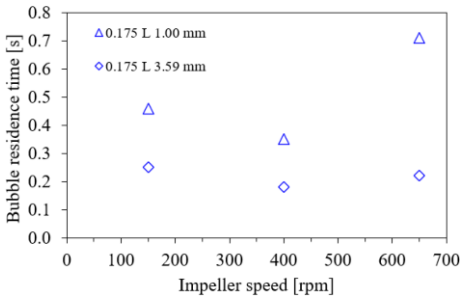

(a) $t_{r,avg}$ for 175 mL

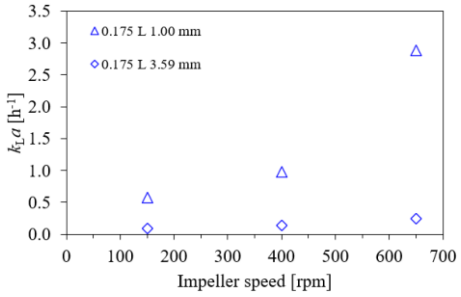

(b) k_La for 175 mL

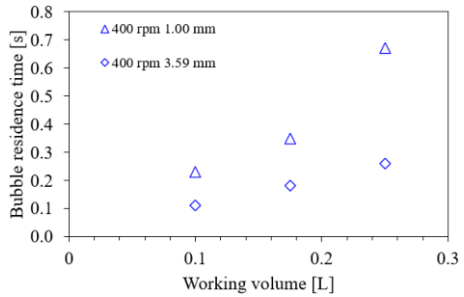

(c) $t_{r,avg}$ for 400 rpm

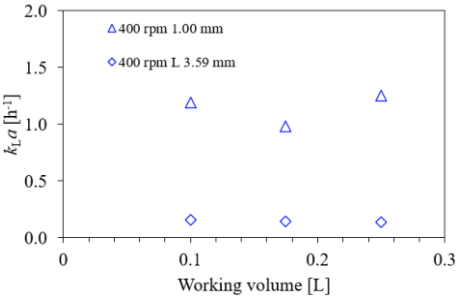

(d) k_La for 400 rpm

Figure 4.82: Bubble residence time and k_La at the intermediate working volume of 175 mL (top) and at the intermediate impeller speed of 400 rpm (bottom). The k_La is calculated for a sparging rate of 5 mL min^{-1}. The bubble diameters of 1.00 mm and 3.59 mm are indicated by triangles and diamonds, respectively.

for a working volume of 200 mL and an impeller speed of 350 rpm with a submerged sparging of 5 mL min^{-1}. For the most similar condition of the present study with a working volume of 175 mL and an impeller speed of 400 rpm the simulated k_La values are 0.98 h^{-1} for a bubble diameter of 1.00 mm and 0.14 h^{-1} for a bubble diameter of 3.59 mm. The comparison of the k_La values indicates that a bubble diameter of 1.00 mm or less should be expected in the Ambr® 250.

4.6.5 Selection of Operating Conditions for Cell Cultivation

Based on the present characterization results on the hydrodynamic stress and the cell culture results reported by Šrom et al. [38], no cell damage is expected up to the highest considered impeller speed of 650 rpm. Despite the small volume, the mixing times of the Ambr® 250 are comparable to those of the CR3 and the XDR-10 and are reduced by increasing the impeller speed. The simulated k_La values for the Ambr® 250 are lower than those for other bioreactors considered in the present study, which is related to the use of the open pipe sparger instead of a microporous spargers. Both for the k_La and the mixing time, the highest considered impeller speed of 650 rpm provides the best conditions.

5. Selection of Operating Conditions for Scale-Up

So far, the presented results were focused on the characterization of the individual bioreactors and the selection of optimal operating conditions for each of them. This section is now focused on comparing the characterization results of the XR3, the XDR-10, the XDR-200, and the XDR-2000 to obtain a comprehensive picture on how a cell culture process developed with the CR3 can be scaled-up. In essence, the three process goals of fast mixing, low mechanical stress (to avoid damage to the cultivated cells), and sufficient oxygen transfer that have been discussed for the individual bioreactors are also guiding the selection of the operating conditions for scale-up. However, the ease or the difficulty with which suitable cultivation conditions can be achieved changes between the bioreactors due to their different sizes and configurations. The quantitative data on the hydrodynamic characteristics collected in the previous chapters is used to evaluate the scale-up of a cell culture process using the investigated bioreactors.

As has been summarized in section 1.2 different scale-up criteria can be found in the literature but no universal scale-up strategy has been identified so far. The points below summarize the general findings on the effect of the operating parameters on the cell culture relevant process characteristics for the individual bioreactors. This evaluation forms the basis for how the different operating parameters are prioritized during scale-up:

Working volume

- major impact on the mixing
- minor impact on the $k_{\mathrm{L}}a$
- no effect on the risk of cell damage due to mechanical force
- must be maximized for a optimal final product amount

Impeller speed

- major impact on the mixing
- major impact on the $k_{\mathrm{L}}a$
- major impact on the risk of cell damage due to mechanical force

- must balance the contradicting goals of fast mixing and low mechanical force

Sparging strategy

- minor impact on the mixing
- sparger type and sparging rate need to be considered in combination
- major impact on the $k_{\mathrm{L}}a$
- minor impact on the risk of cell damage due to mechanical force
- must match the oxygen mass transfer to the changing cell culture requirements

The working volume has a strong impact on the economic aspects of the cell cultivation, since the total product amount depends on the final volume and the final product concentration of the last cultivation step. As is evident from Eq. (4.4), a lower working volume will only increase the total product amount if the final product concentration strongly increases. For example, operating at half the maximum volume will only result in a higher final product amount, if the product concentration is more than doubled. While the working volume is usually not a parameter used for process optimization, it is important to be aware that the volumetric power input and the liquid height are affected by the working volume. In line with the observations described in the previous chapters and the established empirical correlations [20, 13, 46], this means that the working volume has an impact on both mixing and $k_{\mathrm{L}}a$. The further evaluation of the operating parameters focuses on the impeller speed and the sparging strategy, while the working volume is fixed to the intermediate level, which is representative of the early and intermediate stages of fed-batch cultivations.

The observation of a higher impeller speed, which also corresponds to a higher volumetric power input, improving the mixing and the oxygen transfer but at the same time increasing the hydrodynamic stress are in agreement to the results and empirical correlations reported in the literature [20, 13, 44, 23, 46]. Since the impeller speed has a major impact on all hydrodynamic characteristics relevant for cell culture, whereas the sparging strategy mainly impacts the oxygen transfer, the selection of the impeller speed is considered before the sparging strategy. For the selection of the impeller speed, a constant volumetric power input across different scales is one of the most commonly used criteria [20, 51, 41]. However, Xing et al. [29] report issues with inhomogeneities and reduced $k_{\mathrm{L}}a$ when scaling up form 5 L to 5000 L even when using a four times higher volumetric power input. Yang et al. [26] evaluate the impeller tip speed, as well as the shear rate at the impeller tip, the circulation time, and the mixing time obtained from empirical correlations as potential criteria for selecting the impeller speed to scale-up a cell culture process from 3 L to 2500 L. However, due to impractically low or high values of the impeller speed obtained for these criteria Yang et al. [26] use a constant impeller speed of 65 rpm for all larger scales, i.e., 75 L, 300 L, and 2500 L, and 50 rpm for the 3 L scale in their cell culture experiments. Neunstoecklin et al. [30] successfully verified that the maximum hydrodynamic stress limits derived from a 3 L testing equipment [47] explained the growth and metabolite profiles observed for a

cultivation of Sp2/0 cells in a 300 L bioreactor. Li et al. [23] report the successful scale-up from 7.5 L to 1000 L of a cell culture process with *Spodoptera frugiperda* Sf9 insect cells based on a three-dimensional space of the average strain rate within the impeller zone, the tank zone, and the complete liquid.

Once the impeller speed is fixed, the sparging rate and sparger type as well as the composition of the sparged gas can be optimized with minimal impact on the mixing and the mechanical forces in the liquid. The opposite approach of fixing the sparging rate for example based on the volumetric sparging rate and then adjusting the impeller speed to adjust the has also been reported for scaled-up studies with focus on controlling the dissolved carbon dioxide concentration [41, 53]. Before providing a case study on the scale-up, the impact of the different bioreactor scales investigated in the present study on the mixing time, the average hydrodynamic stress as well as the average strain rate of the impeller zone, and the $k_L a$ are summarized.

5.1 Impact of the Bioreactor Scale

This chapter summarizes how the three important process aspects of the mixing, the risk of cell damage due to mechanical force, and the oxygen mass transfer change for different bioreactor scales.

Figure 5.1 shows the mixing time across the different impeller speeds for the intermediate working volumes of 1.7 L, 7.0 L, 120 L, and 1,200 L as well as the intermediate sparging rates of 0.05 L min^{-1}, 0.25 L min^{-1}, 5.0 L min^{-1}, and 13.5 L min^{-1} for the CR3, XDR-10, XDR-200, and XDR-2000, respectively. Similar to the longer mixing times at a larger working volume observed for the individual bioreactors as described in Sects. 4.1.4, 4.2.4, 4.3.4, and 4.5.4, the mixing time also increases for a larger bioreactor scale. At the same time, the mixing time at each scale depends on the impeller speed, allowing to control the mixing time within a certain range.

Figure 5.1a shows the mixing times across the considered impeller speeds. At a similar impeller speed, the mixing times for the XDR-200 and XDR-2000 are clearly

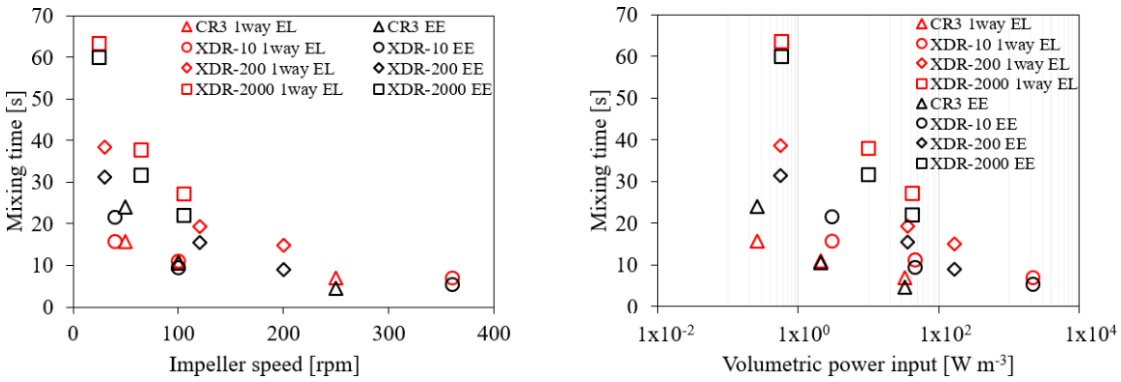

(a) t_m over n (b) t_m over P/V

Figure 5.1: Mixing times t_m for different impeller speeds n and volumetric power inputs P/V.

higher than for the CR3 and XDR-10 for which the mixing times are similar. Based on empirical correlations [20, 150], the mixing time for geometrically similar stirred tank reactors increases for larger reactor scales if the volumetric power input is kept constant. Consequently, to maintain a constant mixing time, a higher volumetric power input is required for larger bioreactors scales. Moreover, for a constant bioreactor volume and power input, a larger impeller diameter to vessel diameter ratio $d_{\mathrm{imp}}/d_{\mathrm{V}}$ results in faster mixing. However, Greenfield [176] reported that at a given volume for a constant volumetric power input and size ratio the mixing time is independent of the impeller type. The volumetric power input can be obtained from the power number and the impeller diameter [20] as

$$P/V = \frac{N_{\mathrm{P}} \rho_{\mathrm{l}} n^3 d_{\mathrm{imp}}^5}{V} \tag{5.1}$$

and is calculated throughout Sect. 5 according to the supplier specified power numbers of 0.3, 1.5, 1.15, and 0.72 for the CR3, XDR-10, XDR-200, and XDR-2000, respectively, since this would be the information typically at hand for the operator of the bioreactor. The simulated volumetric power input slightly deviates from the supplier specification as described in the previous chapter. The volume used to determine the P/V is the intermediate working volume, because this is the volume for which the mixing times have been evaluated.

Figure 5.1b shows the mixing times for the corresponding values of the volumetric power input. The increasing mixing times for larger bioreactor scales found in the present study is in agreement with the effects reported in the literature, which are discussed in the previous paragraph even though geometric similarity is not maintained. The data in Fig. 5.1b indicates that the similar mixing times for CR3 and XDR-10 are not only related to the smaller differences in bioreactor sizes and working volumes compared to the XDR-200 or XDR-2000, but also to the higher volumetric power input for the XDR-10 compared to the CR3. A higher volumetric power input is required, even though the XDR-10 has a slightly larger $d_{\mathrm{imp}}/d_{\mathrm{V}}$ of 0.67 compared to 0.56 for the CR3. For the XDR-200 and the XDR-2000 with $d_{\mathrm{imp}}/d_{\mathrm{V}}$ of 0.39 and 0.34, respectively, the difference in size to the CR3 is even larger and the mixing times are even higher than for the CR3 and the XDR-10. Consequently, the volumetric power input must be increased even further to achieve the mixing times similar to those of the CR3. In summary, a constant mixing time can only be achieved, if the difference in the size of the considered bioreactors is small or if extremely high and low values of impeller speed and volumetric power input are used for the large and small scales, respectively. Accordingly, the mixing time is a parameter that is strongly affected by the bioreactor scale and may be difficult to use as a scale-up criterion. Furthermore, while mixing is considered important for scale-up [24, 31, 13] for mammalian cells with lower cell densities and metabolic rates, issues due to insufficient mixing are related to fluctuations of the nutrient concentration and the pH caused by the addition of feed and base solutions. These issues can (at least partially) be addressed by other means such as adjusting the concentration of the added solutions, adjusting the time intervals of the addition, or changing the location of the addition.

In addition to the mixing, the risk of cell damage due to mechanical forces is another important aspect that strongly depends on the impeller speed. Various parameters can be found in the literature [12, 74, 13, 23] to quantify the mechanical force acting on the cultivated cells including the maximum or average energy dissipation rate, the Kolmogorov length scale, the strain rate, the shear stress, and the hydrodynamic stress. As discussed in Sect. 4.1.4, the present study focuses on the hydrodynamic stress and the strain rate. In the present study, the reported maximum hydrodynamic stress is the upper limit of the highest bin of the volume fraction distributions reported in Sects. 4.1.4, 4.2.4, 4.3.4, and 4.5.4. In Fig. 5.2a the maximum hydrodynamic stress is plotted against the impeller tip speed $u_{\mathrm{tip}} = \pi d_{\mathrm{imp}} n$, since u_{tip} is the parameter typically used in empirical correlations to calculate the maximum stress [44]. In agreement to the literature [74, 30, 44], an increase of the maximum hydrodynamic stress with the impeller tip speed can be observed. In Fig. 5.2b the average strain rate of the impeller zone is also plotted over of the impeller tip speed. In agreement to the results of Li et al. [23], the average strain rate of the impeller zone increases with the impeller tip speed. The CR3 has the smallest impeller diameter and consequently, the range of

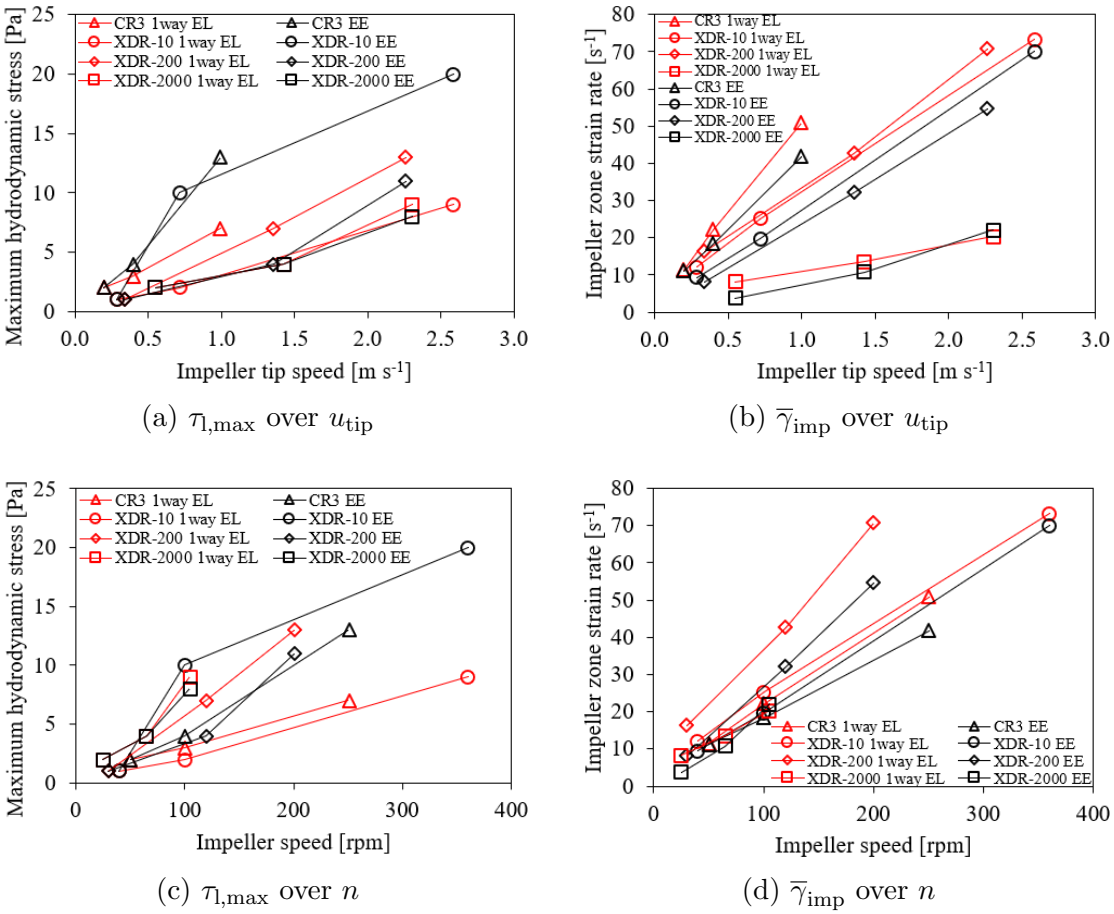

(a) $\tau_{\mathrm{l,max}}$ over u_{tip}

(b) $\overline{\gamma}_{\mathrm{imp}}$ over u_{tip}

(c) $\tau_{\mathrm{l,max}}$ over n

(d) $\overline{\gamma}_{\mathrm{imp}}$ over n

Figure 5.2: Maximum hydrodynamic stress $\tau_{\mathrm{l,max}}$ and average strain rate of the impeller zone $\overline{\gamma}_{\mathrm{imp}}$ for the different impeller speeds n and impeller tip speeds u_{tip}. Connecting lines are added to better indicate the individual data series.

the impeller tip speed is smaller than for the larger bioreactors with larger impeller diameters. The opposite is the case when the impeller speed in revolutions per minute (rpm) is considered where the considered range of the impeller speed for the XDR-2000 is the smallest. The maximum hydrodynamic stress and the average strain rate of the impeller zone are directly plotted against the impeller speed in Figs. 5.2c and 5.2d. The ranges of the observed maximum hydrodynamic stress show a larger overlap for the CR3 and the XDR-2000, with an even wider range covered by the two intermediate scales, the XDR-10 and the XDR-200. The impeller average strain rate of the XDR-2000 is slightly lower than of the CR3, the XDR-10, and the XDR-200. While at all scales the maximum hydrodynamic stress and the impeller zone average strain rate increase with the impeller speed as well as the impeller tip speed, the results shown in Fig. 5.2 indicate different slopes and the need to be fit separate correlations for each of the considered bioreactors. Consequently, while a constant maximum hydrodynamic stress or average strain rate of the impeller zone can likely be maintained during scale-up, they first must be evaluated for each of the considered bioreactors and cannot substituted by a comparison of the impeller speeds or tip speeds.

The third important process aspect for cell culture is the oxygen mass transfer. The amount of oxygen needed during the cultivation increases with the number of cells and an insufficient maximum oxygen transfer results in a reduced maximum cell density. The k_La depends on the agitation by the impeller and the sparging rate. The two options for a scale independent representation of the sparging rate are the volumetric sparging rate $Q_V = Q/V$ and the superficial gas velocity $u_s = 4Q/(\pi d_V^2)$, which are the sparging rate divided by the working volume and the cross-sectional area of the bioreactor, respectively. Figures 5.3a and 5.3b summarize the k_La for the different bioreactor scales at the intermediate working volume of 1.7 L, 7.0 L, 120 L, and 1,200 L and impeller speeds of 100 rpm, 100 rpm, 120 rpm, and 65 rpm, for the CR3, the XDR-10, the XDR-200, and the XDR-2000, respectively. The selected conditions

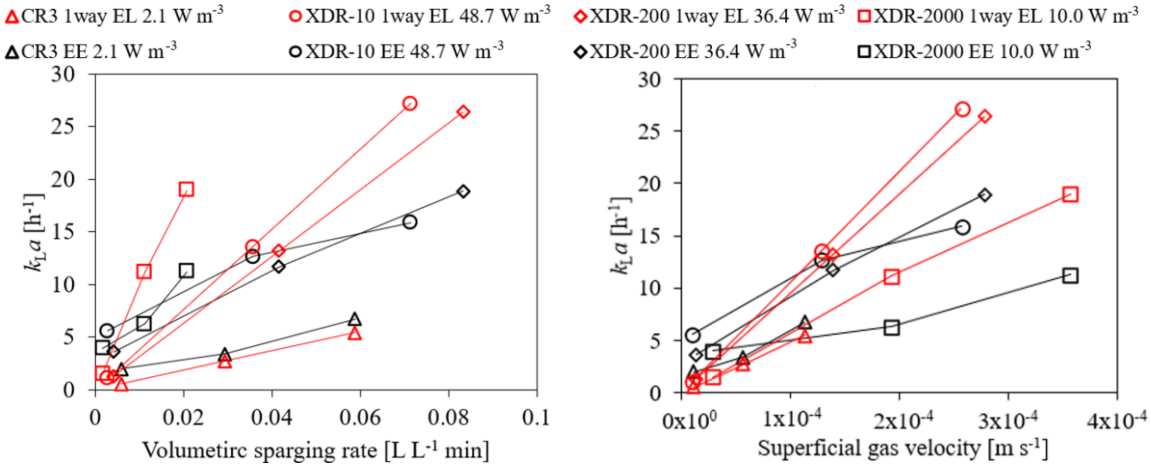

(a) k_La over Q_V (b) k_La over u_s

Figure 5.3: k_La for the considered volumetric sparging rates Q_V and superficial gas velocities u_s. Connecting lines are added to better indicate the individual data series.

with the intermediate working volumes and impeller speeds correspond to different volumetric power inputs of 2.1 W m^{-1}, 48.7 W m^{-3}, 36.4 W m^{-3}, and 10 W m^{-3} for the CR3, the XDR-10, the XDR-200, and the XDR-2000, respectively. A higher volumetric power input is expected to provide a better k_La if the same specific interface area is achieved due to a higher liquid transfer coefficient and thus the results for the different bioreactors cannot be compared directly. The expectation of a higher k_La for a higher volumetric power input at a similar superficial gas velocity in Fig. 5.3b, matches with the observations for the one-way EL simulations across all considered superficial gas velocities. For the EE simulations, this is only correct for low superficial gas velocities, while at values of 1.9x10^{-4} m s^{-1} or higher the k_La does not increase linearly for the XDR-10 and the XDR-2000 and consequently the observed k_La values are lower. A diminishing increase of k_La for high sparging rates or superficial gas velocities is in agreement with experimental observations for the XDR-10 and have been discussed in the Sect. 4.2.4. For the considered operating conditions, the observed maximum k_La values is lowest for the smallest considered bioreactor, the CR3. Consequently, no problems with achieving the required k_La for the XDR-10, the XDR-200, or the XDR-2000 are expected. For all considered bioreactors, microporous spargers are used, which generate smaller bubbles since they provide a larger number of orifices with a smaller size than drilled hole or open pipe spargers. As a consequence, for the same sparging rate, microporous spargers provide higher k_La values than drilled hole or open pipe spargers.

While the present section provided an overview how the relevant process aspects are affected by the bioreactor scale, the next section focuses on the selection of the operating conditions for the scale-up from the CR3 to the XDR-10, the XDR-200 and the XDR-2000.

5.2 Selection of the Impeller Speed for Scale-Up

During scale-up, the impeller speed must balance two competing goals: avoiding cell damage by mechanical stress and achieving fast homogenization of solutes in the liquid. A qualitative depiction of this goals is provided by Fig. 5.4, where the mechanical stress is represented by the average strain rate of the impeller zone and the homogenization is represented by the mixing time. The optimal case is fast mixing at low mechanical stress, which is indicated by the green region in the bottom left corner. For high values of the mixing time, which are associated with low impeller speeds, and for high values of mechanical stress, which are associated with high impeller speeds, reduced cell growth, cell viability and productivity must be expected. The results for the different bioreactors considered in the present study already indicate that smaller bioreactors like the CR3 and XDR-10 (triangles and circles in Fig. 5.4) are closer to the optimal process conditions than the XDR-200 and XDR-2000 (diamonds and squares).

The difficulties with providing hard quantitative limits into this qualitative analysis stem from two sources: on the one hand, the negative effects of sub-optimal mixing on the cell growth and productivity increase gradually and data on cell line specific tolerances mechanical stress is sparse [47, 38]. On the other hand, quantitative

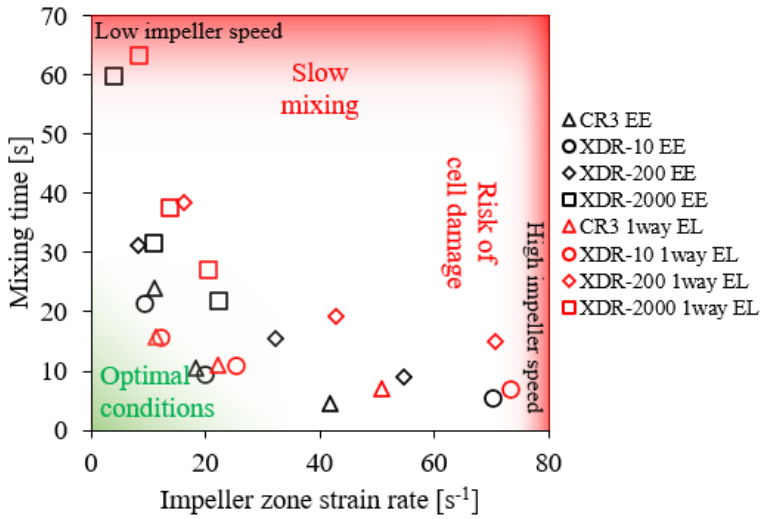

Figure 5.4: Average strain rates of the impeller zone and associated mixing times.

data on spatially resolved stress criteria and the maximum stress as well as the mixing time require a characterization of each of the considered bioreactors through simulations or experiments. While empirical correlation exist to calculate relevant process characteristics based on the operating conditions, the coefficients of these correlations need to be fitted to the characterization results of each individual bioreactor and are not universally applicable. In the present study, the impeller speed for the larger bioreactor scales is selected through the following three steps:

1. Identify a correlation for the selected scale-up criterion with the impeller speed
2. Identify the target value or range for the selected scale-up criterion
3. Use the identified correlation to determine the required impeller speed for matching the target range

These steps can be applied to all potential scale-up criteria that mainly depend on the impeller speed, i.e., the mechanical stress in the impeller region or the mixing time for a fixed volume. Since different scale-up criteria might provide deviating results, keeping the maximum mechanical stress below the maximum limit is selected as the primary goal and fast mixing as the secondary goal. Satisfying the oxygen requirements of the cultivated cell lines is equally important and corresponds to maintaining a constant $k_{\mathrm{L}}a$ across the scales. The $k_{\mathrm{L}}a$ can be controlled through an appropriate sparging strategy after the impeller speed has been selected and is discussed separately.

5.2.1 Correlations for the Potential Scale-Up Criteria

There are two general options for obtaining the correlations between the operating conditions and the scale-up criteria: one approach is to apply a design of experiments type of analysis to identify correlations without any prior knowledge on which kind of correlations is expected. Another option is to take empirical correlations established

in the literature [20, 44, 46, 23] and fit the coefficients to the characterization results of the newly investigated bioreactors. The second approach requires less data than a design of experiments study, since the number of values must only be as high as the number of the coefficients that need to be fitted. However, the accuracy and reliability of the fitted coefficients increases with the number of values used. In the present study, the second approach is taken and the parameters are fitted by minimizing the sum of the squared errors in MATLAB [144] using the *fminsearch*f function, which is an implementation of the Nelder-Mead Simplex algorithm [177].

The scale-up criteria considered by Neunstoecklin et al. [30] and Li et al. [23] are the maximum hydrodynamic stress and the average strain rate of the impeller zone, respectively. These two are selected in the present study as the two potential scale-up criteria that represent the mechanical stress on the cells suspended in the liquid. The hydrodynamic stress is derived from the turbulence energy dissipation rate and thus depends on the accuracy of the turbulence model, while the latter is derived from the velocity gradients of the Reynolds averaged velocities. The reported linear correlations of the maximum shear rate $\gamma_{\mathrm{l,max}}$ with the impeller speed n in the review by Chisti [44] and the average strain rate of the impeller zone $\overline{\gamma}_{\mathrm{imp}}$ with the impeller tip speed found by Li et al. [23] are the basis for selecting a linear correlation type for the $\tau_{\mathrm{l,max}}$ and $\overline{\gamma}_{\mathrm{imp}}$ in the present study. The impeller speed n is related to the impeller tip speed u_{tip} through $u_{\mathrm{tip}} = \pi d_{\mathrm{imp}} n$ and in the present study fitted coefficients for the impeller speed are reported. Accordingly, correlations for both $\tau_{\mathrm{l,max}}$ and $\overline{\gamma}_{\mathrm{imp}}$ are fitted as linear functions of n as per Eqs. 5.2 and 5.3

$$\tau_{\mathrm{l,max}} = k_{\tau}\, n \tag{5.2}$$

$$\overline{\gamma}_{\mathrm{imp}} = k_{\gamma_{\mathrm{imp}}}\, n \tag{5.3}$$

where k_{τ} and $k_{\gamma_{\mathrm{imp}}}$ are the respective model coefficients. The values of the fitted coefficients, the RMSE, and the R^2 values for the respective bioreactors and modeling

Table 5.1: Fitted coefficients, Root Mean Square Error (RMSE), and R^2 values for Eq. (5.2) and Eq. (5.3).

Bioreactor	Modeling approach	Fit for Eq. (5.2)			Fit for Eq. (5.3)		
		k_{τ}	RMSE	R^2	$k_{\gamma_{\mathrm{imp}}}$	RMSE	R^2
CR3	one-way EL	0.0287	0.35	0.9972	0.2067	1.20	0.9994
	EE	0.0500	0.71	0.9950	0.1698	1.78	0.9998
XDR-10	one-way EL	0.0246	0.28	0.9961	0.2080	3.47	0.9992
	EE	0.0584	2.59	0.9035	0.1952	0.93	0.9997
XDR-200	one-way EL	0.0627	0.65	0.9988	0.3575	3.29	0.9972
	EE	0.0490	1.32	0.9334	0.2720	0.33	0.9997
XDR-2000	one-way EL	0.0791	0.77	0.9423	0.2027	1.94	0.9660
	EE	0.0724	0.48	0.9643	0.1962	1.56	0.9820

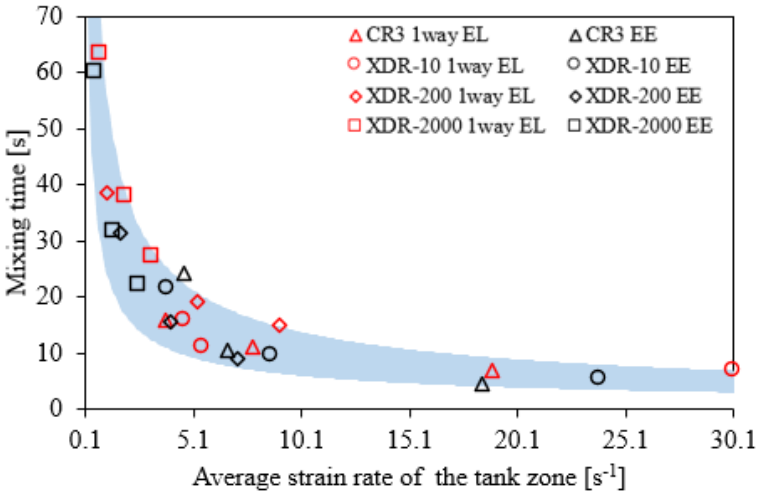

Figure 5.5: Average strain rate of the tank zone and corresponding mixing times.

approaches are reported in Tab. 5.1. Especially for the maximum hydrodynamic stress of the CR3 and the XDR-10, there is strong deviation in the obtained coefficients for the maximum hydrodynamic stress, which is also evident in Fig. 5.2c. This is caused by the effect of the bubble motion on the liquid turbulence, which has been described in sections 4.1.4 and 4.2.4.

The mixing time and average strain rate of the tank zone are considered as potential scale-up criteria, that represent hydrodynamic characteristics of the complete working volume. As discussed in Sect. 4.1.4, the mixing time $t_\mathrm{m} \propto (P/V)^{-1/3}$ [20, 13], which through the definition of the power number corresponds to a correlation with the inverse of the impeller speed $t_\mathrm{m} \propto n^{-1}$. Consequently, the model parameter k_{t_m} is fitted to provide a linear correlation of the t_m with n^{-1} according to Eq. (5.4). The values of the fitted coefficients and the R^2 values for the different bioreactors and modeling approaches are reported in Tab. 5.2. In addition to t_m, the average strain rate of the tank zone $\overline{\gamma}_\mathrm{tank}$, which has been reported by Li et al. [23] in combination with $\overline{\gamma}_\mathrm{imp}$ as a second required scale-up criterion, is also considered.

$$t_\mathrm{m} = k_{t_\mathrm{m}}\, n^{-1} \tag{5.4}$$

$$\overline{\gamma}_\mathrm{tank} = k_{\gamma_\mathrm{tank}}\, n \tag{5.5}$$

The value of $\overline{\gamma}_\mathrm{tank}$ represents how well the liquid bulk is agitated by the impeller. When plotting the mixing time and the strain rate of the considered operating conditions against each other, a comparable $\overline{\gamma}_\mathrm{tank}$ is observed to correspond to a similar t_m across all considered bioreactor scales, irrespective of the modeling approach, as indicated by the blue region in Fig. 5.5. Thus, $\overline{\gamma}_\mathrm{tank}$ is selected as a second scale-up criterion that could potentially substitute t_m. Similar to $\overline{\gamma}_\mathrm{imp}$, the linear correlation of $\overline{\gamma}_\mathrm{tank}$ with u_tip reported by Li et al. [23] is the basis for selecting a linear correlation as per Eq. (5.5). The fitted coefficients for $\overline{\gamma}_\mathrm{tank}$ for the different bioreactors and modeling approaches and the corresponding R^2 values are also reported in Tab. 5.2.

Table 5.2: Fitted coefficients, RMSE, and R^2 values for Eq. (5.4) and Eq. (5.5).

Bioreactor	Modeling approach	Fit for Eq. (5.4)			Fit for Eq. (5.5)		
		k_{t_m}	RMSE	R^2	$k_{\gamma_{tank}}$	RMSE	R^2
CR3	one-way EL	875.2	2.57	0.9892	0.0760	0.14	0.9997
	EE	1173.3	0.80	0.9935	0.0737	0.70	0.9883
XDR-10	one-way EL	713.3	3.85	0.9703	0.0682	1.33	0.9969
	EE	883.7	1.78	0.9941	0.0820	1.77	0.9784
XDR-200	one-way EL	1259.0	7.35	0.9959	0.0449	0.16	0.9999
	EE	1009.5	4.85	0.9669	0.0355	0.41	0.9853
XDR-2000	one-way EL	1751.4	9.50	0.9882	0.0307	0.01	0.9998
	EE	1678.8	6.34	0.9960	0.0239	0.09	0.9927

Figures 5.6 and 5.7 provide a visualization of the different fitted correlations for the four considered scale-up criteria, where the symbols indicate the simulation results

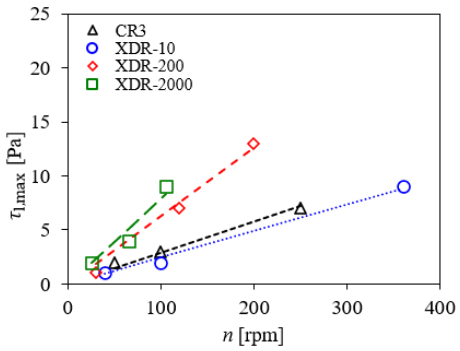

(a) Maximum hydrodynamic stress

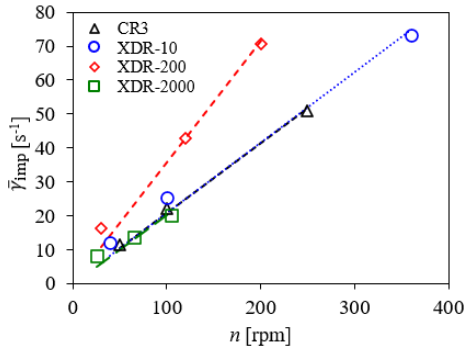

(b) Average strain rate of the impeller zone

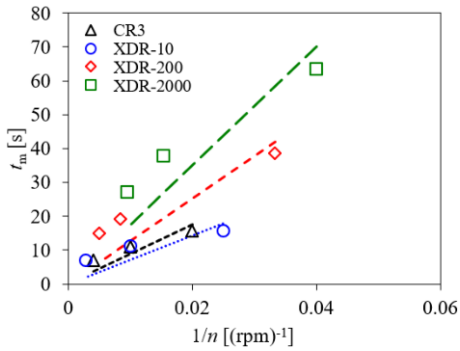

(c) Mixing time

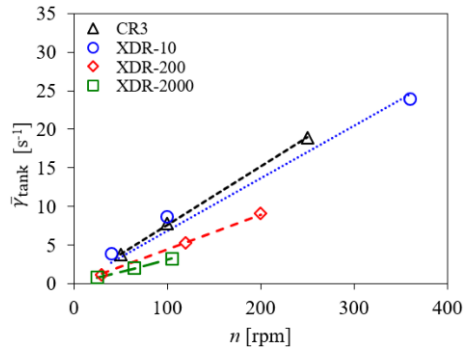

(d) Average strain rate of the tank zone

Figure 5.6: Correlations for the investigated scale-up criteria with the impeller speed n based on the one-way EL simulations, with the lines and the symbols indicating the results obtained from the correlations and the simulation, respectively.

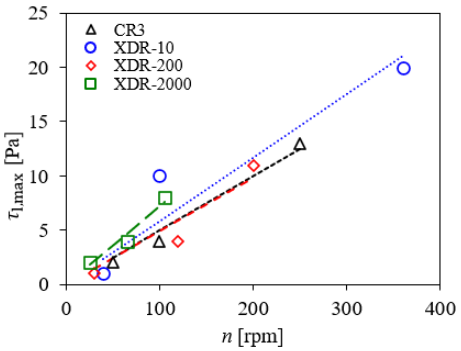

(a) Maximum hydrodynamic stress

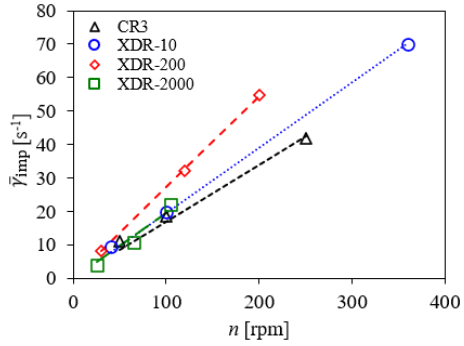

(b) Average strain rate of the impeller zone

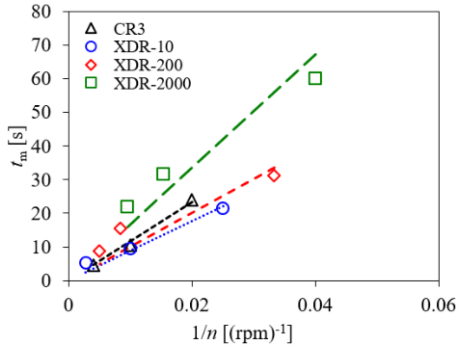

(c) Mixing time

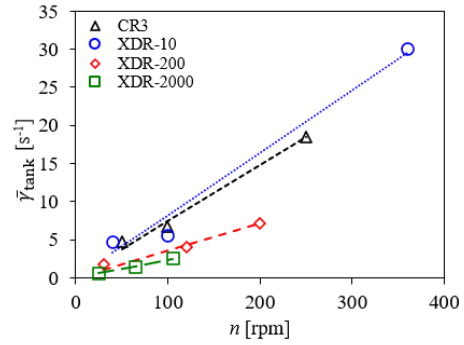

(d) Average strain rate of the tank zone

Figure 5.7: Correlations for the investigated scale-up criteria with the impeller speed n based on the EE simulations with with the lines and the symbols indicating the results obtained from the correlations and the simulation, respectively.

used to fit the coefficients. To improve visibility, only the one-way EL results are shown in Fig. 5.6 and the identical representation for the EE simulations can be found in Fig. 5.7. Identical slopes of the fitted correlations indicate that a constant impeller speed would provide the same value for the respective scale-up criterion. The largest difference between the modeling approaches is found for $\tau_{l,max}$, where the one-way EL simulations predict lower values than the EE simulations, since they neglect the effect of the bubbles on the liquid motion, which has been discussed in the previous sections.

Figs. 5.6c and 5.7c show that while the R^2 values for Eq. (5.4) in Tab. 5.2 are reasonably high, i.e., larger than 0.9, the correlation systematically under-predicts the mixing time for the maximum impeller speeds and over-predicts the mixing time for the minimum impeller speeds. To improve the correlation provided by Eq. (5.4), a second coefficient is introduced for adjusting the exponent as described by Eq. (5.6).

$$t_m = k_{1,t_m} \, n^{k_{2,t_m}} \tag{5.6}$$

The resulting fitted coefficients and R^2 values are summarized in Tab. 5.3, where the increased R^2 values compared to Tab. 5.4 indicate an improved fit for Eq. (5.6) compared to Eq. (5.4). The highest deviation of the fitted exponent k_{2,t_m} to the fixed

Table 5.3: Fitted coefficients, RMSE, and R^2 values for Eq. (5.6).

Bioreactor	Modeling approach	Fit for Eq. (5.6)			
		k_{1,t_m}	k_{2,t_m}	RMSE	R^2
CR3	one-way EL	116.0	-0.5113	0.01	0.9999
	EE	1905.7	-1.1187	0.49	0.9968
XDR-10	one-way EL	62.6	-0.3750	0.02	0.9999
	EE	330.3	-0.745	1.03	0.9792
XDR-200	one-way EL	211.6	-0.5010	0.02	0.9999
	EE	230.0	-0.5847	1.22	0.9832
XDR-2000	one-way EL	401.3	-0.5723	0.77	0.9975
	EE	548.7	-0.6871	0.35	0.9995

value of '-1' in Eq. (5.4) is observed for the one-way EL simulations of the XDR-10. Figure 5.8a shows the two correlations and the simulation results for the considered impeller speeds, where the improved agreement of Eq. (5.6) especially for the lowest impeller speed is evident. In Fig. 5.8b, the correlations are directly compared with the simulations results. Both fitted correlations show a linear relationship with the simulation results and reasonably high R^2 values, meaning that in both cases changes in the mixing time are well explained by changes of the value predicted by the correlation. However, if the correlation perfectly predicts the simulated mixing times the data points in Fig. 5.8b should be on the unity line, which has a slope of '1' and a y-intercept of '0'. Only the results of Eq. (5.6) comes close to this expectation. This indicates that though the mixing time has an hyperbolic relationship with the impeller speed, an exponent deviating from the literature reported value of '-1' better explains the present results. This might be caused by the deviation of the bioreactor configurations

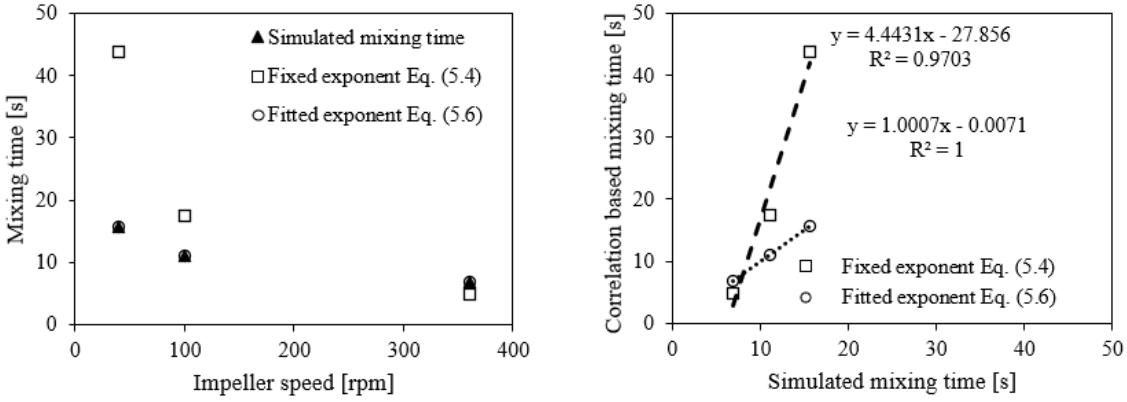

(a) Simulated and correlation based t_m over n (b) Correlation based t_m over simulated t_m

Figure 5.8: Comparison of the simulated mixing times t_m with the fitted correlations according to Eqs. (5.4) and (5.6) for the one-way EL simulations of the XDR-10.

investigated in the present study from the standard configuration of a baffled vessel with one or more centered impellers.

5.2.2 Selection of the Impeller Speed for Different Scale-Up Criteria

If the relevant scale-up criteria can be fitted by linear correlations with the impeller speed n as described in the previous section, the ratio of the coefficients provides a multiplication factor to calculate the n for the targeted bioreactor scale from that of the initial bioreactor. This scale-up factor lumps the effects of the changes of the sizes and configurations of the respective bioreactors into a single value that is specific to the considered initial and target bioreactors. With further characterization data for other bioreactors to compute the required coefficients, this approach would be easily to extended to additional bioreactors.

Table 5.4 summarizes the scale-up factors for the n with the CR3 as the initial bioreactor and the larger bioreactor scales, i.e. the XDR-10, XDR-200, and XDR-2000, as the target scales. For the maximum hydrodynamic stress $\tau_{\mathrm{l,max}}$ and the average strain rate of the impeller zone $\overline{\gamma}_{\mathrm{imp}}$, which represent the mechanical stress in the bioreactor, the highest scale-up factor is 1.17, while nine out of twelve scale-up factors are smaller than one. Consequently, these two scale-up criteria both indicate that the n must be kept constant or reduced for the larger bioreactors. The deviations in the scale-up factors for the different modeling approaches range from 0.4 to 0.55 for $\tau_{\mathrm{l,max}}$ and 0.05 to 0.15 for $\overline{\gamma}_{\mathrm{imp}}$. The lower deviation for $\overline{\gamma}_{\mathrm{imp}}$ suggests that it might be a more robust criterion for the selection of n, since it is less sensitive to the treatment of the disperse phase. The difference in the scale-up factors required for the two different scale-up criteria ranges from 0.12 to 0.66 for the one-way EL simulations and 0.01 to 0.40 for the EE simulations. This indicates that while $\tau_{\mathrm{l,max}}$ and $\overline{\gamma}_{\mathrm{imp}}$ are both representations of the risk of cell damage, they cannot be used interchangeably. Both

Table 5.4: Scale-up factors for scaling-up the impeller speed n CR3 to that of the respective bioreactor according to the selected scale-up criterion.

Scale-up criterion	Modeling approach	Scale-up factors for the		
		XDR-10	XDR-200	XDR-2000
$\tau_{\mathrm{l,max}}$	one-way EL	1.17	0.46	0.36
	EE	0.86	1.02	0.69
$\overline{\gamma}_{\mathrm{imp}}$	one-way EL	0.99	0.58	1.02
	EE	0.87	0.62	0.87
t_{m}	one-way EL	0.82	1.44	2.00
	EE	0.75	0.86	1.43
$\overline{\gamma}_{\mathrm{tank}}$	one-way EL	1.11	1.69	2.48
	EE	0.90	2.08	3.08

Table 5.5: Scale-up factors for the impeller tip speed u_{tip} for scaling-up from the CR3 to the respective bioreactor according to the selected scale-up criterion.

Scale-up criterion	Modeling approach	Scale-up factor		
		XDR-10	XDR-200	XDR-2000
$\tau_{\mathrm{l,max}}$	one-way EL	2.11	1.30	2.00
	EE	1.55	2.90	3.81
$\overline{\gamma}_{\mathrm{imp}}$	one-way EL	1.79	1.64	5.62
	EE	1.57	1.77	4.77
t_{m}	one-way EL	1.47	4.09	11.04
	EE	0.75	0.86	1.43
$\overline{\gamma}_{\mathrm{tank}}$	one-way EL	2.01	4.81	13.65
	EE	1.62	5.90	17.00

are successfully applied in the respective studies that report them [30, 23] and their relative importance cannot be determined without cell culture experiments that allow for a direct comparison.

The impeller tip speed u_{tip} has also been reported as a scale-up criterion [20]. To compare u_{tip} to the scale-up criteria of the present study, scale-up factors for u_{tip} for maintaining a constant $\tau_{\mathrm{l,max}}$ or $\overline{\gamma}_{\mathrm{imp}}$ are summarized in Tab. 5.5. If the scale-up criteria of the present study were equivalent to u_{tip} the scale-up factors would be one. However, all scale-up factors for $\tau_{\mathrm{l,max}}$ and $\overline{\gamma}_{\mathrm{imp}}$ are larger than one, meaning that based on the present analysis u_{tip} should be increased during scale-up. This is in agreement with the simulations of Li et al. [23], who found that different bioreactors require different coefficients to correlate the maximum and average strain rates with u_{tip}. For the same impeller type and a constant u_{tip}, Li et al. [23] observed a decrease in the maximum and average strain rates for the larger bioreactor scales. In agreement with the results of Li. et al. [23], in the present study the coefficients for the larger XDR-2000 are smaller than for the XDR-200, which is equipped with a similar off-centered, pitched-blade impeller with a smaller diameter. This emphasizes that using a constant tip speed as a scale-up criterion might limit the impeller speed to values that are lower than necessary. Moreover, operating below the limits provided by the mechanical stress, potentially exacerbates homogenization issues at larger scales.

Similar to the $\tau_{\mathrm{l,max}}$ and $\overline{\gamma}_{\mathrm{imp}}$, the correlations for the mixing time t_{m} and the average strain rate of the tank zone $\overline{\gamma}_{\mathrm{tank}}$ with n^{-1} and n, respectively, can also provide scale-up factors for n and u_{tip}. The resulting scale-up factors are reported in Tabs. 5.4 and 5.5. However, as discussed previously, the linear correlation of the mixing time with n^{-1} does not provide as good a fit as Eq. (5.6), which allows for adjustment of the exponent. The scale-up factors based on Eq. (5.4) are provided and discussed here for the sake of completeness, but for all further considerations of the t_{m} as a scale-up criterion, the n is selected by solving Eq. (5.6).

For the XDR-10, the scale-up factors based on t_{m} and $\overline{\gamma}_{\mathrm{tank}}$ are similar to those

obtained for $\tau_{\mathrm{l,max}}$ or $\overline{\gamma}_{\mathrm{imp}}$ and range from 0.75 to 1.17 for the n. This suggests that n can be kept constant or even be reduced slightly when scaling-up from the CR3 to the XDR-10. Furthermore, maintaining all the considered scale-up criteria in a similar range is relatively easy for the small difference in scales between the CR3 and the XDR-10.

However, when scaling from the CR3 to the two larger bioreactors, the XDR-200 and the XDR-2000, a higher n and u_{tip} are needed to achieve the same $\overline{\gamma}_{\mathrm{tank}}$ for the larger bioreactor scales. The same is found for t_{m} for the XDR-2000. For the XDR-200, the one-way EL simulations indicate that n must be increased, whereas the EE simulations suggest a slight reduction of n. This is caused by the deviation of the mixing times predicted by Eq. (5.4) from the simulation results and is not confirmed when using Eq. (5.6) instead. The need for a higher n at larger scales to achieve the same $\overline{\gamma}_{\mathrm{tank}}$ and t_{m} is in direct conflict with the requirement of a constant or a smaller n for a constant $\tau_{\mathrm{l,max}}$ or $\overline{\gamma}_{\mathrm{imp}}$. This emphasizes the challenge of correctly selecting and balancing the scale-up criteria, when the differences between the considered bioreactor scales are large. The scale-up factors for scaling-up from the XDR-10, or the XDR-200 can be obtained by dividing the scale-up factor for scaling-up from the CR3 to the larger bioreactor by that for scaling up to the smaller bioreactor. For scaling-up from the XDR-10 or the XDR-200 the same qualitative observations for the selection of the impeller speed as for scaling-up form the CR3 are made, with the exception that for scaling up from the XDR-10 to the XDR-200 based on the maximum hydrodynamic stress based on the EE simulations the impeller speed has to be increased and that for scaling-up from the XDR-200 to the XDR-2000 based on the average strain rate of the impeller zone the impeller speed also has to be increased based on both the one-way coupled EL and the EE simulations.

5.2.3 Case Study on the Scale-Up of the Impeller Speed

To provide a more concrete case study on scale-up than the scale-up factors discussed so far, a fixed operating range for the CR3 is selected. In Sect. 4.1.4, no restrictions on the investigated impeller speeds of 50 rpm to 250 rpm based on the maximum tolerable hydrodynamic stress for CHO and Sp2/0 cells reported by Neunstoecklin et al. [47] are found. The limits for the impeller zone average strain rate identified by Li et al. [23] for Sf9 cells are exceeded for all impeller speeds. Consequently, according to these studies all impeller speeds are either equally well- or ill-suited for cell cultivation. Instead, cell culture results for a CHO cell line expressing a monoclonal antibody provided by Yuichi Aki from Daiichi-Sankyo Co., Ltd., Japan are used to identify the operating range for the CR3. The viable cell density and the product titer observed during the cultivation time of 14 days are shown in Fig. 5.9. The two cultivation runs at 100 rpm and the one at 150 rpm show slightly higher cell density during the time course of the cultivation, see Fig. 5.9a, and slightly higher product titer on the final cultivation day, see Fig. 5.9b than the run at 50 rpm. This results indicate that impeller speeds of 100 rpm and 150 rpm provide slightly better process conditions than 50 rpm. Accordingly, the operating range of the impeller speed for the CR3 is selected as 100 rpm to 150 rpm, however, even higher impeller speeds, which have not been investigated, might also be

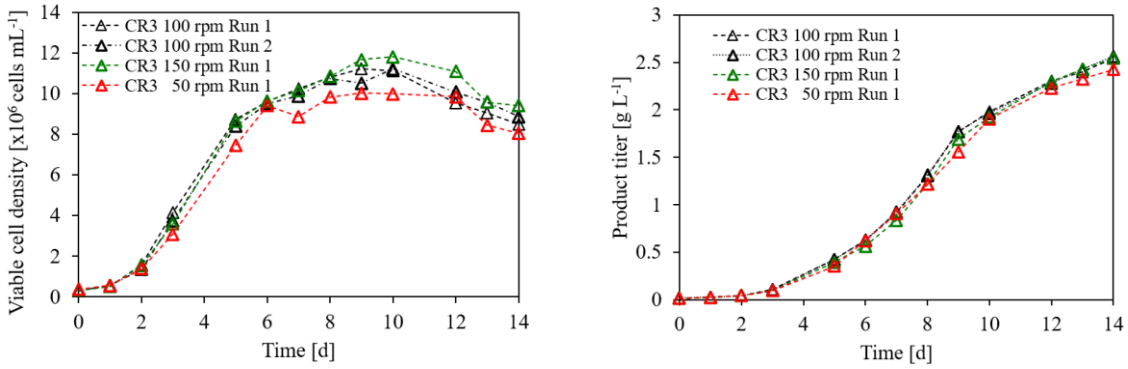

(a) Viable cell density (b) Antibody titer

Figure 5.9: Viable cell density and antibody titer for different impeller speeds with the CR3. Repetitions of cell culture experiments at the same operating are shown individually and distinguished from each other through different line styles and by numbering as different "Run".

able to provide suitable cell culture conditions.

The selected operating range for the CR3 is used to identify the target ranges for the different scale-up criteria. These target ranges as well as the range of the impeller speed n, the volumetric power input P/V, and the impeller tip speed u_{tip} are summarized in Tab. 5.6. The values of the maximum hydrodynamic stress $\tau_{\text{l,max}}$, the average strain rate of the impeller zone $\overline{\gamma}_{\text{imp}}$, the mixing time t_{m}, and he average strain rate of the tank zone $\overline{\gamma}_{\text{tank}}$ are obtained from Eqs. (5.2), (5.3), (5.5), and (5.6).

After the target ranges of the scale-up criteria have been identified based on the

Table 5.6: Operating range for the CR3 and corresponding target ranges for the considered scale-up criteria.

Parameter			Data source	Bound 1	Bound 2
Impeller speed	n	[rpm]		100	150
Impeller tip speed	u_{tip}	[m s^{-1}]		0.4	0.6
Volumetric power input*	P/V	[W m^{-3}]	Supplier N_{P}	2.1	7.1
Maximum hydrodynamic stress*	$\tau_{\text{l,max}}$	[Pa]	one-way EL	2.9	4.3
			EE	5.0	7.5
Average strain rate of the impeller zone*	$\overline{\gamma}_{\text{imp}}$	[s^{-1}]	one-way EL	20.7	31.0
			EE	17.0	25.5
Mixing time*	t_{m}	[s]	one-way EL	11.0	8.9
			EE	11.0	7.0
Average strain rate of the tank zone*	$\overline{\gamma}_{\text{tank}}$	[s^{-1}]	one-way EL	7.6	11.4
			EE	7.4	11.1

* evaluated for the intermediate working volume of 1.7 L

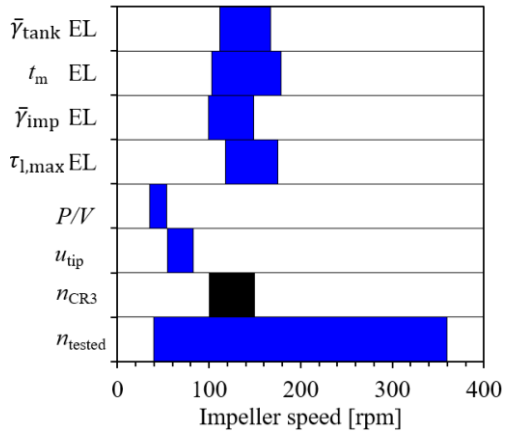

(a) XDR-10, one-way EL simulations

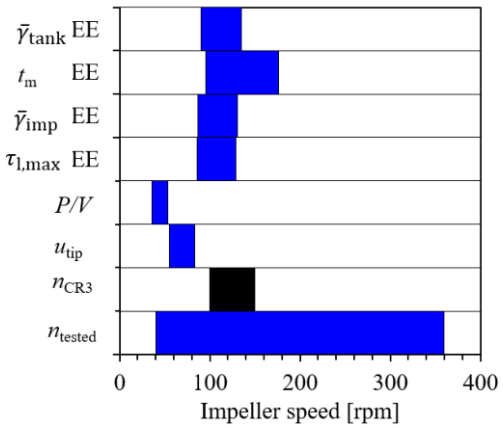

(b) XDR-10, EE simulations

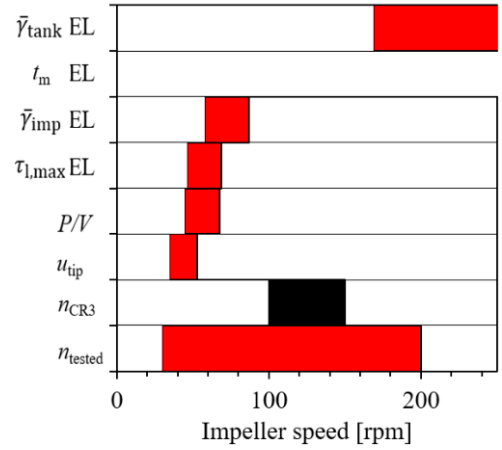

(c) XDR-200, one-way EL simulations

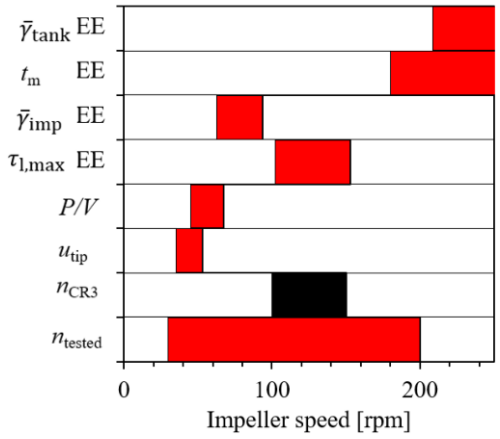

(d) XDR-200, EE simulations

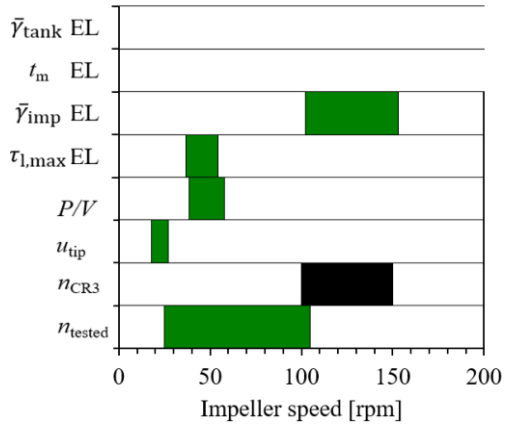

(e) XDR-2000, one-way EL simulations

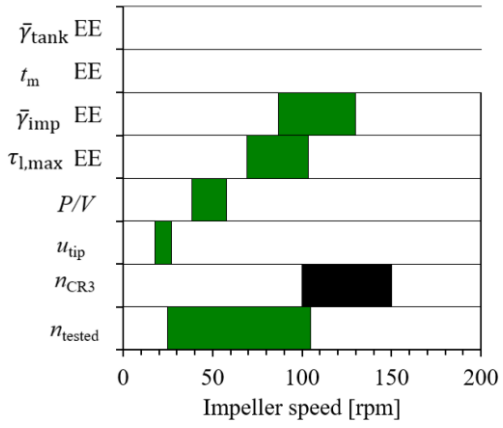

(f) XDR-2000, EE simulations

Figure 5.10: Impeller speed ranges for the XDR-10, the XDR-200, and the XDR-2000 to fulfill the different scale-up criteria listed in Tab. 5.6.

cell cultivation results of the small scale, the impeller speed range of each of the larger bioreactors can be selected to match these target ranges. Fig. 5.10 provides a visual representation of the impeller speeds required to meet the different scale-up criteria, with their values listed in Tab. 5.6. Due to the observed differences of the simulation results between the one-way EL and the EE approaches and the derived coefficients, the results of these two modeling approaches are presented separately, on the left hand side and right hand side of Fig. 5.10, respectively. The different rows of subfigures correspond to the considered bioreactors and are colored blue, red and green for the XDR-10, XDR-200, and XDR-2000, respectively. The volumetric power input P/V and the impeller tip speed u_{tip} are classical scale-up parameters for scale-up between geometrically similar bioreactors and are added to compare them to the other scale-up criteria based on the present characterization results. The black bar indicates the operating range of the impeller speed selected for the CR3, and the impeller speed range considered in the characterization simulations is indicated by n_{tested}.

The first step during experimental scale-up or the seed train is the transfer of the cultivation from the CR3 to the XDR-10. For this relatively small difference in bioreactor scales there is overlap between the impeller speeds required to match the four considered scale-up criteria, see Figs. 5.10a and 5.10b. Impeller speeds of 118 rpm to 149 rpm and 96 rpm to 128 rpm for the one-way EL and EE approach, respectively. Accordingly, all four scale-up criteria, i.e., $\overline{\gamma}_{\mathrm{tank}}$, t_{m}, $\overline{\gamma}_{\mathrm{imp}}$, and $\tau_{\mathrm{l,max}}$ can be kept within the ranges given in Tab. 5.6. The target ranges for the impeller speed of the XDR-10 are incidentally quite close to just maintaining a constant impeller speed. The classical scale-up criteria for geometrically similar bioreactors, P/V and u_{tip}, indicate much lower impeller speeds of 36 rpm to 53 rpm and 55 rpm to 83 rpm, respectively. This would result in slower mixing and consequently is expected to have a negative impact on the cell culture performance. The observed discrepancy between the classical scale-up criteria and the present characterization based scale-up criteria clearly shows that even for small differences in the bioreactor scale, scale-up between geometrically dissimilar bioreactors requires quantitative data on the hydrodynamic characteristics. Since the scale-up criteria representing the mechanical forces, $\tau_{\mathrm{l,max}}$ and $\overline{\gamma}_{\mathrm{imp}}$, and those representing the mixing, $\overline{\gamma}_{\mathrm{tank}}$ and t_{m}, are both met simultaneously, no issues are expected during scale-up.

The available characterization results also allow for a direct scale-up from the CR3 to the XDR-200 and the XDR-2000. However, the increased liquid volumes result in a strongly increased t_{m} and a lower $\overline{\gamma}_{\mathrm{tank}}$. Consequently, the impeller speeds required to match these two criteria lie at the upper end of the investigated impeller speed range for the XDR-200 and more than 100 rpm beyond the investigated impeller speed for the XDR-2000. The scale-up criteria that consider the mechanical stress in the liquid, $\tau_{\mathrm{l,max}}$ and $\overline{\gamma}_{\mathrm{imp}}$, require a reduction of the impeller speed well below the values required by $\overline{\gamma}_{\mathrm{tank}}$ and t_{m}. As the primary goal in the present study has been defined as keeping the hydrodynamic stress levels below the selected critical values, the impeller speed limits for the $\overline{\gamma}_{\mathrm{tank}}$ and t_{m} take precedence over those obtained for $\overline{\gamma}_{\mathrm{tank}}$ and t_{m}. However, a decreased cell culture performance due to slower mixing cannot be ruled out. As mentioned earlier, the maximum impeller speed selected for the CR3 may not

be at the upper limit of the tolerable mechanical stress but due to the lack of further evidence an increase beyond the current level is not considered.

For the XDR-200, the evaluation based on the one-way EL results in Fig. 5.10c indicates that impeller speeds of 58 rpm to 69 rpm allow to keep both $\overline{\gamma}_{\text{tank}}$ and t_{m} within the selected range. For results based on the EE simulations, the impeller speed ranges required to keep $\overline{\gamma}_{\text{tank}}$ and t_{m} constant, shown in Fig. 5.10d do not overlap. In this case, there are two options, either the lower of the two upper limits is taken in an conservative estimate of the maximum tolerable impeller speed, or the relevance of both criteria has to be decided. Considering how $\tau_{\text{l,max}}$ and $\overline{\gamma}_{\text{imp}}$ are obtained, $\overline{\gamma}_{\text{imp}}$ is considered to be the more robust and thus the more relevant scale-up criterion because of the following reasons:

1. $\overline{\gamma}_{\text{imp}}$ represents a larger volume of the bioreactor than $\tau_{\text{l,max}}$

2. in the simulations $\overline{\gamma}_{\text{imp}}$ is obtained from the Reynolds average velocity, which is less sensitive to the grid resolution than the turbulence energy dissipation rate [129], and thus can be expected to provide more robust results than $\tau_{\text{l,max}}$ when coarse computational grids are used

3. the agreement between the one-way EL and EE simulations is better for $\overline{\gamma}_{\text{imp}}$ indicating that $\overline{\gamma}_{\text{imp}}$ is less sensitive to the modeling of the disperse phase

For the XDR-200, both using the lower of the two different limits for the impeller speed or selecting $\overline{\gamma}_{\text{imp}}$ as the more relevant criterion result in the same outcome. The required impeller speed range is 63 rpm to 94 rpm for matching $\overline{\gamma}_{\text{imp}}$ to the target range. As the mixing in the XDR-200 is slower than for the CR3, the upper bound of this range, i.e., 94 rpm appears to be the optimal scale-up condition.

Based on the one-way EL for the XDR-2000, see Fig. 5.10e, the impeller speed range to maintain a constant $\tau_{\text{l,max}}$ is significantly lower than that for a constant $\overline{\gamma}_{\text{imp}}$. For the same reasons as discussed for the XDR-200, $\overline{\gamma}_{\text{imp}}$ is considered to be the more relevant criterion. The corresponding impeller speed range is 102 rpm to 153 rpm, which exceeds the maximum impeller speed of 105 rpm. Based on the EE simulations, an impeller speed range of 87 rpm to 104 rpm allows to keep both the $\tau_{\text{l,max}}$ and $\overline{\gamma}_{\text{imp}}$ in the target range, see Fig. 5.10f. Based on $\overline{\gamma}_{\text{imp}}$, impeller speeds up to 130 rpm would be suitable, which similar to the one-way EL results are already beyond the tested operating range with a maximum impeller speed of 105 rpm. Based on the slow mixing and the impeller speed ranges required to achieve a value of $\overline{\gamma}_{\text{imp}}$ within the target range, 105 rpm appears the optimal impeller speed within the considered operating range for the XDR-2000.

The next section considers how a constant $k_{\text{L}}a$ can be achieved for scale-up across all considered bioreactor scales. Both the impeller speed and the sparging strategy impact the $k_{\text{L}}a$. To select a sparging strategy for the scale-up of the $k_{\text{L}}a$, fixed impeller speeds of 150 rpm, 130 rpm, 94 rpm, and 105 rpm are selected. These correspond to a constant $\overline{\gamma}_{\text{imp}}$ based on the EE results for the CR3, XDR-10, and XDR-200, and the upper limit of the investigated operating range for the XDR-2000, respectively. The considered target range of $\overline{\gamma}_{\text{imp}}$ might be smaller than necessary, and its upper limit

and the corresponding upper limits of the impeller speeds could be further explored by additional cell cultivation runs. However, for the XDR-2000 the resulting impeller speed range is already close to the upper limit of 115 rpm suggested by the supplier characterization [166]. Consequently, an increased upper limit for $\overline{\gamma}_{\mathrm{imp}}$ would not affect the selection of the impeller speed for the XDR-2000 due to the limitations of the equipment.

5.3 Oxygen Transfer during Scale-Up

As described in the previous sections, the $k_{\mathrm{L}}a$ depends on the working volume, the impeller speed, and the sparging rate. Similar to the selection of the impeller speed, the working volume is considered to be fixed to the intermediate level for the evaluation of the $k_{\mathrm{L}}a$. The Van't Riet equation [46] is a well established empirical correlation [32, 20] to capture the effect of the impeller speed and the sparging rate on the $k_{\mathrm{L}}a$:

$$k_{\mathrm{L}}a \;=\; C_1 \; (P/V)^{C_2} \; u_{\mathrm{s}}^{C_3} \tag{5.7}$$

where changes in the impeller speed are reflected by the volumetric power input P/V and changes in the sparging rate are captured through the superficial gas velocity u_{s}, which is the sparing rate normalized by the cross-sectional area of bioreactor. Similar to the previous section on the scale-up of the impeller speed, this established correlation is used to fit the coefficients for each of the considered bioreactors and the two modeling approaches are considered separately. The fitted coefficients are summarized in Tab. 5.7.

The linear coefficient C_1 is known to show large variation [46] and is not discussed further. The exponents of the volumetric power input C_2 ranges from 0.149 to 0.499, which is on the lower end of the values reported in literature [46, 132], where the typical range is given as 0.4 to 1. This indicates that the volumetric power input

Table 5.7: Fitted coefficients, RMSE, and R^2 values for the Van't Riet equation given in Eq. (5.7).

Bioreactor	Modeling approach	Fit Eq. (5.7)				
		C_1	C_2	C_3	RMSE	R^2
CR3	one-way EL	16268.4	0.499	0.921	2.24	0.997
	EE	33694.9	0.187	0.958	0.79	0.888
XDR-10	one-way EL	341268.8	0.159	1.216	1.22	0.985
	EE	104.3	0.227	0.337	0.78	0.994
XDR-200	one-way EL	9969.2	0.287	0.958	9.61	0.999
	EE	458.6	0.200	0.537	5.30	0.980
XDR-2000	one-way EL	57278.9	0.260	1.085	0.91	0.980
	EE	333.2	0.149	0.479	0.85	0.908

has a lower impact on the k_La of the considered bioreactors than is typical for other bioreactor types. This is likely caused by the microporous spargers with which all of the bioreactors are equipped and which generate small bubbles without the need for bubble break-up through the impeller and the liquid turbulence [174]. Thus, the effect of the P/V on the bubble size is strongly reduced and its impact on the k_La is mainly related to its effect on k_L and the bubble residence time, while the bubbles size mainly depends on the initial size of the bubbles generated at the microporous sparger.

The exponent for the superficial gas velocity differs for the two considered modeling approaches. For the one-way EL simulations C_3 ranges from 0.921 to 1.216 and is close to 1, which corresponds to the linear correlation of the gas hold-up and consequently the k_La with the sparging rate defined by Eq. (2.35). For the EE approach, which can capture changes in the bubble residence for different sparging rates, the values for C_3 range from 0.337-0.958 and are in better agreement to the experimental results discussed in Sects. 4.1.4, 4.2.4, 4.3.4 and the range of $0 < C_3 < 0.7$ reported by Van't Riet [46]. This again shows that one-way EL simulations are likely over-predict the k_La at higher sparging rates.

If the impeller speed is fixed, the k_La can be identified as a function of the superficial gas velocity. Figure 5.11 shows the k_La at different the superficial gas velocity u_s for the different bioreactors. The mentioned deviations in C_3 for the one-way EL and EE simulations, are clearly reflected in the differences in the slopes of the one-way EL and EE results. For the further discussion on the scale-up of the k_La and the selection of the sparging rate, only the EE results are used because of the consistency with the previous selection of the impeller speeds and the higher accuracy of the simulated k_La values at high sparging rates. For the selected impeller speeds, similar k_La values can easily be achieved for the CR3, XDR-200, and XDR-2000 up to a superficial gas velocity of $1x10^{-4}$ m s^{-1}, which corresponds to sparging rates of 0.09 L min^{-1}, 1.48 L min^{-1} and 7.01 L min^{-1}. For the XDR-10, even higher k_La values are observed for this range of superficial gas velocities. Accordingly, a k_La value comparable to or larger than that of the CR3 can easily be achieved during scale-up.

During cell cultivation the oxygen requirements of the cultivated cell line increase with the cell density. For this reason, the sparging rate is dynamically controlled to maintain a constant oxygen saturation in the liquid by the process control unit. For the CHO cell line considered in the previous section for the selection of the impeller speed, intermittent sparging strategy with a sparging rate of 50 mL min^{-1} is used for the CR3. For the intermittent sparging strategy the gas flow is switched on and off depending on the dissolved oxygen tension being below or above the set-point. This means that the oxygen requirements of this considered cell line can be achieved at a sparging rate below 50 mL min^{-1}. The corresponding sparging rates for the larger bioreactors to match the k_La found for the CR3 at 50 mL min^{-1} are 0.11 L min^{-1}, 0.84 L min^{-1}, and 4.0 L min^{-1} for the XDR-10, XDR-200, and the XDR-2000, respectively. These are the upper limits of the expected sparging rates for each of the larger bioreactor scales and indicate that the same k_La can be achieved across the different bioreactor scales. The next section presents cell culture results that test the present results on the operating conditions for scaling-up from the considered CR3 cultivation at 150 rpm to

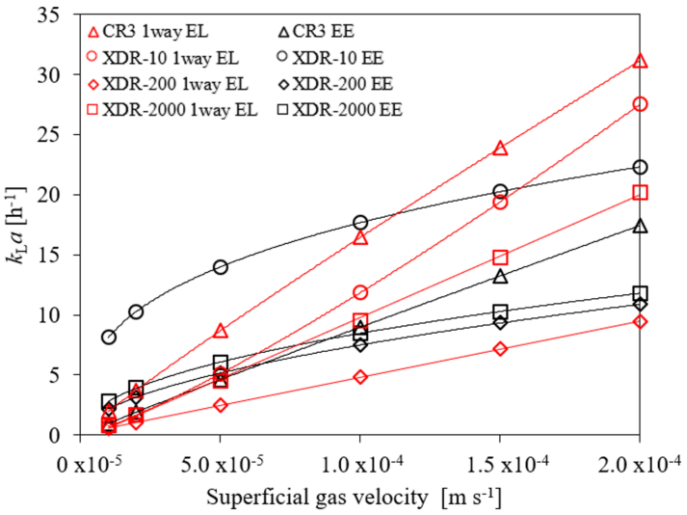

Figure 5.11: The k_La based on the fit to the Van't Riet equation for the CR3, XDR-10, XDR-200, and XDR-2000 at the respective intermediate working volumes of 1.7 L, 7.0 L, 120 L, and 1200 L and the respective impeller speeds of 150 rpm, 130 rpm, 94 rpm, and 105 rpm selected in Sect. 5.2.

the XDR-10 and XDR-200.

5.4 Cell Culture Results for the Scale-Up

In addition to the already presented cell culture results, two cultivation runs for the larger biroeactor scales, one with the XDR-10 and one with the XDR-200 at an impeller speeds of 130 rpm and 94 rpm, respectively, have been performed by Yuichi Aki from Daiichi-Sankyo Co., Ltd., Japan. Moreover, three cultivation runs with the CR3 at 150 rpm and one at 50 rpm have been performed with the same cell bank and media lots. Figure 5.12 compares the viable cell density of these cultivation runs with each other and to the CR3 cultivation results for 50 rpm and 150 rpm of the initial runs. The initial CR3 results from Fig. 5.9 are indicated by open triangles, the new results are indicated by filled triangles (Run 2 to 4) with the different line styles indicating the different runs. The XDR-10 and XDR-200 cultivations are indicated by circles and diamonds, respectively.

The different viable cell densities are shown in Fig. 5.12a and the product titer is shown in Fig. 5.12b. There is a clear difference between the initial data for the CR3 and the new results, with a higher viable cell density and product titer for the initial runs at the respective impeller speeds. These deviations are unrelated to the hydrodynamic conditions and are likely caused by the different cell bank or media lots. When considering the initial and the new cultivation runs separately, a clear effect of the hydrodynamic conditions is found with a lower viable cell density and reduced product titer for the lower impeller speed of 50 rpm. The two scale-up runs for the XDR-10 and XDR-200, which are executed with the same cell bank and media lots as the new cultivation runs, have as similar maximum cell density and product titer

as the new 150 rpm runs for the CR3. The XDR-10 cultivation has a slightly longer lag-phase with a delayed exponential growth phase, the reasons for which are unknown, but achieves a similar maximum viable cell density on day 10 and almost the same maximum product titer on day 14, confirming that the selected operating condition can successfully be used for scale-up. The XDR-200 shows a very similar exponential growth as the CR3 runs at 150 rpm with a slightly lower cell density on day 10. The final product titer on day 14 is almost identical to that of the CR3, also indicating successful scale-up.

These results support that the proposed scale-up strategy of selecting the impeller speed in order to achieve the same average strain rate in the impeller zone could successfully be applied for the scale-up between the considered geometrically dissimilar single-use bioreactors, the CR3, the XDR-10, and the XDR-200. Even though, for the XDR-200 the mixing time is higher and the tank zone average strain rate is lower than for the CR3 no negative impact on the final product titer is observed. In summary, the average strain rate in the impeller zone, which is also part of the scale-up strategy proposed by Li et al. [23] for Sf9 cells, is successfully used with the present simulation data for the scale-up of a CHO cell cultivation. However, different process ranges for the average strain rate in the impeller zone than those proposed by Li et al. [23] are identified for the present bioreactors and cell lines, and in contrast to the study by Li et al. [23] the same average strain rate of the tank zone could not be maintained for the XDR-200. This might be related to the fact that Li et al. [23] considered bioreactors with two impellers for working volume of 90 L and more. The impeller speeds selected for the present scale-up study do not correspond to the classic scale-up criteria of a constant tip speed or volumetric power input, as is evident from Tab. 5.8. The cell culture results discussed here suggest that a constant P/V or u_{tip} as scale-up criteria might limit the impeller speed to lower values than required for a successful scale-up. This emphasizes the increased insight gained by hydrodynamic

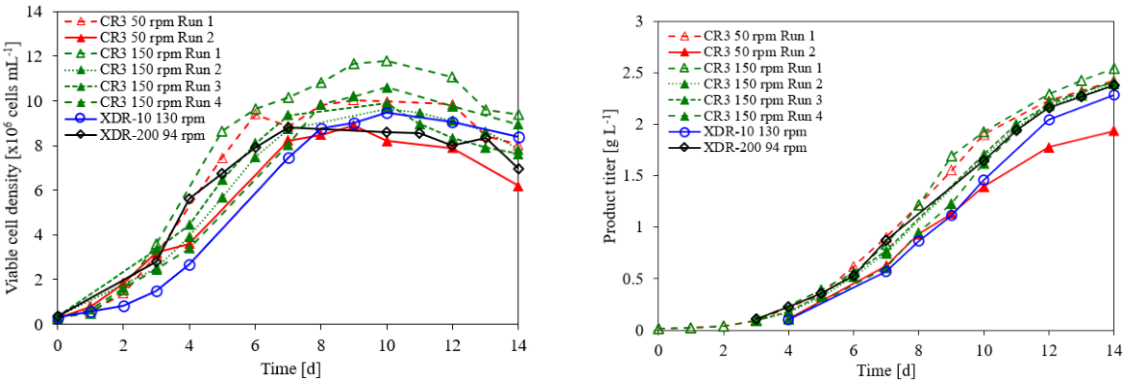

(a) Viable cell density (b) Antibody titer

Figure 5.12: Viable cell density and antibody titer for the considered scale-up strategy. Repetitions of cell culture experiments at the same operating are shown individually and distinguished from each other through different line styles and by numbering as different “Run”.

Table 5.8: Impeller speed, tip speed and volumetric power input for the impeller speeds selected for scale-up.

Parameter		CR3	XDR-10	XDR-200	XDR-2000
n	[rpm]	150	130	94	105
u_{tip}	[m s^{-1}]	0.6	0.9	1.1	2.3
P/V^*	[W m^{-3}]	7.1	102.5	19.2	42.4

* for the intermediate working volumes of 1.7 L, 7.0 L, 120 L, and 1200 L, respectively

characterization studies that, in contrast to the P/V or u_{tip}, capture the combined effect of the operating condition and the bioreactor configuration on the cell culture relevant process characteristics. While the present verification of the implemented scale-up strategy is based on the cultivation of CHO cells, the presented operating conditions can be used for any cell line that can be successfully cultivated with the CR3 at 150 rpm. With the microporous spargers available for the considered bioreactors, the same maximum $k_{\text{L}}a$ as for the CR3 can be achieved for the XDR-10, XDR-200, and XDR-2000.

5.5 Carbon Dioxide Transfer during Scale-Up

Another process aspect that must be taken into account for cell cultivation at large scales is the carbon dioxide mass balance. The solubility of carbon dioxide in water is higher than that of oxygen, i.e., for the same concentration in the liquid phase the partial pressure of carbon dioxide in the gas phase at equilibrium is lower than that of oxygen. As a consequence, for long bubble residences, time the bubbles are saturated with carbon dioxide long before they reach the liquid the surface but continue transferring oxygen throughout the rise time [4]. This results in an imbalance of oxygen and carbon dioxide transfer and the accumulation of carbon dioxide for bioreactors large working volumes and correspondingly large liquid heights, which result in long bubble residence times. Depending on the cultivated cell line, a high concentration of dissolved carbon dioxide can have a negative impact on the productivity and viability of the cells [178, 4].

To avoid the imbalance of carbon dioxide stripping and oxygen transfer Doi et al. [40] used the ratio of the volumetric mass transfer coefficients of oxygen and carbon dioxide as a criterion for scaling up a CHO cultivation from a 200 L to a 2000 L bioreactor. Xing et al. [59] and He et al. [179] developed different models based on empirical correlations and the measured cell specific oxygen uptake rate of the investigated cell line to predict the carbon dioxide accumulation in the liquid for the transfer of CHO cultivations from 5000 L to 25000 L scale and 2 L to 1500 L scale, respectively. The carbon dioxide concentration in the liquid depends on the composition of the sparged gas(es) and the sparging strategy and strategies to control the carbon dioxide concentration in the liquid have also been investigated with experiments [180, 181, 53].

In the present study, the approach described by Sieblist et al. [4] to calculate the oxygen and carbon dioxide transfer rates based on the transfer dynamics of single bubbles is extended by combining the results with the bubble residence times obtained through CFD simulations to predict the liquid mass balance of carbon dioxide during cell cultivation. First the effect of different parameter on the transfer dynamics is single bubbles evaluated, before these results are used to predict the dissolved carbon dioxide concentrations for different hypothetical cultivation runs.

5.5.1 Mass Transfer of Individual Bubbles

The present sections starts with the evaluation of the mass transfer from the perspective of a single bubble, similar to the results presented by Sieblist et al. [4]. For the evaluation of the diffusive transport of oxygen and air according to Eq. (3.1) a bubble size of 1.3 mm is selected, which has been used for the evaluation of the $k_{\mathrm{L}}a$ of the XDR-200 and the XDR-2000. The liquid transfer coefficient k_{L} is evaluated as per Eq. (2.32) for an average energy dissipation rate of 0.01 $\mathrm{m^2\ s^{-3}}$, which corresponds to a volumetric power input of 10 $\mathrm{W\ m^{-3}}$, and the diffusion coefficients at 37°C of 3.0x10^{-9} $\mathrm{m^2\ s^{-1}}$ for oxygen [131] and 2.8x10^{-9} $\mathrm{m^2\ s^{-1}}$ for carbon dioxide [182]. For the composition of the sparged gas, both air and pure oxygen are considered and the Henry constant of oxygen and carbon dioxide at 37°C are 1.08x10^{-5} $\mathrm{mol\ m^{-3}\ Pa^{-1}}$ and 2.49x10^{-4} $\mathrm{mol\ m^{-3}\ Pa^{-1}}$, respectively. The dissolved oxygen concentration in the liquid is always set to 50 % air saturation, which is a typical value for cell cultivation [142, 143] and different carbon dioxide concentrations in the liquid between 0.01 $\mathrm{g\ L^{-1}}$ and 0.4 $\mathrm{g\ L^{-1}}$ are considered.

By solving Eq. (3.1) for both oxygen and carbon dioxide, the change in the amount of substance (or chemical amount) of both oxygen and carbon dioxide inside the bubble as shown in Fig. 5.13a-d is obtained. The initial uptake of carbon dioxide by both the air and the oxygen bubble is indicated by the increase in the amount of substance of carbon dioxide insides the bubble, which is quite comparable as shown in Figs. 5.13a and 5.13b with a rapid uptake of carbon dioxide in the first second and decreasing speed as the bubble becomes saturated. The partial pressure at equilibrium and thus the maximum amount of carbon dioxide uptake increases with the concentration of dissolved carbon dioxide in the liquid. When sparging bubbles consisting of pure oxygen, carbon dioxide is transferred back to the liquid after saturation has been reached to maintain a constant molar fraction due to the continued transfer of oxygen to the liquid as shown in Fig. 5.13b. This also indicates that the bubble volume is slightly reduced, however, the effect of this on surface area of the bubbles is neglected in the present study as is the potential increase in volume due to the evaporation of water. The initial amount substance of oxygen in the bubble and the amount substance of oxygen transferred to the liquid, which the difference between the initial and the considered time point, strongly depend on the composition of the sparged bubble. An air bubble has only 21 % of the initial oxygen content of an oxygen bubble and the much lower partial pressure also results in a much lower oxygen transfer to the liquid (see Figs. 5.13c and 5.13d). The transfer of oxygen to the liquid is also affected by the carbon dioxide, since the molar fraction of oxygen and thus its partial pressure is reduced through the uptake of carbon dioxide, which is observed for both the air and

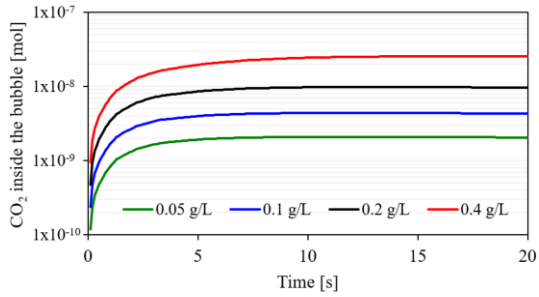

(a) Carbon dioxide in an air bubble

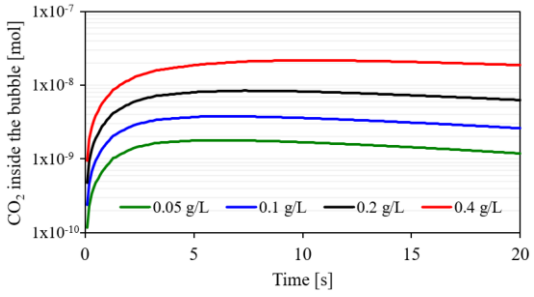

(b) Carbon dioxide in an oxygen bubble

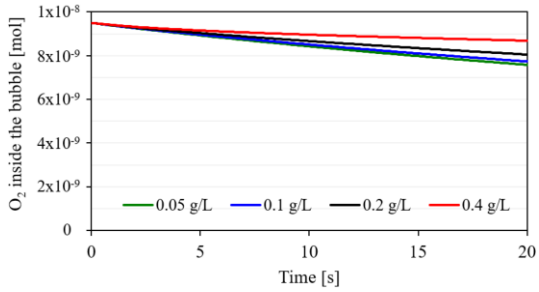

(c) Oxygen in an air bubble

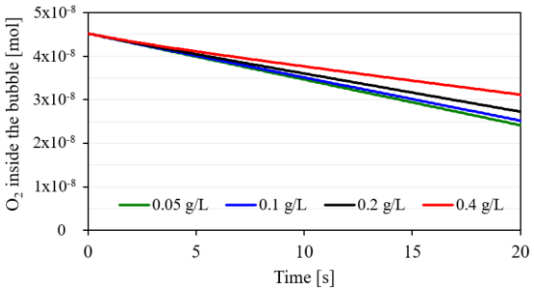

(d) Oxygen in an oxygen bubble

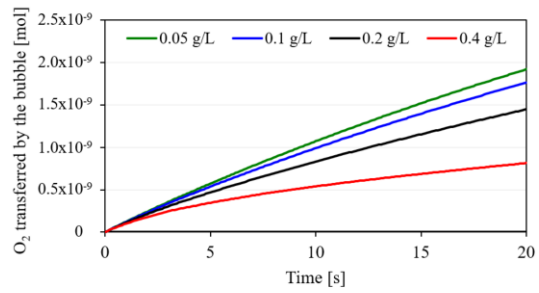

(e) Oxygen transfer by an air bubble

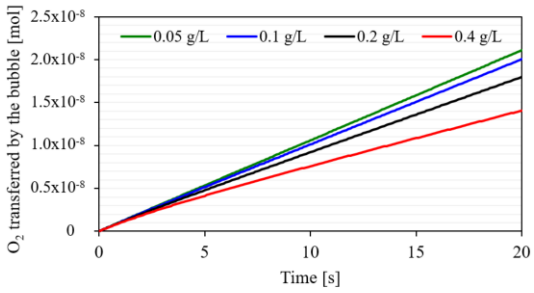

(f) Oxygen transfer by an oxygen bubble

Figure 5.13: Amount of substance of carbon dioxide and oxygen inside as well as oxygen transferred by single air and oxygen bubbles of 1.3 mm diameter at 10 W m^{-3} and 37°C for different dissolved carbon dioxide concentrations.

the oxygen bubble (see Figs. 5.13e and 5.13f).

To increase the $k_L a$, the impeller speed and consequently the volumetric power input can be increased or the bubble size can be reduced, which has been discussed previously in sections on the individual bioreactors. In Fig. 5.14 the carbon dioxide content and oxygen transfer for oxygen bubbles with a smaller diameter of 1.0 mm at the same volumetric power input of 10 W m^{-3} and with the same bubble diameter of 1.3 mm at an increased volumetric power input of 25 W m^{-3} are shown. For the smaller bubble diameter (Fig. 5.14a) as well as for the higher volumetric power input (Fig. 5.14b), the bubbles are saturated with carbon dioxide at an earlier time. The total uptake of carbon dioxide at saturation of bubbles with 1.0 mm diameter is about half of that of those with 1.3 mm diameter, since the volume of the smaller bubble is

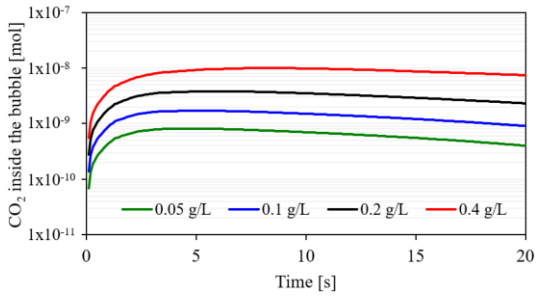

(a) Carbon dioxide for $d_b = 1.0$ mm at 10 W m^{-3}

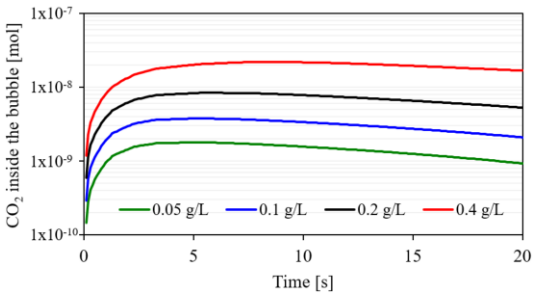

(b) Carbon dioxide $d_b = 1.3$ mm at 25 W m^{-3}

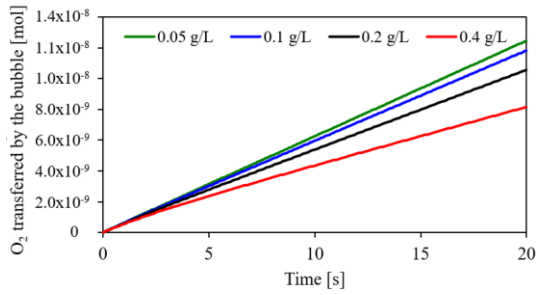

(c) Oxygen transfer for $d_b = 1.0$ mm at 10 W m^{-3}

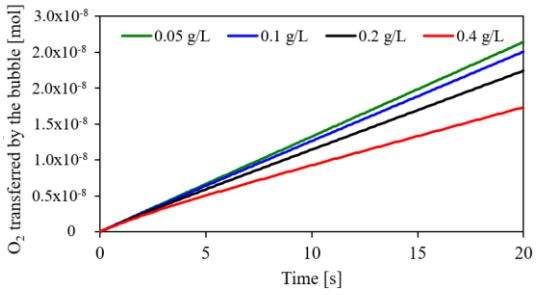

(d) Oxygen transfer for $d_b = 1.3$ mm at 25 W m^{-3}

Figure 5.14: Amount of substance of carbon dioxide inside as well as oxygen transferred by single oxygen bubbles at 37°C with 1.0 mm diameter at 10 W m^{-3} and with 1.3 mm diameter at 25 W m^{-3} for different dissolved carbon dioxide concentrations.

only about 46 % of that of the larger ones. The maximum uptake of carbon dioxide per volume of sparged gas is not increased by the smaller bubble size or the higher volumetric power input. The total amount of oxygen transferred by a single bubble is lower for the smaller bubble with diameter of 1.0 mm (see Fig. 5.14c) than for a larger one with a diameter of 1.3 mm (see Fig. 5.13f). However, when normalizing the total transfer by the bubble volume, the normalized oxygen transfer for the 1.0 mm bubble is higher, due to the higher specific interface area. At a higher volumetric power input both for the same bubbles size the oxygen transfer is also increased as can be seen by comparing Fig. 5.13f and 5.14d for 10 W m^{-3} and 25 W m^{-3}, respectively. In summary, while the oxygen transfer is improved by increasing the volumetric power input or decreasing the bubble diameter, the carbon dioxide stripping is not. If the bubbles are saturated with carbon dioxide, the carbon dioxide removal can only be improved through higher sparging rates.

If the bubble residence time is known, the dissolved carbon dioxide concentration in the liquid at steady conditions is the concentration at which the ratio of the oxygen transfer and the carbon dioxide removal by the bubbles equals the respiratory quotient, as described by Eq. (3.9). The residence times of bubbles generated by the microporous sparger for the XDR-200 and XDR-2000 are evaluated through one-way coupled Euler-

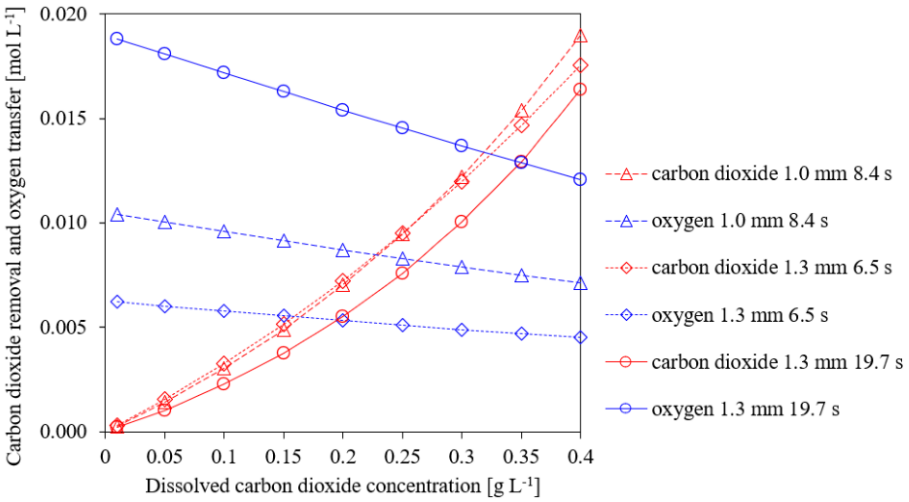

Figure 5.15: Mass transfer per L of sparged oxygen for different bubble residence times at 37°C and 10 W m^{-3}.

Lagrange simulations using MixIT [64]. For the XDR-200, the residence time of bubbles with 1.0 mm and 1.3 mm diameter at the maximum working volume of 200 L and an impeller speed of 91 rpm, which corresponds to a volumetric power input of 10 W m^{-3}, is determined as 8.4 s and 6.5 s, respectively. For the XDR-2000, the residence time of bubbles with 1.3 mm diameter for the maximum working volume of 2000 L at the impeller speed of 75 rpm, which also corresponds to 10 W m^{-3}, is 19.7 s. The oxygen transfer and carbon dioxide stripping per volume of sparged gas for the mentioned bubble residence times in dependence of the carbon dioxide concentration in the liquid are shown in Fig. 5.15.

The difference in the amount of carbon dioxide removed (red symbols) is relatively small for the different considered bubble residence times and diameters. For the evaluated operating condition of the XDR-200, the larger bubbles with 1.3 mm show slightly lower carbon dioxide removal at dissolved carbon dioxide concentrations of 0.4 g L^{-1} and higher than the 1.0 mm bubbles as they are not fully saturated at the considered residence time of 6.5 s (see Fig. 5.13b). For the considered residence time of the XDR-2000, the carbon dioxide removal is lower than for both considered bubble diameters of the XDR-200 because the continued transfer of oxygen from the bubbles to the liquid after the bubbles are saturated with carbon dioxide requires the transfer of carbon dioxide from the bubbles back to the liquid to maintain a constant molar fraction of both. The oxygen transfer per volume of sparged gas (blue symbols) is increased both by a smaller bubble size and a longer bubble residence time. For a respiratory quotient (see Eq. 3.10 of 1, the concentration at the intersect of the carbon dioxide removal and oxygen transfer plots in Fig. 5.15 for one specific combination of bubble size and bubbles residence time (indicated by the different markers) provides the expected dissolved carbon dioxide concentration in the liquid. For 1.3 mm and a residence time of 6.5 s (diamonds) the corresponding concentration is about 0.16 g L^{-1}, which equals a partial pressure of about 110 mmHg or about 14 % saturation with

carbon dioxide. For bubbles with 1 mm diameter and a residence time of 8.4 s and for bubbles with the 1.3 mm diameter and a residence time of 19.7 s, the expected concentrations are 0.23 g L^{-1} and 0.35 g L^{-1}, respectively.

In summary, the main observations are :

- sparging with pure oxygen instead of air increases the oxygen mass transfer but not the carbon dioxide mass transfer
- a higher volumetric power input increases transfer coefficients for both oxygen and carbon dioxide but when bubbles are saturated with carbon dioxide only the oxygen mass transfer is increased
- smaller bubbles with longer residence times improve the oxygen mass transfer but exacerbate the issue of carbon dioxide accumulation in the liquid
- the accumulation of carbon dioxide is more prevalent in larger bioreactors due the longer bubble residence time

These findings are in agreement with the observations reported by Sieblist et al. [4] and underline the fact that strategies enhancing oxygen mass transfer, i.e., sparging with pure oxygen, using microporous spargers, and increasing the impeller speed, do not improve the carbon dioxide mass transfer. If bubbles are saturated with carbon dioxide only larger sparging rates can improve the carbon dioxide stripping and to control both the dissolved oxygen and carbon dioxide simultaneous independent control of oxygen and carbon dioxide transfer is needed. One option to achieve this are dual sparging strategies [180, 181] using separate spargers for oxygen transfer and carbon dioxide stripping. Dual sparigng can also be used with the XDR-200 and the XDR-2000, which are both available with separate microporous and T-shaped drilled hole spargers. The next section considers the carbon dioxide concentration in the liquid phase.

5.5.2 Carbon Dioxide Mass Balance in the Liquid Phase

For calculating the liquid phase mass balance of carbon dioxide as described by Eq. (3.8), the oxygen transfer and carbon dioxide transfer by the bubbles must be known and depend on the bubble residence time. To account for variations of the amount of oxygen and carbon dioxide transferred for different carbon dioxide concentrations in the liquid, correlations for the transfer of oxygen and carbon dioxide per bubble normalized by the bubble volume, labeled $\Delta n^*_{O_2}$ and $\Delta n^*_{CO_2}$, are required. Based on the results shown in Fig. 5.15 a linear correlation for the oxygen transfer and a quadratic correlation for the carbon dioxide transfer as defined in Eqs. (5.8) and (5.9) are selected. The parameters of both correlation are fitted by minimizing the squared error with the *fminsearch* function in MATLAB [144].

$$\Delta n^*_{O_2} = k_1 + k_2 c_{CO_2^*} \tag{5.8}$$

$$\Delta n^*_{CO_2} = k_3 c^2_{CO_2^*} + k_4 c_{CO_2^*} \tag{5.9}$$

The fitted coefficients k_1, k_2, k_3, and k_4 for a bubble size of 1.3 mm and the residence times of 6.3 s and 19.7 s for the XDR-200 and XDR-2000, respectively, are given in

Table 5.9: Fitted coefficients for $\Delta n^*_{O_2}$ at 10 W m^{-3} and RMSE.

Bubble diameter [mm]	Residence time [s]	Gas composition	Fit Eqs. (5.8) k_1	k_2	RMSE
1.3	6.5	oxygen	0.0062	-0.0043	2.66x10^{-5}
1.3	19.7	oxygen	0.0189	-0.0173	4.27x10^{-5}
1.3	6.5	air	0.00067	-0.00080	0.38x10^{-5}
1.3	19.7	air	0.0018	-0.0027	1.72x10^{-5}

Tables 5.9 and 5.10. When considering different compositions of the bubbles, i.e., an initial molar fraction of 0.21 for air bubbles instead of 1.00 for oxygen bubbles, the coefficient k_1 for the transfer is reduced to about one tenth. This agrees well to the strong difference observed for the oxygen transfer of an air and an oxygen bubble, shown in Figs. 5.13e and 5.13f, respectively.

In addition to the transfer by the bubbles, the cell specific oxygen uptake rate q_{O_2} and carbon dioxide production rate q_{O_2} as well as the cell density are required to calculate the liquid phase mass balance of carbon dioxide. Goudar et al. [143] report values of 4.98 pmol d^{-1} cell^{-1} and 5.36 pmol d^{-1} cell^{-1} and a growth rate μ of 0.56 d^{-1} for CHO cells in perfusion culture at a pH of 7 and a dissolved oxygen concentration of 50 % air saturation. The change in cell density c_x is modeled based on the growth rate [183] as

$$\frac{dc_x}{dt} = \mu c_x. \tag{5.10}$$

To determine the biomass concentration, a hypothetical batch cultivation of this cell line with an exponential growth phase from inoculation until day 7 with $\mu = 0.56$ and a stationary phase from day 7 to 10 with $\mu = 0$ is considered. The initial cell density c_x is 0.3x10^9 cells L^{-1} and the initial concentration of the combined dissolved carbon dioxide and carbonic acid pool $c_{CO_2^*}$ is 0.073 g L^{-1}, which corresponds to partial pressure in the gas phase of 50 mmHg.

While in the ideal case of no adverse effects of changes in the bioreactor scale, the cell growth and the viable cell density are independent of the selected bioreactor.

Table 5.10: Fitted coefficients for $\Delta n^*_{CO_2}$ at 10 W m^{-3} and RMSE.

Bubble diameter [mm]	Residence time [s]	Gas composition	Fit Eq. (5.9) k_3	k_4	RMSE
1.3	6.5	oxygen	0.0386	0.0285	0.32x10^{-4}
1.3	19.7	oxygen	0.0643	0.0147	1.34x10^{-4}
1.3	6.5	air	0.0354	0.0325	0.32x10^{-4}
1.3	19.7	air	0.0609	0.0299	1.30x10^{-4}

However, the bubble residence time and consequently the oxygen and carbon dioxide transfer depend on the working volume of the bioreactor. Since the carbon dioxide accumulations is most severe for large biorector scales, the XDR-2000, which is the bioreactor with largest maximum working volume considered in the present study and the XDR-200 as bioreactor with an intermediate maximum working volume are considered in the further evaluation. The time profiles for c_x and $c_{CO_2^*}$ shown in Fig. 5.17 are obtained by solving Eqs. (5.10) and (3.8). For sparging with oxygen, $c_{CO_2^*}$ increases during the cultivation until it reaches a plateau at which the the oxygen and carbon dioxide transfer rates are equal as shown in Fig. 5.16a. The concentration at which this plateau is reached is slightly higher as that of the intersection points shown in Fig. 5.15, since the respiratory quotient for the considered cell specific rates of 1.08 is slightly larger than 1. Both the intersect in Fig. 5.15 and the steady concentration in Fig. 5.16a result in a higher $c_{CO_2^*}$ for the XDR-2000 due to the longer bubble residence time for the larger bioreactor as discussed above.

For sparging with air, $c_{CO_2^*}$ decreases during the cultivation until it reaches a plateau at a value lower than the initial concentration. Due to the much lower oxygen transfer rate of air bubbles, the oxygen and carbon dioxide transfer of the bubbles reach a comparable magnitude at a much lower carbon dioxide concentration. Similar to sparging with oxygen the steady value of $c_{CO_2^*}$ is lower for the XDR-200. While this is advantageous to avoid the accumulation of inorganic carbon species in the liquid, the draw back is that based on the transfer by the single bubbles about eight times higher sparging rates are required to match the oxygen requirements at the maximum cell density of 15.2x10^9 cells L^{-1}, i.e., 16.1 L min^{-1} instead of 1.9 L min^{-1} and 63.6 L min^{-1} instead of 8.4 L min^{-1} for the XDR-200 and the XDR-2000, respectively.

To simulate $c_{CO_2^*}$ for a dual sparging strategy for the XDR-2000, the bubble size and bubble residence time for bubble generated by the T-sparger must be known. The initial bubble diameter for the T-sparging wand with drilled holes of 2 mm diameter according to the correlation by Jamialahmadi et al. [173] changes with the sparging rate. For a sparging rate of 5 L min^{-1}, which corresponds to a volumetric sparging

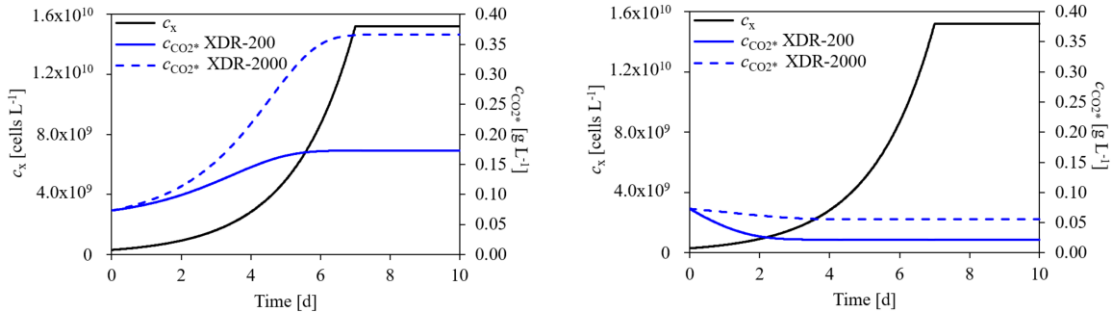

(a) Sparging with oxygen

(b) Sparging with air

Figure 5.16: Biomass concentration $c_{x,0}$ and concentration of the combined dissolved carbon dioxide and carbonic acid pool $c_{CO_2^*,0}$ for a hypothetical cultivation run at 10 W m^{-3} for sparging with oxygen and air for the XDR-200 and the XDR-2000.

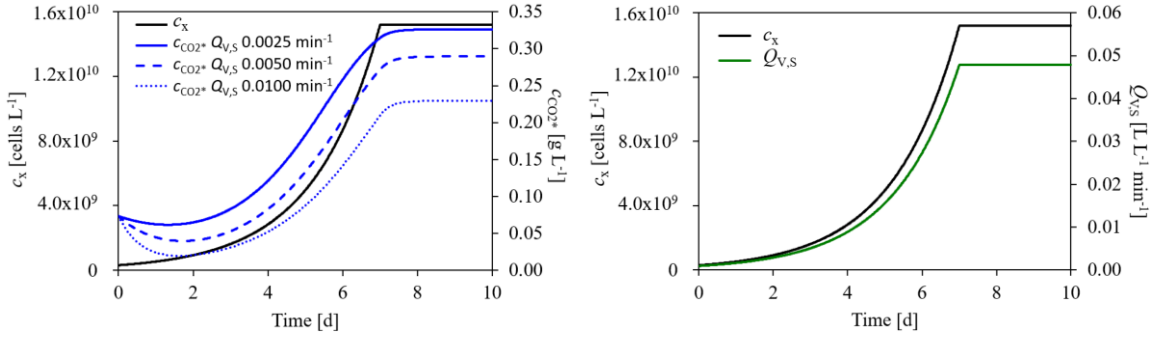

(a) $c_{CO_2^*}$ for constant $Q_{V,S}$ (b) $Q_{V,S}$ for constant $c_{CO_2^*}$

Figure 5.17: Biomass concentration c_x and concentration of the combined dissolved carbon dioxide and carbonic acid pool $c_{CO_2^*}$ for different volumetric stripping flow rates $Q_{V,S}$ (Fig. 5.17a) and required volumetric stripping flow rates to maintain a constant $c_{CO_2^*}$ (Fig. 5.17b) for the XDR-2000.

rate of 0.0025 min^{-1}, a bubble diameter of 5.7 mm is predicted for which the bubble residence time is 4.1 s. For carbon dioxide stripping typically air or nitrogen gas are used. To exclude any contribution of the stripping to the oxygen transfer, pure nitorgen gas is considered int he present simulations. The corresponding fitted coefficients k_3 and k_4 as well as the RMSE for the removal of carbon dioxide by sparging with nitrogen $\Delta n^*_{CO_2,S}$ are 0.0012, 0.0149, 7.15x10^{-6}, respectively. The additional removal of carbon dioxide is included in Eq. (3.8) as

$$\frac{dc_{CO_2^*}}{dt} = \phi_{CO_2^*}\left(c_x\left(q_{CO_2} - \frac{\Delta n^*_{CO_2}}{\Delta n^*_{O_2}} q_{O_2}\right) - \Delta n^*_{CO_2,S} Q_{V,S}\right). \tag{5.11}$$

A higher volumetric flow rate of nitrogen $Q_{V,S}$ results in a lower $c_{CO_2^*}$ as shown in Fig. 5.17a. At low cell densities during the first days of the cultivation, $c_{CO_2^*}$ is reduced below the initial concentration, while at higher cell densities $c_{CO_2^*}$ increases. To maintain a constant value of $c_{CO_2^*}$, $Q_{V,S}$ must increase with the cell density as shown in Fig. 5.17b. The value of $Q_{V,S}$ can be obtained by setting the right hand side of Eq. (5.11) to zero.

By combining single bubble mass transfer and the evaluation of the residence time of the bubbles from the one-way coupled Euler-Lagrange simulations, the present study provides insight into the mechanisms behind the accumulation of carbon dioxide during cell cultivation in large scale bioreactors. The present analysis is focused on the effects of the composition and the residence time of the bubbles on the carbon dioxide mass balance in the liquid and further details could be added to the model by including other aspects like Na_2CO_3 addition for pH control or changes of the working volume during fed batch cultivation.

6. Summary and Outlook

The present study provides cell culture relevant hydrodynamic characteristic for six commercially available single-use bioreactors of different volumes, the Mobius® CellReady 3 L (CR3), the Xcellerex™ XDR-10, the Xcellerex™ XDR-200, the Xcellerex™ XDR-500, the Xcellerex™ XDR-2000, and the Ambr® 250. One-way coupled Euler-Lagrange simulations using either the commercial software tool MixIT [64] or with the open source software tool OpenFOAM [63] have been carried out for all bioreactors. Additionally, Euler-Euler simulations have been carried out for the the Mobius® CellReady 3 L (CR3), the Xcellerex™ XDR-10, the Xcellerex™ XDR-200, and the Xcellerex™ XDR-2000 using OpenFOAM [63]. Moreover, two-way coupled Euler-Lagrange simulations have also been performed with OpenFOAM [63]. For the Euler-Lagrange and the Euler-Euler simulations, turbulence in the liquid is modeled with the standard $k-\varepsilon$ [120, 117] and the mixture $k-\varepsilon$ [127] models, respectively.

The investigated process aspects concern the mixing in the liquid phase, the risk of cell damage by mechanical stresses, and the volumetric oxygen mass transfer coefficient. As is expected for stirred tank bioreactors, the mixing time is found to increase with the working volume for any of the individual bioreactors and also for the larger working volume of the larger bioreactor scales. While a higher impeller speed can reduce the mixing time, mixing times as short as for the smallest considered bioreactor, the CR3, cannot be achieved for the largest considered bioreactor, the XDR-2000. For the CR3, the XDR-10, and the XDR-200, the experimental results on the mixing time shared by Tomomi Matsuura from Daiichi-Sankyo Co., Ltd., Japan confirm the described observations.

When comparing the results of the different modeling approaches against each other and with the experimental results, the expected strong impact of the working volume and the impeller speed on the mixing time are observed with all modeling approaches. The impact of the sparging rate on the mixing time is smaller than that of the working volume and the impeller speed. For this observation there is good agreement between the two-way coupled Euler-Lagrange and the Euler-Euler simulations but it cannot be captured in the one-way coupled Euler-Lagrange simulations, since the effect of the bubbles on the liquid motion is neglected. This also leads to slight differences in the liquid turbulence: for the considered range of operating conditions the average velocity magnitude is slightly higher and the average turbulence kinetic energy is slightly lower for the one-way coupled Euler-Lagrange simulations compared to the Euler-Euler and one-way coupled Euler-Lagrange simulations. Thus, it can be concluded that the impact of the bubbles on the liquid velocity and turbulence is minor compared

to that of the impeller speed but not negligible. Therefore, one-way coupled Euler-Lagrange simulations are good and fast method to achieve a first estimate of the relevant hydrodynamic process characteristics and might already be sufficient for many engineering purposes. However, by its design the one-way coupled Euler-Lagrange approach is not capable to resolve the interaction of the liquid with bubbles.

The Euler-Euler and the two-way coupled Euler-Lagrange approach both are able to capture the effect of the bubbles on the liquid motion and are in good agreement on the effect of the sparging rate on the mixing time. Both have their individual benefits and limitations. The two-way coupled Euler-Lagrange approach can resolve the motion of individual bubbles for which different diameters can be specified and the individual bubble's velocity is calculated. On the other hand, the Lagrangian treatment of the bubbles does not allow for phase inversion and the point mass treatment of the bubbles makes this approach sensitive to violations of the criterion that the bubbles should always be smaller than the control volumes. For a defined working volume within a stirred tank reactor, including volumetric coupling in the two-way coupled Euler-Lagrange simulations also poses a challenge. Since the computational domain has a fixed volume the displacement of the liquid by the bubbles cannot easily be compensated by the slight changes in the liquid height, which occur in an actual sparged stirred tank bioreactor, but require an appropriate design of the computational boundaries to allow for in and outflow of the liquid, while at the same time maintaining the correct liquid surface. The Euler-Euler approach provides less detailed information on the motion of the individual bubbles, since it only tracks the volume fraction of the considered phases, which on the other hand makes it numerically less sensitive to bubbles not being smaller than the computational control volume and always include volumetric coupling of the phases. Another aspect of tracking the disperse and continuous phases only by their volume fraction, is the fact that his cannot provide information on the type of the interface present within a control volume, i.e., disperse bubbles in a continuous liquid, disperse droplets in a continuous gas phase, or a segregated gas-liquid interface. However, despite the lack of resolution, the Euler-Euler approach can directly include changes of the shape and position of the liquid surface, allowing to capture surface vortex formation. Which modeling approach is better also depends on the investigated system and the focus of the simulations, e.g., resolving individual bubble trajectories or the shape of the liquid surface.

With regard to the selection of the impeller speed for cell culture scale-up, different criteria are reported in the literature to evaluate the risk of cell damage through mechanical stress [13, 44, 135, 47, 23]. The presented work has focused on the maximum hydrodynamic stress and the average strain rate in the impeller zone and both increase with the impeller (tip) speed for any of the individual bioreactors. However, despite the increase of the impeller tip speed associated with the larger impeller diameter for increasing bioreactor sizes, both the maximum hydrodynamic stress and the average strain rate of the impeller zone cover a comparable range of values for all considered bioreactor scales for the respective range of operating conditions. Moreover, the values observed for the largest scale, the XDR-2000, actually are on the lower end of the observed range. These results indicate that the impeller type and bioreactor

configuration also has a significant impact on the considered stress criteria and that they cannot simply be substituted by the impeller tip speed. Moreover, for the considered bioreactors, the impeller tip speed can be increased by a factor of 1.3 or more when scaling-up from the CR3 without increasing the risk of cell damage. No experimental results are available for the considered stress criteria but the described effects of the impeller speed and the bioreactor scale are in agreement to the results reported by Li et al. [23].

Across all bioreactor scales, the volumetric oxygen mass transfer coefficient increases for higher sparging rates and for spargers that generate smaller bubbles. A higher impeller speed and a lower working volume can also increase the volumetric oxygen mass transfer coefficient trough their impact on the bubble dispersion and the volumetric power input. However, the strength of the effect of the impeller speed and the working volume varies between the different bioreactors. For a given sparger type and bioreactor, a fixed bubble size has been selected and reasonable agreement of the simulated values of the volumetric oxygen mass transfer coefficient to the experimental results provided by Tomomi Matsuura, Takuya Nakano, and Takuma Eguchi from Daiichi-Sankyo Co., Ltd., Japan is found. By considering bubble diameters specific to the respective operating condition, the agreement between the simulations and the experiments is expected to be further improved, similar to the work of Bach et al. [97]. In the present study, only a monodisperse bubble size distribution is considered. This is sufficient to understand how the volumetric oxygen mass transfer coefficient is affected by changes in the operating conditions but does not capture the complexity of the polydisperse bubble size distribution actually present in stirred tank bioreactors. The modeling of the bubble size distributions with populations balance models is a topic that is still being investigated at the moment [114, 115, 61, 99] and further research in this direction, in combination with experimental observations on the bubble size can be expected to greatly improve the understanding of the complex interaction of the bubbles and the liquid.

In the present study, the focus is on the effect of the bioreactor scale on the volumetric oxygen mass transfer coefficient and comparable values can be achieved across all of the considered bioreactor scales. However, especially for the XDR-2000 a sufficiently high impeller speed is required to disperse the bubbles well across the cross-section of the bioreactor. The numerical results of the present study can be combined with the knowledge on the oxygen requirements and the stress tolerance of any cell line to optimally select the operating conditions using the investigated bioreactors. To leverage its full potential more information on the tolerances and requirements of different cell lines is required.

A scale-up strategy based on a constant average strain rate in the impeller zone, selected as the highest observed tolerable value for the initial lab-scale bioreactor, the CR3, for scaling up to the XDR-10, the XDR-200, and the XDR-2000 is proposed. The success of this strategy for scaling up from the CR3 to the XDR-10 and the XDR-200 is confirmed by cell culture results provided by Yuichi Aki from Daiichi-Sankyo Co., Ltd., Japan. The motivation for this strategy is to increase the impeller speed in order to optimize the mixing process as much as possible without the risk of cell damage.

However, the mixing time will increase for larger scales even for the proposed strategy and might still have negative impact on the cell cultivation, if the difference in the bioreactor scales is very large. The cell line considered in the present study might possibly tolerate even higher impeller speeds and strain rates but cell culture data on this has not been available. Moreover, increasing the averages strain rate of the impeller zone beyond the considered range is not possible for the largest investigated bioreactor, the XDR-2000, within the impeller speed range suggested by the supplier [166]. For the selected impeller speeds, for a constant superficial gas velocity comparable values of the volumetric oxygen mass transfer coefficient for the CR3, the XDR-200, and the XDR-2000 of up to about 8 h^{-1} are achieved, while for the XDR-10 the same superficial gas velocity results in higher values of the volumetric oxygen mass transfer coefficient. This emphasizes that the volumetric oxygen mass transfer coefficient depends on the bioreactor configuration and sparger type but, at least for the bioreactors considered in the present study, not on the bioreactor scale.

The present study provides an example how the comprehensive data available from CFD simulations can be used to scale-up the operating conditions of single-use bioreactors with geometrically dissimilar configurations by taking quantitative data on the mixing time, the risk of cell damage, and the volumetric oxygen mass transfer into account. The control of the hydrodynamic characteristics during scale-up is an important part of cell culture process development. The CFD simulations are independent of the cultivated cells, which makes them applicable to any cell line for which the rheological properties of the cultivation medium are the same.

The extension of the CFD simulations to model the biological processes of an actual cultivation including the cell growth, the substrate uptake, and the waste product formation must find solutions to handle a huge difference in time scales. The processes relevant for the hydrodynamic characteristics of the bioreactors, i.e., a single rotation of the impeller or a bubble rising from the sparger to the liquid surface, are processes taking place within a fraction of a second or up to several seconds. In contrast, the cell growth depends on the doubling time of the cultivated cells, which for mammalian cells is in the range of multiple hours or days with typical cultivations times of 10-14 days. One possibility to include both aspects are compartment models, where the CFD results are used to subdivide results on the (pseudo) steady flow conditions inside the bioreactor into different zones. Based on these zones the exchange between the different zones and the growth kinetics within each zone are calculated [73, 184]. A comprehensive model of cell culture within stirred tank bioreactors requires the inclusion of different model aspects with regard to the disperse bubbles and the cultivated cells and the combination of different modeling strategies is needed to cover the wide range of process time scales.

Bibliography

[1] F. Li, N. Vijayasankaran, A. Shen, R. Kiss, and A. Amanullah. Cell culture processes for monoclonal antibody production. *mAbs*, 2(5):466–479, 2010. doi: 10.4161/mabs.2.5.12720.

[2] N. K. Tripathi and A. Shrivastava. Recent developments in bioprocessing of recombinant proteins: Expression hosts and process development. *Front. Bioeng. Biotechnol.*, 7:420, 2019. doi: 10.3389/fbioe.2019.00420.

[3] R. Sander. Compilation of Henry's law constants (version 4.0) for water as solvent. *Atmos. Chem. Phys.*, 15(8):4399–4981, 2015. doi: 10.5194/acp-15-4399-2015.

[4] C. Sieblist, O. Hageholz, M. Aehle, M. Jenzsch, M. Pohlscheidt, and A. Lubbert. Insights into large-scale cell-culture reactors: II. Gas-phase mixing and CO_2 stripping. *Biotechnol. J.*, 6(12):1547–1556, 2011. doi: 10.1002/biot.201100153.

[5] F. M. Wurm. Production of recombinant protein therapeutics in cultivated mammalian cells. *Nat. Biotechnol.*, 22(11):1393–1398, 2004. doi: 10.1038/nbt1026.

[6] V. Jossen, R. Eibl, and D. Eibl. Single-use bioreactors – an overview. In *Single-Use Technology in Biopharmaceutical Manufacture*, book section 4, pages 37–52. John Wiley & Sons, Inc., 2019.

[7] R. Eibl, C. Löffelholz, and D. Eibl. Single-use bioreactors— an overview. In Regine Eibl and Dieter Eibl, editors, *Single-Use Technology in Biopharmaceutical Manufacturing*. John Wiley & Sons, Inc., 2011.

[8] S. Junne and P. Neubauer. How scalable and suitable are single-use bioreactors? *Curr. Opin. Biotechnol.*, 53:240–247, 2018. doi: 10.1016/j.copbio.2018.04.003.

[9] S. J. Wewetzer, M. Kunze, T. Ladner, B. Luchterhand, S. Roth, N. Rahmen, R. Kloss, E. Silva A. Costa, L. Regestein, and J. Buchs. Parallel use of shake flask and microtiter plate online measuring devices (RAMOS and BioLector) reduces the number of experiments in laboratory-scale stirred tank bioreactors. *J. Biol. Eng.*, 9:9, 2015. doi: 10.1186/s13036-015-0005-0.

[10] F. Kensy, C. Engelbrecht, and J. Buchs. Scale-up from microtiter plate to laboratory fermenter: evaluation by online monitoring techniques of growth and protein expression in *Escherichia coli* and *Hansenula polymorpha* fermentations. *Microb. Cell Fact.*, 8:68, 2009. doi: 10.1186/1475-2859-8-68.

[11] Cytiva, 2022. https://CDn.cytivalifesciences.com/dmm3bwsv3/AssetStream.aspx ?mediaformatid=10061&destinationid=10016&assetid=16212, (Accessed on March 15,2022).

[12] W. J. Kelly. Using computational fluid dynamics to characterize and improve bioreactor performance. *Appl. Biochem. Biotechnol.*, 49(4):225–238, 2008. doi: 10.1042/BA20070177.

[13] A. W. Nienow. Reactor engineering in large scale animal cell culture. *Cytotechnology*, 50:9–33, 2006. doi: 10.1007/s10616-006-9005-8.

[14] E. Ratcliffe, K. E. Glen, V. L. Workman, A. J. Stacey, and R. J. Thomas. A novel automated bioreactor for scalable process optimisation of haematopoietic stem cell culture. *J. Biotechnol.*, 161(3):387–390, 2012. doi: 10.1016/j.jbiotec.2012.06.025.

[15] M. Tai, A. Ly, I. Leung, and G. Nayar. Efficient high-throughput biological process characterization: Definitive screening design with the ambr250 bioreactor system. *Biotechnol. Prog.*, 31(5):1388–1395, 2015. doi: 10.1002/btpr.2142.

[16] D. B. Nickel, M. N. Cruz-Bournazou, T. Wilms, P. Neubauer, and A. Knepper. Online bioprocess data generation, analysis, and optimization for parallel fed-batch fermentations in milliliter scale. *Eng. Life Sci.*, 17(11):1195–1201, 2017. doi: 10.1002/elsc.201600035.

[17] N. Kantarci, F. Borak, and K. O. Ulgen. Bubble column reactors. *Process. Biochem.*, 40(7):2263–2283, 2005. doi: 10.1016/j.procbio.2004.10.004.

[18] S. C. Kaiser, C. Löffelholz, S. Werner, and D. Eibl. CFD for characterizing standard and single-use stirred cell culture bioreactors. In Igor Minin, editor, *Computational Fluid Dynamics Technologies and Applications*, chapter 4, pages 97–122. InTech, 2011.

[19] C. Löffelholz, U. Husemann, G. Greller, W. Meusel, J. Kauling, P. Ay, M. Kraume, R. Eibl, and D. Eibl. Bioengineering parameters for single-use bioreactors: Overview and evaluation of suitable methods. *Chem. Ing. Tech.*, 85(1-2):40–56, 2013. doi: 10.1002/cite.201200125.

[20] E. L. Paul, V. A. Atiemo-Obeng, and S. M. Kresta. *Handbook of Industrial Mixing: Science and Practice*. John Wiley & Sons, Inc., Hoboken, New Jersey, 2004.

[21] F. R. Schmidt. Optimization and scale up of industrial fermentation processes. *Appl. Microbiol. Biotechnol.*, 68(4):425–35, 2005. doi: 10.1007/s00253-005-0003-0.

[22] R. C. Telling and R. Elsworth. Submerged culture of hamster kidney cells in a stainless steel vessel. *Biotechnol. Bioeng.*, 7:417–434, 1965.

[23] C. Li, X. Teng, H. Peng, X. Yi, Y. Zhuang, S. Zhang, and J. Xia. Novel scale-up strategy based on three-dimensional shear space for animal cell culture. *Chem. Eng. Sci.*, 212:115329, 2020. doi: 10.1016/j.ces.2019.115329.

[24] J. Scully, L. B. Considine, M. T. Smith, E. McAlea, N. Jones, E. O'Connell, E. Madsen, M. Power, P. Mellors, J. Crowley, N. O'Leary, S. Carver, and D. Van Plew. Beyond heuristics: CFD-based novel multiparameter scale-up for geometrically disparate bioreactors demonstrated at industrial 2kL-10kL scales. *Biotechnol. Bioeng.*, 117(6):1710–1723, 2020. doi: 10.1002/bit.27323.

[25] J. Xia, G. Wang, M. Fan, M. Chen, Z. Wang, and Y. Zhuang. Understanding the scale-up of fermentation processes from the viewpoint of the flow field in bioreactors and the physiological response of strains. *Chin. J. Chem. Eng.*, 30: 178–184, 2021. doi: 10.1016/j.cjche.2020.12.004.

[26] J. D. Yang, C. Lu, B. Stasny, J. Henley, W. Guinto, C. Gonzalez, J. Gleason, M. Fung, B. Collopy, M. Benjamino, J. Gangi, M. Hanson, and E. Ille. Fed-batch bioreactor process scale-up from 3-L to 2,500-L scale for monoclonal antibody production from cell culture. *Biotechnol. Bioeng.*, 98(1):141–54, 2007. doi: 10.1002/bit.21413.

[27] H. M. Jung, S. Y. Kim, P. Prabhu, H. J. Moon, I. W. Kim, and J. K. Lee. Optimization of culture conditions and scale-up to plant scales for teicoplanin production by actinoplanes teichomyceticus. *Appl Microbiol Biotechnol*, 80(1): 21–27, 2008. doi: 10.1007/s00253-008-1530-2.

[28] B. S. Borys, E. L. Roberts, A. Le, and M. S. Kallos. Scale-up of embryonic stem cell aggregate stirred suspension bioreactor culture enabled by computational fluid dynamics modeling. *Biochem. Eng. J.*, 133:157–167, 2018. doi: 10.1016/j.bej.2018.02.005.

[29] Z. Xing, B. M. Kenty, Z. J. Li, and S. S. Lee. Scale-up analysis for a CHO cell culture process in large-scale bioreactors. *Biotechnol Bioeng*, 103(4):733–746, 2009. doi: 10.1002/bit.22287.

[30] B. Neunstoecklin, T. K. Villiger, E. Lucas, M. Stettler, H. Broly, M. Morbidelli, and M. Soos. Pilot-scale verification of maximum tolerable hydrodynamic stress for mammalian cell culture. *Appl. Microbiol. Biotechnol.*, 100(8):3489–98, 2016. doi: 10.1007/s00253-015-7193-x.

[31] G. Nadal-Rey, D. D. McClure, J. M. Kavanagh, S. Cornelissen, D. F. Fletcher, and K. V. Gernaey. Understanding gradients in industrial bioreactors. *Biotechnol. Adv.*, 46:107660, 2021. doi: 10.1016/j.biotechadv.2020.107660.

[32] F. Garcia-Ochoa and E. Gomez. Bioreactor scale-up and oxygen transfer rate in microbial processes: an overview. *Biotechnol. Adv.*, 27(2):153–176, 2009. doi: 10.1016/j.biotechadv.2008.10.006.

[33] L. Veiter, V. Rajamanickam, and C. Herwig. The filamentous fungal pellet-relationship between morphology and productivity. *Appl Microbiol Biotechnol*, 102(7):2997–3006, 2018. doi: 10.1007/s00253-018-8818-7.

[34] W. Hu, C. Berdugo, and J. J. Chalmers. The potential of hydrodynamic damage to animal cells of industrial relevance: current understanding. *Cytotechnology*, 63:445–460, 2011. doi: 10.1007/s10616-011-9368-3.

[35] S. Seidel, R. W. Maschke, S. Werner, V. Jossen, and D. Eibl. Oxygen mass transfer in biopharmaceutical processes: numerical and experimental approaches. *Chem. Ing. Tech.*, 93(1):42–61, 2021. doi: 10.1002/cite.202000179.

[36] K. Paul and C. Herwig. Scale-down simulators for mammalian cell culture as tools to access the impact of inhomogeneities occurring in large-scale bioreactors. *Eng. Life Sci.*, 20(5-6):197–204, 2020. doi: 10.1002/elsc.201900162.

[37] R. Jiang, H. Chen, and S. Xu. ph excursions impact CHO cell culture performance and antibody N-linked glycosylation. *Bioprocess Biosyst Eng*, 41(12):1731–1741, 2018. doi: 10.1007/s00449-018-1996-y.

[38] O. Šrom, V. Trávníková, J. Wutz, M. Kuschel, A. Unsoeld, T. Wucherpfennig, and M. Šoóš. Characterization of hydrodynamic stress in ambr250® bioreactor system and its impact on mammalian cell culture. *Biochem. Eng. J.*, 177, 2022. doi: 10.1016/j.bej.2021.108240.

[39] M. P. C. Marques, J. M. S. Cabral, and P. Fernandes. Bioprocess scale-up: quest for the parameters to be used as criterion to move from microreactors to lab-scale. *Chem. Technol. Biotechnol.*, 85(9):1184–1198, 2010. doi: 10.1002/jctb.2387.

[40] T. Doi, H. Kajihara, Y. Chuman, S. Kuwae, T. Kaminagayoshi, and T. Omasa. Development of a scale-up strategy for chinese hamster ovary cell culture processes using the $k_{\mathrm{L}}a$ ratio as a direct indicator of gas stripping conditions. *Biotechnol. Prog.*, 36(5):e3000, 2020. doi: 10.1002/btpr.3000.

[41] S. Xu, L. Hoshan, R. Jiang, B. Gupta, E. Brodean, K. O'Neill, T. C. Seamans, J. Bowers, and H. Chen. A practical approach in bioreactor scale-up and process transfer using a combination of constant P/V and vvm as the criterion. *Biotechnol. Prog.*, 33(4):1146–1159, 2017. doi: 10.1002/btpr.2489.

[42] S. Werner, S. Kaiser, M. Kraume, and D. Eibl. Computational fluid dynamics as a modern tool for engineering characterization of bioreactors. *Pharm. Bioprocess.*, 2:85–99, 2014.

[43] C. Sieblist, M. Jenzsch, and M. Pohlscheidt. Equipment characterization to mitigate risks during transfers of cell culture manufacturing processes. *Cytotechnology*, 68(4):1381–1401, 2016. doi: 10.1007/s10616-015-9899-0.

[44] Y. Chisti. Hydrodynamic damage to animal cells. *Crit. Rev. Biotechnol.*, 21: 67–110, 2001. doi: 10.1080/20013891081692.

[45] S. C. Kaiser, R. Eibl, and D. Eibl. Engineering characteristics of a single-use stirred bioreactor at bench-scale: The Mobius CellReady 3L bioreactor as a case study. *Eng. Life Sci.*, 11(4):359–368, 2011. doi: 10.1002/elsc.201000171.

[46] K. Van't Riet. Review of measuring methods and results in nonviscous gas-liquid mass transfer in stirred vessels. *Ind. Eng. Chem. Process Des. Dev.*, 18(3): 357–362, 1979.

[47] B. Neunstoecklin, M. Stettler, T. Solacroup, H. Broly, M. Morbidelli, and M. Soos. Determination of the maximum operating range of hydrodynamic stress in mammalian cell culture. *J. Biotechnol.*, 194:100–109, 2015. doi: 10.1016/j.jbiotec.2014.12.003.

[48] R. Takors. Scale-up of microbial processes: Impacts, tools and open questions. *J. Biotechnol.*, 160(1):3–9, 2012. doi: 10.1016/j.jbiotec.2011.12.010. Genome-based Microbiology From -omics Research to Systems and Synthetic Biology.

[49] A. S. Rathore. Roadmap for implementation of quality by design (QbD) for biotechnology products. *Trends. Biotechnol*, 27(9):546–53, 2009. doi: 10.1016/j.tibtech.2009.06.006.

[50] J. A. Serrato, L. A. Palomares, A. Meneses-Acosta, and O. T. Ramírez. Heterogeneous conditions in dissolved oxygen affect N-glycosylation but not productivity of a monoclonal antibody in hybridoma cultures. *Biotechnol. Bioeng.*, 88(2): 176–188, 2004. doi: 10.1002/bit.20232.

[51] J. Gimbun, C. D. Rielly, and Z. K. Nagy. Modelling of mass transfer in gas–liquid stirred tanks agitated by Rushton turbine and CD-6 impeller: A scale-up study. *Chem. Eng. Res. Des.*, 87(4):437–451, 2009. doi: 10.1016/j.cherd.2008.12.017.

[52] M. C. Martinetz, F. Kaiser, M. Kellner, D. Schlosser, A. Lange, M. Brueckner-Pichler, C. Brocard, and M. Šoóš. Hybrid approach for mixing time characterization and scale-up in geometrical nonsimilar stirred vessels equipped with eccentric multi-impeller systems—an industrial perspective. *Processes*, 9(5):880, 2021. doi: 10.3390/pr9050880.

[53] X. Zhang, J. Moroney, L. Hoshan, R. Jiang, and S. Xu. Systematic evaluation of high-throughput scale-down models for single-use bioreactors (SUB) using volumetric gas flow rate as the criterion. *Biochem. Eng. J.*, 151:107307, 2019. doi: 10.1016/j.bej.2019.107307.

[54] J. B. Sieck, T. Cordes, W. E. Budach, M. H. Rhiel, Z. Suemeghy, C. Leist, T. K. Villiger, M. Morbidelli, and M. Soos. Development of a scale-down model of hydrodynamic stress to study the performance of an industrial CHO cell line under simulated production scale bioreactor conditions. *J. Biotechnol.*, 164(1): 41–49, 2013. doi: 10.1016/j.jbiotec.2012.11.012.

[55] A. W. Nienow, C. D. Rielly, K. Brosnan, N. Bargh, K. Lee, K. Coopman, and C. J. Hewitt. The physical characterisation of a microscale parallel bioreactor platform with an industrial CHO cell line expressing an IgG4. *Biovhem. Eng. J.*, 76:25–36, 2013. doi: 10.1016/j.bej.2013.04.011.

[56] Y. Gao, S. Ray, S. Dai, A. R. Ivanov, N. R. Abu-Absi, A. M. Lewis, Z. Huang, Z. Xing, M. C. Borys, Z. J. Li, and B. L. Karger. Combined metabolomics and proteomics reveals hypoxia as a cause of lower productivity on scale-up to a 5000-liter CHO bioprocess. *Biotechnol J*, 11(9):1190–200, 2016. doi: 10.1002/biot.201600030.

[57] R. Godoy-Silva, J. J. Chalmers, S. A. Casnocha, L. A. Bass, and N. Ma. Physiological responses of CHO cells to repetitive hydrodynamic stress. *Biotechnol Bioeng*, 103(6):1103–1117, 2009. doi: 10.1002/bit.22339.

[58] C. He, P. Ye, H. Wang, X. Liu, and F. Li. A systematic mass-transfer modeling approach for mammalian cell culture bioreactor scale-up. *Biochem. Eng. J.*, 141: 173–181, 2019. doi: 10.1016/j.bej.2018.09.019.

[59] Z. Xing, A. M. Lewis, M. C. Borys, and Z. J. Li. A carbon dioxide stripping model for mammalian cell culture in manufacturing scale bioreactors. *Biotechnol. Bioeng.*, 114(6):1184–1194, 2017. doi: 10.1002/bit.26232.

[60] A. O. Odeleye, D. T. Marsh, M. D. Osborne, G. J. Lye, and M. Micheletti. On the fluid dynamics of a laboratory scale single-use stirred bioreactor. *Chem. Eng. Sci.*, 111(100):299–312, 2014. doi: 10.1016/j.ces.2014.02.032.

[61] S. Mishra, V. Kumar, J. Sarkar, and A. S. Rathore. CFD based mass transfer modeling of a single use bioreactor for production of monoclonal antibody biotherapeutics. *Chem. Eng. J.*, 412, 2021. doi: 10.1016/j.cej.2021.128592.

[62] B. Minow, J. Seidemann, S. Tschoepe, A. Gloeckner, and P. Neubauer. Harmonization and characterization of different single-use bioreactors adopting a new sparger design. *Eng. Life Sci.*, 14(3):272–282, 2014. doi: 10.1002/elsc.201300130.

[63] OpenFOAM. The OpenFOAM Foundation. 2019. www.openfoam.org, (Accessed on August 20, 2019).

[64] MixIT. Tridiagonal® Solutions. 2019. https://tridiagonal.com/mixit/, (Accessed on April 4, 2019).

[65] A. Brucato, M. Ciofalo, F. Grisafi, and G. Micale. Numerical prediction of flow fields in baffled stirred vessels: A comparison of alternative modelling approaches. *Chem. Eng. Sci.*, 53(21):3653–3684, 1998. doi: 10.1016/S0009-2509(98)00149-3.

[66] I. González-Neria, A. Alonzo-Garcia, S. A. Martínez-Delgadillo, V. X. Mendoza-Escamilla, J. A. Yáñez-Varela, P. G. Verdin, and G. Rivadeneyra-Romero. PIV and dynamic LES of the turbulent stream and mixing induced by a V-grooved

blade axial agitator. *Chem. Eng. J.*, 374:1138–1152, 2019. doi: 10.1016/j.cej.2019.06.033.

[67] M. Laakkonen, M. Honkanen, P. Saarenrinne, and J. Aittamaa. Local bubble size distributions, gas–liquid interfacial areas and gas holdups in a stirred vessel with particle image velocimetry. *Chem. Eng. J.*, 109(1-3):37–47, 2005. doi: 10.1016/j.cej.2005.03.002.

[68] D. Gradov. *Experimentally validated numerical modelling of reacting multiphase flows in stirred tank reactors*. Ph.D. thesis, Lappeenranta-Lahti University of Technology, Lappeenranta, 2019.

[69] M. Kuschel, F. Siebler, and R. Takors. Lagrangian trajectories to predict the formation of population heterogeneity in large-scale bioreactors. *Bioeng.*, 4(2), 2017. doi: 10.3390/bioengineering4020027.

[70] C. Haringa, W. Tang, A. T. Deshmukh, J. Xia, M. Reuss, J. J. Heijnen, R. F. Mudde, and H. J. Noorman. Euler-Lagrange computational fluid dynamics for (bio)reactor scale down: An analysis of organism lifelines. *Eng. Life Sci.*, 16(7): 652–663, 2016. doi: 10.1002/elsc.201600061.

[71] A. Lapin, D. Reuss, and M. Müller. Dynamic behavior of microbial populations in stirred bioreactors simulated with Euler-Lagrange methods: Traveling along the lifelines of single cells. *Ind. Eng. Chem. Res*, 43:4547–4656, 2004. doi: 10.1021/ie030786k.

[72] Y. Liu, Z.-J.n Wang, J. Xia, C. Haringa, J. Liu, Y.and Chu, Y.-P. Zhuang, and S.-L. Zhang. Application of Euler-Lagrange CFD for quantitative evaluating the effect of shear force on *Carthamus tinctorius* L. cell in a stirred tank bioreactor. *Biochem. Eng. J.*, 114:209–217, 2016. doi: 10.1016/j.bej.2016.07.006.

[73] A. Delafosse, M. Collignon, S. Calvo, F. Delvigne, M. Crine, P. Thonart, and D. Toye. CFD-based compartment model for description of mixing in bioreactors. *Chem. Eng. Sci.*, 106:76–85, 2014. doi: 10.1016/j.ces.2013.11.033.

[74] M. Soos, R. Kaufmann, R. Winteler, M. Kroupa, and B. Lüthi. Determination of maximum turbulent energy dissipation rate generated by a Rushton impeller through large eddy simulation. *AIChE J.*, 59(10):3642–3658, 2013. doi: 10.1002/aic.14206.

[75] C. Johnson, V. Natarajan, and C. Antoniou. Verification of energy dissipation rate scalability in pilot and production scale bioreactors using computational fluid dynamics. *Biotechnol. Prog.*, 30(3):760–4, 2014. doi: 10.1002/btpr.1896.

[76] A. de Lamotte, A. Delafosse, S. Calvo, and D. Toye. Identifying dominant spatial and time characteristics of flow dynamics within free-surface baffled stirred-tanks from CFD simulations. *Chem. Eng. Sci.*, 192:128–142, 2018. doi: 10.1016/j.ces.2018.07.024.

[77] T. Yamamoto, Y. Fang, and S. V. Komarov. Surface vortex formation and free surface deformation in an unbaffled vessel stirred by on-axis and eccentric impellers. *Chem. Eng. J.*, 367:25–36, 2019. doi: 10.1016/j.cej.2019.02.130.

[78] S. Başbuğ, G. Papadakis, and J.C. Vassilicos. DNS investigation of the dynamical behaviour of trailing vortices in unbaffled stirred vessels at transitional Reynolds nufmbers. *Phys. Fluids*, 29:0614101, 2017. doi: 10.1063/1.4983494.

[79] S. Başbuğ, G. Papadakis, and J.C. Vassilicos. Direct numerical simulations of creeping to early turbulent flow in unbaffled and baffled stirred tanks. *Chem. Eng. Sci.*, 192:161–175, 2018. doi: 10.1016/j.ces.2018.07.023.

[80] Chang. Q., S. Di, J. Xu, and W. Ge. Direct numerical simulation of turbulent liquid-solid flow in a small-scale stirred tank. *Chem. Eng. J.*, 420:127562, 2021. ISSN 1385-8947. doi: https://doi.org/10.1016/j.cej.2020.127562.

[81] M.-L. Collignon, A. Delafosse, S. Calvo, C. Martin, A. Marc, D. Toye, and E. Olmos. Large-eddy simulations of microcarrier exposure to potentially damaging eddies inside mini-bioreactors. *Biochem. Eng. J.*, 108:30–43, 2016. doi: 10.1016/j.bej.2015.10.020.

[82] A. Delafosse, A. Line, J. Morchain, and P. Guiraud. LES and URANS simulations of hydrodynamics in mixing tank: Comparison to PIV experiments. *Chem. Eng. Res. and Des.*, 86(12):1322–1330, 2008. doi: 10.1016/j.cherd.2008.07.008.

[83] M. Sommerfeld. Numerical methods for dispersed multiphase flows. In T. Bodnár, G. P. Galdi, and Š. Nečasová, editors, *Particles in Flows*, Advances in Mathematical Fluid Mechanics, chapter 6, pages 327–396. Springer International Publishing, 2017. doi: 10.1007/978-3-319-60282-0_6.

[84] J. Wutz, Alexey Lapin, F. Siebler, J. E. Schäfer, T. Wucherpfennig, M. Berger, and R. Takors. Predictability of k_La in stirred tank reactors under multiple operating conditions using an Euler-Lagrange approach. *Eng. Life Sci.*, 16(7): 633–642, 2016. doi: 10.1002/elsc.201500135.

[85] R. Sungkorn, J. J. Derksen, and J. G. Khinast. Modeling of aerated stirred tanks with shear-thinning power law liquids. *Int. J. Heat Fluid Flow*, 36:153–166, 2012. doi: 10.1016/j.ijheatfluidflow.2012.04.006.

[86] R. Sungkorn, J. J. Derksen, and J. G. Khinast. Euler-Lagrange modeling of a gas-liquid stirred reactor with consideration of bubble breakage and coalescence. *AIChE J.*, 58(5):1356–1370, 2012. doi: 10.1002/aic.12690.

[87] M. Muniz and M. Sommerfeld. On the force competition in bubble columns: A numerical study. *Int. J. Multiph. Flow*, 128:103256, 2020. doi: 10.1016/j.ijmultiphaseflow.2020.103256.

[88] M. V. Masterov, M. W. Baltussen, and J. A. M. Kuipers. Numerical simulation of a square bubble column using detached eddy simulation and Euler–Lagrange approach. *Int. J. Multiph. Flow*, 107:277–288, 2018. doi: 10.1016/j.ijmultiphaseflow.2018.06.006.

[89] G. Sardina, K. Jareteg, H. Ström, and S. Sasic. Assessing the ability of the Eulerian-Eulerian and the Eulerian-Lagrangian frameworks to capture meso-scale dynamics in bubbly flows. *Chem. Eng. Sci.*, 201:58–73, 2019. doi: 10.1016/j.ces.2019.02.022.

[90] E. Shams, J. Finn, and S. V. Apte. A numerical scheme for Euler-Lagrange simulation of bubbly flows in complex systems. *Int. J. Numer. Methods Fluids*, 67(12):1865–1898, 2011. doi: 10.1002/fld.2452.

[91] J. Xue, F. Chen, N. Yang, and E. Ge. A study of the soft-sphere model in eulerian- lagrangian simulation of gas-liquid flow. *Int. J. Chem. React.*, 15(1):57–67, 2017. doi: 10.1515/ijcre-2016-0064.

[92] J. Wutz, A. Lapin, F. Siebler, J. E. Schäfer, T. Wucherpfennig, M. Berger, and R. Takors. Predictability of k_La in stirred tank reactors under multiple operating conditions using an Euler-Lagrange approach. *Eng. Life Sci.*, 16:633–642, 2016. doi: 10.1002/elsc.201500135.

[93] V. Santos-Moreau, J. C. B. Lopes, and C. P. Fonte. Estimation of k_la values in bench-scale stirred tank reactors with self-inducing impeller by multiphase CFD simulations. *Chem. Eng. Technol.*, 2019. doi: 10.1002/ceat.201900162.

[94] Chenghui Zheng, Jiashun Guo, Chengkai Wang, Yuanfeng Chen, Huidong Zheng, Zuoyi Yan, and Qinggen Chen. Experimental study and simulation of a three-phase flow stirred bioreactor. *Chin. J. Chem. Eng.*, 2018. doi: 10.1016/j.cjche.2018.06.010.

[95] A. Kazemzadeh, C. Elias, M. Tamer, and F. Ein-Mozaffari. Hydrodynamic performance of a single-use aerated stirred bioreactor in animal cell culture: applications of tomography, dynamic gas disengagement (DGD), and CFD. *Bioprocess Biosyst. Eng.*, 41(5):679–695, 2018. doi: 10.1007/s00449-018-1902-7.

[96] T. T. Devi and B. Kumar. Mass transfer and power characteristics of stirred tank with Rushton and curved blade impeller. *Eng. Sci. Technol. an Int. J.*, 20 (2):730–737, 2017. doi: 10.1016/j.jestch.2016.11.005.

[97] C. Bach, J. Yang, H. Larsson, S. M. Stocks, K. V. Grenaey, M. O. Albaek, and U. Kühne. Evaluation of mixing and mass transfer in a stirred pilot scale bioreactor utilizing CFD. *Chem. Eng. Sci.*, 171:19–26, 2017. doi: 10.1016/j.ces.2017.05.001.

[98] X. Guan, X. Li, N. Yang, and M. Liu. CFD simulation of gas-liquid flow in stirred tanks: Effect of drag models. *Chem. Eng. J.*, 386:121554, 2020. doi: 10.1016/j.cej.2019.04.134.

[99] A. Mühlbauer, M. W. Hlawitschka, and H.-J. Bart. Models for the numerical simulation of bubble columns: A review. *Chem. Ing. Tech.*, 91(12):1747–1765, 2019. doi: 10.1002/cite.201900109.

[100] J. Sarkar, L. K. Shekhawat, V. Loomba, and A. S. Rathore. CFD of mixing of multi-phase flow in a bioreactor using population balance model. *Biotechnol. Prog.*, 32:613–628, 2016. doi: 10.1002/btpr.2242.

[101] P. Moilanen, M. Laakkonen, O. Visuri, V. Alopaeus, and J. Aittamaa. Modelling mass transfer in an aerated 0.2 m^3 vessel agitated by Rushton, Phasejet and Combijet impellers. *Chem. Eng. J.*, 142(1):95–108, 2008. doi: 10.1016/j.cej.2008.01.033.

[102] G. Montante, D. Horn, and A. Paglianti. Gas-liquid flow and bubble size distribution in stirred tanks. *Chem. Eng. Sci.*, 63:2107–2118, 2008. doi: 10.1016/j.ces.2008.01.005.

[103] F. Kerdouss, A. Bannari, P. Proulx, R. Bannari, M. Skrga, and Y. Labrecque. Two-phase mass transfer coefficient prediction in stirred vessel with a CFD model. *Comput. Chem. Eng.*, 32(8):1943–1955, 2008. doi: 10.1016/j.compchemeng.2007.10.010.

[104] M. Petitti, M. Vanni, D. L. Marchisio, A. Buffo, and F. Podenzani. Simulation of coalescence, break-up and mass transfer in a gas–liquid stirred tank with CQMOM. *Chem. Eng. J.*, 228:1182–1194, 2013. doi: 10.1016/j.cej.2013.05.047.

[105] B. Selma, R. Bannari, and P. Proulx. Simulation of bubbly flows: Comparison between direct quadrature method of moments (DQMOM) and method of classes (CM). *Chem. Eng. Sci.*, 65(6):1925–1941, 2010. doi: 10.1016/j.ces.2009.11.018.

[106] H. Luo. *Coalescence, breakup, and liquid circulation in bubble column reactors.* Ph.D. thesis, The University of Trondheim, 1993.

[107] H. Luo and H. F. Svendsen. Theoretical model for drop and bubble breakup in turbulent dispersions. *AIChE J.*, 42(5):1225–1233, 1996.

[108] M. Laakkonen, V. Alopaeus, and J. Aittamaa. Validation of bubble breakage, coalescence and mass transfer models for gas-liquid dispersion in agitated vessel. *Chem. Eng. Sci.*, 61(1):218–228, 2006. doi: 10.1016/j.ces.2004.11.066.

[109] C.A. Coulaloglou and L.L. Tavlarides. Description of interaction processes in agitated liquid-liquid dispersions. *Chem. Eng. Sci.*, 32(11):1289–1297, 1977. doi: 10.1016/0009-2509(77)85023-9.

[110] S. S. Alves, C. I. Maia, J. M. T. Vasconcelos, and A. J. Serralheiro. Bubble size in aerated stirred tanks. *Chem. Eng. J.*, 89:109–117, 2002.

[111] A. R. Khopkar, A. R. Rammohan, V. V. Ranade, and M. P. Dudukovic. Gas–liquid flow generated by a Rushton turbine in stirred vessel: CARPT/CT measurements and CFD simulations. *Chem. Eng. Sci.*, 60(8-9):2215–2229, 2005. doi: 10.1016/j.ces.2004.11.044.

[112] Z. Kálal, M. Jahoda, and I. Fořt. Modelling of the bubble size distribution in an aerated stirred tank: Theoretical and numerical comparison of different breakup models. *Chem. and Process Eng.*, 35(3):331–348, 2014. doi: 10.2478/cpe-2014-0025.

[113] M. Laakkonen, M. Honkanen, P. Saarenrinne, and J. Aittamaa. Local bubble size distributions, gas–liquid interfacial areas and gas holdups in a stirred vessel with particle image velocimetry. *Chem. Eng. J.*, 109(1-3):37–47, 2005. doi: 10.1016/j.cej.2005.03.002.

[114] D. Li, Z. Li, and Z. Gao. Quadrature-based moment methods for the population balance equation: An algorithm review. *Chin. J. Chem. Eng.*, 27(3):483–500, 2019. doi: 10.1016/j.cjche.2018.11.028.

[115] E. M. A. Frederix, T. L. W. Cox, J. G. M. Kuerten, and E. M. J. Komen. Poly-dispersed modeling of bubbly flow using the log-normal size distribution. *Chem. Eng. Sci.*, 201:237–246, 2019. doi: 10.1016/j.ces.2019.02.013.

[116] Y. Liao, D. Lucas, E. Krepper, and M. Schmidtke. Development of a generalized coalescence and breakup closure for the inhomogeneous MUSIG model. *Nucl. Eng. Des.*, 241(4):1024–1033, 2011. doi: 10.1016/j.nucengdes.2010.04.025.

[117] H. K. Versteeg and W Malalasekera. *An introduction to CFD finite volume method, 2nd Ed.* Prentice Hall, Harlow, England, 2007.

[118] D. Kreitmayer, S. G. Gopireddy, T. Matsuura, Y. Aki, Y. Katayama, H. Kakihara, K. Nonaka, T. Profitlich, N. A. Urbanetz, and E. Gutheil. Numerical and experimental characterization of the single-use bioreactor Xcellerex^{TM} XDR-200. *Biochem. Eng. J.*, 177:108237, 2022. doi: 10.1016/j.bej.2021.108237.

[119] R. H. Perry and D. W. Green. *Perry's Chemical Engineers' Handbook.* McGraw-Hill, New York, 1997.

[120] J. H. Ferziger and M. Peric. *Computational Methods for Fluid Dynamics, 3rd Ed.* Springer-Verlag, Berlin, 2002.

[121] L. Schiller and A. Naumann. A drag coefficient correlation. *Zeitschrift des Vereins Deutscher Ingenieure*, 77:318–320, 1935.

[122] A. A. Amsden, T. D. Butler, and P. J. O'Rourke. KIVA-II: a computer program for transient multidimensional chemically reactive flows with sprays. *Los Alamos National Lab. (LANL), Los Alamos, NM (United States)*, 1989. doi: 10.2172/6228444.

[123] J. B. Joshi, N. K. Nere, C. V. Rane, B. N. Murthy, C. S. Mathpati, A. W. Patwardhan, and V. V. Ranade. CFD simulation of stirred tanks: Comparison of turbulence models (Part II: Axial flow impellers, multiple impellers and multiphase dispersions). *Can. J. Chem. Eng.*, 89(4):754–816, 2011. doi: 10.1002/cjce.20465.

[124] Y. Zhang, Y. Bai, and H. Wang. CFD analysis of inter-phase forces in a bubble stirred vessel. *Chem. Eng. Res. Des.*, 91(1):29–35, 2013. doi: 10.1016/j.cherd.2012.07.002.

[125] A. Tomiyama, H. Tamai, I. Zun, and S. Hosokawa. Transverse migration of single bubbles in simple shear flow. *Chem. Eng. Sci.*, 57:1849–1858, 2002. doi: 10.1016/S0009-2509(02)00085-4.

[126] H. Rusche. *Computational Fluid Dynamics of Dispersed Two-Phase Flows at High Phase Fractions*. Ph.D. thesis, Imperial College of Science, Technology & Medicine, London, 2002.

[127] A. Behzadi, R. I. Issa, and H. Rusche. Modelling of dispersed bubble and droplet flow at high phase fractions. *Chem. Eng. Sci.*, 59(4):759–770, 2004. doi: 10.1016/j.ces.2003.11.018.

[128] D. Kreitmayer, S.R. Gopireddy, T. Matsuura, Y. Aki, Y. Katayama, T. Nakano, T. Eguchi, H. Kakihara, K. Nonaka, T. Profitlich, N. A. Urbanetz, and E. Gutheil. CFD-based and experimental hydrodynamic characterization of the single-use bioreactor Xcellerex^{TM} XDR-10. *Bioeng.*, 9(1):22, 2022. doi: 10.3390/bioengineering9010022.

[129] M. Coroneo, G. Montante, A. Paglianti, and F. Magelli. CFD prediction of fluid flow and mixing in stirred tanks: Numerical issues about the RANS simulations. *Comput. Chem. Eng.*, 35(10):1959–1968, 2011. doi: 10.1016/j.compchemeng.2010.12.007.

[130] J. C. Lamont and D. S. Scott. An eddy cell model of mass transfer into the surface of a turbulent liquid. *AIChE J.*, 16(4):513–519, 1970.

[131] P. Han and D. M. Bartels. Temperature dependence of oxygen diffusion in H_2O and D_2O. *J. Phys. Chem.*, pages 5597–5602, 1996.

[132] T. K. Villiger, B. Neunstoecklin, D. J. Karst, E. Lucas, M. Stettler, H. Broly, M. Morbidelli, and M. Soos. Experimental and CFD physical characterization of animal cell bioreactors: From micro- to production scale. *Biochem. Eng. J.*, 131:84–94, 2018. doi: 10.1016/j.bej.2017.12.004.

[133] G. K. Gakingo, K. G. Clarke, and T. M. Louw. A numerical investigation of the hydrodynamics and mass transfer in a three-phase gas-liquid-liquid stirred tank reactor. *Biochem. Eng. J.*, 157:107522, 2020. doi: 10.1016/j.bej.2020.107522.

[134] B. Neunstoecklin, M. Stettler, T. Solacroup, H. Broly, M. Morbidelli, and M. Soos. Determination of the maximum operating range of hydrodynamic stress in mammalian cell culture. *J. Biotechnol.*, 194:100–109, 2015. doi: 10.1016/j.jbiotec.2014.12.003.

[135] S. Wollny. *Experimentelle und numerische Untersuchungen zur Partikelbeanspruchung in gerührten (Bio-)Reaktoren*. PhD Thesis, Technische Universität Berlin, 2010.

[136] R. B. Bird, E. N. Lightfoot, and W. E. Stewart. *Transport Phenomena*. J. Wiley & Sons, New York, 2002.

[137] C. Löffelholz. *CFD als Instrument zur bioverfahrenstechnischen Charakterisierung von single-use Bioreaktoren und zum Scale-up für Prozesse zur Etablierung und Produktion von Biotherapeutika*. Ph.D. thesis, Brandenburgische Technische Universität Cottbus, 2013.

[138] Kitware. paraView. 2019.

[139] C. Geuzaine and J.-F. Remacle. Gmsh: a three-dimensional finite element mesh generator with built-in pre- and post-processing facilities. *Int. J. Numer. Methods. Eng.*, 79:1309–1331, 2009.

[140] E. M. Contreras. Carbon dioxide stripping in bubbled columns. *Ind. Eng. Chem. Res.*, 46:6332–6337, 2007.

[141] E. V. Musvoto, M. C. Wentzel, R. E. Loewenthal, and G. A. Ekama. Integrated chemical-physical processes modelling - i. development of a kinetic-based model for mixed weak acid/base systems. *Wat. Res.*, 34(6):1857–1867, 2000.

[142] F. Li, N. Vijayasankaran, A. Shen, R. Kiss, and A. Amanullah. Cell culture processes for monoclonal antibody production. *Monoclonal Antibodies*, 2(5): 466–479, 2010. doi: 10.4161/mabs.2.5.12720.

[143] C. T. Goudar, J. M. Piret, and K. B. Konstantinov. Estimating cell specific oxygen uptake and carbon dioxide production rates for mammalian cells in perfusion culture. *Biotechnol. Prog.*, 27(5):1347–57, 2011. doi: 10.1002/btpr.646.

[144] MATLAB. *9.7.0.1190202 (R2019b)*. The MathWorks Inc., Natick, Massachusetts, 2018.

[145] Cytiva. Xcellerex XDR cell culture bioreactor systems, 2021. https://CDn.cytivalifesciences.com/dmm3bwsv3/AssetStream.aspx?mediaformatid=10061&destinationid=10016&assetid=23694, (Accessed on March 09, 2021).

[146] D. Kreitmayer, S. R. Gopireddy, T. Matsuura, Y. Aki, Y. Katayama, T. Sawada, H. Kakihara, K. Nonaka, T. Profitlich, N. A. Urbanetz, and E. Gutheil. Numerical and experimental investigation of the hydrodynamics in the single-use bioreactor Mobius® CellReady 3 L. *Bioeng.*, 9(5):206, 2022. doi: 10.3390/bioengineering9050206.

[147] S. C. Kaiser. *Characterization and optimization of single-use bioreactors and biopharmaceutical production processes using computational fluid dynamics*. Ph.D. thesis, Technische Universität Berlin, 2014.

[148] A. O. O. Odeleye. *Engineering Characterisation of single-use bioreactor technology for mammalian cell culture applications*. Ph.D. thesis, University College London, 2015.

[149] H. A. Jakobsen, B. H. Sannæs, S. Grevskott, and H. F. Svendsen. Modeling of vertical bubble-driven flows. *Ind. Eng. Chem. Res.*, 36:4052–4074, 1997.

[150] A. W. Nienow. On impeller circulation and mixing effectiveness in the turbulent flow regime. *Chemial Engineering Science*, 52(15):2557, 1997.

[151] C. Löffelholz, U. Husemann, G. Greller, W. Meusel, J. Kauling, P. Ay, M. Kraume, R. Eibl, and D. Eibl. Bioengineering parameters for single-use bioreactors: overview and evaluation of suitable methods. *Chem. Ing. Tech.*, 85(1-2):40–56, 2013. doi: 10.1002/cite.201200125.

[152] C. Haringa, H. J. Noorman, and R. F. Mudde. Lagrangian modeling of hydrodynamic–kinetic interactions in (bio)chemical reactors: Practical implementation and setup guidelines. *Chem. Eng. Sci.*, 157:159–168, 2017. doi: 10.1016/j.ces.2016.07.031.

[153] T. K. Villiger, M. Morbidelli, and M. Soos. Experimental determination of maximum effective hydrodynamic stress in multiphase flow using shear sensitive aggregates. *AIChE J.*, 61(5):1735–1744, 2015. doi: 10.1002/aic.14753.

[154] Cytiva, 2022. https://www.cytivalifesciences.com/en/us/support/products/xcellerex-xdr-50-to-2000-single-vessel-29048372, (Accessed on March 14,2022).

[155] V. Machon, A. W. Pacek, and A. W. Nienow. Bubble sizes in electrolyte and alcohol solutions in a turbulent stirred vessel. *Chem. Eng. Res. Des.*, 75(3): 339–348, 1997. doi: 10.1205/026387697523651.

[156] M. Bouaifi and M. Roustan. Bubble size and mass transfer in coefficients in dual-impeller agitated reactors. *Can. J. Chem. Eng.*, 76:390–397, 1998.

[157] Mariano Martín, Francisco J. Montes, and Miguel A. Galán. Bubbling process in stirred tank reactors I: Agitator effect on bubble size, formation and rising. *Chem. Eng. Sci.*, 63(12):3212–3222, 2008. doi: 10.1016/j.ces.2008.03.028.

[158] A. Busciglio, F. Grisafi, F. Scargiali, and A. Brucato. On the measurement of local gas hold-up, interfacial area and bubble size distribution in gas–liquid contactors via light sheet and image analysis: Imaging technique and experimental results. *Chem. Eng. Sci.*, 102:551–566, 2013. doi: 10.1016/j.ces.2013.08.029.

[159] N. Hashemi, F. Ein-Mozaffari, S. R. Upreti, and D. K. Hwang. Experimental investigation of the bubble behavior in an aerated coaxial mixing vessel through electrical resistance tomography (ert). *Chem. Eng. J.*, 289:402–412, 2016. doi: 10.1016/j.cej.2015.12.077.

[160] B. O. Hasan. Experimental study on the bubble breakage in a stirred tank. Part 1. mechanism and effect of operating parameters. *Int. J. Multiph. Flow*, 97:94–108, 2017. doi: 10.1016/j.ijmultiphaseflow.2017.08.006.

[161] B. O. Hasan. Experimental study on the bubble breakage in a stirred tank Part 2: Local dependence of breakage events. *Exp. Therm. Fluid Sci.*, 96:48–62, 2018. doi: 10.1016/j.expthermflusci.2018.02.013.

[162] D. Mesa and P. R. Brito-Parada. Bubble size distribution in aerated stirred tanks: Quantifying the effect of impeller-stator design. *Chem. Eng. Res. Des.*, 160:356–369, 2020. doi: 10.1016/j.cherd.2020.05.029.

[163] N.A. Kazakis, A.A. Mouza, and S.V. Paras. Experimental study of bubble formation at metal porous spargers: Effect of liquid properties and sparger characteristics on the initial bubble size distribution. *Chem. Eng. J.*, 137:265–281, 2008. doi: 10.1016/j.cej.2007.04.040.

[164] N. Ma, J. J. Chalmers, J. G. Aunin, W. Zhou, and L. Xie. Quantitative studies of cell-bubble interactions and cell damage at different pluronic f-68 and cell concentrations. *Biotechnol. Prog.*, 20(4), 2004.

[165] J. B. Joshi, K. Nandakumar, G. M. Evans, V. K. Pareek, M. M. Gumulya, M. J. Sathe, and M. A. Khanwale. Bubble generated turbulence and direct numerical simulations. *Chem. Eng. Sci.*, 157:26–75, 2017. doi: 10.1016/j.ces.2016.03.041.

[166] Cytiva. Engineering characterization of the single-use xcellerex XDR-2000 stirred-tank bioreactor system, 2021. https://CDn.cytivalifesciences.com/dmm3bwsv3/AssetStream.aspx?media formatid=10061&destinationid=10016&assetid=23694, (Accessed on March 09,2021).

[167] V. Sandner, L. P. Pybus, G. McCreath, and J. Glassey. Scale-down model development in ambr systems: An industrial perspective. *Biotechnol J*, page e1700766, 2018. ISSN 1860-7314 (Electronic) 1860-6768 (Linking). doi: 10.1002/biot.201700766. URL `https://www.ncbi.nlm.nih.gov/pubmed/30350921`.

[168] T. Tajsoleiman, L. Mears, U. Kruhne, K. V. Gernaey, and S. Cornelissen. An industrial perspective on scale-down challenges using miniaturized bioreactors. *Trends Biotechnol*, 37(7):697–706, 2019. doi: 10.1016/j.tibtech.2019.01.002.

[169] P. Xu, C. Clark, T. Ryder, C. Sparks, J. Zhou, M. Wang, R. Russell, and C. Scott. Characterization of TAP Ambr 250 disposable bioreactors, as a reliable scale-down model for biologics process development. *Biotechnol Prog*, 33(2):478–489, 2017. doi: 10.1002/btpr.2417.

[170] C. Maske. *Simulation of multiphase flows in Single-use bioreactor system Ambr250.* Master thesis, Technical University Munich, 2020.

[171] Sartorius. https://www.sartorius.com/en/products/fermentation-bioreactors/ambr-multi-parallel-bioreactors/ambr-250-high-throughput, (Accessed on May 11,2022).

[172] X. Li, K. Scott, W. J. Kelly, and Z. Huang. Development of a computational fluid dynamics model for scaling-up Ambr bioreactors. *Biotechnol. Bioprocess Eng.*, 23:710–725, 2018. doi: 10.1007/s12257-018-0063-5.

[173] M. Jamialahmadi, M. R. Zehtaban, H. Müller-Steinhagen, A. Sarrafi, and J. M. Smith. Study of bubble formation under constant flow conditions. *Chem. Eng. Res. Des.*, 79(5):523–532, 2001. doi: 10.1205/02638760152424299.

[174] P. H. Calderbank. Physical rate process in industrial fermentation - Part I: The interfacial area in gas-liquid contacting with mechanical agitation. *Trans. Inst. Chem. Eng*, 36:443–463, 1958.

[175] S. T. You, A. A. A. Raman, R. S. S. R. E Shah, and M. I. M. Nor. Multiple-impeller stirred vessel studies. *Rev. Chem. Eng.*, 30(3):323–336, 2014. doi: 10.1515/revce-2013-0028.

[176] R. K. Grenville. *Blending of viscous Newtonian and pseudo-plastic fluids.* Ph.D. thesis, Cranfield Institute of Technology, 1992.

[177] J. C. Lagarias, J. A. Reeds, M. H. Wright, and P. E. Wright. Convergence properties of the Nelder–Mead simplex method in low dimensions. *SIAM J. Optim*, 9(1):112–147, 1998. doi: 10.1137/s1052623496303470.

[178] S. Xu, R. Jiang, R. Mueller, N. Hoesli, T. Kretz, J. Bowers, and H. Chen. Probing lactate metabolism variations in large-scale bioreactors. *Biotechnology Progress*, 34(3):756–766, 2018. doi: 10.1002/btpr.2620.

[179] C. He, P. Ye, H. Wang, X. Liu, and F. Li. A systematic mass-transfer modeling approach for mammalian cell culture bioreactor scale-up. *Biochem. Eng. J.*, 141: 173–181, 2019. doi: 10.1016/j.bej.2018.09.019.

[180] S. Xu and H. Chen. High-density mammalian cell cultures in stirred-tank bioreactor without external pH control. *J. Biotechnol.*, 231:149–159, 2016. doi: 10.1016/j.jbiotec.2016.06.019.

[181] L. Hoshan, R. Jiang, J. Moroney, A. Bui, X. Zhang, T. C. Hang, and S. Xu. Effective bioreactor pH control using only sparging gases. *Biotechnol. Prog.*, 35 (1):e2743, 2019. doi: 10.1002/btpr.2743.

[182] A. A. Unver and D. M. Himmelblau. Diffusion coefficients of CO_2, C_2H_4, CsHe, and C_4H_8 in water from 6° to 65° c. *J. Chem. Eng. Data*, 9(3):428 –431, 1964.

[183] H. Shirahata, . Diab, H. Sugiyama, and D. I. Gerogiorgis. Dynamic modelling, simulation and economic evaluation of two CHO cell-based production modes towards developing biopharmaceutical manufacturing processes. *Chem. Eng. Res. and Des.*, 150:218–233, 2019. doi: 10.1016/j.cherd.2019.07.016.

[184] M. Pigou and J. Morchain. Investigating the interactions between physical and biological heterogeneities in bioreactors using compartment, population balance and metabolic models. *Chem. Eng. Sci.*, 126:267–282, 2015. doi: 10.1016/j.ces.2014.11.035.

Abbreviations and Symbols

Abbreviation	Meaning
CFD	Computational Fluid Dynamics
CHO	Chinese hamster ovary
dCO_2	dissolved carbon dioxide
EE	Euler-Euler
EL	Euler-Lagrange
MRF	Multiple Reference Frame
QbD	Quality by Design
RMSE	root mean square error
rpm	revolutions per minute
vvm	volume per volume per minute

Symbol	Unit	Meaning
a	[m^{-1}]	specific interface area
A	[m^2]	area
c	[mol m^{-3}]	concentration
C	[-]	model coefficient
c_x	[cells L^{-1}]	cell density
CTR	[mol L^{-1} d^{-1}]	carbon dioxide transfer rate
d	[m]	diameter
D	[m^2 s^{-1}]	diffusion coefficient
DO	[N m^{-2}]	dissolved oxygen tension
Eo	[-]	Eötvös number
$\mathbf{F}$	[N]	force
f	[-]	function
$\mathbf{g}$	[m s^{-2}]	gravitational acceleration
G	[kg $m^{-1}s^{-3}$]	turbulence kinetic energy generation
h	[m]	height
He	[mol L^{-1} Pa^{-1}]	Henry constant
k	[m^2 s^{-2}]	turbulence kinetic energy
k_L	[m h^{-1}]	liquid transfer coefficient
k_La	[h^{-1}]	volumetric oxygen mass transfer coefficient
l_K	[m]	Kolmogorov length scale
m	[kg]	mass
M	[N m]	torque
n	[s^{-1}]	rotational speed
n_{CO_2} or n_{CO_2}	[mol]	amount of substance
n_b	[-]	number of bubbles
N_P	[-]	impeller power number
p	[Pa]	pressure
OTR	[mol L^{-1} d^{-1}]	oxygen transfer rate
P	[W]	impeller power input
P/V	[W m^{-3}]	volumetric power input
Q	[m^3s^{-1}]	gas flow rate
q	[mol d^{-1} per cell]	cell specific exchange rate
$\mathbf{R}_{eff}$	[kg m^{-1} s^{-2}]	effective stress tensor
Re	[-]	impeller Reynolds number
$\mathbf{S}$	[kg m^{-1} s^{-2}]	momentum exchange term
Sc_t	[-]	turbulent Schmidt number
$\mathbf{T}$	[s^{-1}]	strain rate tensor
t	[s]	time
$\mathbf{u}$	[m s^{-1}]	velocity vector
u_s	[m s^{-1}]	superficial gas velocity
V	[m^3]	volume
$\mathbf{x}$	[m]	position vector

Symbol	Unit	Meaning
x	[m]	spatial coordinate
y	[m]	spatial coordinate
y_i	[-]	molar fraction
z	[m]	spatial coordinate
α	[-]	volume fraction
β	[-]	model coefficient
γ	[s^{-1}]	strain rate
ε	[m^2 s^{-3}]	turbulence energy dissipation rate
θ	[s]	mixing time
μ	[d^{-1}]	growth rate
μ_l or μ_g	[Pa s]	dynamic viscosity
ν	[m^2 s^{-1}]	kinematic viscosity
ρ	[kg m^{-3}]	density
σ_k	[-]	model coefficient
σ_ϵ	[-]	model coefficient
τ_l	[Pa]	hydrodynamic stress
τ_{tn}	[Pa]	shear stress
$\phi_{CO_2^*}$	[-]	fraction of dCO_2 and H_2CO_3 of the total dissolved inorganic carbon species

Subscript	Meaning
b	bubble
c	continuous phase
cyl	cylinder
CV	control volume
D	drag
d	disperse phase
eff	effective
g	gas
G	gravity
imp	impeller
L	lift
l	liquid
m	mixture
O_2	oxygen
CO_2	carbon dioxide
P	pressure gradient force
pro	product
T	tracer
t	turbulent
tot	total
tn	normal direction
rel	relative
VM	virtual mass
V	vessel

Acknowledgments

This project is funded by Daiichi-Sankyo Japan and carried out in collaboration with Daiichi-Sankyo Europe and Prof. Dr. Eva Gutheil from the University of Heidelberg.

First and foremost I want to thank Prof. Dr. Eva Gutheil, head of the research group for multiphase flows and combustion, for her guidance and supervision. She made it possible for me to be integrated into her search group despite the physical distance through my regular workplace within the project at Daiichi-Sankyo Europe in Pfaffenhofen (Ilm). Her insightful comments enabled the progress of the work. Her perseverance and eye for detail when providing comments and corrections on papers, publications and this thesis helped me to improve and refine them. She also supported me by enabling me to attend her group seminar and lecture remotely. She also provided me with access to the computational resources needed for this work.

My special thanks also go to Dr. Nora A. Urbanetz from Daiichi-Sankyo Europe the second supervisor in this collaboration project. The regular discussions as well as the continuous and kind support from her helped me to keep a broader perspective on the overall project. Her guidance on the statistical analysis of the experimental results, and her help by reviewing publications and presentations as well as this thesis allowed me to improve my work.

Dr. Srikanth R. Gopireddy from Daiichi-Sankyo Europe guided my work within the collaboration project on a day to day basis. I want to thank him for the many fruitful discussions, his open ear for all major and minor questions, and his ongoing support in the preparation of publications and presentations. He also took the role of technically support providing, managing, and fixing the simulation workstations at Daiichi-Sankyo Europe.

For his Master thesis at the Technical University of Munich, Christopher Maske performed the simulations of the Ambr® 250 at Daiichi-Sankyo Europe. Kristof Pandi, Bachelor student of the Technical University of Munich, ran the XDR-500 during his time as a working student at Daiichi-Sankyo Europe. I want to thank both for their great work and effort.

Moreover, I want to thank the experimental partners of the collaboration Tomomi Matsuura, Yuichi Aki, and Yuta Katayama from Daiichi-Sankyo Japan for supporting me with their expertise on cell cultivation and sharing their hands on experience on the cell culture process development and scale-up. Tomomi Matsuura, Takuya Nakano, and Takuma Eguchi provided me with the experimental results on the vortex formation, the mixing time, and the volumetric oxygen mass transfer coefficient reported in this thesis. The presented experimental results of the different cell cultivation experiments have

been provided by Yuichi Aki. The discussion with them helped me better understand the interests and concerns from an cell culture operators point of view. My thanks also go to Hirofumi Kakihara and Dr. Koichi Nonaka, who provided supervision and resources at Daiichi-Sankyo Japan.

Last but not least I want to thank my family for always giving me their continued and full support and enabling me to focus on my work.

GESAMTFAKULTÄT FÜR MATHEMATIK, INGENIEUR- UND NATURWISSENSCHAFTEN

COMBINED FACULTY OF MATHEMATICS, ENGINEERING AND NATURAL SCIENCES

RUPRECHT-KARLS-
UNIVERSITÄT
HEIDELBERG

Eidesstattliche Versicherung gemäß § 8 der Promotionsordnung für die Gesamtfakultät für Mathematik, Ingenieur- und Naturwissenschaften der Universität Heidelberg /
Sworn Affidavit according to § 8 of the doctoral degree regulations of the Combined Faculty of Mathematics, Engineering and Natural Sciences at Heidelberg University

1. Bei der eingereichten Dissertation zu dem Thema / The thesis I have submitted entitled

   Computational Fluid Dynamics Simulations of Single-Use Bioreactors for the Scale-Up of Cell Culture Processes

   handelt es sich um meine eigenständig erbrachte Leistung / is my own work.

2. Ich habe nur die angegebenen Quellen und Hilfsmittel benutzt und mich keiner unzulässigen Hilfe Dritter bedient. Insbesondere habe ich wörtlich oder sinngemäß aus anderen Werken übernommene Inhalte als solche kenntlich gemacht. / I have only used the sources indicated and have not made unauthorised use of services of a third party. Where the work of others has been quoted or reproduced, the source is always given.

3. Die Arbeit oder Teile davon habe ich ~~wie folgt/~~bislang nicht[1)] an einer Hochschule des In- oder Auslands als Bestandteil einer Prüfungs- oder Qualifikationsleistung vorgelegt. / I have not yet/have already[1)] presented this thesis or parts thereof to a university as part of an examination or degree.

   Titel der Arbeit / Title of the thesis: ……

   Hochschule und Jahr / University and year: ……

   Art der Prüfungs- oder Qualifikationsleistung / Type of examination or degree: ……

4. Die Richtigkeit der vorstehenden Erklärungen bestätige ich. / I confirm that the declarations made above are correct.

5. Die Bedeutung der eidesstattlichen Versicherung und die strafrechtlichen Folgen einer unrichtigen oder unvollständigen eidesstattlichen Versicherung sind mir bekannt. / I am aware of the importance of a sworn affidavit and the criminal prosecution in case of a false or incomplete affidavit.

Ich versichere an Eides statt, dass ich nach bestem Wissen die reine Wahrheit erklärt und nichts verschwiegen habe. / I affirm that the above is the absolute truth to the best of my knowledge and that I have not concealed anything.

…….. ……..

Ort und Datum / Place and date — Unterschrift / Signature

[1)] Nicht Zutreffendes streichen. Bei Bejahung sind anzugeben: der Titel der andernorts vorgelegten Arbeit, die Hochschule, das Jahr der Vorlage und die Art der Prüfungs- oder Qualifikationsleistung. / Please cross out what is not applicable. If applicable, please provide: the title of the thesis that was presented elsewhere, the name of the university, the year of presentation and the type of examination or degree.

The German text is legally binding.